Nonlinear Dynamics of Acid- and Base-Regulated Chemical Systems

Rachel Elizabeth McIlwaine

Submitted in accordance with the requirements for the degree of

Doctor of Philosophy

The University of Leeds

School of Chemistry

Physical Chemistry Section

April 2007

Acknowledgements

The continued wisdom and friendship of my supervisor, Annette Taylor, has meant that my PhD has not only been enjoyable, but an experience I will never forget. Her knowledge, enthusiasm, teaching and laughter has always been appreciated - Thank you Annette! Thanks also go to Steve Scott.

I would like to thank all the people I've met and worked with in this department over the past four years - it was a pleasure! Great thanks to my colleague and friend Klara Kovacs who provided the excellent experimental pictures for chapter four. It was also a pleasure and privilege to work with the patient and most amazing teacher Vilmos Gaspar. Cheers to Kelly Gannon for gossip and lunches, Panos. Kapetanopoulos, Sally Taylor, Dave Golwacki, Drs Shona Smith, Rita Toth, Gav. Armstrong, Mark Blitz, Andy Rickard, Andy Goddard and Matt. Davies. Of course my dearest and most useless friends Tom and Dave must get a special mention – thanks a lot guys. Now to you kids that have kept me sane, supported and always been there for me - big love to Mark for always being able to make me laugh and for our friendship, to Annie who helped me through some hard times, always listened and managed to say what I needed to hear, and of course to Cathy for always believing in me when I did not. Thank you friends, you're wonderful.

This thesis is dedicated to my fantastic family - Sez, Mum and Dad (and Cluedo) - without your support, love, laughter and unfaltering belief in me I wouldn't have been able to do this. I love you all LOADS!!!

Abstract

Interest in the interdisciplinary field of nonlinear dynamics has increased significantly over the past three decades. Nonlinear dynamics is the study of the temporal and spatio–temporal evolution of dynamical systems whose behaviour depends on the values of the key variables in a nonlinear manner.

Nonlinear chemical reactions, chemical oscillations and their spatial behaviour play an important part in the field of nonlinear dynamics. This thesis is concerned primarily with those chemical systems which feature the proton, or its counterpart the hydroxide ion, as a main kinetic driving species. A review of the area is presented to provide a background for the developments discussed in this thesis. Experimental and numerical investigation of the methylene glycol–sulfite reaction leads to the development of a complete kinetic model for this system. This new mechanism provides the basis of a reduced model for the design of novel pH oscillators. This reduced model, discussed in chapter 4, is used to design the first organic substrate based, non–redox, pH oscillating reaction, the methylene glycol–sulfite–gluconolactone system. In an open reactor this reaction displays large amplitude oscillations in pH which are well modelled with a proposed mechanism.

In chapter 5 experimental results of an acid autocatalytic reaction performed in nano–meter size water droplets are presented. The effects of confinement on the kinetics is established and shown to be affected by changes in droplet size and dispersion of droplets. The effect of the microheterogeneties of the microenvironment on reaction–diffusion fronts in this system is also investigated. The results show the propagation of acid fronts with interesting structural instabilities.

List of Figures

CHAPTER 1

CHAPTER 2

CHAPTER 3

CHAPTER 4

CHAPTER 5

List of Tables

CHAPTER 1

CHAPTER 3

CHAPTER 4

CHAPTER 5

CHAPTER 1

Introduction and review of pH regulated nonlinear kinetics

1.1 Introduction

Oscillations in homogenous chemical systems were not accepted by the chemical community until the late 20th century, after much controversy. The oscillations reported by Bray (1) in the iodate, iodine hydrogen peroxide mixture were thought to be a product of dust or bubbles in the mixture (2). Similarly, the work of Boris Belousov on the oscillations in an inorganic analogue of the Krebs cycle were unpublished, as reviewers did not believe his 'supposed discovered discovery' (3). Finally in 1964 the graduate student Anatol Zhabotinsky continued Belousov's earlier work and the results were published (4), acknowledging the first experimental evidence for oscillations in a chemical system, the Belousov-Zhabotinsky reaction. This publication, along with the work of Ilya Prigogine (5) and his group in Brussels, began to pave the way for the acceptance of oscillating chemical reactions as a legitimate area of study. In 1972 Field *et al.* (6) produced the first full chemical mechanism of an oscillating chemical reaction which could explain the quantitative behaviour in the BZ reaction. This mechanism was based on the same principles of chemical kinetics and thermodynamics that govern 'normal' chemical systems, and so provided irrefutable evidence for the existence of oscillations in chemical systems. This model was later successfully reduced from its twenty something elementary steps to a three variable model (7) which maintained all the essential features of the BZ reaction. Extensive numerical analysis of the BZ reaction was now also feasible with the 'Oregonator' model.

The initial unwillingness of the chemical community to accept the results of chemical oscillations in closed systems was because these 'oscillations' apparently violated the 2nd law of thermodynamics. This law states that "the entropy of an isolated system not in equilibrium will tend to increase over time, approaching a

maximum value at equilibrium"(8). Thus, the free energy of a closed system will decrease monotonically in time on approach to equilibrium. There cannot be oscillations about the chemical equilibrium. However, the possibility of initiating (or indeed maintaining) a system far from equilibrium allows a finite time in which oscillations and other behaviour may be seen. Classical thermodynamics cannot dictate what might happen in the early stages of a reaction far from equilibrium, only that the free energy must decrease monotonically. The ability to keep a system open (which incidentally is what most real systems are, with a continual change of mass with the surroundings) allows us to maintain a permanent non-equilibrium state governed by the laws of nonequilibrium thermodynamics (9).

The next challenge for chemists was the search for additional chemical reactions that could display oscillations. By the late 1970s there were only two experimental examples of oscillating reactions, the BZ and Bray reaction (or slight variations of these). In order for scientists to understand and elucidate the nature of these fascinating systems, more examples were needed. The identification of several autocatalytic inorganic reactions by the Epstein group in 1976 (10,11) provided a starting point for the development for the design of more chemical oscillators. Simultaneously, the Bordeaux group (12) were pioneering the use of the CSTR as an experimental tool in the study of nonlinear reactions and in 1980 (13) a theoretical model was produced showing how oscillations may be obtained in a CSTR by appropriate perturbation of a bistable, autocatalytic chemical system. By 1981 the first systematically designed chemical oscillator, the arsenite-iodate-chlorite system (14) was produced. The technique (the cross shaped phase diagram method, see section 1.2.4) was then refined to produce dozens of new chemical oscillators over the next decade.

Chemical oscillations occur widely in biology (15.16) as a natural consequence of feedback processes that occur in living systems (17). Table 1.1 gives an example of some biological oscillators and their oscillatory period.

Type	Period
Neural	0.01- 10s
Cardiac	1 s
Calcium	1 s to several minutes
Glycolytic	Several minutes
Microtubules	2 – 10 min
cAMP in *Dictyostelium*	5 – 10 min
Cell cycle (vertebrates)	24 h
Circadian	24 h
Human Ovarian	28 days
Annual (e.g. plants)	1 year

Table 1.1 Examples of some biological oscillators (18).

The ability to develop simple chemical oscillators that mimic certain features of these biological systems may provide insight into these nonlinear processes, as the underlying mechanisms (i.e. feedback based instabilities (19)) are similar. Interest in chemical oscillators is therefore many fold, from academic interest of chemical kinetics to the design and control of laboratory based chemical reactions that mimic biological features.

The design of pH oscillators is of particular interest (20). pH oscillators display large amplitude oscillations in pH which are a driving force for, rather than a consequence or indicator of, the oscillations. Hydrogen ion concentration (and that of its counterpart the hydroxide ion) plays a very important part in nearly all reactions

in aqueous solution from inorganic systems to complex processes in living organisms. The development of pH oscillating reactions has potential applications for the design of novel chemomechanical and biomimetic devices (20-26). The coupling of pH oscillators with chemo-sensitive polymers has been suggested as a means of directly converting chemical into mechanical energy (20). A pH oscillating reaction has been used to change the conformation of DNA from folded to a random coil motif, thereby creating a pH driven nano-switch (24). pH oscillators have also been suggested as a source of fuel to drive synthetic muscles (22) or periodic drug delivery (25). Such devices may find applications in periodic drug delivery (26). as actuators (22) or micropumps or switches (21,22,25). Recently, the coupling of a pH oscillator with fast complexation or precipitation equilibria has lead to the design of systems which can produce pulses of Ca^{2+} and Al^{3+} ions (27). This has been suggested as a means to probe the dynamics of certain biological processes (28).

For pH oscillating chemical systems to be used in conjunction with polymer gels and chemo-sensitive polymers the development of less aggressive, biocompatible pH oscillators is necessary. To date, aside from the complex heterogenous reaction of palladium catalysed phenylacetylene oxidation (29), pH oscillating reactions are limited to redox reactions (30,31). H^+ is produced autocatalytically from the oxidation of S(IV) species, arsenite or hydroxylamine (32) (AsO_3^-, NH_2OH) by inorganic oxidants (i.e. IO_3^- (33), BrO_3^-, ClO_3^- or H_2O_2 (34)). The negative feedback/ proton consumption in open reactors has generally been provided by the use of reductants such as ferrocyanide (35), thiosulfate (36,37) thiourea (38) and more recently novel reductants such as marble chips (39) or manganate species (40). These systems display large amplitude oscillations in redox

potential accompanying oscillations in pH. indicating they are aggressive oxidation reduction processes.

In biological systems (41) changes in the pH of the reaction medium play an important role, as many physiological parameters are affected by pH value. Small amplitude pH oscillations have been observed in glycolysis (42), although these are a consequence of the feedback in enzyme driven processes rather than being the kinetic driving force. Propagating waves of protons have been observed in a cellular medium such as in neutrophil cells (43), glial cells (44), and yeast cells during glycolysis (42). Complex pH patterns, which are dependent on light intensities have also been observed near the surface of *chara carallina* cells (45). Transitions have been observed from homogenous pH distribution to alternating pH bands which are thought to proceed through the initial appearance of multiple patches, with a localized H^+ transporting activity and subsequent spot rearrangements leading to alternating band formation.

Recent work by Kovacs *et al.* (46,47) has shown that temperature compensation exists in the hydrogen peroxide-sulfite ion-thiosulfite system. Oscillating chemical reactions can show a dependence on temperature and oscillations may only occur in a certain temperature range. Temperature can also effect transitions between steady and oscillatory states and induce more complex behaviour in chaotic systems. However, many biological clocks and circadian rhythms are independent of temperature changes within a reasonable physiological range. This phenomenon, called temperature compensation, is observed in many systems and is responsible for keeping the period length constant under a range of environmental conditions. The temperature compensation in the chemical systems examined is thought to occur through antagonistic balance between the positive and

negative feedback reactions of the system. They successfully showed that an increase in temperature increases the rate constants of the positive feedback reactions, thus shortening the period length. The increase in temperature will also increase the rate constants of the negative feedback thus decreasing the period length. Thus, for certain sets of reactions the effects on both the positive and the negative feedback reactions will compensate each other and the period length will stay constant.

This introductory chapter is an overview of the thermodynamics of nonlinear chemical systems, and the numerical and experimental methods used in their analysis. The accepted model for the design of autocatalytic pH systems is discussed along with mechanistic analysis of the bromate-sulfite reaction - a prototypical autocatalytic pH system. The spatio-temporal evolution of this reaction is also discussed. The structure of the thesis is given in section 1.5.

1.2 Kinetics

1.2.1 Requirements of the system

There are two criteria for a chemical system to fulfil if it is to display any interesting features such as clocks, bistability and chaos. First, the system must be *far from equilibrium*. In the experimental study of nonlinear dynamics there are two common methods of achieving this. The simplest is a closed batch reactor where the reaction is set up with initial conditions far from the equilibrium compositions. The system can then display interesting behaviour on its approach to equilibrium. Nonlinear kineticists also utilise flow reactors where there is a fresh inflow of reactants and a matched outflow of products. Here there is a continuous exchange of matter with the surroundings so that the system is maintained far from equilibrium. The use of well stirred open or flow reactors allows true stationary states to be realized so that time

dependent features such as oscillations can be studied. Figure 1.1 shows a schematic of a batch and open reactor, both reactors contain a stirrer to ensure complete mixing.

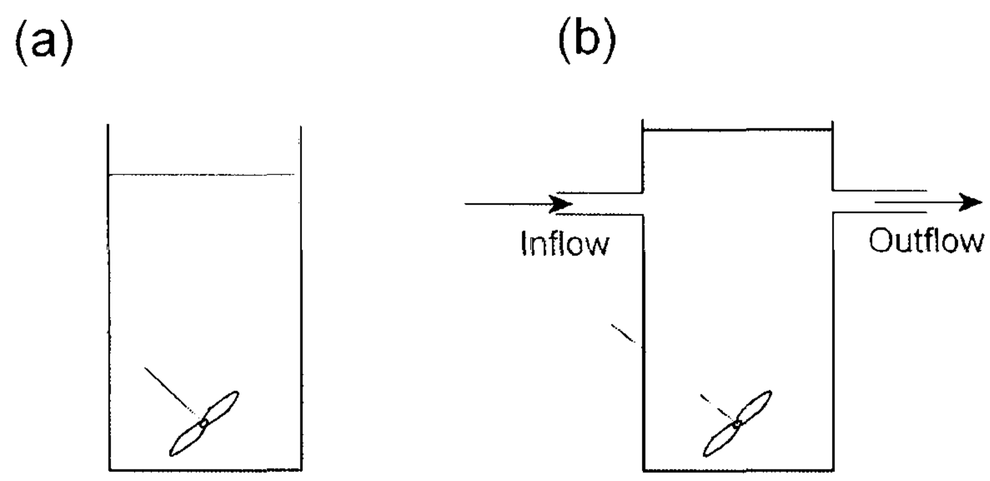

Figure 1.1 Schematic batch and flow experimental set up.

In the open reactor (b), reactants are pumped through an inflow port at a constant total rate q ($m^3\ s^{-1}$). The reactant volume pumped in pushes out an equal volume of the solution at the same rate q. In practice a peristaltic pump is normally used as this facilitates constant smooth pumping. If the volume of the reactor is taken as V (m^3), the volume divided by the flow rate has units of s. This is the residence time of the reactor and represents the average time spent by a molecule in the reactor.

$$t_{res} = \frac{V\ (m^3)}{q\ (m^3 s^{-1})} = (s)$$

The reciprocal of the residence time is the flow rate (velocity), having units of s^{-1}. High flow rates are equivalent to short residence times, and vice versa.

The second requirement for any 'interesting' behaviour is the presence of feedback in the kinetics of the reaction. Feedback is defined as occurring when 'the products of later steps in the mechanism influence the rate of some of the earlier reactions, and hence the rate of their own production' (48). For any reacting chemical system there exists a set of differential equations that describe how the concentrations of all the chemical species change with time. The rate of change of species X, calculated from mass balance, can be written as:

$$\text{Rate of change of X} = \frac{dX}{dt} = \text{Production} - \text{Consumption } \mathbf{(+ Inflow - Outflow)}$$

The inflow and outflow terms (bold) are applicable to open systems. They are calculated from the flow rate (k_0) through the reactor and the initial concentration of the inflowing species. The production and consumption terms are determined by the chemical reaction and calculated from the elementary steps that make up the reaction. For a mechanism with many elementary steps it is possible to construct differential rate equations for each variable that describe the rate of change of each concentration by adding the contributions from all the elementary steps. The differentials are classified as either linear, or nonlinear. If the dynamic laws for a chemical system are linear, its behaviour must be reasonably simple. That is the concentrations of the reactants must decrease monotonically with time, the concentration of products must increase monotonically with time, and the concentration of any intermediate must pass through a maximum or a minimum through the course of reaction. Most systems are not linear. Figure 1.2 shows the rate extent plots for ordinary deceleratory systems. Only the middle curve is linear, representing an ideal first order, isothermal reaction. The rate of all these reactions is at a maximum at the beginning of the reaction, and decreases as the reactants are consumed.

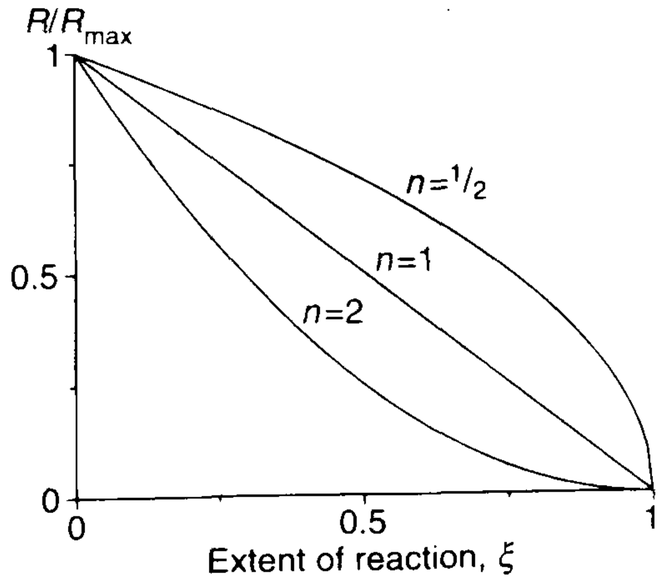

Figure 1.2 Rate extent plots for deceleratory processes having no feedback in their kinetic mechanism. Only the middle line (n = 1) is linear.

Figure 1.3 shows rate extent plots which are not only nonlinear. but also display feedback. Here the maximum rate is at some nonzero extent of reaction.

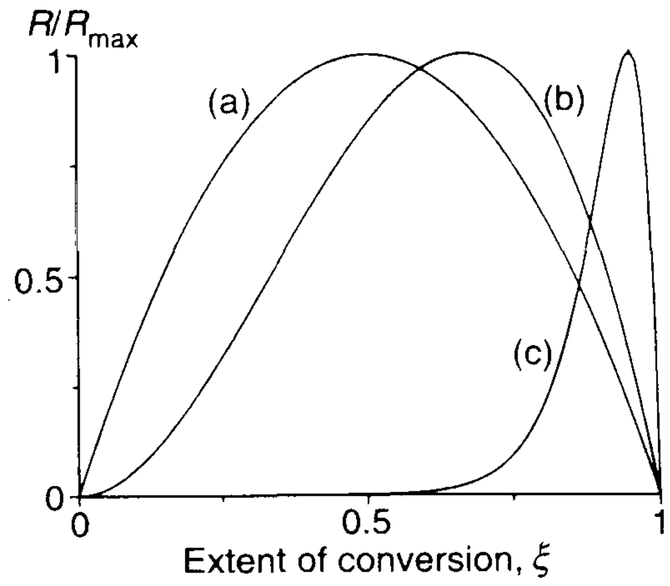

Figure 1.3 Rate extent plots for chemical systems which have feedback in their kinetic mechanisms (a) quadratic autocatalysis (b) cubic autocatalysis and (c) an exothermic reaction with thermal feedback.

Systems which display feedback have nonlinear rate equations and show a maximum in their rate at some non zero extent of reaction. It is feedback that is the origin of the interesting behaviour such as clocks, bistability and oscillations. Feedback can be positive (acceleratory) or negative (inhibitory). The most common form of feedback in chemical kinetics is autocatalysis, for example:

$A + B \rightarrow 2B$	$Rate = kab$	Quadratic autocatalysis
$A + 2B \rightarrow 3B$	$Rate = kab^2$	Cubic autocatalysis

1.2.2 Closed reactors

The simplest. nontrivial behaviour displayed by chemical systems displaying feedback, far from equilibrium, is clock behaviour. In a batch reactor there is an induction time during which the concentration of the clock chemical is low. At the end of the induction period (t_{ind}) the concentration of the clock chemical increases rapidly. In the case of a pH clock reaction this species will be H^+ or OH^-. Clock reactions are usually depicted as temporal evolution of a concentration, an example of which is shown in Figure 1.4

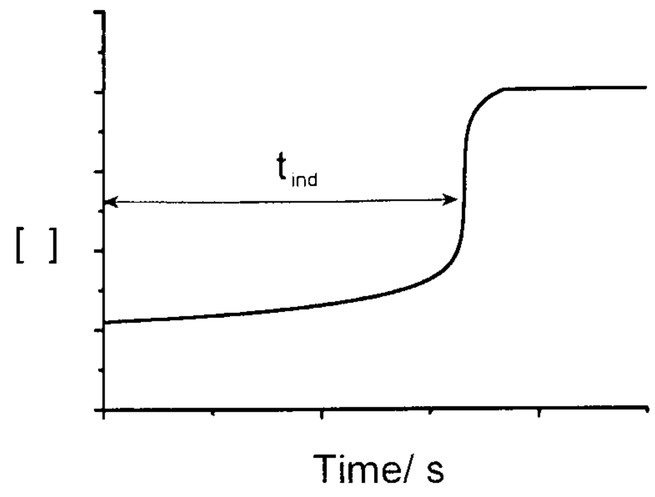

Figure 1.4 Schematic of clock reaction behaviour of a system possessing feedback in a batch reactor, showing the variation of concentration in time.

The clock reaction terminates after a change in concentration of several orders of magnitude of one of the intermediates. The system is then at its globally stable equilibrium state. The equilibrium state is the *only* stable steady state for reactions in closed reactors. After the clock event the system is unable to return to its initial state as there is no mechanism which facilitates the 'resetting' of the clock. Some chemical systems are able to display oscillations in batch (the most famous being the BZ) but this behaviour is still transient and the oscillations must eventually 'die out'. In the BZ reaction there is an additional chemical step in the mechanism where the clock chemical is removed so that the clock process can restart. It is the concentration of 'intermediate' species that gives rise to the oscillatory time series in batch BZ experiments, not the oscillation of the concentration of the major reactants. The concentration of these species must decay continuously throughout the reaction as the system approaches equilibrium. To date there are no systems known to exhibit long-term periodic pH oscillations under batch conditions.

Needham and Billingham (49), (50) have discussed two conventional routes to clock behaviour in chemical systems. They found that the induction period can involve slow formation of the autocatalyst (activator species) which is initially present in small amounts, or the removal of an inhibitor species, which is preventing a reaction from taking place.

1.2.3 Open reactors

The simplest, non-trivial behaviour displayed by chemical systems displaying feedback, maintained far from equilibrium in an open reactor, is bistability. This is the coexistence of two stable steady states over a range of operating parameters e.g. temperature, inflow concentration of one of the species, or flow rate. When studied in a CSTR, bistable systems undergo transitions from one asymptotic stable steady state to another when suitably perturbed or when a control parameter is varied beyond its bistability limit or bifurcation point. It is also possible for chemical systems to display multistability i.e. the coexistence of more than two stable steady states (51). The transition to bistability or more complex behaviour is usually represented using bifurcation diagrams. Here the response of a system variable is plotted as a control parameter is changed. Bifurcation points are identified as the point at which the nature of the solution to the set of differential equations describing the system changes. This includes a change in the number of steady states, changes in stability and the appearance of periodic or chaotic solutions as the control parameter is changed. An example bifurcation diagram is shown in Figure 1.5 for a system with two stable steady states and one unstable steady state. The unstable steady state is shown as the dashed line and although it can be calculated numerically it cannot be obtained experimentally. This is because the system is always subject to small perturbations that will drive it away from the unstable steady state to the attractor of another stable steady state. Which of the stable steady states is approached depends on the history of the reaction system. This is hysteresis. The steady state value of the system in Figure 1.5 for a particular flow rate depends on whether the flow rate is increased or decreased.

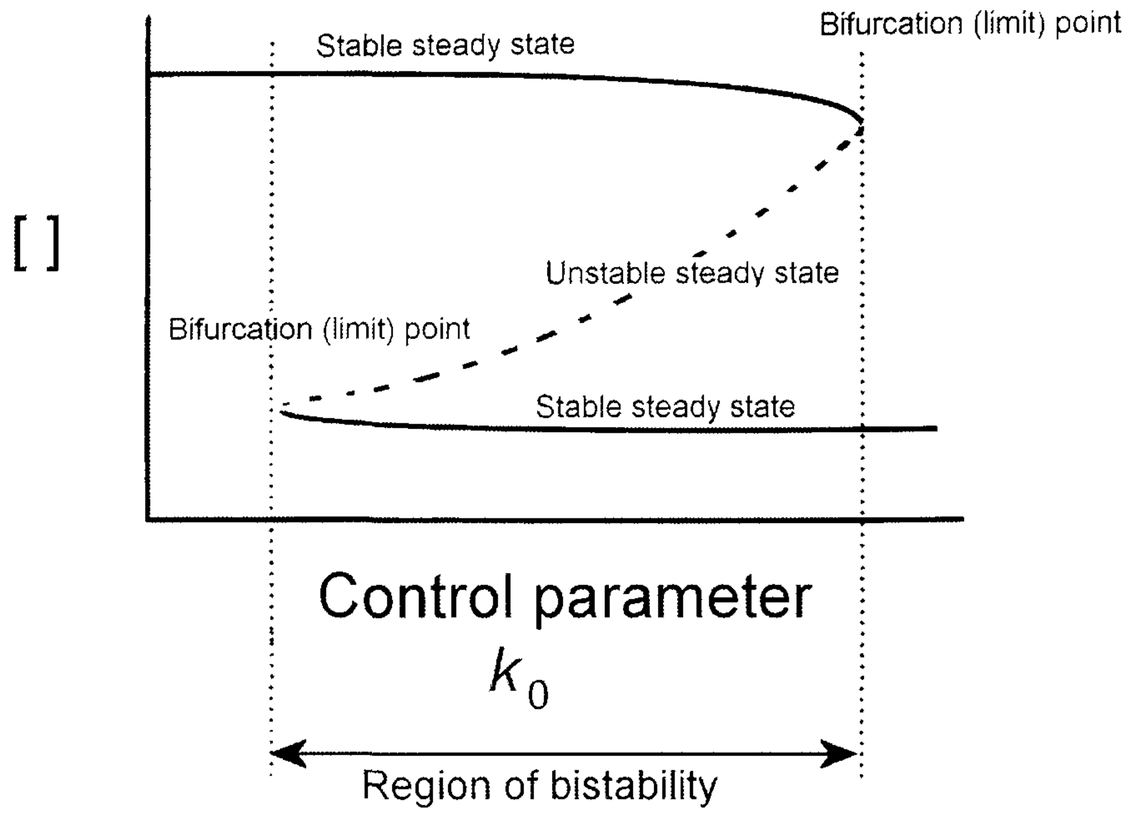

Figure 1.5 Schematic of a chemical system displaying bistability in an open reactor.

For a thorough discussion of stationary steady states, stability analysis and bifurcation theory the reader is directed to one of the many texts on the topic (19). The important point here is that a nonlinear system is better understood if the qualitative aspects of its solution are examined over a range of parameters, rather than by only looking at its quantitative behaviour for a single parameter set. Parameter (phase) diagrams plot the range of behaviour of a system as the function of two control parameters.

Bistable systems can usually be perturbed with an additional negative feedback pathway to give rise to oscillatory chemical systems in open, flow reactors. The addition of a chemical step where the autocatalyst or activator is removed at an appropriate rate can give rise to oscillations, and other time-dependent asymptotic states like chaos. This approach, the addition of a negative feedback pathway to a bistable system, is the route of the systematic design series which has been successful in producing dozens of oscillating chemical systems.

1.2.4 Systematic design - the cross shaped flow diagram

The design of chemical oscillators provides a means to understand and control complex dynamical behaviour. The use of systematic design algorithms has produced dozens of chemical oscillators based on inorganic redox chemistry (52). These systems mainly consist of an autocatalytic growth in the concentration of a species (the autocatalyst) and the subsequent removal of the autocatalyst through coupling with negative feedback, in an open reactor. A key component is that the negative feedback must be delayed relative to the positive feedback such that a kinetic instability can arise and limit cycle oscillations can emerge. The cross shaped phase diagram is a particularly useful method for the design of chemical oscillators, as it requires no prior detailed knowledge of the often complex chemistry involved.

Under flow conditions, the approach starts with a bistable system. Most autocatalytic reactions display bistability when performed in a flow reactor (53). For low inflow concentrations of inhibitor, bistability between low and high autocatalyst concentration state is observed, within a bounded range of flow rates. The inhibitor must remove the autocatalyst at a relatively slow rate. Chemically this means that the system must have time to return to its bistable state after perturbation away from these stable steady states by the inhibitor. As the inflow concentration of the inhibitor is increased, the region of bistability shrinks. As the region shrinks the nature of the two different steady states separated by the bistability retain their individual identities and do not merge in character. If this were to happen it would indicate that the negative feedback (removal of inhibitor) was not sufficiently slow compared to the reactions which constitute the original bistability.

Providing the above criteria are met, a plot can be constructed of the range of behaviour as a function of two system parameters, such as flow rate and inflow

concentration of inhibitor. The fact that the general topological character of the diagram, the meeting of the four regions (steady states I and II bistability and oscillatory region) can be seen in a variety of systems allows a systematic approach to the design of oscillating chemical systems.

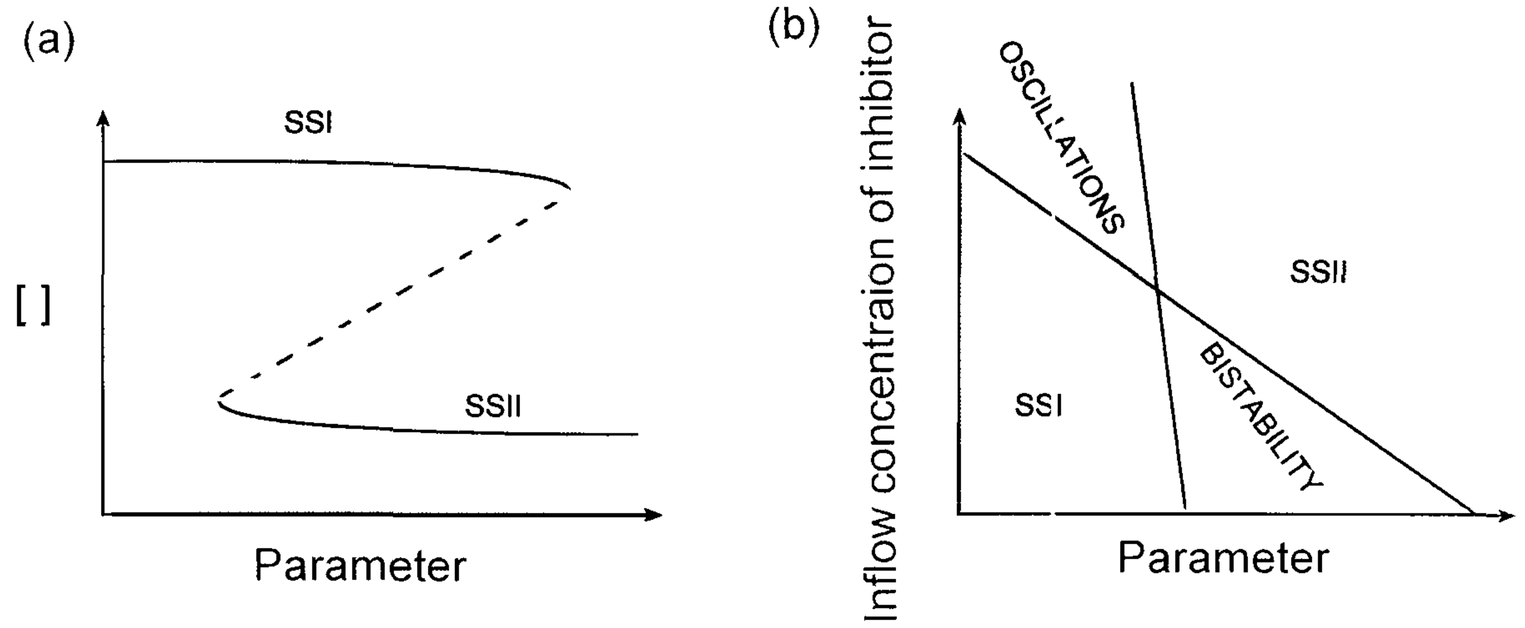

Figure 1.6 Systematic design of a chemical oscillator. (a) The fundamental bistable system in a flow reactor showing concentration of species as a function of a parameter. Steady state concentrations SSI and SSII are distinct stable steady states, dashed line shows unstable steady state. (b) Phase diagram obtained as the inflow concentration of inhibitor is increased. Figure (a) corresponds to a zero inflow of inhibitor.

De Kepper, Kustin and Epstein (14) were the first to systematically design an oscillatory chemical reaction using the generic mathematical model detailed above. They were able to show the chlorite – iodate - arsenite system could support oscillations in a CSTR, without having prior in-depth knowledge of the kinetics of this complex system.

The ability to elucidate the mechanism of these complex chemical reactions allows the rate laws, determined from mass balance, for each variable to be constructed. The integration of these ordinary differential equations in time can reproduce the behaviour seen in experiments, so the connection between kinetics and

theory can be made. The chemical mechanism cannot be proved, rather disproved by new experimental evidence. Nevertheless, mechanisms have been invaluable in guiding experimentalists in their search for oscillating chemical reactions.

1.3 The design of acid- or base-regulated oscillating chemical reactions

Most pH oscillators to date are redox reactions (30). A model for the systematic design of pH oscillators has been given (31). In batch conditions the model exhibits (as do experiments) a clock reaction, with an induction period followed by a sudden jump of several orders of magnitude in H^+. When the clock reaction is coupled with the appropriate negative feedback (acid consumption here) there is an exponential decrease in $[H^+]$ in batch. Under flow conditions, bistability and oscillations are obtained. The model can easily be adapted to describe a wide variety of pH oscillators, including the iodate-sulfite-thiourea (38), iodate-sulfite-thiosulfate (54) periodate-thiosulfite (37) periodate-hydroxylamine, iodate-hydroxylamine (33) and the hydroxylamine-periodate (32) reactions.

Rabai (55) suggested the following model, the simplest algorithm for the design of a pH regulated oscillator. The hydrogen ion affects the reaction rate in an aqueous solution through fast protonation equilibria, as acidic and basic forms of the reagents have different reactivities. The importance of such fast protonation equilibria has been noted by many groups (31) with regard to full mechanistic models of specific pH oscillatory systems. Here, we consider the following scheme consisting of (1.1) a rapid protonation equilibria and (1.2) a hydrogen ion catalyzed rate determining irreversible reaction.

$$A^- + H^+ \rightleftharpoons AH \qquad (1.1)$$

$$AH + H^+ + \{B\} \rightarrow 2H^+ + P^- \tag{1.2}$$

AH and A^- are the acidic and basic forms respectively of the reactant species. The concentration of B is assumed to be constant, and the non catalytic reactions between A^- and AH with B are assumed to be slow and negligible. In reality reaction (1.2) cannot be an elementary step, and the simplest mechanism of this step is a fast, second protonation equilibrium (1.3) and the rate determining step (1.4) as follows.

$$AH + H^+ \rightleftharpoons AH_2^+ \tag{1.3}$$

$$AH_2^+ + \{B\} \rightarrow 2H^+ + P^- \tag{1.4}$$

If we focus on the non-elementary scheme, reactions (1.1) and (1.2) the corresponding rate laws are given as follows.

$$v_{1.1} = k_{1.1}[A^-][H^+] \tag{1.5}$$

$$v_{1.1r} = k_{1.1r}[AH] \tag{1.6}$$

$$v_{1.2} = k_{1.2}[AH][H^+] \tag{1.7}$$

The ordinary differential equations for the variables are then;

$$\frac{d[H^+]}{dt} = -v_{1.1} + v_{1.1r} - v_{1.2} \tag{1.8}$$

$$\frac{d[A^-]}{dt} = -v_{1.1} + v_{1.1r} \tag{1.9}$$

$$\frac{d[AH]}{dt} = v_{1.1} - v_{1.1r} - v_{1.2} \tag{1.10}$$

$$\frac{d[P]}{dt} = v_{1.2} \tag{1.11}$$

If appropriate parameters are chosen, the system displays an increase in the rate of reaction as the reaction proceeds. Numerical integration of the resulting differential equations gives rise to a pH clock in batch. Figure 1.7 shows temporal evolution of pH and the corresponding rate extent plot.

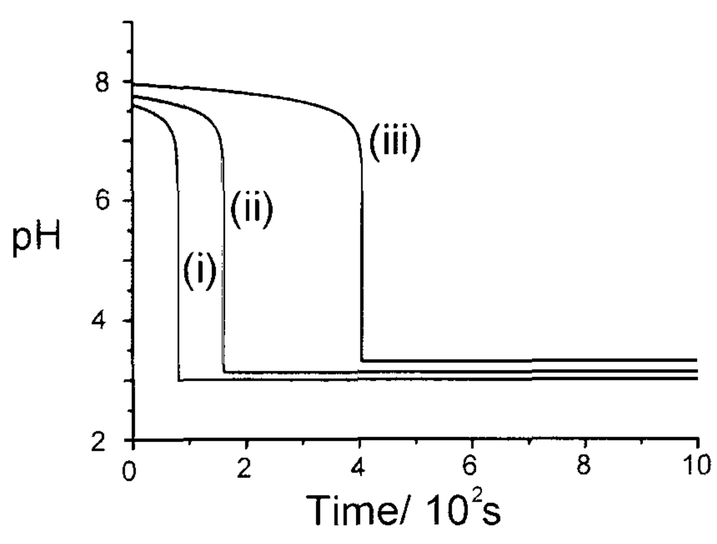

Figure 1.7 (a) pH clocks simulated on the basis of steps 1.1- 1.2. $k_{1.1} = 1 \times 10^{10}$ M^{-1} s^{-1}, $k_{1.1r}$ $= 1 \times 10^{3}$ s^{-1}, $k_{1.2} = 1 \times 10^{6}$ M^{-1} s^{-1}, $[A^-]_0 = 5 \times 10^{-3}$ M, $[H^+]_0 = 1 \times 10^{-3}$ M, (i), 0.75×10^{-3} M (ii), 0.5×10^{-3} M (iii). (b) Smoothed rate extent plot for curve (i). These plots were produced using XPPAUT (56), see appendix I for full details.

The differential rate equations can now be augmented with appropriate flow terms of the form $k_0([X]_0 - [X])$ where k_0 is the flow rate and $[X]_0$ is the inflow concentration of species X. The model displays bistability, that is two different coexisting dynamic states that are simultaneously stable for the same experimental parameter (in this case flow rate) in an open reactor.

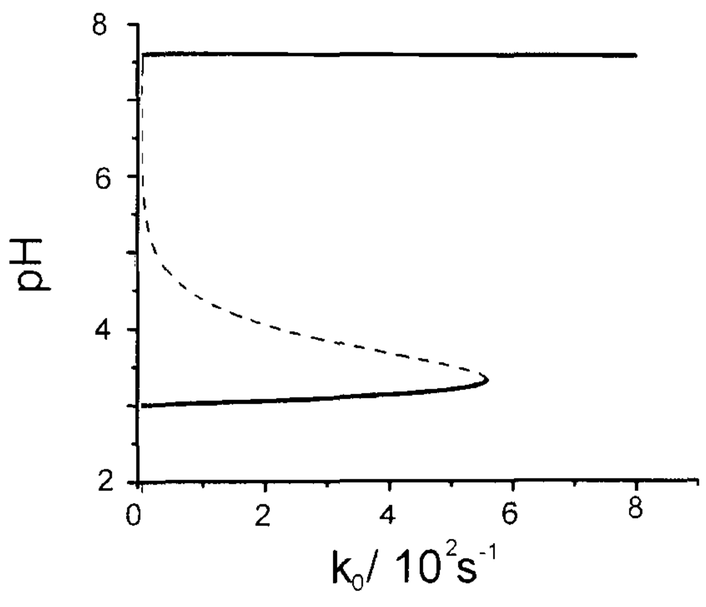

Figure 1.8 Bistability in a model of a pH regulated nonlinear system, modeled on 1.1 and 1.2. $k_{1.1} = 1 \times 10^{10}$ M^{-1} s^{-1}, $k_{1.1r} = 1 \times 10^{3}$ s^{-1}, $k_{1.2} = 1 \times 10^{5}$ M^{-1} s^{-1}, $[A^-]_0 = 5 \times 10^{-3}$ M, $[H^+]_0 = 1 \times 10^{-3}$ M.

Figure 1.9 shows the calculated region of bistability in the log ($k_{1.2}$/ M^{-1} s^{-1}) log (k_0/ s^{-1}) plane at fixed inflow concentrations of A and H^+.

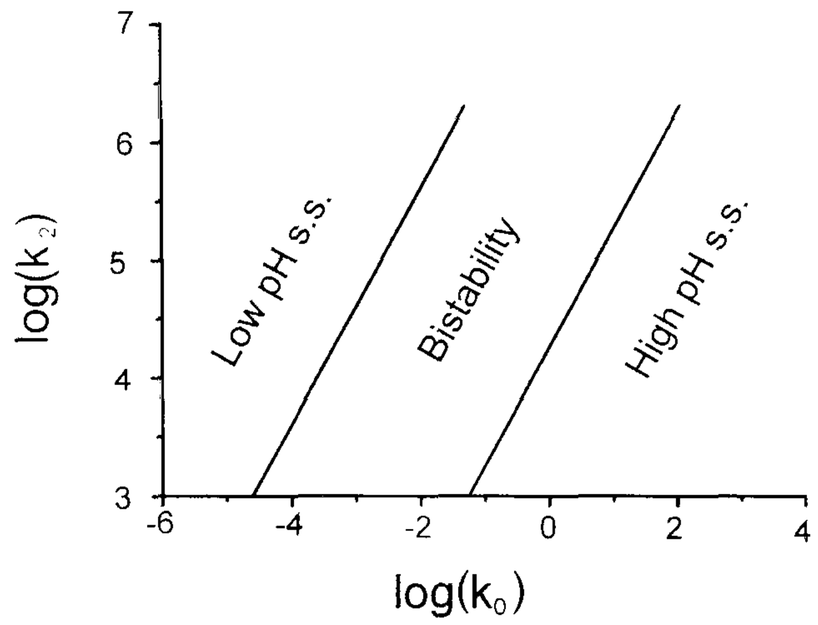

Figure 1.9 Phase diagram for model 1.1– 1.2 showing regions of bistability. $k_{1.1} = 1 \times 10^{10}$ M^{-1} s^{-1}, $k_{1.1r} = 1 \times 10^{3}$ s^{-1}, $[A^-]_0 = 5 \times 10^{-3}$ M, $[H^+]_0 = 1 \times 10^{-3}$ M.

In order to observe oscillations in this simplified model, it is necessary to have two major composite reactions - one that produces H^+ (or OH^-) autocatalytically (positive feedback, step 1.1) and another that removes H^+ (or OH^-) (negative feedback). It is also important that there is a necessary time delay between these two reactions, meaning that the rate of reaction responsible for negative feedback should be slower than the fastest part of the autocatalytic process. Thus, steps (1.1) and (1.2) can be coupled with a simple linear (or more complex) decay of H^+ (1.12)

$$H^+ + \{C^-\} \rightarrow CH \qquad (1.12)$$

where the rate of (1.12) is given as:

$v_{1.12} = k_{1.12}[H^+]$ (assuming C^- is in excess, so $k_{1.12} = k_{1.12}' \times [C^-]$)

Numerical integration of the 4 resulting differential equations now gives rise to oscillations under flow conditions (Figure 1.10(a)). Figure 1.10 (b) shows the stable limit cycle in the [AH] – $[H^+]$ plane.

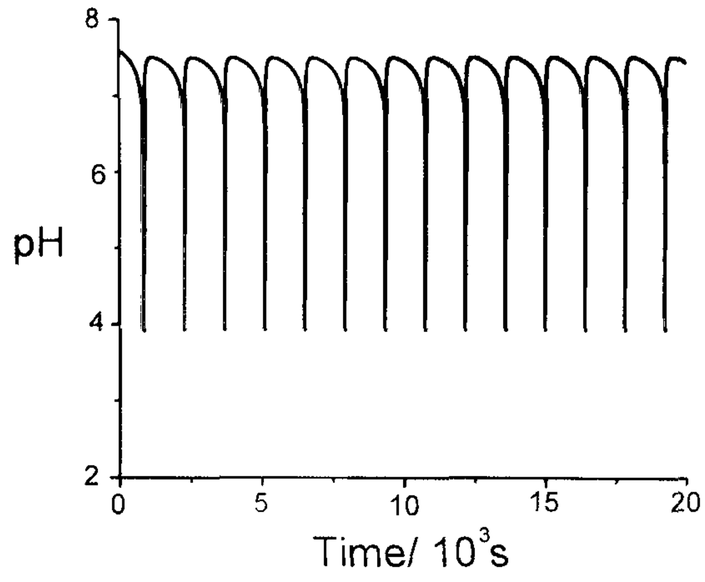

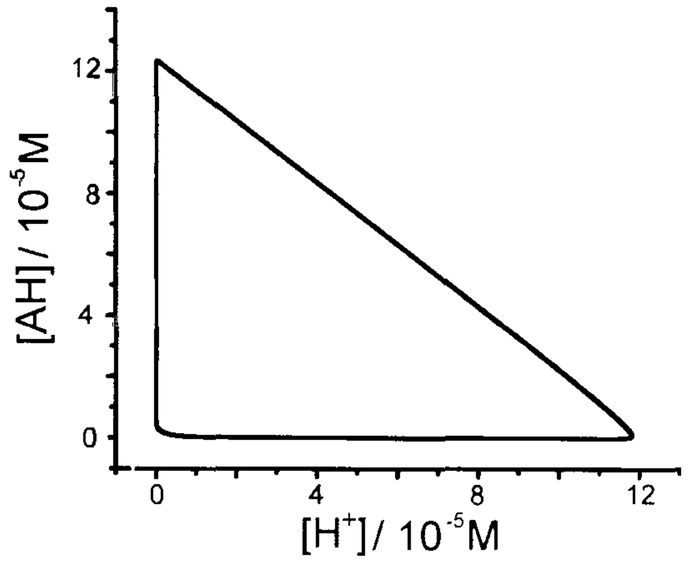

Figure 1.10 (a) Numerically simulated pH oscillations on the basis of steps (1.1), (1.2) and (1.12). $k_{1.1} = 1 \times 10^{10}$ M^{-1} s^{-1}, $k_{1.1r} = 1 \times 10^{3}$ s^{-1}, $k_{1.2} = 1 \times 10^{5}$ M^{-1} s^{-1}, $k_{1.12} = 0.1$ s^{-1} $[A^-]_0 = 5 \times 10^{-3}$ M, $[H^+]_0 = 1 \times 10^{-3}$ M, $k_0 = 1 \times 10^{-4}$ s^{-1}.(b) Limit cycle in the [AH] – $[H^+]$ plane, same conditions as (a).

Figure 1.11 (a) shows a bifurcation diagram for $k_{1.2} = 1 \times 10^{5}$ M^{-1} s^{-1} and $k_{1.3} = 0.1$ s^{-1} ($[A^-]_0 = 5 \times 10^{-3}$ M, $[H^+]_0 = 1 \times 10^{-3}$ M). Oscillations emerge via a supercritical Hopf bifurcation at $k_0 = 2.84 \times 10^{-6}$ s^{-1} and disappear at $k_0 = 4.05 \times 10^{-4}$ s^{-1}. The oscillations grow in amplitude and decrease in period as the flow rate is increased. The regions of bistability and oscillations are shown in Figure 1.11(b).

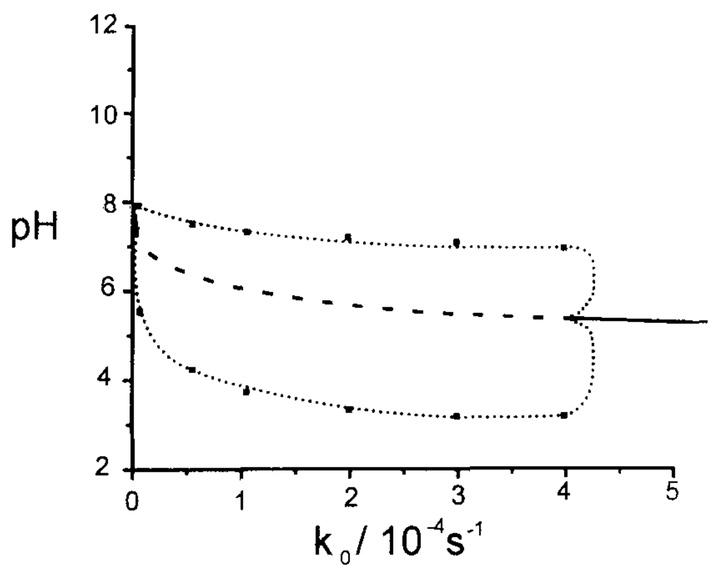

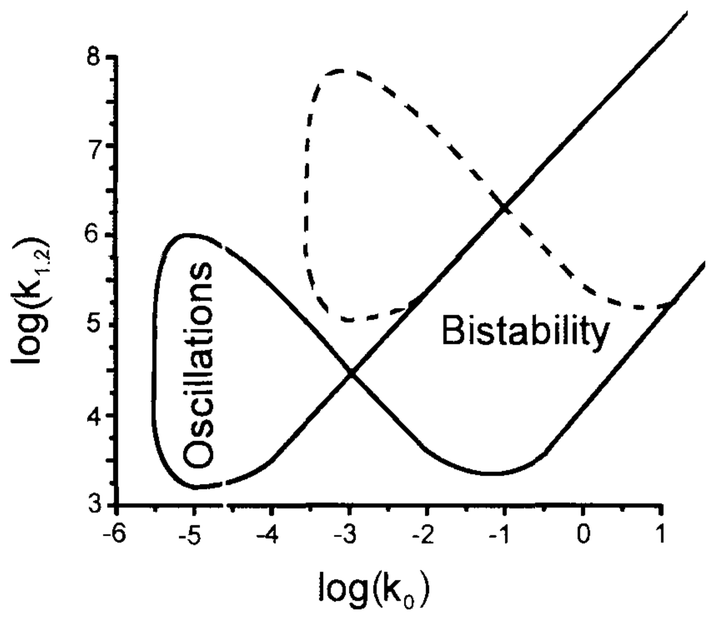

Figure 1.11 (a) Bifurcation diagram for $k_{1.2} = 1 \times 10^{5}$ M^{-1} s^{-1}. Dotted line with points is oscillation limits, dashed line is unstable steady state, solid line is stable steady state, $k_{1.12} = 0.1$ s^{-1}. (b) Phase diagram showing regions of calculated bistability and oscillations in the log

($k_{1.2}$/ M^{-1} s^{-1}) – log (k_0/ s^{-1}) plane. Solid line $k_{1.12} = 0.1$ s^{-1}, dashed line $k_{1.12} = 10$ s^{-1} ($[A^-]_0 = 5 \times 10^{-3}$ M, $[H^+]_0 = 1 \times 10^{-3}$ M in both).

As a result of addition of reaction 1.12 to steps 1.1 and 1.2, the open region of bistability (Figure 1.9) now gives rise to a region of oscillations at low flow rates, and the system possesses a typical cross shaped phase diagram. There are two stable steady state regions, a region of bistability and a region of oscillations. The regions of bistability and oscillations shift up in the log ($k_{1.2}$/ M^{-1} s^{-1}) – log (k_0/ s^{-1}) plane if the value of the rate constant for reaction 1.12 is increased. This shift occurs as a consequence of the necessary time delay between hydrogen ion consumption and production.

Reactions 1.1, 1.2 and 1.12 constitute the simplest possible 'realistic' model for pH regulated oscillations.

1.4 A Chemical Example - The bromate-sulfite reaction

The reaction between sodium sulfite/ bisulfite and sodium bromate exhibits pH clock behaviour in a batch reactor (57). The reaction displays bistability in a CSTR, and pH oscillations with an additional inflow of ferrocyanide (57). The reaction is also able to support reaction diffusion fronts in unstirred mixtures (58). The following is a consideration of the behaviour of this reaction. Trends in induction time, in experiments and numerical simulations, are discussed. Stirring effects are explained and the spatio-temporal behaviour of the system is examined.

1.4.1 Chemical Mechanism (59)

The following chemical mechanism is suggested for the oxidation of sulfur (IV) species by bromate.

$$3HSO_3^- + BrO_3^- \rightarrow 3SO_4^{2-} + Br^- + 3H^+ \quad (1.13)$$

$$HSO_3^- \rightleftharpoons SO_3^{2-} + H^+ \quad (1.14)$$

$$HSO_4^- \rightleftharpoons SO_4^{2-} + H^+ \quad (1.15)$$

$$H_2SO_3 \rightleftharpoons HSO_3^- + H^+ \quad (1.16)$$

$$3H_2SO_3 + BrO_3^- \rightarrow 3SO_4^{2-} + Br^- + 6H^+ \quad (1.17)$$

$$H_2O \rightleftharpoons H^+ + OH^- \quad (1.18)$$

With the corresponding rate equations for steps (1.13) – (1.18) shown in table 1.2.

$R_{1.13} = k_{1.13}[BrO_3^-][HSO_3^-]$	$k_{1\,13} = 0.03\ M^{-1}s^{-1}$
$R_{1.14} = k_{1.14}[HSO_3^-]$ $R_{1\,14r} = k_{1.14r}[SO_3^{2-}][H^+]$	$k_{1\,14} = 3\times10^{3}\,s^{-1}$ $k_{1\,14r} = 5\times10^{10}\,M^{-1}s^{-1}$
$R_{1.15} = k_{1.15}[HSO_4^-]$ $R_{1.15r} = k_{1.15r}[H^+][SO_4^{2-}]$	$k_{1\,15} = 1\times10^{8}\,s^{-1}$ $k_{1\,15r} = 1\times10^{10}\,M^{-1}s^{-1}$
$R_{1.16} = k_{1.16}[H_2SO_3]$ $R_{1.16r} = k_{1.16r}[HSO_3^-][H^+]$	$k_{1\,16} = 1\times10^{8}\,s^{-1}$ $k_{1\,16r} = 6\times10^{9}\,M^{-1}s^{-1}$
$R_{1.17} = k_{1.17}[BrO_3^-][H_2SO_3]$	$k_{1\,17} = 18\ M^{-1}s^{-1}$
$R_{1.18} = k_{1.18}$ $R_{1.18r} = k_{1.18r}[OH^-][H^+]$	$k_{1\,18} = 1\times10^{-3}\,Ms^{-1}$ $k_{1\,18r} = 1\times10^{11}\,M^{-1}s^{-1}$

Table 1.2 Rate Laws for the bromate-sulfite clock reaction.

The overall reaction (1.13) proceeds according to:

$$BrO_3^- + HSO_3^- \rightarrow BrO_2^- + HSO_4^- \quad (1.19)$$

$$BrO_2^- + HSO_3^- + H^+ \rightarrow HOBr + HSO_4^- \quad (1.20)$$

$$HOBr + HSO_3^- \rightarrow Br^- + HSO_4^- + H^+ \quad (1.21)$$

Additional reactions such as the disproportionation of bromine-containing species are only important at low pH. Acid autocatalysis in this reaction can be demonstrated from consideration of reactions (1.16) and (1.17). As the concentration of acid increases, the rate of production of H_2SO_3 increases in reverse reaction (1.16), and the rate of formation of acid increases in reaction (1.17). A typical clock simulated from the model is shown in Figure 1.12, illustrating the temporal variation of concentrations of the important species H_2SO_3, H^+ and HSO_3^-, during the course of the reaction.

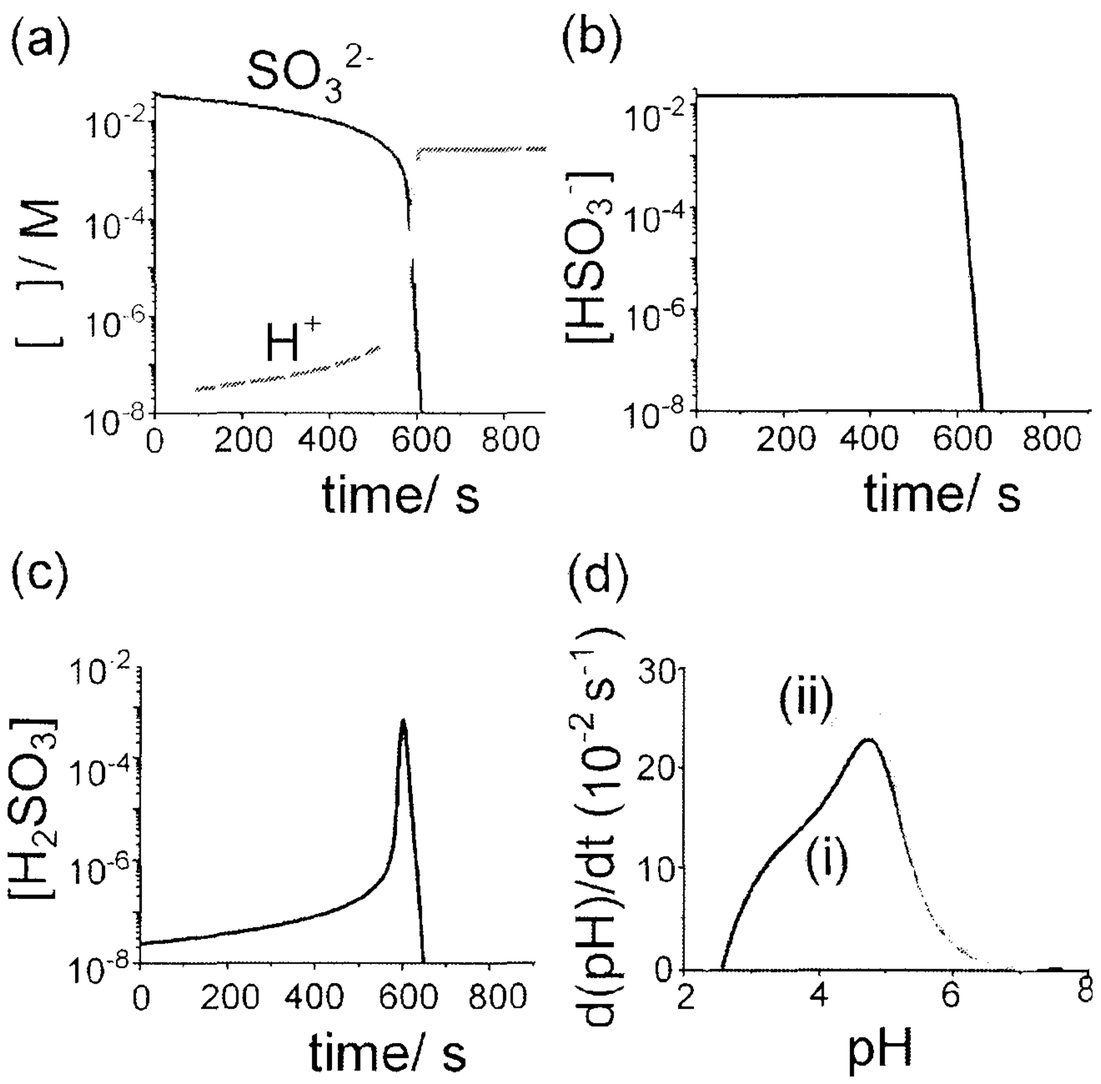

Figure 1.12 Simulated clock reaction (from model in Table 1) with (i) $[BrO_3^-]_0$ = 0.05 M, $[SO_3^{2-}]_0$ = 0.035 M, $[HSO_3^-]_0$ = 0.015 M and (ii) $[BrO_3^-]_0$ = 0.05 M, $[SO_3^{2-}]_{0,aq}$ = 0.03 M, $[HSO_3^-]_{0,aq}$ = 0.02 M.

The induction time in this reaction can be explained by consideration of the sulfite-bisulfite buffer present initially (reaction (1.14)). The acid produced from the overall reaction (1.13) protonates sulfite in reverse reaction (1.14). As the sulfite is depleted, the buffering capacity of reaction (1.14) decreases. Typically, buffering exists between pH values of the pKa ± 2. The induction time, defined as the time to reach the maximum rate of change of pH, corresponds to the time taken to consume the

buffer (pH ~ 5.1 – Figure 1.12(d)). The value of t_{ind} decreases with increasing initial concentrations of bisulfite and bromate. The overall pH change depends on the total initial concentration of sulfite plus bisulfite.

The model reproduces experimental results. For appropriate initial conditions the model displays clock behaviour in batch, where there is an induction time before a reaction event (60). The reaction (clock) event is evidenced by an increase in $[H^+]$ and a corresponding drop in pH from ~ pH 7.5 to pH 2. Figure 1.13 shows the simulated and experimental pH clock in batch.

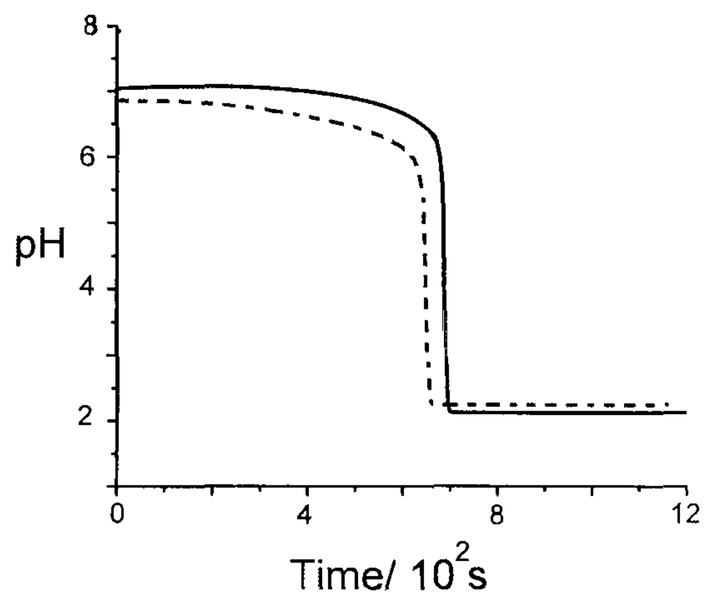

Figure 1.13 Numerical and experimental clock (batch) behaviour in the bromate-sulfite reaction, $[BrO_3^-]_0 = 0.05$ M, $[SO_3^{2-}] = 0.05$ M, $[HSO_3^-]_0 = 0.008$ M in both. The dotted line is experimental trace, thick solid line is numerical.

1.4.2 Trends in induction time

Figures 1.14 (a) (b) and (c) show how the induction time of the clock reaction depends on the initial concentration of bromate, bisulfite and sulfite. In each Figure experimental results are shown as a dashed line with points and numerical trends are depicted with a solid thick line. Reactions are started by adding sodium bromate solution to the sodium sulfite- bisulfite solution. The concentrations reported are the calculated concentrations in the reactor before reaction takes place (i.e. $[X]_s$ / 2) where $[X]_s$ is the concentration in the stock solution.

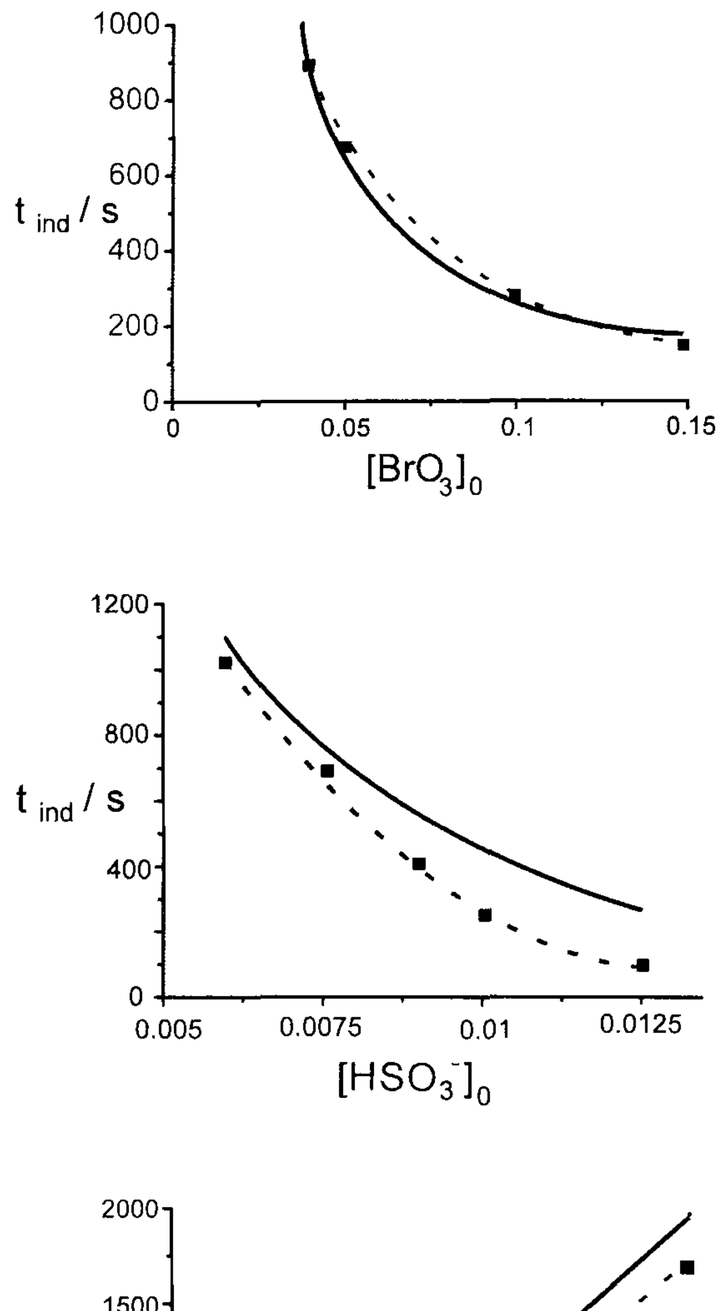

Figure 1.14 Variation of induction time with initial conditions in the bromate-sulfite clock reaction. (a) Variation of $[BrO_3^-]_0$, $[HSO_3^-]_0$ = 0.0075 M, $[SO_3^{2-}]_0$ = 0.05 M (b) Variation of $[HSO_3^-]_0$, $[BrO_3^-]_0$ = 0.05 M, $[SO_3^{2-}]_0$ = 0.05 M (c) Variation of, $[SO_3^{2-}]_0$, $[HSO_3^-]_0$ = 0.0075 M, $[BrO_3^-]_0$ = 0.05 M. Thin dash line with points is experimental results (stirred at 525 r.p.m.) thick solid line is numerically calculated induction times.

The induction time decreases with increasing initial concentrations of bromate and bisulfite, as the rates of reaction (1.13) and (1.17) increase. The clock time increases with initial sulfite due to an increase in the buffering capacity in step (1.14).

The aqueous phase clock times are reproducible in the experimental system, but depend on stirring rate (Figure 1.15 showing a decrease in t_{ind} with decreasing stirring rate). This demonstrates the sensitivity of the reaction to the evolution of a critical acid concentration. Lengthening of the clock time with increased stirring rate in autocatalytic reactions has been observed in the Briggs-Rauscher (61), the chlorite-iodide (62) and the chlorite-thiosulfite (63) reactions. Melikhov *et al.* (64)

showed that this stirring effect is connected with the effects of fluctuations or nuclei on the dynamics of the averages. They defined nuclei as short living accidentally appearing microvolumes where autocatalysis, induced by large-scale fluctuations, starts much earlier than the rest of the reactionary volume (65). Thus, at low stirring rates 'nucleation' occurs and the autocatalysis proceeds (64). This effect is evident in the experimental bromate-sulfite system where the induction time increases with stirring rate. At low stirring rates there is an increased opportunity for the critical concentration of acid (autocatalyst) to be achieved. Above this critical acid concentration the rate of the autocatalysis greatly increases and the reaction happens. With vigorous stirring, the critical acid concentration is not so easily achieved per unit volume, thus induction times are longer.

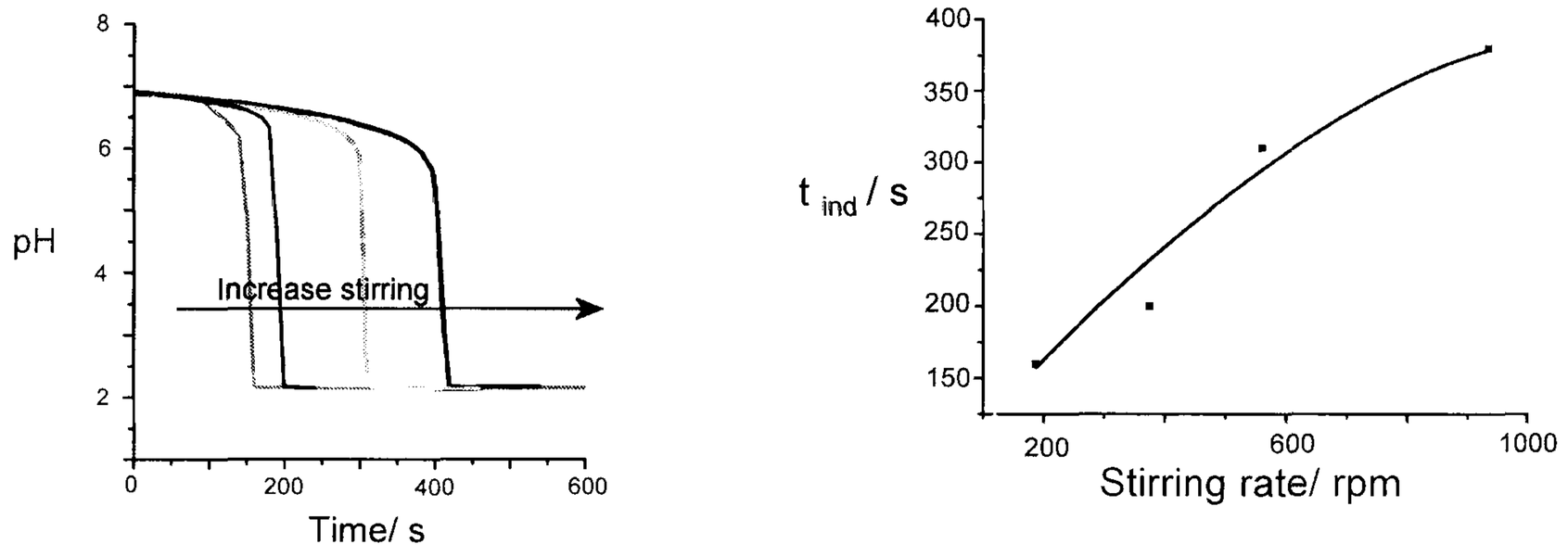

Figure 1.15 (a) pH-time traces for a bromate-sulfite clock reaction at different stirring rates (b) Dependence of induction time on stirring rate. $[BrO_3^-]_0$ = 0.1 M, $[HSO_3^-]_0$ = 0.075 M, $[SO_3^{2-}]_0$ = 0.05 M.

1.4.3 Open reactor: Bistability and Oscillations

In a flow, open reactor the bromate-sulfite reaction displays bistability between the low and high pH steady states, in both simulations (66) and experiments (57). Figure 1.16 (a) and (b) shows the simulated (reactions (1.13) to (1.18)) and experimental flow behaviour respectively.

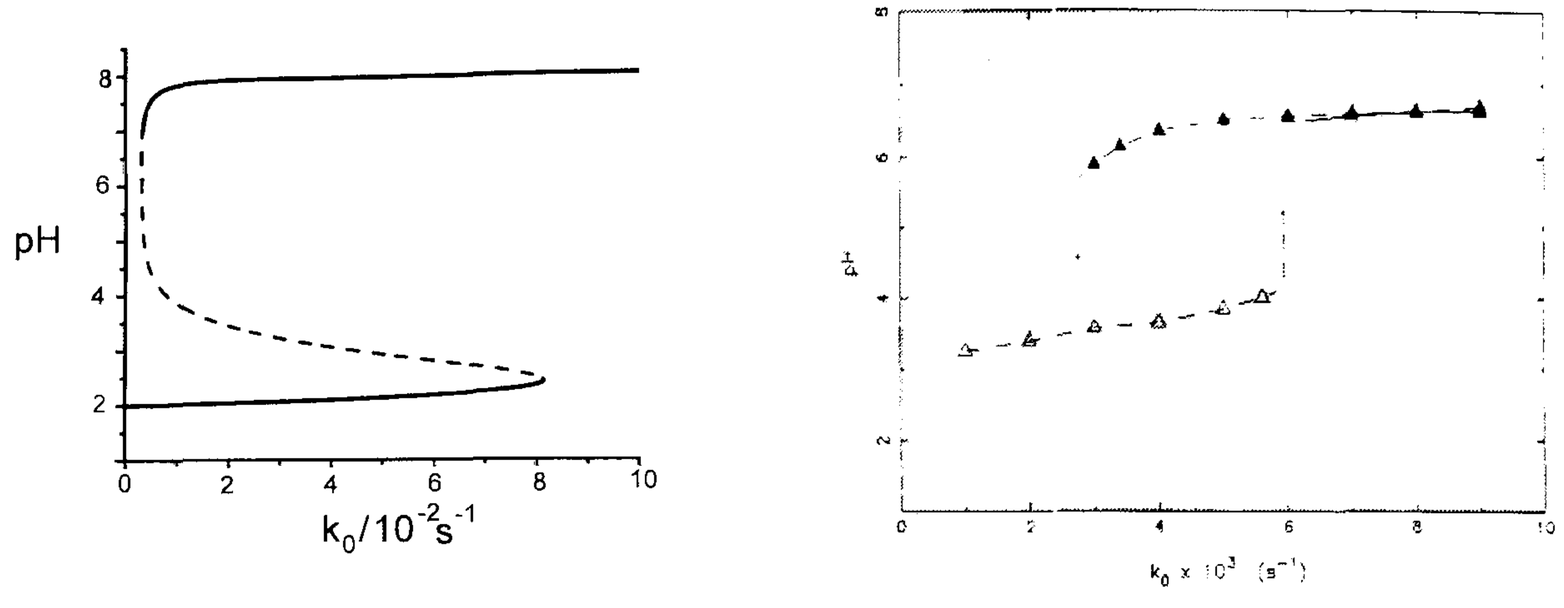

Figure 1.16 (a) Numerically simulated flow behaviour showing bistability in the bromate-sulfite reaction, in the absence of negative feedback. Solic line is stable steady state, dashed line is unstable steady state $[BrO_3^-]_0 = 0.065$ M, $[SO_3^{2-}] = 0.075$ M, $[HSO_3^-]_0 = 0.02$ M (b) Experimental regions of bistability in the bromate-sulfite reaction, taken from (57)

With an additional inflow of ferrocyanide the system displays pH oscillations. The negative feedback is supplied by Reaction 1.22.

$$BrO_3^- + 6Fe(CN)_6^{4-} + 6H^+ \rightarrow Br^- + 6Fe(CN)_6^{3-} + 6H_2O \qquad R_{1.22} = k_{1.22}[H^+]/k_{1.22'} + [H^+] \qquad (1.22)$$

$$k_{1.22} = 1.5 \times 10^{-5}\,\mathrm{Ms}^{-1}$$
$$k_{1.22'} = 2.5 \times 10^{-4}\,\mathrm{M} \qquad (60)$$

Figure 1.17 shows the numerical and experimental and k_0 – $[SO_3^{2-}]$ phase diagrams respectively.

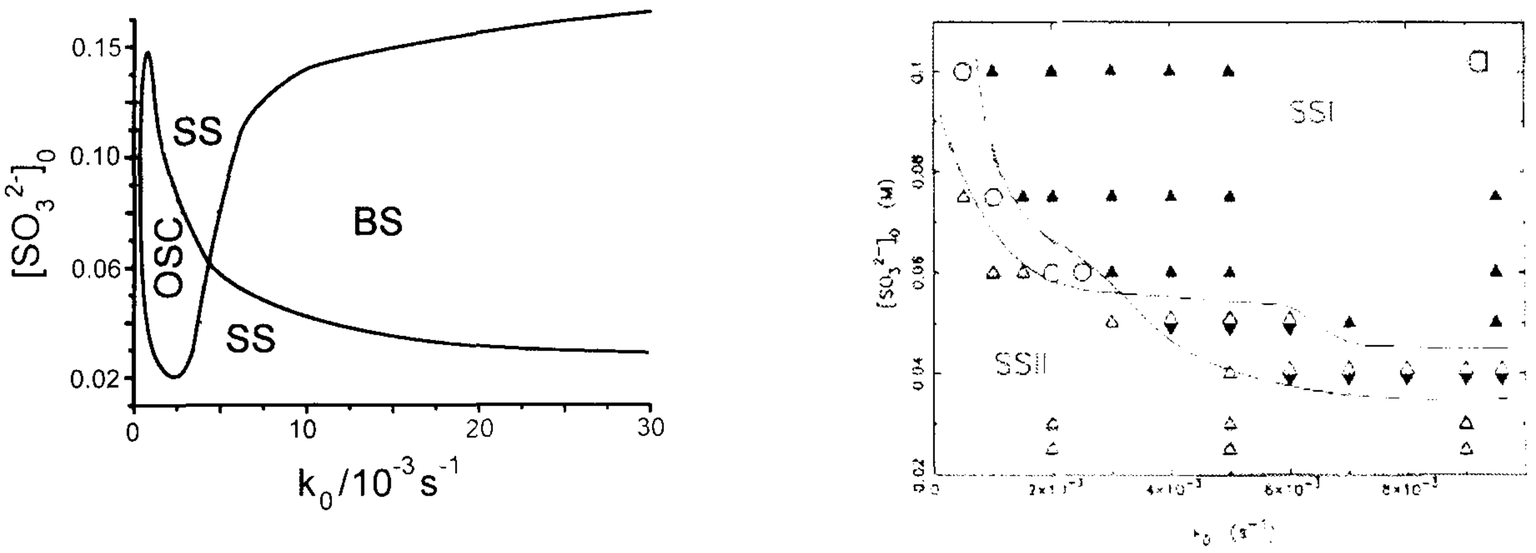

Figure 1.17 (a) Numerically simulated k_0 – $[SO_3^{2-}]_0$ cross shaped phase with reactions (1.13) – (1.18) and (1.22) $[BrO_3^-]_0 = 0.065$ M, $[HSO_3^-]_0 = 0.02$ M (b) Experimental regions of bistability in the bromate sulfite reaction, taken from (57).

Figure 1.18 shows numerical and experimental examples of the pH oscillations observed in the bromate sulfite reaction system.

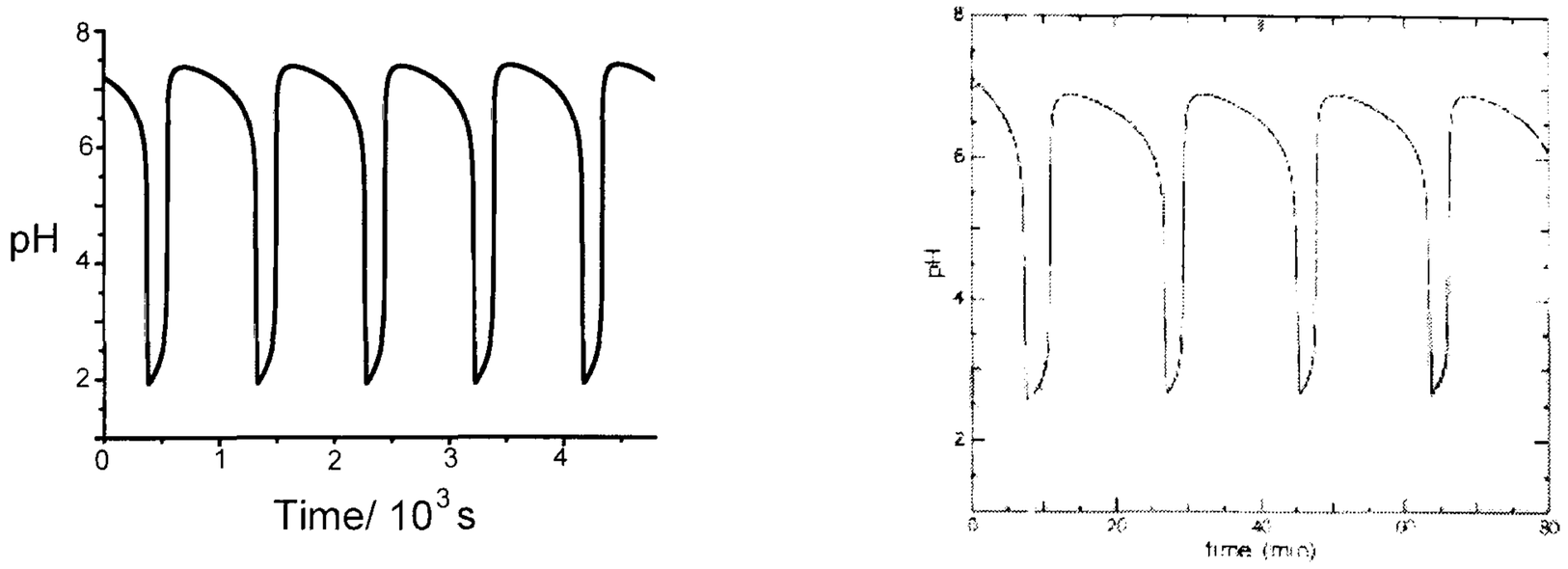

Figure 1.18 (a) Numerical and (b) experimental (taken from (60)) pH oscillations in the bromate sulfite reaction $[BrO_3^-]_0 = 0.065$ M, $[SO_3^{2-}]_0 = 0.075$ M, $[HSO_3^-]_0 = 0.02$ M, $k_0 = 0.00125$ s^{-1}.

1.4.4 Spatial behaviour – Reaction-Diffusion Fronts

The coupling of diffusion and nonlinear chemical kinetics can give rise to propagating waves of chemical reactivity and structured patterns. This pattern formation in reaction-diffusion systems is often invoked as a mechanism for biological morphogenesis (67), and the resemblance between some structures and patterns formed in inorganic nonlinear chemical reactions and those found in living systems (68, 69, 70) can be startling.

Propagating reaction fronts in autocatalytic reactions were discovered by Luther (71) in 1906. Chemical fronts are ubiquitous in biological (72), chemical (18), physical (73) and environmental systems (74). A chemical reaction diffusion front may be triggered in an unstirred reactant mixture of an autocatalytic reaction by supplying the autocatalyst in a confined space (75, 76). The reaction can be initiated at a point in a thin layer of reactants spread in a Petri dish (2 dimensional) or at the end of a thin tube filled with reactants (1 dimensional). Single reaction-diffusion

fronts in one dimension, generated from autocatalytic (clock) reactions, are the simplest experimental example of coupling diffusion with nonlinear chemical reaction. The following discussion focuses on single reaction diffusion fronts in the bromate sulfite reaction.

If the reaction system is set up with initial conditions so that equivalent clock time is long, the spontaneous formation of products from reactants will be slow. If we envisage a long tube containing a spatially uniform distribution of reactants (1 dimension) the reaction can be initiated at one end through addition of a small amount of autocatalyst. In terms of the bromate-sulfite reaction, this corresponds to adding a small drop of acid. The reaction will then spread along the tube, converting reactants to products, high to low pH. The composition of the solution behind and ahead of the front is different and the boundary between the two constitutes the wavefront. The wavefront will move through the solution with a constant speed. Figure 1.19 shows a schematic of a reaction-diffusion front.

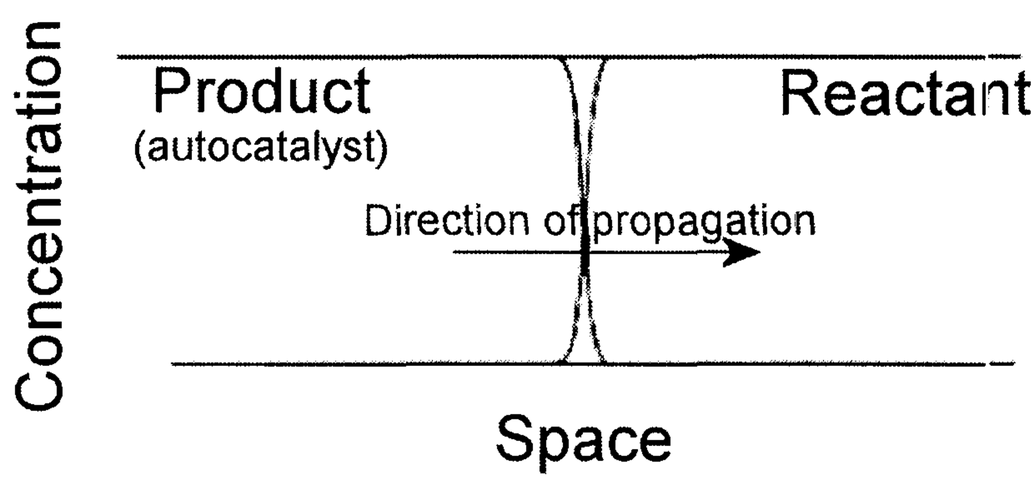

Figure 1.19 Schematic of a reaction diffusion front showing the boundary between reacted and un-reacted solution.

The successful initiation of a front depends on the size of the initiation site in the reactant mixture. In the case of the bromate sulfite system, a front can only propagate if enough acid is produced locally to diffuse and trigger the autocatalytic reaction in the surrounding area. If too little acid diffuses, the reaction will not take place and

the surrounding solution will remain in the un-reacted steady state (this is true for times up to approximately the equivalent induction time in batch). There is therefore a critical nucleation size below which the outward diffusion of the autocatalyst is insufficient to support front propagation.

The propagation of the reaction-diffusion front is driven by the diffusion of the autocatalyst, in this case H^+, and the rate of the autocatalytic reaction. A general formula for the speed of an isolated planar reaction diffusion front is approximately given as (71):

$$c = 2\sqrt{Dk} \tag{1.23}$$

where c is the speed of the reaction-diffusion front, D is the diffusion coefficient (of H^+) and k is the pseudo first order rate constant for the autocatalytic reaction.

The distance travelled by a molecule experiencing solely diffusion can be calculated from:

$$x = 2\sqrt{Dt} \tag{1.24}$$

where x is the distance travelled in time t, and D is the diffusion coefficient.

We can calculate the distance travelled in a 60 s for a molecule with a typical diffusion coefficient of D ~ 1×10^{-5} cm^2 s^{-1} as about 0.5 mm. Compared to this. reaction diffusion fronts in the bromate-sulfite reaction can travel with speeds of up to 14 mm min^{-1}.

The curvature of the wavefront also affects its velocity. A planar front will diffuse quicker than the same front with the curvature shown in Figure 1.2 (b). This is due to the diffusion path of the autocatalyst as shown below. The area ahead of the planar front reaches the critical acid concentration for autocatalytic quicker than that of the curved front.

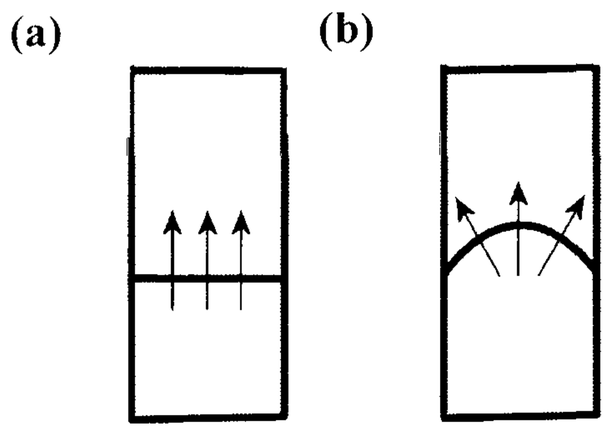

Figure 1.20 Diffusion path of the autocatalyst for planar and curved fronts

The curvature of any point on a waveform can be quantitatively characterised in terms of its radius of curvature. If the radius of curvature is R, the curvature K is defined as $1/R$. If front curves toward the direction of front propagation, K is positive (e.g., an arc of a circle moving toward the centre of the circle). K is negative if the front curves in the opposite direction. Therefore, a plane wave has $K = 0$, and uniformly contracting and expanding circular waves of radius r have curvatures of $K = 1/r$ and $-1/r$ respectively. The speed of the front is related to the curvature by the eikonal equation;

$$c = c_{\infty} + DK \qquad (1.25)$$

Where c is the velocity of the curved front, c_{∞} is the speed of the corresponding planar front, D is the diffusion coefficient for the autocatalytic species (H^+) and K is the curvature.

(i) Experimental examples of fronts in the bromate-sulfite clock reaction

Figure 1.21 (a) (b) and (c) shows how the speed of the front depends on the initial concentration of bromate, bisulfite and sulfite, respectively. The strongest dependence is on the initial concentration of bromate, the substrate.

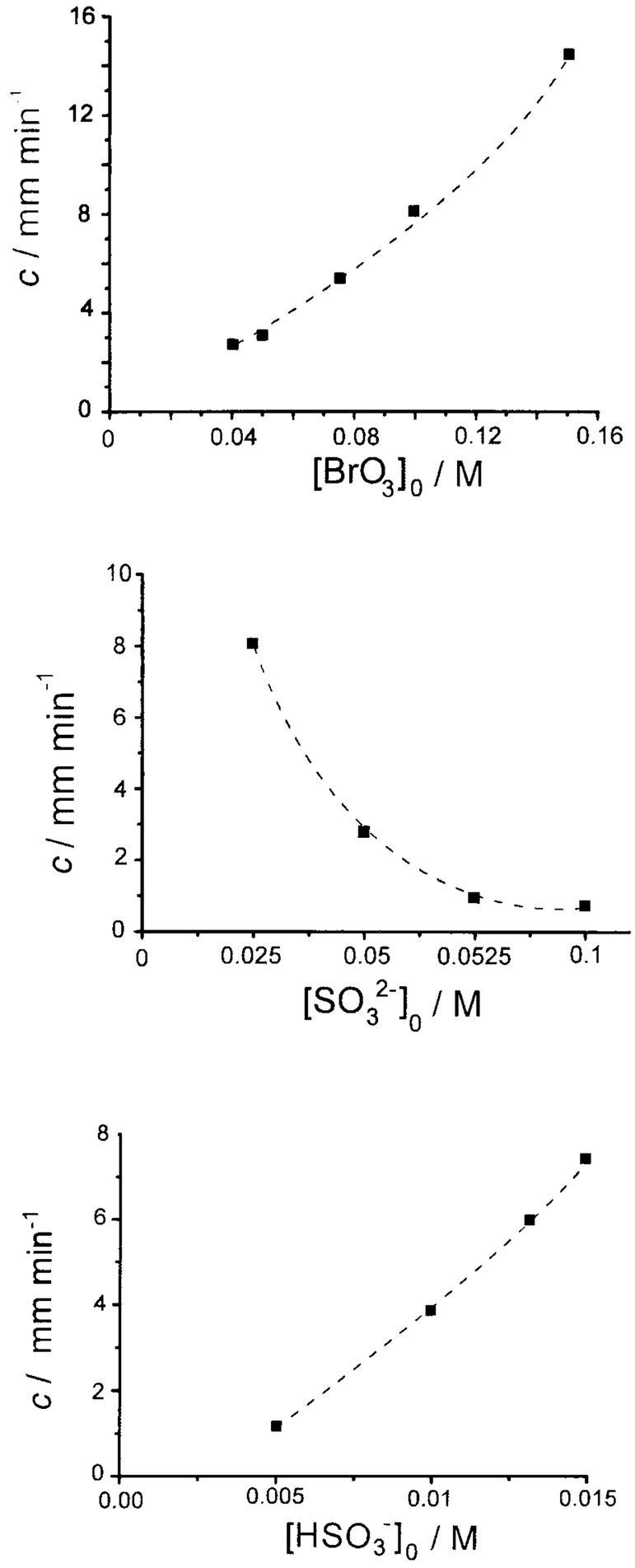

Figure 1.21 Dependence of front speed on initial conditions (a) Variation of $[BrO_3^-]_0$, $[HSO_3^-]_0$ = 0.075 M, $[SO_3^{2-}]_0$ = 0.05 M (b) Variation of $[HSO_3^-]_0$, $[BrO_3^-]_0$ = 0.05 M, $[SO_3^{2-}]_0$ = 0.05 M (c) Variation of, $[SO_3^{2-}]_0$, $[HSO_3^-]_0$ = 0.0075 M, $[BrO_3^-]_0$ = 0.05 M.

The trends in front speed depend on initial concentrations in a similar manner to the induction times. Higher initial bromate and bisulfite concentrations lead to faster consumption of the buffer, giving rise to faster fronts. High initial sulfite concentrations mean the time taken to deplete the buffer is longer, thus giving rise to slower fronts.

Figure 1.22 shows a typical time-space series for a propagating reaction diffusion front in the Bromate Sulfite reaction. The tube is approximately 2 mm i.d.

Bromophenol blue indicator is used to visualize the front, with purple corresponding to unreacted basic solution (pH ~ 7.5) ahead of the front, and yellow to acidic reacted (autocatalyst) product (pH ~ 2).

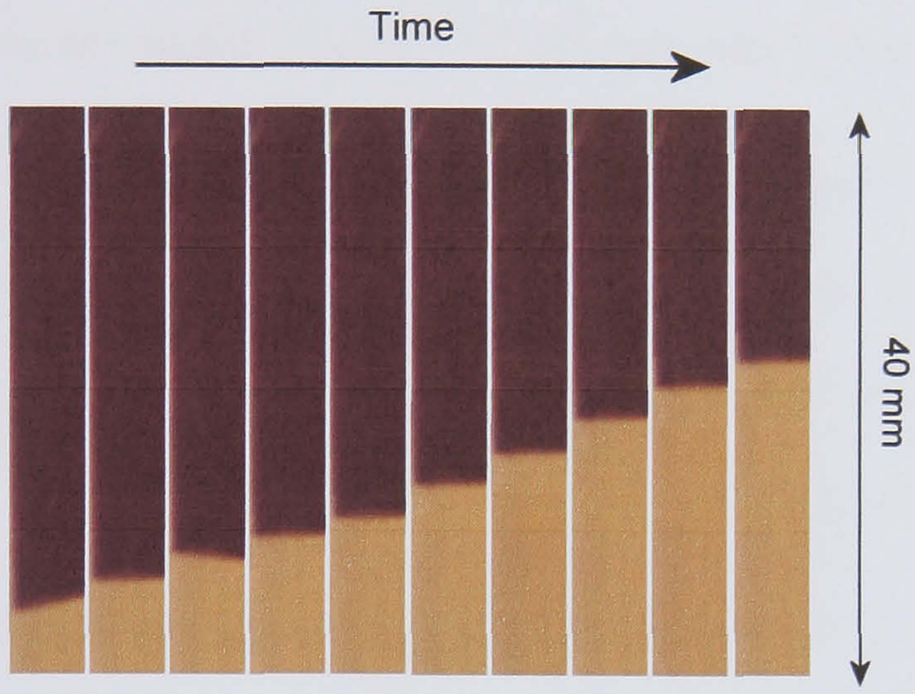

Figure 1.22 Series of tubes showing propagation of an ascending acid reaction diffusion front (yellow) into unreacted solution (purple) in the Bromate Sulfite reaction, c = 3 mm min^{-1}.

The structure of a propagating reaction-diffusion front will depend on the density differences between the products and reactants. The density difference, $\Delta\rho = \rho_p - \rho_r$, where ρ_p and ρ_r are the densities of the product and reactant solution respectively, is a combination of the solutal contribution due to the difference in molar volumes of the reactant and product, and the thermal differences related to the exo/ endo thermicity of the reaction (77). The type of instability observed depends on the relative magnitude and sign of both of these contributions, and has been discussed by Pojman and Epstein (78). Differences in density can lead to fluid convection and the development of curved, non-structured or cellular fronts in chemical systems (79), (80), (81). The bromate-sulfite reaction is exothermic (ΔH = -1070 ± 10 kJ/ mol) and the isothermal density difference between products and reactants is positive (Δq_c = 2.40 × 10^{-4} g/ cm^3) (58). Chemical fronts in the bromate sulfite reaction system can create mass temperature and density gradients, which in the presence of gravity can destabilize planar reaction-diffusion fronts. This convection can mean that ascending fronts travel slower than corresponding descending fronts. Pojman *et al.* (58) showed

that the extent of convection depended on the internal diameter of the tube, and that for some initial conditions the front is sensitive to double-diffusive convective effects. Figure 1.23 shows experimental images of reaction-diffusion fronts in the bromate sulfite reaction, in different size tubes.

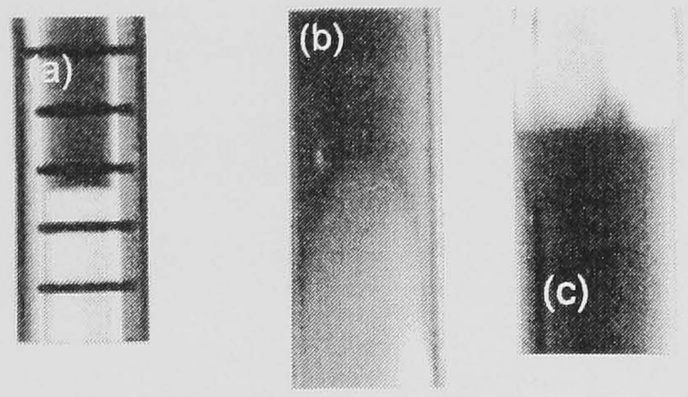

Figure 1.23 Internal tube diameter dependence on front shape in the bromate sulfite reaction. i.d. = 0.26 cm, ascending (a), 0.80 cm, ascending (b), 1.8 cm, descending (c). Taken from (58).

Narrow tubes increase front stability as they tend to oppose fluid motion. Rica *et al.* showed that increases in solution viscosity also lead to a decrease of instability, in reaction-diffusion fronts in the chlorite-tetrathionate reaction (82).

1.5 Thesis structure

In this thesis the kinetics of acid- and base-regulated nonlinear systems are investigated. An experimental investigation into the kinetics of the reaction of methylene glycol with sodium sulfite/ bisulfite buffer (MGS reaction) is presented in chapter two. This reaction displays an acid to base pH clock in a batch reactor. The behaviour of the system in flow is also examined, and new behaviour is reported.

In chapter three these new experimental results are used to develop a model of this reaction system, resulting in a new kinetic mechanism for this organic substrate-based pH regulated nonlinear system. Numerical simulations with this model provide good agreement with reported experimental behaviour. Mixing effects are added to this model to investigate the stability of the thermodynamic and flow braches of the bistability to stirring effects. Addition of these macro-mixing terms improves correlation between experiment and simulation.

A new model is presented for the design of pH regulated oscillators in chapter four. This model, based on the MGS reaction, is shown to provide a new approach for the design of non-redox pH regulated oscillating chemical systems. Experimental evidence of the first non-redox organic substrate based pH oscillator is then given - the methylene glycol-sulfite-gluconolactone reaction (MGSG). The MGSG system is mechanistically analysed and a model is reported that reproduces the behaviour seen in experiments.

An experimental investigation of the acid autocatalytic bromate sulfite reaction in a microemulsion environment is described in chapter five. The behaviour of the pH clock reaction is explored in batch, in a non-ionic and a cationic surfactant-oil-water microemulsion. In these microemulsion systems the reactants are confined in nano-sized droplets containing the polar phase, suspended in a continuous non-polar oil phase. The kinetics of the acid autocatalysis is shown to be affected by the change in droplet size and dispersion of droplets. The effect of the microheterogeneties of the environment on the reaction-diffusion fronts is also investigated. The cationic microemulsion system shows interesting convective instabilities which are not seen in aqueous phase systems. This system may therefore provide a novel environment for the study of convection induced instabilities in acid reaction-diffusion fronts.

Final comments, conclusions from this work and possible future direction are discussed in Chapter 6.

1.6 References

(1) WC Bray: Journal of the American Chemical Society 43 (1921) 1262.

(2) M Peard, C Cullis: Trans. Faraday. Soc. 47 (1951) 616.

(3) R Field, M Burger: Oscillations and Travelling waves in chemical systems. New York, 1985.

(4) A Zhabotinsky: Biophysics 9 (1964) 329.

(5) I Prigogine: Nonequilibrium thermondynamics and chemical evolution: An overview. Advances in Chemical Physics 55 (1984) 43.

(6) R Field, E Koros, R Noyes: Oscillations in Chemical Systems II. Thorough analysis of temporal oscillations in the Ce - BrO_3^- - Malonic acid systems. Journal of the American Chemical Society 94 (1972) 8649.

(7) R Field, R Noyes: Oscillations in Chemical Systems IV. Limit cycle behaviour in a model of a real chemical reaction. Journal of Chemical Physics 60 (1974) 1877.

(8) E Fermi: Thermodynamics, New York, 1956.

(9) SR de Goot, P Mazur: Nonequilibrium Thermodynamics, New York, 1984.

(10) JY Liang, MZ Jacobson: A study of sulfur dioxide oxidation pathways over a range of liquid water contents, pH values, and temperatures. Journal of Geophysical Research-Atmospheres 104 (1999) 13749-69.

(11) RJ Kaner, I Epstein: Induction and Inhibition of Chemical Oscillations by Iodide Ion in the Belousov Zhabotinsky Reaction. Journal of the American Chemical Society 100 (1978) 4073.

(12) A Pacault, P Hanusse, P De Kepper, C Vidal, J Boissonade: Phenomena in Homogeneous Chemical Systems for from Equilibrium. Accounts of Chemical Research. 9 (1976) 438.

(13) J Boissonade, P De Kepper: Transitions from Bistability to Limit-Cycle Oscillations - Theoretical-Analysis and Experimental-Evidence in an Open Chemical-System. Journal of Physical Chemistry 84 (1980) 501-06.

(14) P De Kepper, Epstein, I., Kustin, K.: A systematically designed homogenous oscillating chemical reaction: The arsenite- iodate system. Journal of the American Chemical Society 103 (1981) 2133-4.

(15) WC Chin, J Steed, T Nguyen, P Verdugo: Intraluminal pH oscillations modulate Ca2+/K+ ion-exchange, Ca2+ oscilations and release in from mucin secreory granules. Biophysical Journal 76 (1999) A227-A27.

(16) N Grandin, M Charbonneau: Intracellular Free Calcium Oscillates During Cell-Division of Xenopus Embryos. Journal of Cell Biology 112 (1991) 711-18.

(17) A Goldbetter: Biochemical Oscillations and Cellular Rhythms, Cambridge, U.K., 1996.

(18) I Epstein, J Pojamn: An Introduction to Nonlinear Chemical Dynamics, New York, 1998.

(19) S Strogatz: Nonlinear dynamics and chaos, Westview Press, Cambridge, MA, USA, 1994.

(20) CJ Crook, A Smith, RAL Jones, AJ Ryan: Chemically induced oscillations in a pH-responsive hydrogel. Physical Chemistry Chemical Physics 4 (2002) 1367-69.

(21) R Yoshida, H Ichijo, T Hakutta, T Yamaguchi: Self Oscillating swelling and deswelling of polymer gels. Macromolecular Rapid Communications 16 (1995) 305.

(22) AJ Ryan, CJ Crook, J Howse, P Topham, A Jones, M Geoghagan, A Parnell, L Ruiz-Perez, C MArtin: Resposive Brushes and Gels as components of soft nanotechnology. Faraday Discussions 128 (2005) 55.

(23) T Ohmori, M Nakaiwa, T Yamaguchi, M Kawamura, RYK Yang: Self-sustained pH oscillations in a compartmentalized enzyme reactor system. Biophysical Chemistry 67 (1997) 51-57.

(24) T Liedl, F Simnel: Switching the conformation of a DNA molecule with a chemical oscillator. Nano Letters 5 (2005) 1894.

(25) GP Misra, RA Siegel: Multipulse drug permeation across a membrane driven by a chemical pH-oscillator. Journal of Controlled Release 79 (2002) 293-97.

(26) S Giannos, S Dinh, B Berner: Temporally Controlled Drug Delivery Systems: Coupling of pH Oscillators with Membrane Diffusion. (1995).

(27) K KurinCsorgei, I Epstein, M Orban: Periodic Pulses of Calcium ions in a chemical system. Journal of Physical Chemistry A. (2006) 7588.

(28) M Orban, K Kurin-Csorgei, G Rabai, IR Epstein: Mechanistic studies of oscillatory copper(II) catalyzed oxidation reactions of sulfur compounds. Chemical Engineering Science 55 (2000) 267-73.

(29) K Novakovic, C Grosjean, SK Scott, A Whiting, M Willis, A Wright: Chemical Physics Letters 435 (2007) 142.

(30) GA Frerichs, TM Mlnarik, RJ Grun, RC Thompson: A new pH oscillator: The chlorite-sulfite-sulfuric acid system in a CSTR. Journal of Physical Chemistry A 105 (2001) 829-37.

(31) G Rabai, M Orban, IR Epstein: Systematic Design of Chemical Oscillators .64. Design of pH-Regulated Oscillators. Accounts of Chemical Research 23 (1990) 258-63.

(32) G Rabai, IR Epstein: Systematic Design of Chemical Oscillators. 61. Oxidation of Hydroxylamine by Periodate in a Continuous-Flow Stirred Tank Reactor - a New pH Oscillator. Journal of Physical Chemistry 93 (1989) 7556-59.

(33) G Rabai, IR Epstein: Systematic Design of Chemical Oscillators .63. Large-Amplitude pH Oscillation in the Oxidation of Hydroxylamine by Iodate in a Continuous-Flow Stirred Tank Reactor. Journal of Physical Chemistry 94 (1990) 6361-65.

(34) G Rabai, M Orban, IR Epstein: Systematic Design of Chemical Oscillators 77. A Model for the pH-Regulated Oscillatory Reaction between Hydrogen-Peroxide and Sulfide Ion. Journal of Physical Chemistry 96 (1992) 5414-19.

(35) G Rabai, I Hanazaki: Light-induced route to chaos in the H_2O_2-HSO_3^--HCO_3^- - $Fe(CN)_6^{4-}$ flow system. Journal of the American Chemical Society 119 (1997) 1458-59.

(36) G Rabai, MT Beck: Exotic Kinetic Phenomena and Their Chemical Explanation in the Iodate-Sulfite-Thiosulfate System. Journal of Physical Chemistry 92 (1988) 2804-07.

(37) G Rabai, MT Beck, K Kustin, IR Epstein: Systematic Design of Chemical Oscillators .49. Sustained and Damped Ph Oscillation in the Periodate Thiosulfate Reaction in a Continuous-Flow Stirred Tank Reactor. Journal of Physical Chemistry 93 (1989) 2853-58.

(38) G Rabai, ZV Nagy, MT Beck: Quantitative Description of the Oscillatory Behavior of the Iodate-Sulfite-Thiourea System in CSTR. Reaction Kinetics and Catalysis Letters 33 (1987) 23-29.

(39) G Rabai, I Hanazaki: pH oscillations in the bromate-sulfite-marble semibatch and flow systems. Journal of Physical Chemistry 100 (1996) 10615-19.

(40) N Ozaki, G Rabai, I Hanazaki: Discovery of Novel Broamte-Sulfite pH oscillations with Mn^{2+} or MnO_4^- as a negative feedback species. Journal of Physical Chemistry A. 103 (1999) 10915.

(41) MI Castro, RA Furilla, D Mehta, RD Tallman: Arterial pH oscillations during unidirectional ventilation and spontaneous breathing in pine snakes. Faseb Journal 10 (1996) 2263-63.

(42) T Mair, SC Muller: Travelling NADH and Proton Waves during Oscillatory Glycolysis in vitro. Journal of Biological Chemistry 271 (1996) 627.

(43) H Petty, R Worth, A Kindzelski: Imaging Sustained Dissipative Patterns in the Metabolism of Individual Living Cells. Physical Review Letters 84 (2000) 2754.

(44) S Sanchez-Armass, S Ssennoune, D Maiti, F Ortega, R Martinez- Zaguilan: Spectral imaging microscopy demonstrates cytoplasmic pH oscillations in glial cells. American Journal of Physiology Cell Physiology 290 (2005) C524.

(45) AA Bulychev, S Zykov, A Rubin, SC Muller: Transitions from alkaline spots to regular bands during pH pattern formation at the plasmalemma of chara cells. European Biophysics Journal 32 (2003) 144.

(46) G Rabai, I Hanazaki: Temperature compensation in the oscillatory hydrogen peroxide- thiosulfate-sulfite flow system. Chemical Communications (1999) 1965-66.

(47) KM Kovacs, G Rabai: Temperature-compensation in pH-oscillators. Physical Chemistry Chemical Physics 4 (2002) 5265-69.

(48) SK Scott: Oscillations, Waves, and Chaos in Chemical Kinetics. Oxford. 1995.

(49) J Billingham, DJ Needham: Mathematical-Modeling of Chemical Clock Reactions .1. Induction, Inhibition and the Iodate Arsenious-Acid Reaction. Philosophical Transactions of the Royal Society of London Series a-Mathematical Physical and Engineering Sciences 340 (1992) 569-91.

(50) J Billingham, DJ Needham: Mathematical-Modeling of Chemical Clock Reactions .2. A Class of Autocatalytic Clock Reaction Schemes. Journal of Engineering Mathematics 27 (1993) 113-45.

(51) K Chie, N Okazaki, Y Tanimoto, I Hanazaki: Tristability in the bromate-sulfite-hydrogencarbonate pH oscillator. Chemical Physics Letters 334 (2001) 55-60.

(52) M Orban, IR Epstein: Journal of the American Chemical Society 112 (1990) 1812.

(53) IR Epstein, CE Dateo, P De Kepper, K Kustin, M Orban: Bistability in a C.S.T.R.: New Experimental Examples and Mathematical Modeling-Nonlinear phenomena in Chemical Dynamics, Berlin, 1980.

(54) G Rabai, MT Beck: High-Amplitude Hydrogen-Ion Concentration Oscillation in the Iodate-Thiosulfate-Sulfite System under Closed Conditions. Journal of Physical Chemistry 92 (1988) 4831-35.

(55) G Rabai: Modeling and designing of pH-controlled bistability, oscillations, and chaos in a continuous-flow stirred tank reactor. Ach-Models in Chemistry 135 (1998) 381-92.

(56) http://www.math.pitt.edu/~bard/xpp/xpp.html.

(57) E Edblom, Y Luo, M Orban, K Kustin, I Epstein: Systematic Design of Chemical Oscillators. 45 Kinetics and Mechanism of the oscillatory bromate-sulfite-ferrocyanide reaction. J. Phys. Chem. 93 (1989) 2722.

(58) A Keresztessy, I Nagy, G Bazsa, J Pojman: Travelling Waves in the Iodate Sulfite and Bromate Sulfite Systems. J. Phys. Chem. 99 (1995) 5379.

(59) T Szanto, G Rabai: pH Oscillations in the Bromate Sulfite Bisulfite Reaction in a CSTR. J. Phys. Chem A 109 (2005) 5398.

(60) G Rabai, A Kaminaga, I Hanazaki: Mechanism of the oscillatory bromate oxidation of sulfite and ferrocyanide in a CSTR. Journal of Physical Chemistry 100 (1996) 16441-42.

(61) VK Vanag, MV Alfimov: Journal of Physical Chemistry 97 (1993) 1884.

(62) I Nagypal, IR Epstein: Journal of Chemical Physics 89 (1988) 6925.

(63) I Nagypal, IR Epstein: Journal of Physical Chemistry 90 (1986) 6285.

(64) VK Vanag, D Melikhov: Asymetrical Concentration Fluctuations in the Autocatalytic Bromate-Bromide-Catalyst Reaction and in the Oscillatory Belousov-Zhabotinsky Reaction in a Closed Reactor: Stirring Effects Journal of Physical Chemistry 99 (1995) 17372.

(65) VK Vanag, AO Ait: Russian Journal of Physical Chemistry 67 (1993) 2024.

(66) I Hanazaki, G Rabai: Origin of chemical instability in the bromate-sulfite flow system. Journal of Chemical Physics 105 (1996) 9912-20.

(67) VK Vanag, IR Epstein: Segmented spiral waves in a reaction-diffusion system. Proceedings of the National Academy of Sciences of the United States of America 100 (2003) 14635-38.

(68) K Agladze, I Krinsky: Multi-armed vortices in an active chemical medium. Nature, Letts 296 (1982) 424.

(69) V Castets, E Dulos, J Boissonade, P De Kepper: Experimental Evidence of a sustained standing Turing-type nonequilibrium chemical patters. Phys. Rev. Lett. 64 (1990) 2953.

(70) AS Mikhailov, B Hess: Self Organization in Living Cells: Networks of Protein Machines and Nonequlibrium soft matter. Journal of Biological Physics 28 (2002) 655.

(71) R Luther: Electrochemistry 12 (1906) 596.

(72) S Barlow, GV Buxton, SA Murray, GA Salmon: Free-radical-induced oxidation of hydroxymethanesulfonate in aqueous solution .1. A pulse radiolysis study of the reactions of (OH)-O and SO_4. Journal of the Chemical Society-Faraday Transactions 93 (1997) 3637-40.

(73) AG Merzhanov, EN Rumanov: Rev. Mod. Phys. 71 (1999) 1173.

(74) P Ortoleva: Geochemical self-organization, Oxford, 1994.

(75) l Szirovicza, I.Nagypal, E Boga: an algorithm for the Design of Propogating Acidity Fronts. Journal of the American Chemical Society 111 (1989) 2842-45.

(76) Z Viranyi, D Horvath, A Toth: Migration driven instability in the chlorite tetrathionate reaction. Journal of Physical Chemistry A 110 (2006) 3614.

(77) J D'Hernoncourt, A Zebib, a De Wit: On the classification of buoyancy-driven chemo-hydrodynamic instabilities of chemical fronts. Chaos 17 (2007) 013109-1.

(78) J Pojman, I Epstein: Journal of Physical Chemistry 94 (1990) 4966.

(79) J Masere, D Vasquez, B Edwards, J Wilder, K Showalter: Nonaxisymmetric and Axisymmetric convection in propagating reaction-diffusion fronts. J. Phys. Chem. 98 (1994) 6505.

(80) T Bansagi, D Horvath, A Toth: Multicomponent convection in the chlorite-tetrathionate reaction. Chemical Physics Letters 384 (2004) 153.

(81) D Horvath, A Toth: Diffusion-driven front instabilities in the chlorite-tetrathionate reaction. J. Chem. Phys. 108 (1997) 1447.

(82) T Rica, D Horvath, A Toth: Density fingering in acidity fronts: Effects of viscosity. Chemical Physics Letters 408 (2005) 422.

CHAPTER 2

Experimental Investigation of the Methylene Glycol-Sulfite Reaction

2.1 Introduction

The reaction between methylene glycol (hydrated formaldehyde) and a sulfite bisulfite buffer can exhibit pH clock behaviour in a closed system. with an initial steady increase in pH followed by a sharp increase of ~ 4.5 pH units after a period of time (t_{ind}). The induction time is dependent on the initial concentrations. This dependence can aid in the investigation of the mechanism. As discussed in chapter 1, the typical mechanism of a pH 'clock' is the autocatalytic oxidation of S(IV) species by some inorganic halogenate oxidant. The bromate-sulfite reaction was discussed as a prototype and we saw how the initial concentration of reactants affected the induction time, and overall pH change. The methylene glycol system is different to these 'typical systems' as it not only contains an organic substrate and involves an *increase* in pH, but there is no apparent autocatalysis in what was its accepted mechanism. The system therefore provides an interesting study, not only from a purely kinetic point of view, but also for the design of a new route to pH oscillators. This chapter presents a detailed experimental study of the previously known clock reaction in batch and an investigation of the system's response in an open reactor.

2.2 History

Sodium bisulfite adds to aldehydes in a nucleophilic addition reaction such as the one shown below. The product of this reaction is a bisulfite addition compound which in the case of formaldehyde is hydroxymethanesulfonate (HMS^-).

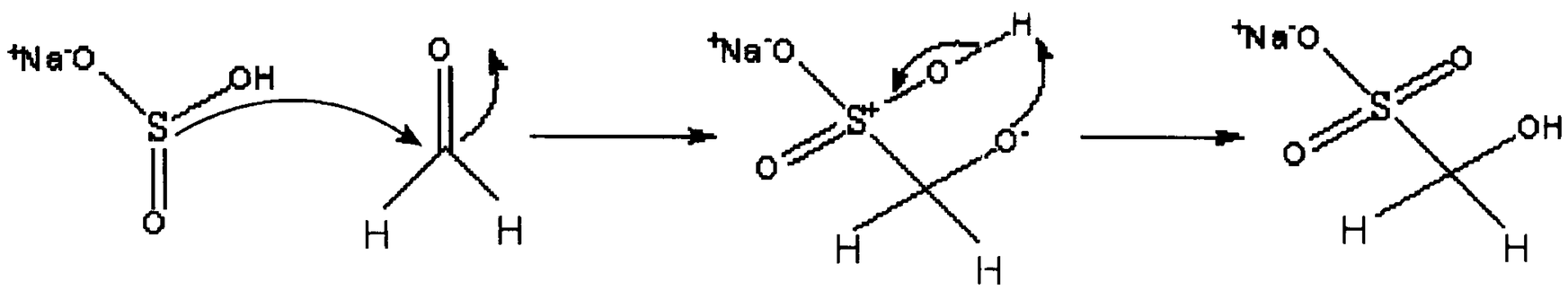

Figure 2.1 The reaction of bisulfite with formaldehyde.

The reaction of formaldehyde with sulfite has been studied previously by Wagner (1), Jones and Oldham (2), Skrabal and Skrabal (3), Sorensen and Andersen (4) and Bell and Evans (5). Wagner determined that the kinetics of the reaction under neutral and alkaline conditions conformed to a two term rate law in which the rate of S(IV) consumption exhibited first order dependencies on the concentrations of formaldehyde and sulfite/ bisulfite. Jones and Oldham later noted that according to Wagner's data HSO_3^- is the only species to undergo reaction with formaldehyde. Conversely Skrabal and Skrabal argued that the reactivity of SO_3^{2-} is much greater than that of HSO_3^- according to the series:

$$SO_3^{2-} > HSO_3^- > SO_2 \cdot H_2O$$

Sulfite was therefore presumed to be the main reactant. Sorensen and Andersen later confirmed this for reaction in basic solution. Bell and Evans proposed that the production of HMS^- occurs via a rapid nucleophilic addition of sulfite to formaldehyde, and that the dehydration of methylene glycol to give free formaldehyde is the rate determining step. Boyce and Hoffman (6) argued that the rate-determining step for the formation of hydroxylmethane sulfonate (HMS^-) in acidic solution was the nucleophilic addition of HSO_3^- and/or SO_3^{2-} to $CH_2(OH)_2$. In this addition step the relative contributions of bisulfite and sulfite ion to the reaction rate is dependent on the relative equilibrium concentrations of SO_3^{2-} and HSO_3^-, as determined by pH, and the nucleophilicity of each species. They found bisulfite to be

the principal reactant at pH values of less than 2, whereas at pH values greater than 4 the sulfite ion was considered the dominant species. The initial pH of the system is determined by the relative concentrations of sulfite and bisulfite through the following relationship:

$$\mathrm{pH} = -\log[\mathrm{H}^+] = \mathrm{p}K_a + \log\frac{[\mathrm{SO_3}^{2-}]}{[\mathrm{HSO_3}^-]}$$

Burnett (7) assumed that the sudden rise in pH corresponded to the complete consumption of HSO_3^- and Warneck (8) later concurred. Most recently Winkelman *et. al.* (9) investigated the formaldehyde-bisulfite system to understand the kinetics of the dehydration of methylene glycol. Under their experimental conditions the rate determining step in the production of HMS^- is the dehydration of methylene glycol which is independent of the concentration of sulfite and hydroxide ions at neutral pH (pH range 6.0-7.8). The reaction of sulfite with formaldehyde is fast and therefore sulfite can be considered to be a trapping agent or chemical scavenger of any formaldehyde produced by the dehydration of methylene glycol. From this they proposed the relevance of the following reactions in the mechanism of HMS^- formation:

$$\mathrm{CH_2(OH)_2} \rightleftharpoons \mathrm{CH_2O + H_2O} \qquad (1.1)$$

$$\mathrm{HSO_3}^- \rightleftharpoons \mathrm{H^+ + SO_3}^{2-} \qquad (1.2)$$

(10)

$$\mathrm{SO_3}^{2-} + \mathrm{CH_2O} \rightleftharpoons \mathrm{CH_2(O^-)SO_3}^- \qquad (1.3)$$

$$\mathrm{CH_2(O^-)SO_3}^- + \mathrm{H_2O} \rightleftharpoons \mathrm{CH_2(OH)SO_3}^- + \mathrm{OH}^- \qquad (1.4)$$

OVERALL: (1.5)

$$\mathrm{CH_2(OH)_2} + \mathrm{SO_3}^{2-} \rightarrow \mathrm{CH_2(OH)SO_3}^- + \mathrm{OH}^-$$

The reaction also serves as a useful educational demonstration and many Journal of Chemical Education papers are published (7,8,11,12) which discuss the most effective concentration ranges and experimental techniques to produce dramatic clock behaviour. In particular Burnett has specified three experimental considerations:

- Bisulfite-sulfite mixture is readily oxidised in air. Boiling out the solutions has only a temporary effect, addition of 10^{-3}M EDTA permits the preservation of the solutions.
- Incomplete depolymerization of the formaldehyde solution produces irreproducible clock times.
- The ratio of bisulfite/ sulfite should never be reduced below unity since the clock behaviour is lost.

The reaction is relevant in atmospheric chemistry as the oxidation of S(IV) species by dissolved formaldehyde occurs in cloud and fog water to give hydroxymethane sulfonate (HMS^-) (13). The process is thought to provide a route for the stabilization of S(IV) with respect to oxidation by H_2O_2 dissolved in microdroplets, which proceeds rapidly to yield sulphuric acid. The formation of the HMS^- product is dependent on the concentrations of the species involved, the pH of the cloud and on the cloud size. The addition of organic ligands to sulphur species is also believed to have an inhibitative effect on the iron catalyzed autoxidation of S(IV) in atmospheric fog water (14). The product HMS^- has also been proposed to participate in radical reactions in clouds contributing to sulfate production through oxidation by OH radical (15).

Previous work (16) shows that considerable ambiguity exists as to the exact mechanism of the reaction. Usual discussions of mechanisms of nonlinear clock

reactions focus on identifying autocatalytic processes where the rate of production of a species is dependent on the concentration of that species. The present mechanism contains no identifiable feedback. The following experiments are an investigation of the system in attempt to define a plausible chemical mechanism. The existence of an induction time in a chemical reaction suggests that the system may exhibit bistability, and therefore be able to support oscillations in flow (17). The system was therefore also studied in an open configuration.

2.2.1 Formaldehyde

Recent work (16) on the system agrees that the rate determining step in the reaction of sulfite with formaldehyde is the dehydration of methylene glycol, not the addition of sulfite/ bisulfite to formaldehyde. Although formaldehyde is a gas at room temperature, it is readily soluble in water and the general commercial form of formaldehyde is a 37 - 40% solution in water (formalin or formol). In water, formaldehyde polymerizes and formalin actually contains very little formaldehyde in the form of H_2CO monomer. The following hydration equilibrium is then important:

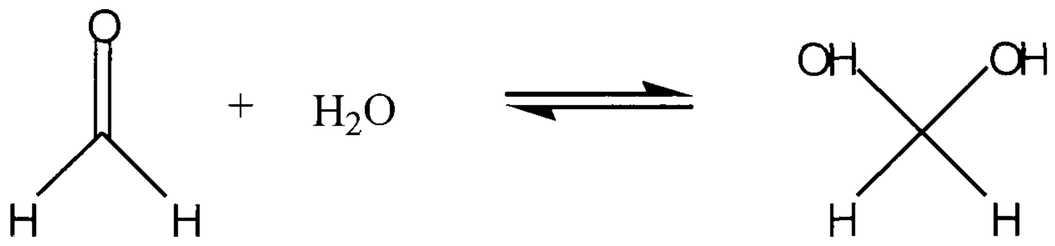

$$K = 5.5\times10^{-4} = \frac{5.5\times10^{-3}\ s^{-1}}{10\ s^{-1}}$$

Figure 2.2 An aqueous solution of formaldehyde contains essentially no CH_2O as it is completely hydrated in the form of methylene glycol.

In aqueous solution the dissolved formaldehyde is mainly present as the monohydrate methylene glycol, $CH_2(OH)_2$ and a series of low molecular weight

polymeric hydrates or poloxymethylene glycols, having the type formula HO-$(CH_2(OH)_n)$-H. It has been confirmed by ^{1}H NMR studies (18) that this is indeed the case and the equilibrium aqueous solution contains about 10% methyl alcohol with about 30% methylene glycol and a mixture of the polyoxymethylene glycols $HO(CH_2O)_nH$. A small concentration of the monomeric form is present but its concentration is well below 0.1% even in concentrated solutions (19). Formalin solutions usually contain a few percent methanol to limit the extent of polymerization and therefore really contain formaldehyde, paraformaldehyde, formic acid, and methanol. It is recommended that any solution is left to stand for 24 hours before use to allow complete depolymerization of these polyoxomethylene glycols.

2.3 Experimental

2.3.1 Materials

Two separate stock solutions were freshly prepared before each set of batch experiments, using analytical grade reagents and doubly distilled deionised water. Formaldehyde solutions were prepared 24 hours in advance to allow dehydration of methylene glycol. The two stock solutions were allowed to stand in a water bath for 20 minutes so were pre-thermostatted to 25^0C.

2.3.2 Preparation of stock formaldehyde solution. Solution A

Formalin, the aqueous solution of formaldehyde, typically contains 37 - 50 wt% formaldehyde. The density of formalin is 1.09 g cm^{-3}. Thus 9.3 ml of 37 weight % (accuracy 99%) formalin (Aldrich) in 100 ml gives a 1.2 M solution.

9.3 ml = 3.7 g formaldehyde

$$\text{moles} = \frac{\text{mass}}{\text{Mr}} = \frac{3.7\text{g}}{30\ \text{g mol}^{-1}} = 0.1233\ \text{moles}$$

$$\text{c} = \frac{\text{moles}}{\text{volume}} = \frac{0.1233\ \text{moles}}{0.1\ \text{dm}^{-3}} = 1.233\ \text{Molar}$$

2.3.3 Preparation of stock bisulfite sulfite buffer solution. Solution B

Sodium metabisulfite does not exist in solution. $NaHSO_3$ is obtained when aqueous solutions of SO_2 and NaOH are dehydrated and crystallize to form the compound. When $Na_2S_2O_5$ is dissolved in water 2 mole equivalents of HSO_3^- are formed according to the following:

$$Na_2S_2O_5 + 2H_2O \leftrightarrow 2Na^+ + S_2O_5^{2-} + 2H_2O$$

$$S_2O_5^{2-} + H_2O \leftrightarrow \underline{\mathbf{2}}HSO_3^-$$

1.0 g of $Na_2S_2O_5$ (Sigma- Aldrich) in 100 ml gives a 0.1 M solution HSO_3^-.

$$\text{n} = \frac{1.0\ \text{g}}{190.4\ \text{g mol}^{-1}} = 5.25\times10^{-3}\ \text{moles}\ Na_2S_2O_5 = 0.0105\ \text{moles}\ HSO_3^-$$

$$\text{c} = \frac{\text{moles}}{\text{volume}} = \frac{0.0105\ \text{moles}}{0.1\ \text{dm}^{-3}} = 0.105\ \text{Molar}$$

0.01 Molar stock solution of sodium sulfite (Aldrich)

$$\frac{0.15\ \text{g}}{126.04\ \text{g mol}^{-1}} = 1.19\times10^{-3}\ \text{moles}$$

$$\text{c} = \frac{\text{moles}}{\text{volume}} = \frac{1.19\times10^{-3}\ \text{moles}}{0.1\text{dm}^{-3}} = 0.0119\ \text{Molar}$$

It is useful to define $[HSO_3^-]/ [SO_3^{2-}]$ as b/c. If b/c <1, no clock behaviour is observed.

2.3.4. Batch procedure

Experiments were carried out in a fixed volume of 10 ml, thus allowing calculation of the concentration from the number of ml of each solution rather than the actual number of moles l^{-1}. The reaction vessel was stirred at a constant rate of 450 r.p.m. A calibrated pH electrode in conjunction with HANNA software was used to accurately measure the pH as a function of time in one second intervals. Three systems of stock solution were employed. The initial concentration of one reactant was varied in separate experiments: $[CH_2(OH)_2]_0$ in system 1, $[HSO_3^-]_0$ and $[SO_3^{2-}]_0$ in system 2 (b/c is constant) and $[SO_3^{2-}]_0$ in system 3.

System 1: Solution A: $CH_2(OH)_2$ (1.2 M, Aldrich); $Na_2S_2O_5$ (0.1 M, Alrdich); SO_3^{2-} (0.02 M, Aldrich). Stock solutions were mixed together to give initial concentrations of:

$[CH_2(OH)_2]_0$ = 0.06 - 0.6 M (5 ml – 0.5 ml of 1.2 M into 10 ml)

$[HSO_3^-]_0$ = 0.1 M (5 ml of solution B into 10 ml)

$[SO_3^{2-}]_0$ = 0.01 M

System 2: Solution A: $CH_2(OH)_2$ (0.192 M, Aldrich); Solution B: $Na_2S_2O_5$ (0.08 M, Alrdich); SO_3^{2-} (0.0016 M, Aldrich). Stock solutions were mixed together to give initial concentrations of:

$[CH_2(OH)_2]_0$ = 0.096 M (5 ml of solution A into 10 ml)

$[HSO_3^-]_0$ = 0.008 - 0.08 M (5 ml – 0.5 ml of stock solution B into 10 ml)

$[SO_3^{2-}]_0$ = 0.0008 - 0.008 M (5 ml- 0.5 ml of stock solution B into 10 ml)

System 3: Solution A: $CH_2(OH)_2$ (0.192 M, Aldrich); Solution B: $Na_2S_2O_5$ (0.063 M, Alrdich); SO_3^{2-} (0.126- 0.0084 M, Aldrich). Stock solutions were mixed together to give initial concentrations of:

$[CH_2(OH)_2]_0$ = 0.096 M (5 ml of solution A into 10 ml)

$[HSO_3^-]_0$ = 0.063 M (5 ml of stock solution B into 10 ml)

$[SO_3^{2-}]_0$ = 0.0042 - 0.063 M (5 ml of different stock solution B into 10 ml)

Additional experiments were conducted in 1 M NaCl to ensure ionic strength had no significant effect on the induction time or pH change.

2.3.5 Experimental procedure: open system

Flow experiments were performed in a continuously filled well stirred tank reactor (CSTR) of volume 22 ml. Stock solutions were supplied to the reactor via two separate tubes with a calibrated peristaltic pump (Gilson). The CSTR was completely filled to ensure there was no solution/ air interface. The reactor was surrounded by a water jacket and reactions were performed at a constant temperature of 25 °C. The solution was stirred at a constant rate of 450 r.p.m. pH and temperature were monitored using a HANNA pH electrode and digital bench meter.

2.4 Results - Batch

Typical pH time traces are shown in Figures 2.3 (a) and (b) for the batch reaction of methylene glycol and a sulfite/ bisulfite buffer. The initial concentrations are $[CH_2(OH)_2]_0$ = 0.096 M (0.192 M stock), $[HSO_3^-]_0$ = 0.0631 M (0.01262 M). The concentration of sulfite is varied in these results. In each case there is an induction time during which the pH increases relatively slowly, followed by a relatively rapid

increase in pH. The increase in pH after the reaction event is between 4 and 5 pH units. The long term behaviour of the system demonstrates a subsequent gradual decrease in pH following the reaction event.

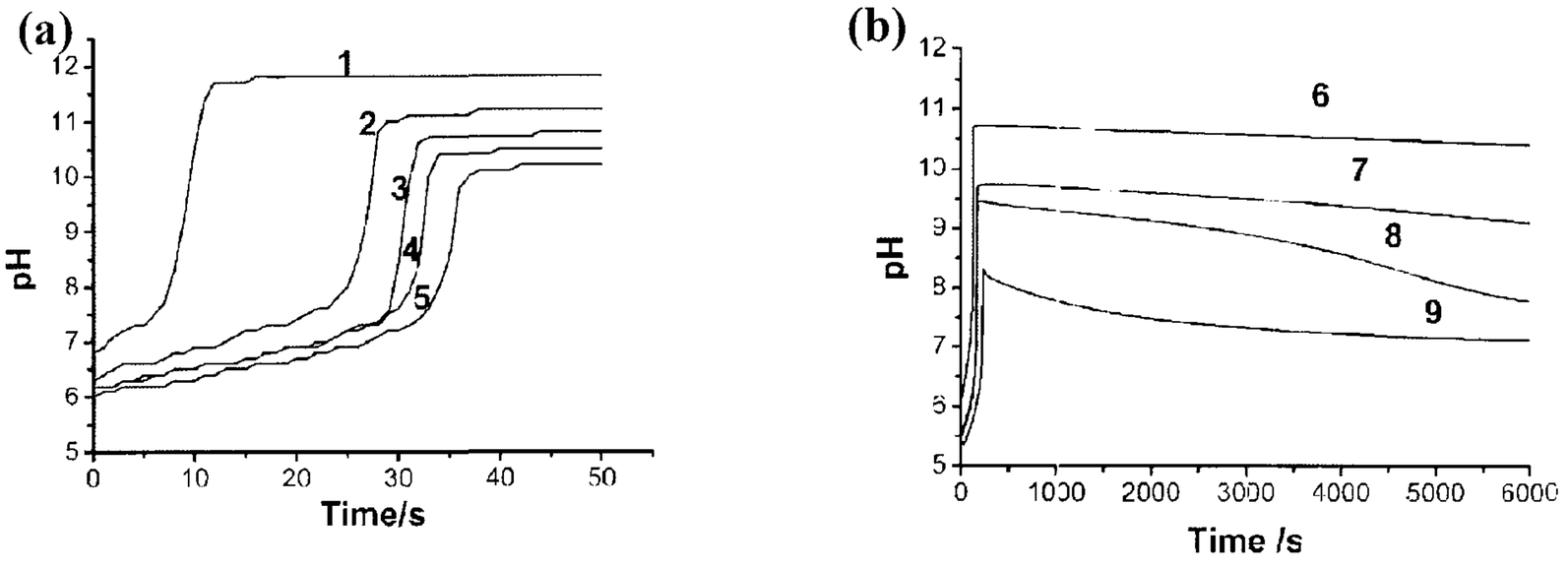

Figure 2.3 (a) Experimental pH time traces in the batch reactor with different initial sulfite concentrations. $[CH_2(OH)_2]_0$ = 0.096 M, $[HSO_3^-]_0$ = 0.063 M, b/c = 1 (1), 5 (2), 8 (3), 10 (4), 15 (5). (b) Long time behavior in batch with different initial sulfite concentrations, $[CH_2(OH)_2]_0$ = 0.025 M, $[HSO_3^-]_0$ = 0.0166 M, b/c = 13 (6), 57 (7), 117 (8) and with $[SO_3^{2-}]_0$ = 0 M (9).

Figures 2.4, 2.5 and 2.6 show the results of three different systems (systems 1, 2 and 3). The induction time is recorded for each system variable. Accurate determination of the clock time was achieved through first derivative plots of the pH – time traces using ORIGIN.

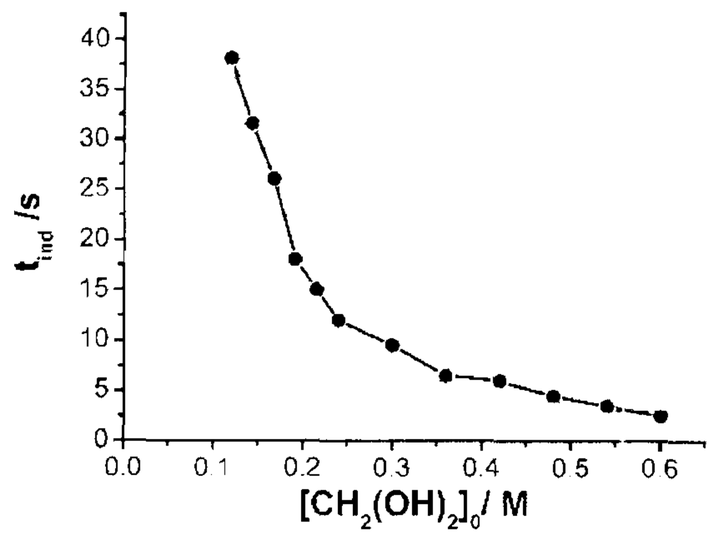

Figure 2.4 Experimental variation of induction time with $[CH_2(OH)_2]_0$ where $[HSO_3^-]_0$ = 0.1 M, b/c = 10.

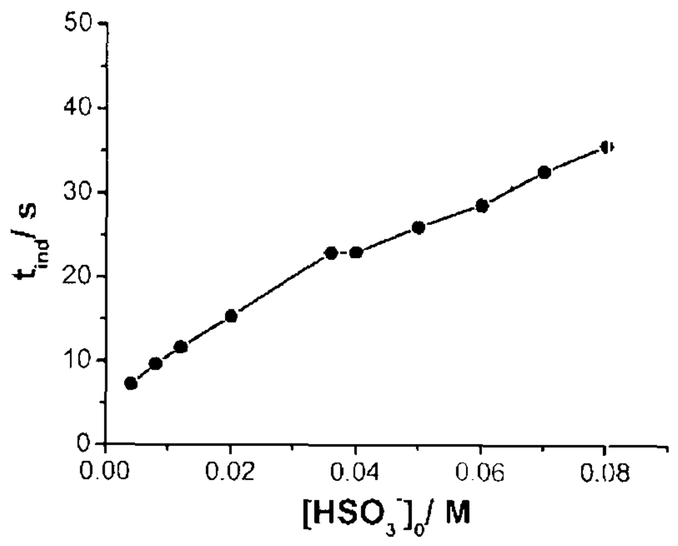

Figure 2.5 Experimental variation of induction time with $[HSO_3^-]_0$ where b/c = 10 and $[CH_2(OH)_2]_0$ = 0.096 M

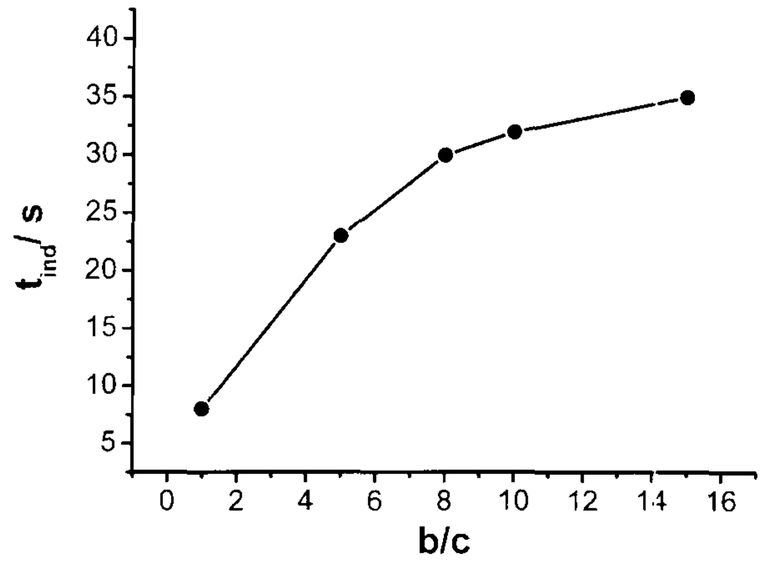

Figure 2.6 Experimental variation of induction time with $[SO_3^{2-}]_0$ where $[HSO_3^-]$ = 0.063 M and $[CH_2(OH)_2]_0$ = 0.096 M.

2.4.1. Results - Open system

Under flow conditions the system is able to support bistability for a range of operating conditions. Example bifurcation diagrams for this response are shown in Figures 2.7 (a) and (b). There is coexistence of the low pH flow branch and the high pH thermodynamic branch at high flow rate. The 'ignition' transition from low pH to high pH occurs at a flow rate of $k_0 = 1.2 \times 10^{-2}$ s^{-1} in Figure (a) and at $k_0 = 2.2 \times 10^{-2}$ s^{-1} in (b). The corresponding 'washout' occurs at a flow rate that is too high to detect, thus the whole region of hysteresis is not shown.

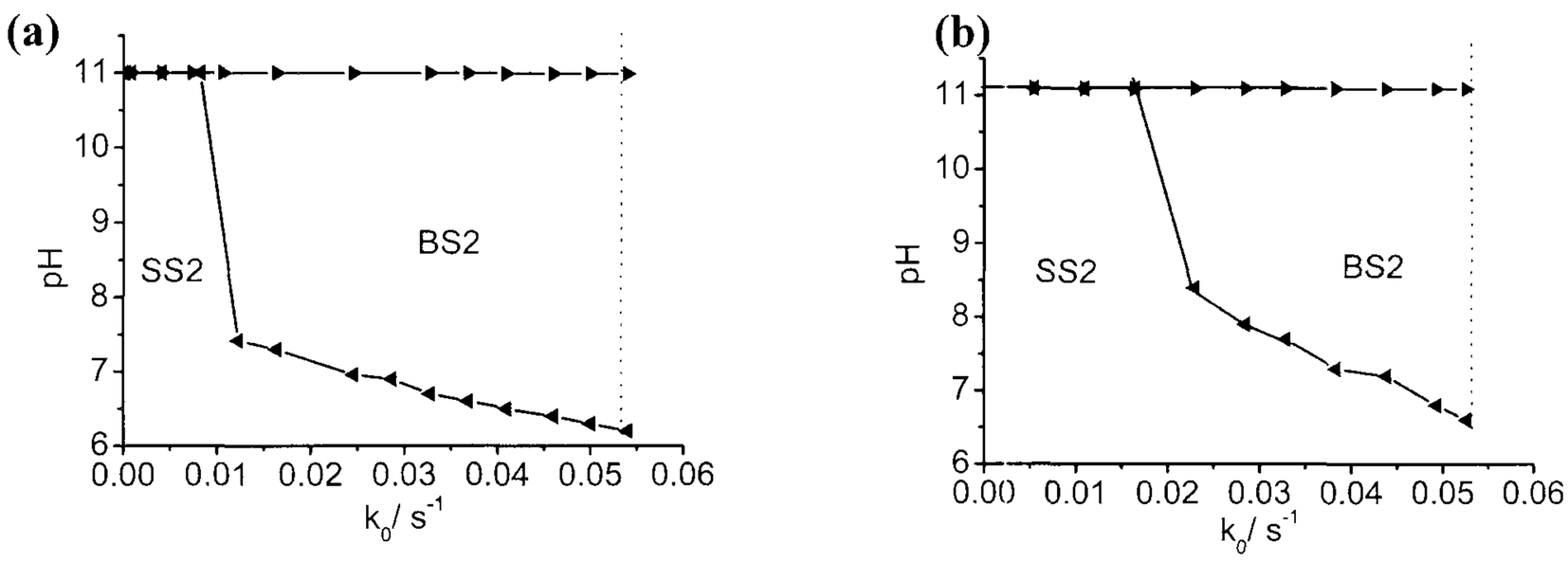

Figure 2.7 Bistability diagrams showing the region of high pH steady state (SS2) and bistability between the two steady states (BS2). (a) $[CH_2(OH)_2]_0 = 0.17$ M, $[HSO_3^-] = 0.1$ M and $[SO_3^{2-}]_0 = 0.01$ M.(b) $[CH_2(OH)_2]_0 = 0.15$ M, $[HSO_3^-] = 0.1$ M and $[SO_3^{2-}]_0 = 0.01$ M.

The form of the bifurcation diagram changes as the inflow concentrations of the species are varied. The response shown in Figure 2.8 again exhibits two branches at low and high pH (flow and thermodynamic respectively), for a system with b/c = 5 and a lower concentration of methylene glycol. The character of the upper branch changes as the flow is increased. There is a Hopf bifurcation at approximately $k_0 = 1.8 \times 10^{-3}$ s^{-1}, where the high pH steady state loses stability and a stable, small

amplitude oscillatory state emerges. There are therefore two different types of bistability evident in this region of phase space; BS2 which is the coexistence of two steady states (as in Figure 2.7) and BS1 which is a region of coexistence of a stable low pH steady state and a high pH oscillatory state.

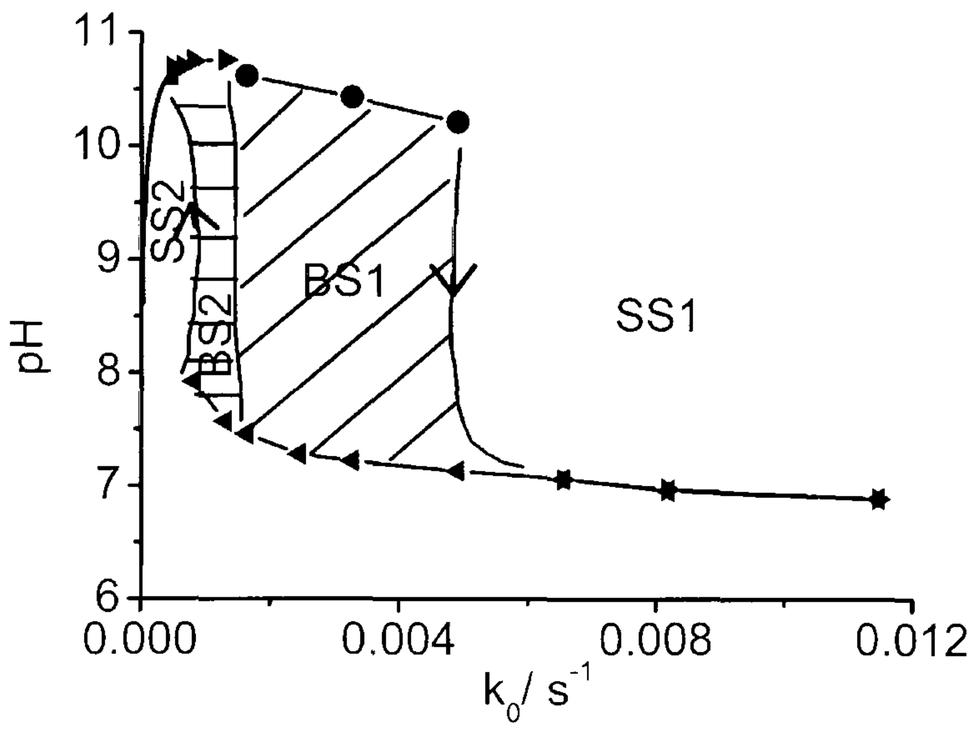

Figure 2.8 Bifurcation diagram showing the regions of high pH steady state (SS2), bistability between two steady states (BS2), bistability between the low pH steady state and the high pH oscillatory state (BS1) and the low pH steady state (SS1). $[CH_2(OH)_2]_0 = 0.067$ M, $[HSO_3^-] = 0.066$ M and $[SO_3^{2-}]_0 = 0.0133$ M, b/c = 5.

A further example of a bifurcation diagram is show in Figure 2.9 (a). Here, $[HSO_3^-]_0 = 0.066$ M, b/c = 116 and $[CH_2(OH)_2]_0 = 0.089$ M. A high pH oscillatory state exists at low flow rates after a region of thermodynamic steady state at pH ~ 8. This is followed by a large region of BS1 with increasing the flow rate. This region represents co-existence of a low pH steady state and high pH oscillatory state. Example time series of the oscillations at $k_0 = 2.1 \times 10^{-3}$ s^{-1}, recorded in potential and pH are shown in Figures 2.9 (b) and (c) respectively. The wave form is essentially that of a period one response. The variation of the amplitude of oscillation with flow rate is shown in Figure 2.9 (a) as the size of the vertical bars superimposed

on the upper branch. The amplitude increases with flow rate, and the period decreases from 40 to 30 s in this particular bifurcation range.

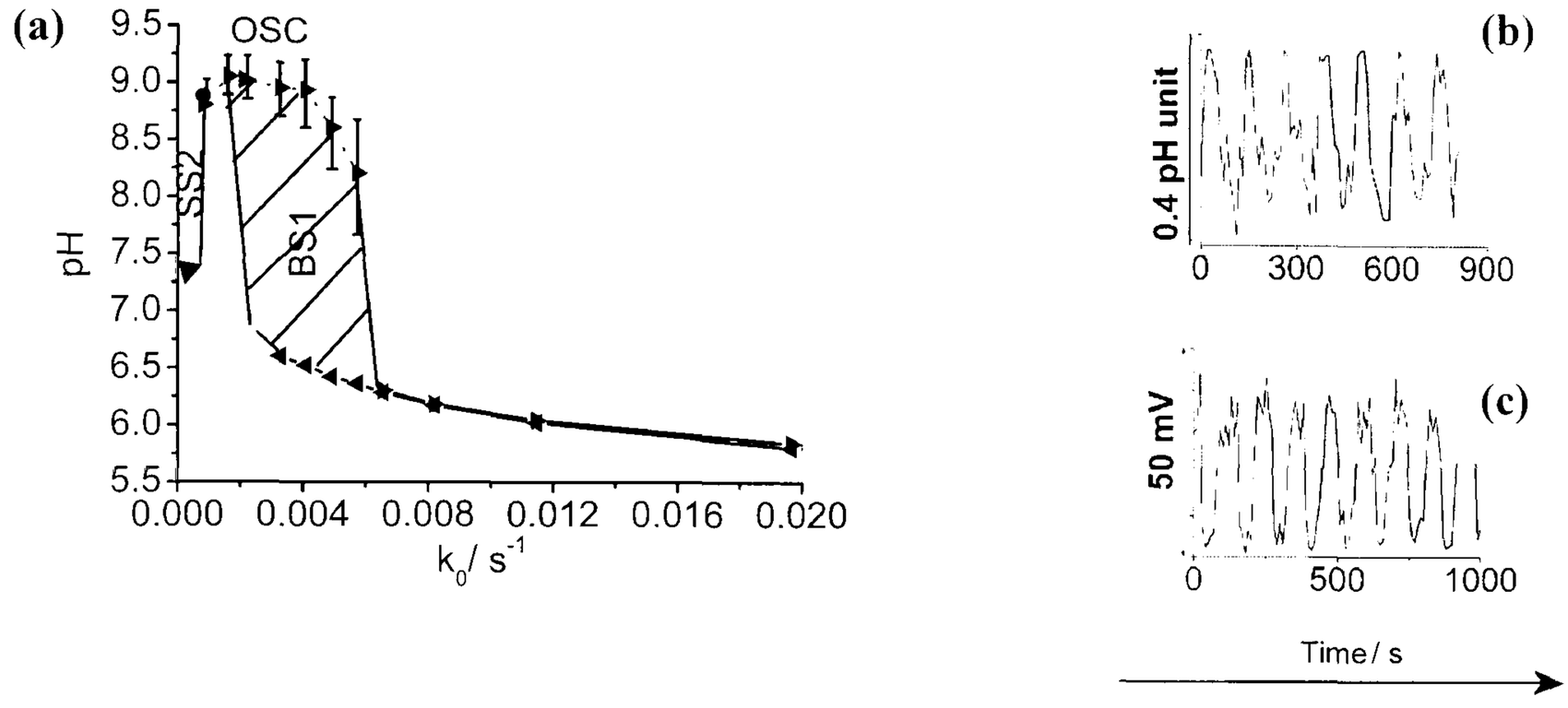

Figure 2.9 Bifurcation diagram showing the region of high pH oscillatory state (OSC), bistability between the high pH oscillatory state and the low pH steady state (BS1) and the low pH steady state (SS1). $[CH_2(OH)_2]_0 = 0.089$ M, $[HSO_3^-] = 0.066$ M and $[SO_3^{2-}]_0 = 5.7 \times 10^{-4}$ M, b/c = 115. Inset shows pH and redox potential time traces at $k_0 = 0.0025$ s^{-1}.

Although the oscillatory amplitude is small in this system, ranging from 0.1 to 1 pH unit, it is distinguishable from the typical levels of noise in experimental time series. The time series in Figure 2.10 of (a) sulfite only solution and (b) a low pH steady state have noise levels of only 0.01 pH units. Time series for genuine oscillatory responses at different flow rates for comparison are shown in Figures 2.10 (c) and (d).

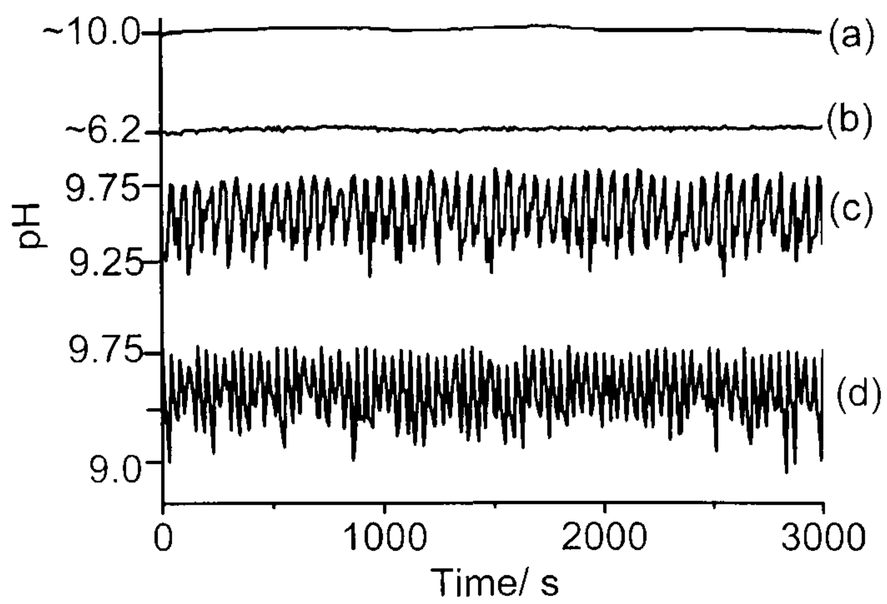

Figure 2.10 pH time traces at different flow rates. (a) $[SO_3^{2-}]_0$ =0.052 M, k_0 = 0.016 s^{-1} (no reaction) (b) $[CH_2(OH)_2]_0$ = 0.1 M, $[HSO_3^-]_0$ = 0.066 M, $[SO_3^{2-}]$ = 5 × 10^{-4} M, k_0 = 0.012 s^{-1} (c) k_0 = 0.0016 s^{-1} (d) k_0 = 0.0025 s^{-1} (same conditions as (b)).

The behaviour is observed over a range of operating conditions and temperatures (10 - 30°C). The different responses exhibited in this system are summarised in the $[CH_2(OH)_2]_0$ - k_0 and the b/c – k_0 phase diagrams in Figures 2.11 and 2.12 respectively. These diagrams indicate the regions of SS1 (flow branch), SS2 (thermodynamic branch), BS1 (bistability between oscillatory and flow branch states) and OSC (regions of oscillations).

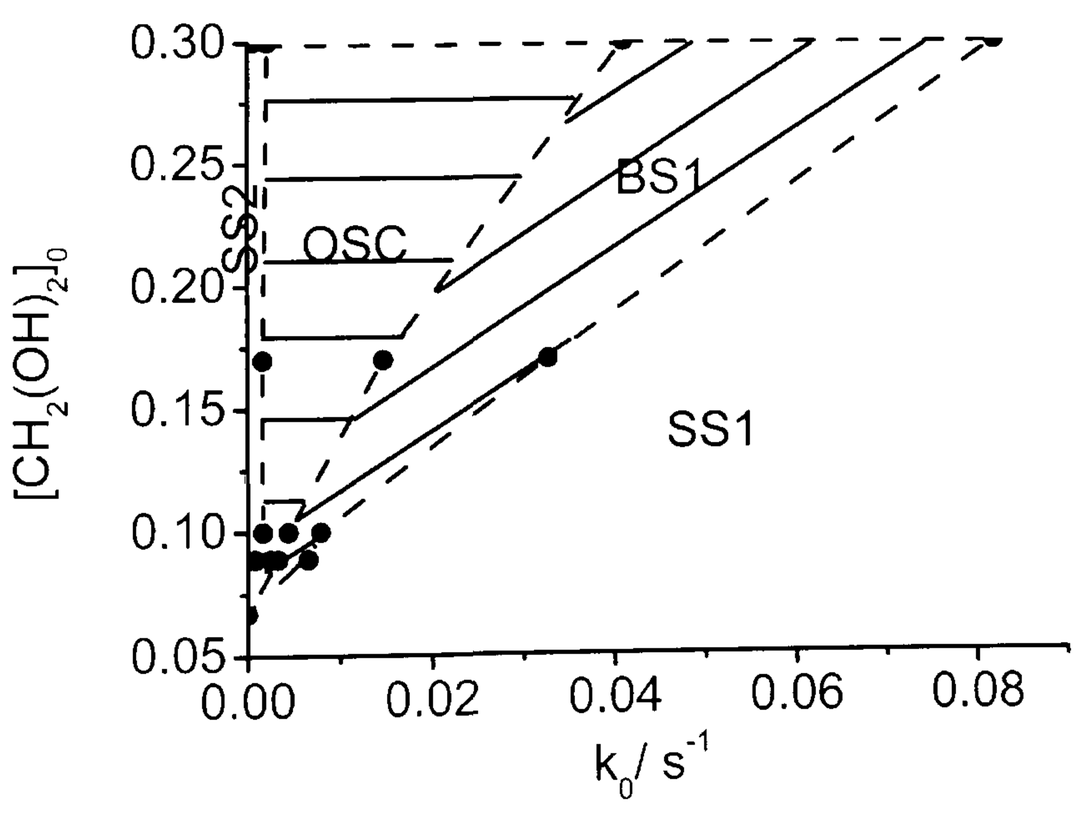

Figure 2.11 $[CH_2(OH)_2]_0$ – k_0 phase diagram showing the regions of high pH steady state (SS2), low pH steady state (SS1), high pH oscillatory state (OSC), bistability between the low pH steady state and the high pH oscillatory state (BS1). $[HSO_3^-]_0$ = 0.066 M, $[SO_3^{2-}]_0$ = 5 × 10^{-4} M (b/c = 116)

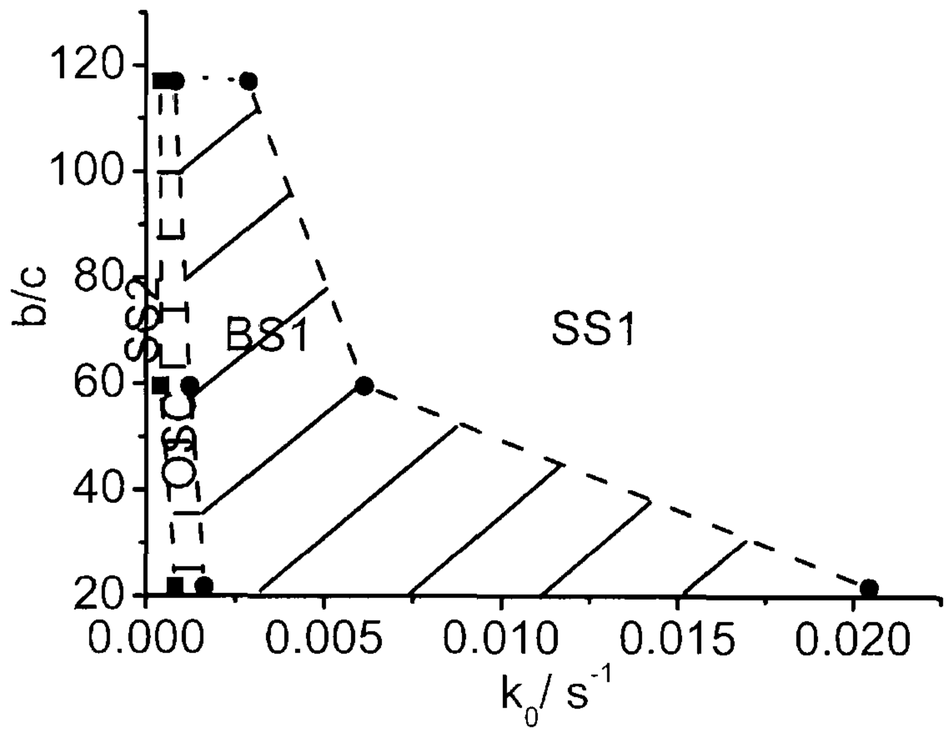

Figure 2.12 b/c – k_0 phase diagram showing the regions of high pH steady state (SS2), low pH steady state (SS1), high pH oscillatory state (OSC), bistability between the low pH steady state and the high pH oscillatory state (BS1). $[HSO_3^-]_0 = 0.066$ M, $[CH_2(OH)_2]_0 = 5 \times 10^{-4}$ M.

It is useful to compare Figure 2.12 with Figure 2.9 and follow the bifurcation structure across the phase plane. At low flow rates there is a region of SS2, at a pH of ~ 7.5. This corresponds to the thermodynamic branch of the reaction. The system bifurcates to an oscillatory response at high pH (OSC) then enters a region of bistability between high pH oscillations and low pH steady state. The system then falls onto the low pH stable steady state flow branch at higher flow rates.

2.5 Conclusions

This chapter has presented an in-depth study of the methylene-glycol sulfite reaction to facilitate a discussion on the effects of the initial conditions on the observed behaviour. The well known clock behaviour has been characterized over a range of initial conditions, including initial sulfite concentration – a result which is previously unreported. The relationship between initial conditions and clock time is now established. The system can also display bistability and oscillations in an open

reactor for a particular range of initial conditions. The region of phase space where this is the case has been characterised (20).

2.6 References

(1) C Wagner: Berichte 62 (1929) 2873.

(2) P Jones, K Oldham: The theory of the formaldehyde clock reaction. Journal of Chemical Education 40 (1963) 366.

(3) A Skrabal, R Skrabal: Dynamics of the formaldehyde-bisulfite reaction. A study of the principle of microscopic reversibility. Monatshefte fuer Chemie 69 (1936) 11-41.

(4) P Sorensen, V Andersen: The formaldehyde hydorgen sulphite system in alkaline aqeous solution. Kinetics, Mechanism and Equilibria. Acta Chemica Scandinavica 24 (1970) 1301- 06.

(5) RP Bell, FRS Evans, PG Evans: Kinetics of the dehydration of methylene glycol in aqueous solution. Proceedings of the Royal Society (1966) 297.

(6) SD Boyce, MR Hoffmann: Kinetics and Mechanism of the Formation of Hydroxymethanesulfonic Acid at Low Ph. Journal of Physical Chemistry 88 (1984) 4740-46.

(7) MG Burnett: The Mechanism of the Formaldehyde Clock Reaction - Methylene Glycol Dehydration. Journal of Chemical Education 59 (1982) 160-62.

(8) P Warneck: The Formaldehyde-Sulfite Clock Reaction Revisited. Journal of Chemical Education 66 (1989) 334-35.

(9) J Winkleman, M Ottens, A Beenackers: The Kinetics of the Dehydration of Methylene Glycol. Chemical Engineering Science 55 (2000) 2065.

(10) E Hayon, A Trenin, J Wilf: Electronic spectra, photochemistry and autoxidation mechanism of the sulfite-bisulfite-pyrosulfate systems. Journal of the American Chemical Society 94 (1972) 47.

(11) JJ Fortman, JA Schreier, T Tuttle: Some Modified 2-Color Formaldehyde Clock Salutes for Schools with Colors of Gold and Green or Gold and Red. Journal of Chemical Education 68 (1991) 324-24.

(12) T Cassen: Faster than a speeding bullet. Journal of Chemical Education 53 (1976) 197.

(13) T Olson, M Hoffmann: Atmospheric Environment 23 (1967- 1989) 985- 97.

(14) W Pasiuk- Bronikowska, T Bronikowski: Journal of Physical Chemistry 107 (2003) 1742- 48.

(15) X Rao, J Collett: Behaviour of S(IV) and Formaldehyde in a chemically heterogeneous cloud. Environmental science and technology 29 (1995) 1023-31.

(16) JGM Winkelman, OK Voorwinde, M Ottens, A Beenackers, L Janssen: Kinetics and chemical equilibrium of the hydration of formaldehyde. Chemical Engineering Science 57 (2002) 4067-76.

(17) SK Scott: Chemical Chaos, Oxford, 1994.

(18) TM Gorrie, SK Raman: Helv. Chim. Acta., 56 (1973) 175.

(19) J Walker: Formaldehyde, New York, 1994.

(20) K Kovacs, R McIlwaine, K Gannon, A Taylor, S Scott: Complex Behaviour in the formaldehyde sulfite reaction. Journal of Physical Chemistry 109 (2005) 283- 88.

CHAPTER 3

Numerical modelling of the Methylene Glycol-Sulfite (MGS) Reaction

3.1 Introduction

The development of a realistic chemical mechanism for an acceleratory reaction presents an exciting challenge to the kineticist. The ability to predict and explain behaviour in terms of a set of chemical reactions allows us to understand the origin of many complex phenomena. This understanding may aid in the design of new chemical oscillators. Fundamental questions such as the nature of the intermediates and the selection of reasonable values for unmeasured rate constants must be addressed. After a tentative mechanism is formulated, its dynamics over relevant phase space must be analysed so that comparisons can be made between the model`s predictions and experimental data. In particular it is important to locate regions of parameter space where certain types of behaviour are seen. Many systems have been adequately characterized by mechanisms (1) which are capable of displaying the same behaviour in numerical simulation as that seen in experiments.

This chapter presents an investigation of the mechanism for the methylene glycol- sulfite (MGS) system, in batch and open configuration. The mechanism for this system is not fully developed and it seems plausible to suggest it will be interesting due to the fact that the system displays an organic- substrate based chemical clock, which may be indicative of autocatalysis. The pH clock also runs from acid to base (typically pH 6.5 to pH 10) which is inverted compared to all other (base to acid) pH regulated feedback systems. The presently accepted model is discussed, and a new model is developed based on experimental batch behaviour. The addition of a base catalysed dehydration step results in the observation of bistability in simulations under open conditions, within experimental ranges. Stirring

effects are then added to this model to obtain better correlation with experimental results.

3.2 Original model. Model A

A viable mechanism for the methylene glycol- sulfite clock must reproduce the sigmoidal batch process curves which are indicative of autocatalysis. The mechanism must also demonstrate the same trends in terms of the dependence of induction times with initial conditions. The accepted mechanism (2) is able to reproduce the clock behaviour providing the concentration of formaldehyde, which exists mainly in its hydrated form, (see previous chapter) is greater than that of bisulfite + sulfite.

$CH_2(OH_2) \rightleftharpoons CH_2O + H_2O$	$K_{3.1} = 5\times10^{-4} = \frac{5.5\times10^{-3}s^{-1}}{10s^{-1}}$	(3.1)
$HSO_3^- \rightleftharpoons SO_3^{2-} + H^+$	$K_{3.2} = 6.2\times10^{-8} = \frac{3110s^{-1}}{5\times10^{10}M^{-1}s^{-1}}$	(3.2)
$CH_2O + SO_3^{2-} \rightarrow CH_2(O^-)SO_3^-$	$k_{3.3} = 5.4\times10^{6}M^{-1}s^{-1}$	(3.3)
$CH_2(O^-)SO_3^- + H^+ \rightleftharpoons CH_2(OH)SO_3^-$	$K_{3.4} = 5\times10^{11} = \frac{1\times10^{9}M^{-1}s^{-1}}{2\times10^{-3}s^{-1}}$	(3.4)
$H_2O \rightleftharpoons H^+ + OH^-$	$K_{3.5} = 1\times10^{-14} = \frac{1\times10^{-3}M^{-1}s^{-1}}{1\times10^{11}M^{-1}s^{-1}}$	(3.5)

Table 3.1 Model for the formaldehyde sulfite clock reaction (2).

The corresponding ordinary differential rate equations for model A, through mass balance, are then:

$$\frac{d[CH_2(OH)_2]}{dt} = -k_{3.1}[CH_2(OH)_2] + k_{3.1r}[CH_2O]$$

$$\frac{d[CH_2O]}{dt} = k_{3.1}[CH_2(OH)_2] - k_{3.1r}[CH_2O] - k_{3.3}[CH_2O][SO_3^{2-}]$$

$$\frac{d[HSO_3^-]}{dt} = -k_{3.2}[HSO_3^-] + k_{3.2r}[H][SO_3^{2-}]$$

$$\frac{d[SO_3^{2-}]}{dt} = k_{3.2}[HSO_3^-] - k_{3.2r}[H^+][SO_3^{2-}] - k_{3.3}[CH_2O][SO_3^{2-}]$$

$$\frac{d[H^+]}{dt} = k_{3.2}[HSO_3^-] - k_{3.2r}[H^+][SO_3^{2-}] - k_{3.4}[CH_2(O^-)SO_3^-][H^+] + k_{3.4r}[CH_2(OH)SO_3^-]$$
$$+ k_{3.5} - k_{3.5r}[OH^-][H^+]$$

$$\frac{d[CH_2(O^-)SO_3^-]}{dt} = k_{3.3}[CH_2O][SO_3^{2-}] - k_{3.3r}[CH_2(O^-)SO_3^-] - k_{3.4}[CH_2(O^-)SO_3^-][H^+]$$
$$+ k_{3.4r}[CH_2(OH)SO_3^-]$$

$$\frac{d[CH_2(OH)SO_3^-]}{dt} = k_{3.4}[CH_2(O^-)SO_3^-][H^+] - k_{3.4r}[CH_2(OH)SO_3^-]$$

$$\frac{d[OH^-]}{dt} = k_{3.5} - k_{3.5r}[OH^-][H^+]$$

3.2.1 Results. Model A

Numerical integration of the 8 resulting differential equations was performed using package XPPAUT (see appendix I). The method of integration was CVODE, with a time step of $dt = 0.01$ and the tolerance set at $tol = 1 \times 10^{-8}$. A typical clock is shown in Figure 3.1.

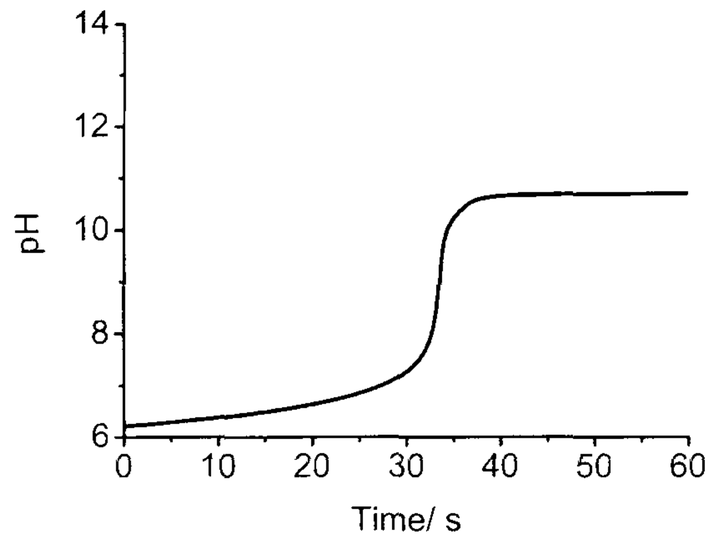

Figure 3.1 pH clock computed on the basis of model A. $[CH_2(OH)_2]_0 = 0.6$, $[HSO_3^-]_0 = 0.1$ M, b/c = 10.

The experiments are compared to the simulated clock times in Figure 3.2 (a) and (b). Model A displays no variation in induction time on variation of $[SO_3^{2-}]_0$.

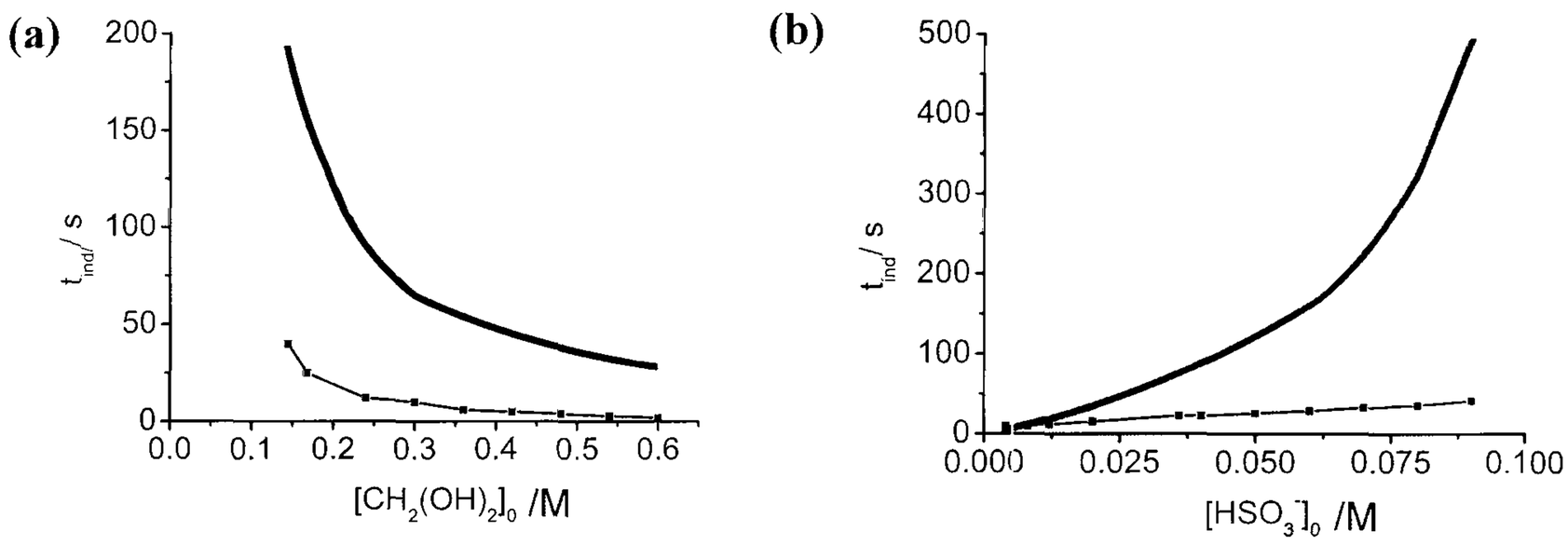

Figure 3.2 Experimental (line with points) and numerical (thick solid line) variation of induction time with (a) $[CH_2(OH)_2]_0$ where $[HSO_3^-]_0 = 0.1$M, b/c = 10; and (b) $[HSO_3^-]_0$ where $[CH_2(OH)_2]_0 = 0.096$ M, b/c =10. Numerical results computed from model A.

3.2.2 Discussion. Model A

Although model A can reproduce the form of the batch pH time trace and the qualitative trend in induction time with initial methylene glycol and total S(IV) concentration, the quantitative agreement between experiment and simulation is poor. Model A grossly overestimates the induction time. Model A also fails to show the dependence of induction time on initial sulfite concentration seen in experiments.

Increasing the rate constant for reaction 3.3 does not result in the desired decrease in simulated induction time.

(i) Effect of $k_{3.1}$ on the clock time

The induction time of the simulated clock is determined by the rate constant of reaction 3.1 as this reaction is rate determining. The rates of reaction 3.2 and 3.5 are well established. There has been much research into the rate of reaction 3.1 by a number of different groups, and a range of values for the dehydration of methylene glycol have been obtained. In 1972 Sutton and Downes (3) used a flow measurement system to monitor formaldehyde production and subsequent reaction in the radiolysis of methanol, calculating a value of $k_{3.1} = 4.4 \times 10^{-3}$ s^{-1}. Chemical scavengers were employed by Le Henaff (4) and then Bell (5) to obtain the following values of $k_{3.1} = 4.5 \times 10^{-3}$ s^{-1} and 5.1×10^{-3} s^{-1} at 293K and 298K respectively. Los and Wetsema (6) used pulse polarography to find $k_{3.1} = 5.7 \times 10^{-3}$ s^{-1} at 298K. Despite the amount of research into this reaction there is no firm agreement on the value which is most likely for the rate coefficient. Varying $k_{3.1}$ has the shown effect on the induction time (Figure 3.3)

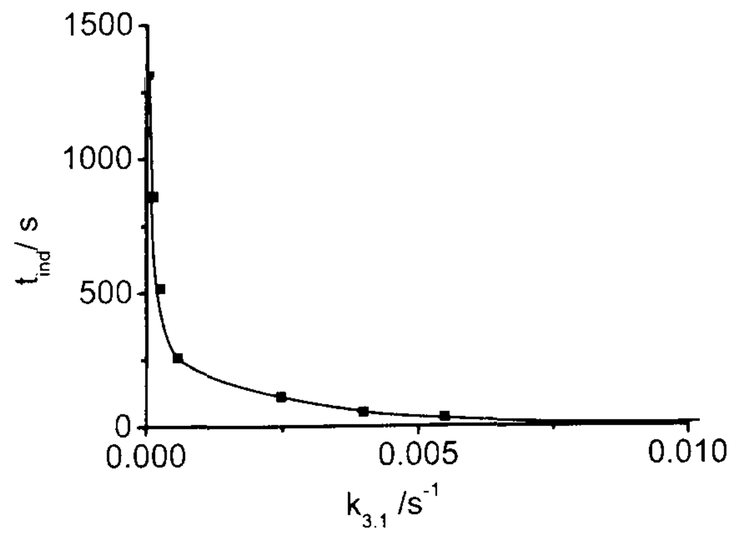

Figure 3.3 Effect of changing $k_{3.1}$ on the induction time. $[CH_2(OH)_2]_0 = 0.6$, $[HSO_3^-]_0 = 0.1$ M, b/c = 10.

Increasing the rate of dehydration of methylene glycol by a factor of 10 gives a much improved induction time in terms of matching simulations to experiments. However,

this is not realistic as the rate constant for reaction 3.1 is limited to an order of 10^{-3} s^{-1} in the literature.

(ii) The effect of $k_{3.4}$/ $k_{3.4r}$ on Δ pH of reaction

The change in pH of the simulated clock is determined by the ratio $k_{3.4}$/ $k_{3.4r}$ Figure 3.4 shows pH time traces calculated with different values for $k_{3.4}$ and $k_{3.4r}$. Increasing $K_{3.4}$ increases the overall pH change. Decreasing $K_{3.4}$ decreases the overall pH change. Maintaining $K_{3.4}$ at 5×10^{11} M^{-1} does not change the overall pH change although a substantial decrease in $k_{3.4}$ (with the corresponding decrease in $k_{3.4r}$) means the system takes a longer to attain the final pH of 10.6 (approximately 2000s for $k_{3.4} = 1 \times 10^{6}$ M^{-1} s^{-1}, $k_{3.4r} = 2 \times 10^{-6}$ s^{-1}).

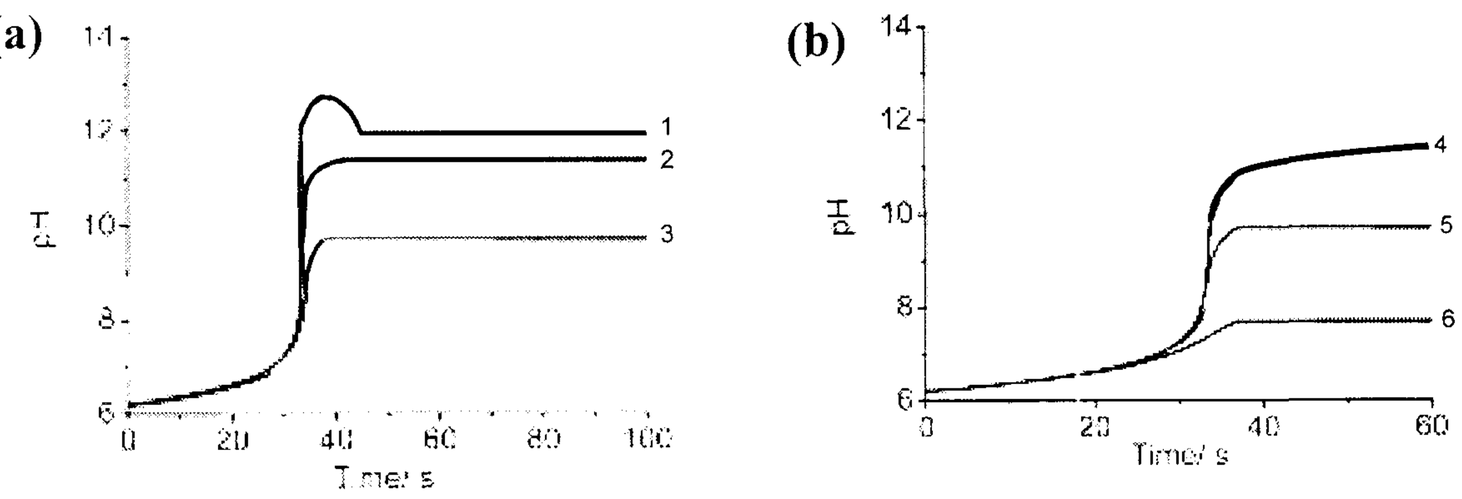

Figure 3.4 Effect of changing (a) $k_{3.4}$,(b) $k_{3.4r}$ on the clock, computed on basis of model A. (a) $k_{3.4} = 1 \times 10^{12}$ M^{-1} s^{-1} (1), 1×10^{10} M^{-1} s^{-1} (2), 1×10^{8} M^{-1} s^{-1} (3), ($k_{3.4r}$ fixed at 0.002 s^{-1}) (b) $k_{3.4r} = 2 \times 10^{-5}$ s^{-1} (4), 0.2 s^{-1} (5), 20 s^{-1} (6), $k_{3.4}$ fixed at 1×10^{9} M^{-1} s^{-1} . $[CH_2(OH)_2]_0 = 0.6$ M , $[HSO_3^-]_0 = 0.1$ M, b/c = 10.

A more in depth investigation of the effect of $k_{3.4}$ and $k_{3.4r}$ is presented later in this chapter. The value of this rate constant effects the overall pH change and becomes important when modelling the system in an open reactor.

(iii) Conclusion- model A

Reasonable adjustments to the rate constants of model A does not improve the fit between numerically calculated behaviour and that seen in experiments. We can conclude that model A is missing chemical steps that contribute to the removal of sulfite, which would result in shortening the induction time.

3.3 Model B

The following additional steps are proposed.

$CH_2O + HSO_3^- \rightarrow CH_2(OH)SO_3^-$	$k_{3.6} = 4.5\times10^2\ M^{-1}s^{-1}$	(3.6) (7)
$CH_2(OH)_2 + SO_3^{2-} \rightarrow CH_2(O^-)SO_3^- + H_2O$	$k_{3.7} = 2.0\ M^{-1}s^{-1}$	(3.7)
$CH_2(OH)_2 + HSO_3^- \rightarrow CH_2(OH)SO_3^- + H_2O$	$k_{3.8} = 0.48\ M^{-1}s^{-1}$	(3.8)
$2\,HCHO + OH^- \rightarrow HCH_2OH + HCOO^-$	$k_{3.9} = 0.5\ M^{-1}s^{-1}$	(3.9)
$HCOOH \rightleftharpoons HCOO^- + H^+$	$K_{3.10} = \dfrac{1780\ s^{-1}}{1\times10^7\ M^{-1}s^{-1}}$	(3.10)

Table 3.2 Additional steps for model A.

The rate constants of reactions (3.7) (8) and (3.8) (8) are small compared to those for reactions (3.3) and (3.4) but these steps can become important as $[SO_3^{2-}]_0$ decreases. The inclusion of the reaction of bisulfite with free formaldehyde is important at low pH (9). The Cannizzaro reaction (reactions 3.9 and 3.10) (10) is added to provide a slight decrease in pH seen at long times in the batch experiments (see Figure 2.3(b)).

3.3.1 Results- Model B

The computed variations of the induction period with initial species concentrations are compared with the experimental results in Figure 3.5.

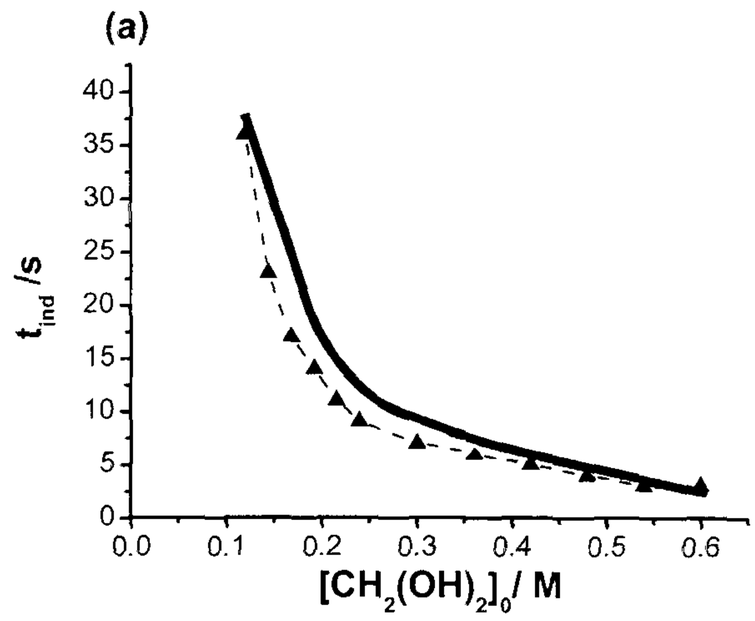

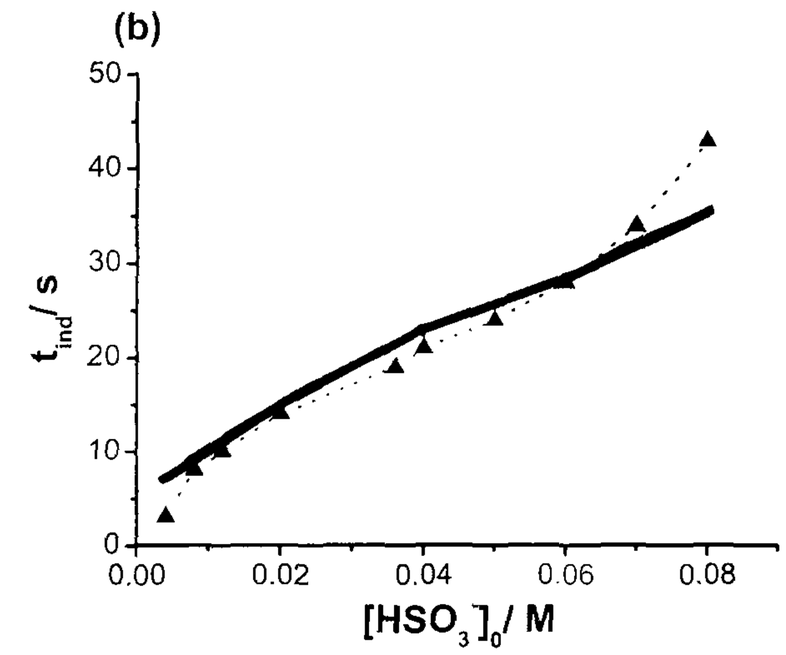

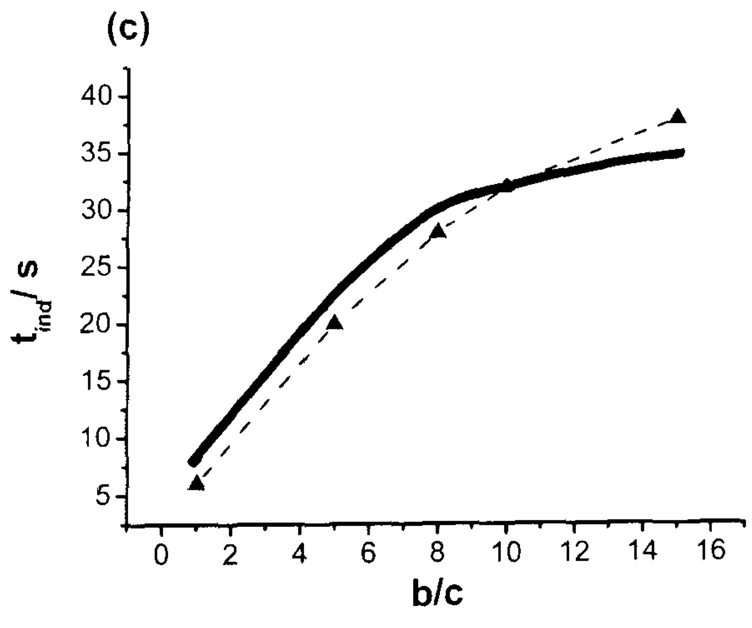

Figure 3.5 Experimental and numerical variation of induction time with (a) $[CH_2(OH)_2]_0$ where $[HSO_3^-]_0$ = 0.1 M, b/c = 10; (b) $[HSO_3^-]_0$ where $[CH_2(OH)_2]_0$ =0.096 M, b/c = 10; and (c) $[SO_3^{2-}]_0$ where HSO_3^- = 0.063 M and $[CH_2(OH)_2]_0$ = 0.096 M.

Figure 3.6 shows the slight decrease in pH observed in batch at long reaction times. This is provided by the addition of the Cannizzaro reaction to model A.

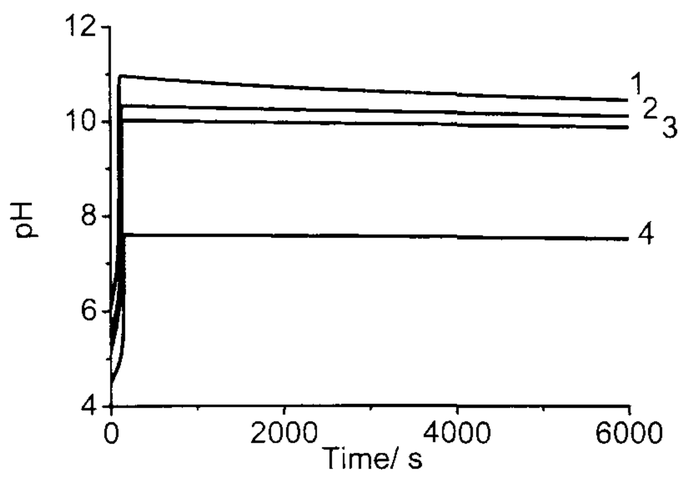

Figure 3.6 Numerical pH time traces showing a gradual decrease in pH at long times, with different initial sulfite concentrations. $[CH_2(OH)_2]_0$ = 0.025 M, $[HSO_3^-]_0$ = 0.0166 M and b/c = 13 (1), 57 (2), 117 (3), and $[SO_3^{2-}]_0$ = 0 M (4).

Model B provides satisfactory agreement in batch configuration between experimental and numerical results. The rate equations derived from model B were therefore augmented by flow terms $k_0[X_0] - k_0[X]$ (where k_0 is the flow rate in s^{-1}, and $[X_0]$ is the inflow concentration of species X) to investigate the model in an open configuration. The inflow species are $CH_2(OH)_2$, CH_2O, HSO_3^-, SO_3^{2-}, OH^- and H^+. The following forms of bistability diagrams were obtained.

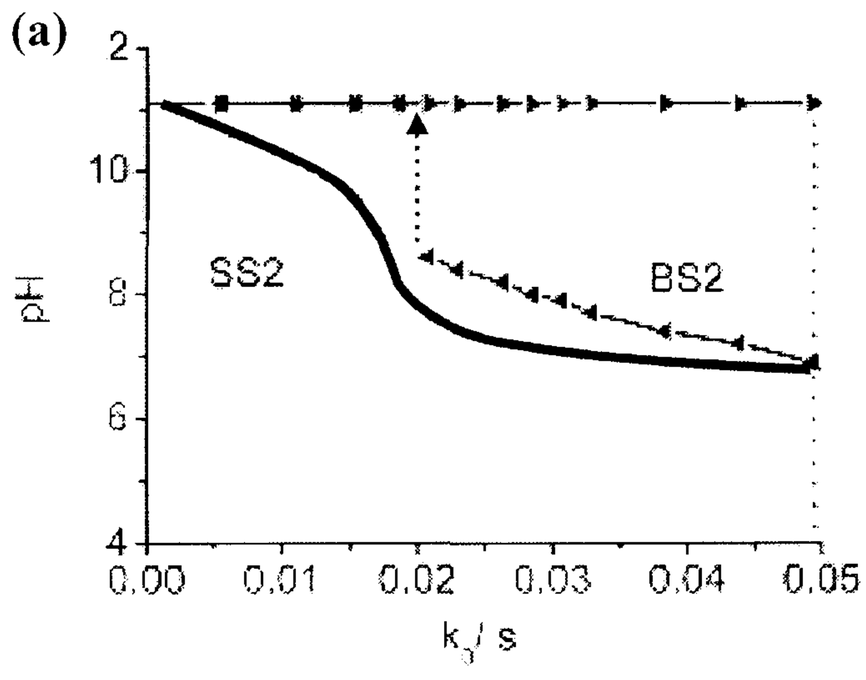

Figure 3.7 Examples of bifurcation diagram calculated from model B (thick line) Experimental curve also shown for comparison. (a) $[CH_2(OH)_2]_0$ = 0.17, $[HSO_3^-]_0$ = 0.1 b/c = 10. (b) $[CH_2(OH)_2]_0$ = 0.15, $[HSO_3^-]_0$ = 0.1 b/c = 10.

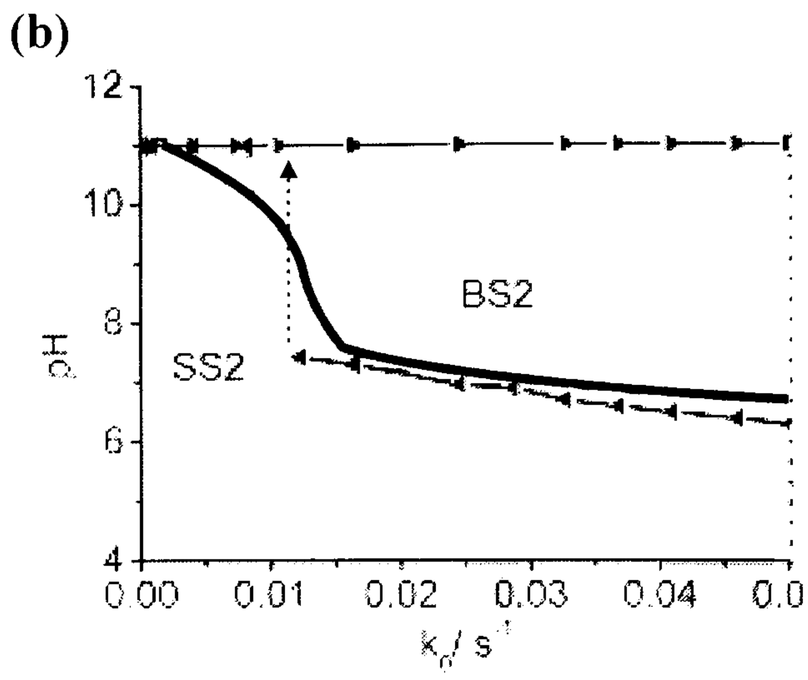

The phase space which was experimentally investigated was fully explored. Numerical simulations with reasonable adjustments to the rate constants, using model B, were unable to display bistability, or oscillations, in any region of this phase space.

3.3.2 Discussion- Model B

Numerical simulations with model B provide good correlation with batch experimental results. The simulations now also show an increase in induction time with a decrease in initial sulfite concentration.

(i) Adjustment of rate constants

The induction time of the numerically simulated clock is sensitive to the rate coefficients of reactions 3.1, 3.7 and 3.8. The rate constants of these reactions were therefore adjusted to best match the experimental data. The effect of k_1 was considered previously. Figure 3.8 and shows the effect of varying $k_{3.7}$ (a) and $k_{3.8}$ (b) on the numerically simulated induction times.

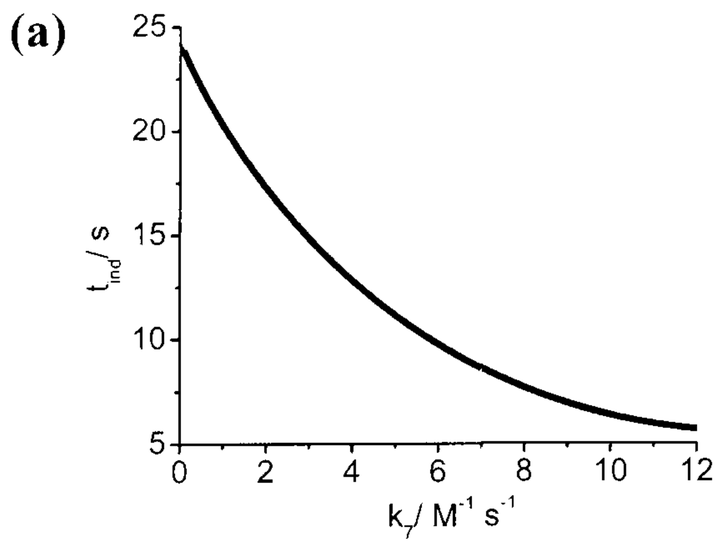

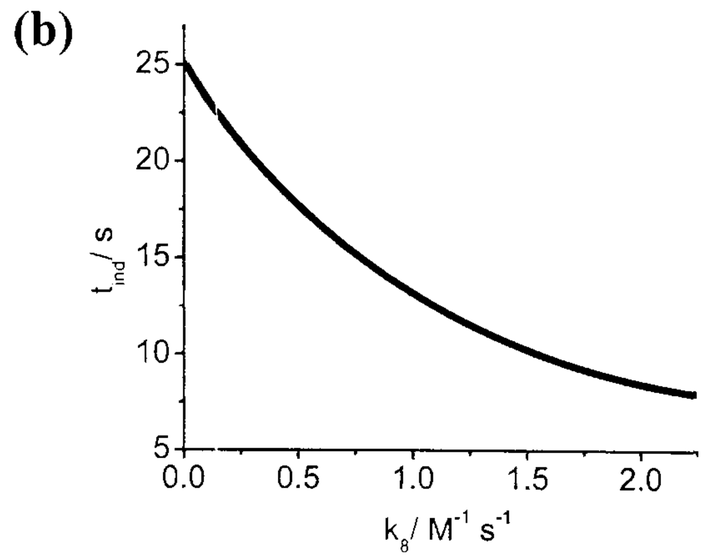

Figure 3.8 Effect of $k_{3.7}$ ($k_{3.8}$ fixed at 0.48 s^{-1}) (a) and $k_{3.8}$ ($k_{3.7}$ fixed at 2.0 s^{-1}) (b) on numerical simulations of induction time with model B. $[CH_2(OH)_2]_0$ = 0.096 M, $[HSO_3^-]_0$ = 0.02 M, b/c = 10.

(ii) The nature of the clock

The clock (batch) reaction is now entirely explained by consideration of the sulfite – bisulfite buffer. The calculated evolution of the concentrations of the main species in a batch reactor is shown in Figure 3.9.

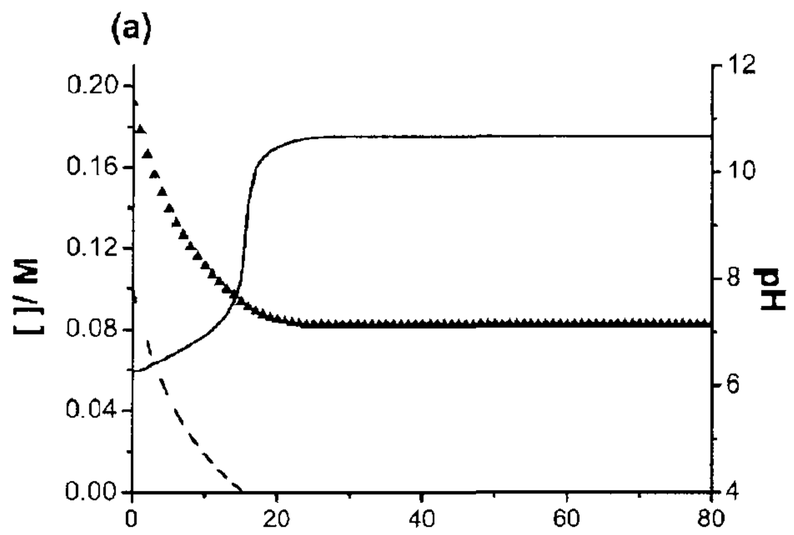

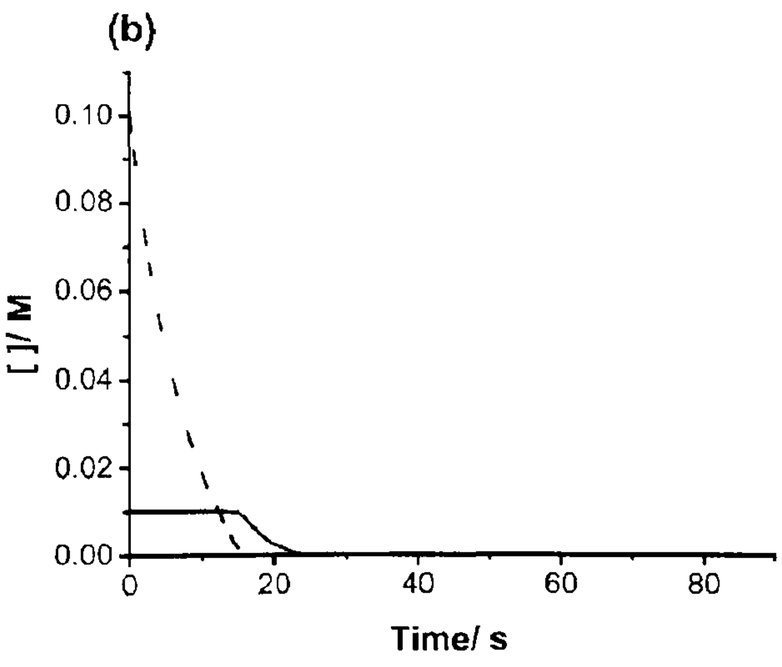

Figure 3.9 Computed variations in time of (a) pH (—). $[CH_2(OH)_2]$ (▲) and $[HSO_3^-]$ (---) and (b) $[HSO_3^-]$ (---) and SO_3^{2-} (—). $[CH_2(OH)_2]_0$ = 0.192 M, $[HSO_3^-]_0$ = 0.1 M, b/c = 10.

During the induction period, the concentrations of $CH_2(OH)_2$ and HSO_3^- decrease and the pH increases, whilst that of SO_3^{2-} remains constant. The buffer pre-equilibrium in step (3.2) is maintained during the induction period (see Figure 3.10) so that $\mathbf{Q}_{3.2} = 6.2 \times 10^{-8}$.

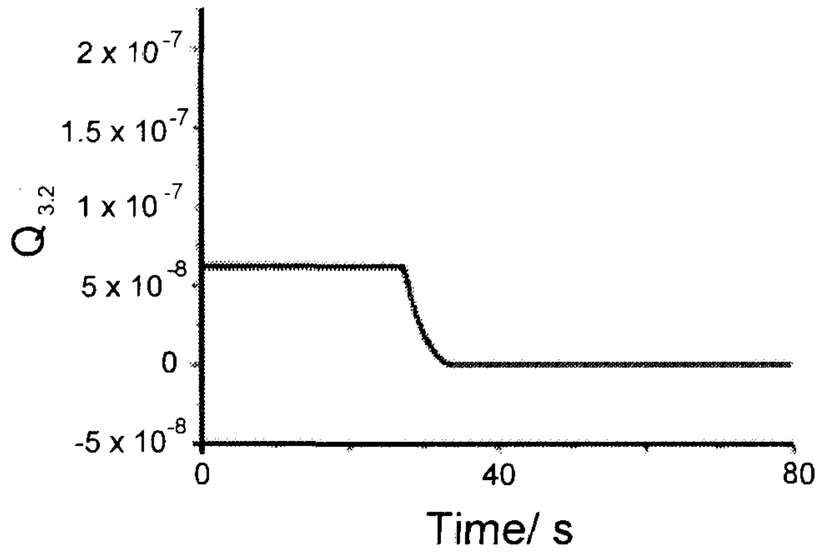

Figure 3.10 Numerical proof from model B that the value of Q (= 6.2×10^{-8}) is kept constant throughout the induction time. $[CH_2(OH)_2]_0 = 0.2$ M, $[HSO_3^-]_0 = 0.1$M, b/c = 10.

The computations indicate that $[HSO_3^-]$ decreases exponentially (pseudo-first order kinetics) and the pH increases linearly in time over the main part of the induction period. Once the bisulfite has been sufficiently consumed, a rapid increase in pH is observed and the sulfite concentration decays. Table 3.3 (11) shows how we expect the pH to change as the ratio of HSO_3^-/ SO_3^{2-} changes for typical starting conditions of 0.1 M to 0.01 M (b/c = 10).

Percentage of reaction completed	$[SO_3^{2-}]$: $[HSO_3^-]$	Calculated pH
0	1: 10	6.2
90	1: 1	7.2
99	1: 0.1	8.2
99.9	1: 0.01	9.2
99.999	1:0.001	10.2

Table 3.3 Table showing how the pH changes throughout the reaction of methylene glycol with a sulfite/ bisulfite buffer, as HSO_3^- reacts.

The rate determining step is the dehydration of methylene glycol, and the pH is determined by the internal bisulfite- sulfite buffer through the following equilibrium:

$$HSO_3^- \leftrightarrow H^+ + SO_3^{2-}$$

The initial pH of the solution depends upon the ratio of bisulfite to sulfite and is calculated through the Henderson Hasselbach equation:

$$pH = pKa + \log\frac{[SO_3^{2-}]}{[HSO_3^-]}$$

Typically the initial pH was 6.2;

$$pH = 7.207 + \log\frac{0.01}{0.1} = 6.2$$

As the reaction proceeds, SO_3^{2-} and H^+ are consumed through reactions 3.3 and 3.4, but are supplied through dissociation of HSO_3^- in reaction 3.2. Thus the pH increases slowly. When HSO_3^- has been completely consumed, reaction 3.2 can no longer supply H^+ to match its consumption through reaction 3.4 and the pH increases rapidly. The acceleration in the change of pH is due to a combination of two factors:

i) A decrease in the buffering effect of the S(IV) couple with decreasing [S(IV)]

ii) An acceleration of the depletion of S(IV) as the reaction proceeds.

The qualitative dependence of induction time on initial concentrations is also well modelled by model B. An increase in $[CH_2(OH)_2]_0$ decreases the induction time (Figure 3.5(a)). An increase in initial methylene glycol concentration will increase the rate of reaction 3.1 and hence the rate of removal of SO_3^{2-}.

An increase in $[HSO_3^-]_0$ increases the induction time. A higher initial concentration of bisulfite means that there is an increase in buffering capacity. The system will take longer to deplete the buffer at high HSO_3^- concentrations, resulting in longer clock times. A decrease in sulfite concentration causes an increase in induction time. The

rates of reaction 3.3 and 3.7 are dependent on $[SO_3^{2-}]$. Low concentrations of this species means the rate of these reactions will be slow. If the rates of these reactions are slow, the system will take longer to deplete the buffer, giving rise to long clock times.

(iii) Autocatalysis and feedback in clock reactions

The rate extent plots of the experimental (Figure 3.11(a)) and numerical (Figure 3.11(b)) clocks calculated through model B display a maximum at some non zero extent, which is indicative of autocatalysis or feedback (12).

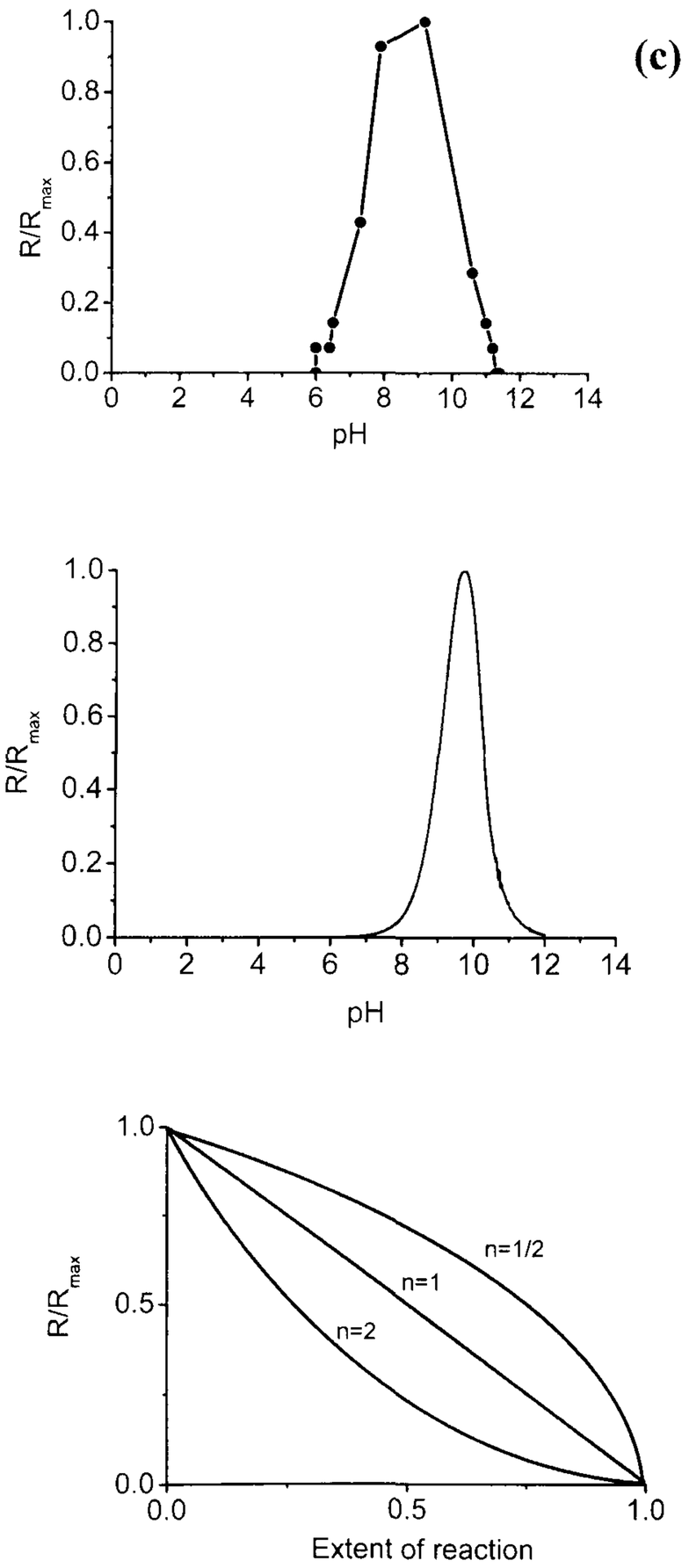

Figure 3.11 (a) Experimental dependence of reaction rate on extent of conversion for the pH clock. The rate is normalized by the maximum reaction rate R_{max}, which occurs at a non zero value of the extent of reaction. (b) Numerical dependence of reaction rate on extent of reaction calculated from model B. The reaction rate is normalized by the maximum reaction rate R_{max} (c) The dependence of reaction rate on extent of reaction for typical non autocatalytic reactions. The maximum rate occurs at the beginning of the reaction.

The rate extent plots illustrated in Figure (3.11 (c)) show rates that decrease monotonically as the extent of reaction increases. These systems have their maximum rate initially and as reactants are consumed, the rate falls. They are deceleratory systems. Acceleratory reactions (typically with feedback) are characterized by rate extent plots which are not only non linear but also display an initial increase in rate with an increase in extent of reaction. The numerical and experimental rate extent plots of the formaldehyde system appear acceleratory. Chemical systems which produce acceleratory rate extent plots are traditionally thought of as possessing feedback in their mechanism, and are therefore may display bistability in open reactors. Indeed, the sharp change in concentration of the clock chemical is expected to be roughly the same magnitude as the difference between the bistable steady state values. Model A contains no feedback and cannot display bistability in numerical simulations under flow conditions. Thus, acceleratory processes can occur in batch buffer based systems containing no feedback. As model B cannot display bistability in flow we can say that 'clocking' does not always guarantee a route to bistability in flow reactors.

Two conventional mechanisms of feedback (and therefore 'clocking') in batch, are discussed by Needham and Billingham (13), (14). The first is known as induction. In this case the rate of production of the clock chemical is small when its concentration is small and increases as the concentration increases, for example, cubic autocatalysis.

$$A + 2B \rightarrow 3B \qquad Rate = kab^2 \qquad (3.11)$$

Clock reactions which are thought to be well modelled by autocatalysis include the iodate-arsenous acid reaction (15) and the iodine-bisulfate clock reaction (16). The other mechanism is inhibition is explained as;

$$P \rightarrow B \qquad Rate = k_0 p \tag{3.12}$$

$$B + C \rightarrow D \qquad Rate = k_1 bc \tag{3.13}$$

Here, the clock chemical, B, is supplied to the system via decay of the precursor chemical P. An inhibitor chemical, C, reacts with the clock chemical limiting its concentration. Once the inhibitor chemical is consumed the concentration of the clock chemical can start to increase. Systems modelled by this type of behaviour are the photosynthesis of hydrogen chloride inhibited by ammonia and the polymerisation of vinyl acetate by benzoquinone (17).

The origin of the nonlinear rate extent plots in the formaldehyde system is the break down of the buffer (see table 4.1) rather than a build up of autocatalyst, or removal of inhibitor. The buffer based model, which contains no conventional autocatalysis, therefore provides a pH clock which is unable to display bistability in flow.

(iv) Conclusion

Addition of reactions 3.6 to 3.8 improves the numerically simulated induction times. The induction time is now shorter and dependent on initial sulfite concentration, in good agreement with experiments. The addition of reaction 3.9 and 3.10 (the Cannizzaro reaction) improves the long term behaviour of the batch pH clock by providing a decrease in pH at long time scales. The behaviour of the closed system is accounted for by the buffer mechanism which contains no feedback. Model B is missing chemical steps which can account for the experimentally observed bistability.

3.4 Model C

The base or acid catalysed dehydration of carbonyls is a general phenomenon (18).

Reaction 3.1 can now be rewritten as:

$$CH_2(OH_2) \underset{OH^-}{\overset{H^+}{\longleftrightarrow}} CH_2O + H_2O \qquad K_{3.14} = 5\times10^{-4} = \frac{5.5\times10^{-3}\,s^{-1}}{10s^{-1}} \tag{3.14}$$

$$k_{3.14OH} = 2100M^{-1}s^{-1}$$

$$k_{3.14H} = 2.84M^{-1}s^{-1}$$

The rate of reaction 3.1, the rate determining step, now becomes:

$$v_1 = k_1[CH_2(OH)_2] + k_{3.14OH}[CH_2(OH)_2][OH^-] + k_{3.14H}[CH_2(OH)_2][H^+]$$

where $k_{3.14OH} = 2100\ M^{-1}\ s^{-1}$ and $k_{3.141H} = 2.84\ M^{-1}\ s^{-1}$.

3.4.1 Results- Model C

Inclusion of the acid catalysis in the rate law makes no difference to the observed behaviour under conditions employed here. The addition of the base catalysed dehydration makes no difference to the induction times and pH changes are unaffected. Figure 3.12 shows the temporal evolution of OH^- (a) and the corresponding rate of reaction (b). The addition of the base catalysis step results in an increase in the rate at the clock time.

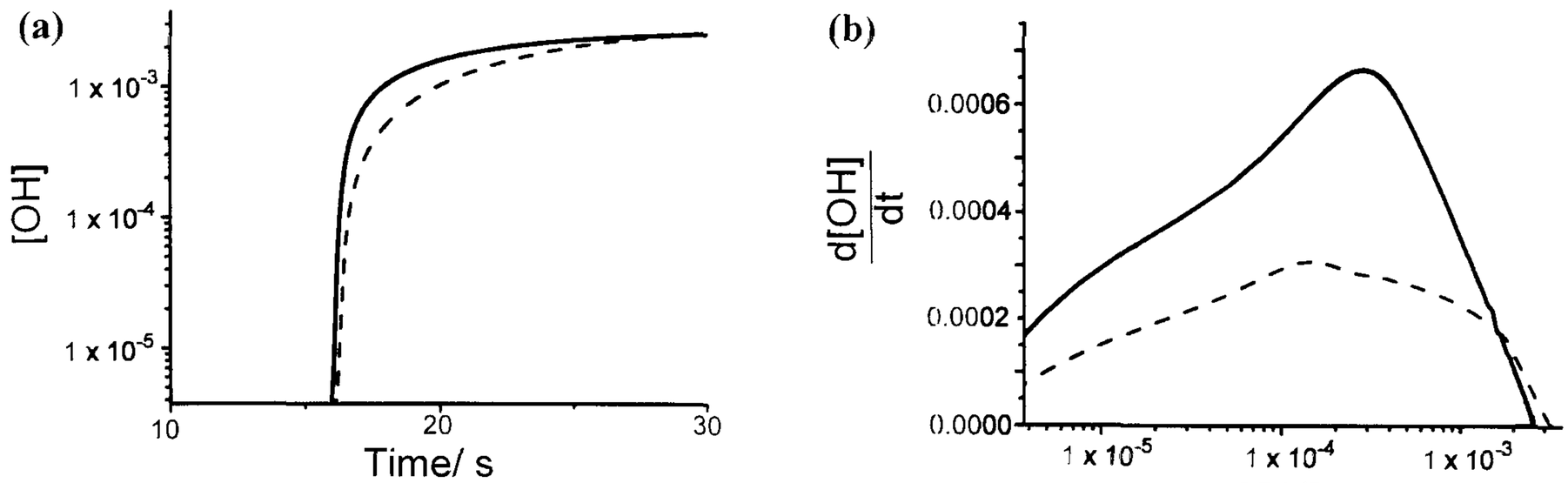

Figure 3.12 (a) Temporal evolution of OH^- in numerical simulations of the clock with model B and model C (dash line and solid line respectively) (b) Rate extent plots for clock reaction simulated with model B and model C (dash line and solid line respectively). $[CH_2(OH)_2]_0$ = 0.2 M, $[HSO_3^-]_0$ = 0.1 M, $[SO_3^{2-}]_0$ = 0.01M in both.

The rate equations derived from model B were augmented by flow terms $k_0[X_0] - k_0[X]$ (where k_0 is the flow rate in s^{-1}, and $[X_0]$ is the inflow concentration of species X) to investigate model C's response in an open configuration. The inflow species are $CH_2(OH)_2$, CH_2O, HSO_3^-, SO_3^{2-}, OH^- and H^+. Numerical integration of the resulting differential equations was again performed using package XPPAUT (see appendix I). Bifurcation diagrams and phase diagrams were calculated with the AUTO interface of XPPAUT. The maximum time step was 1×10^{-4} with tolerances set to 1×10^{-6}. Values of $k_{3.4} = 1 \times 10^{10}$ M^{-1} s^{-1} and $k_{3.4r} = 0.002$ s^{-1} were used in numerical simulations.

(i) Bistability

Model C displays bistability in numerical simulations, for the same concentrations as those used in experiments. Figure 3.13 shows the numerical and experimental regions of bistability.

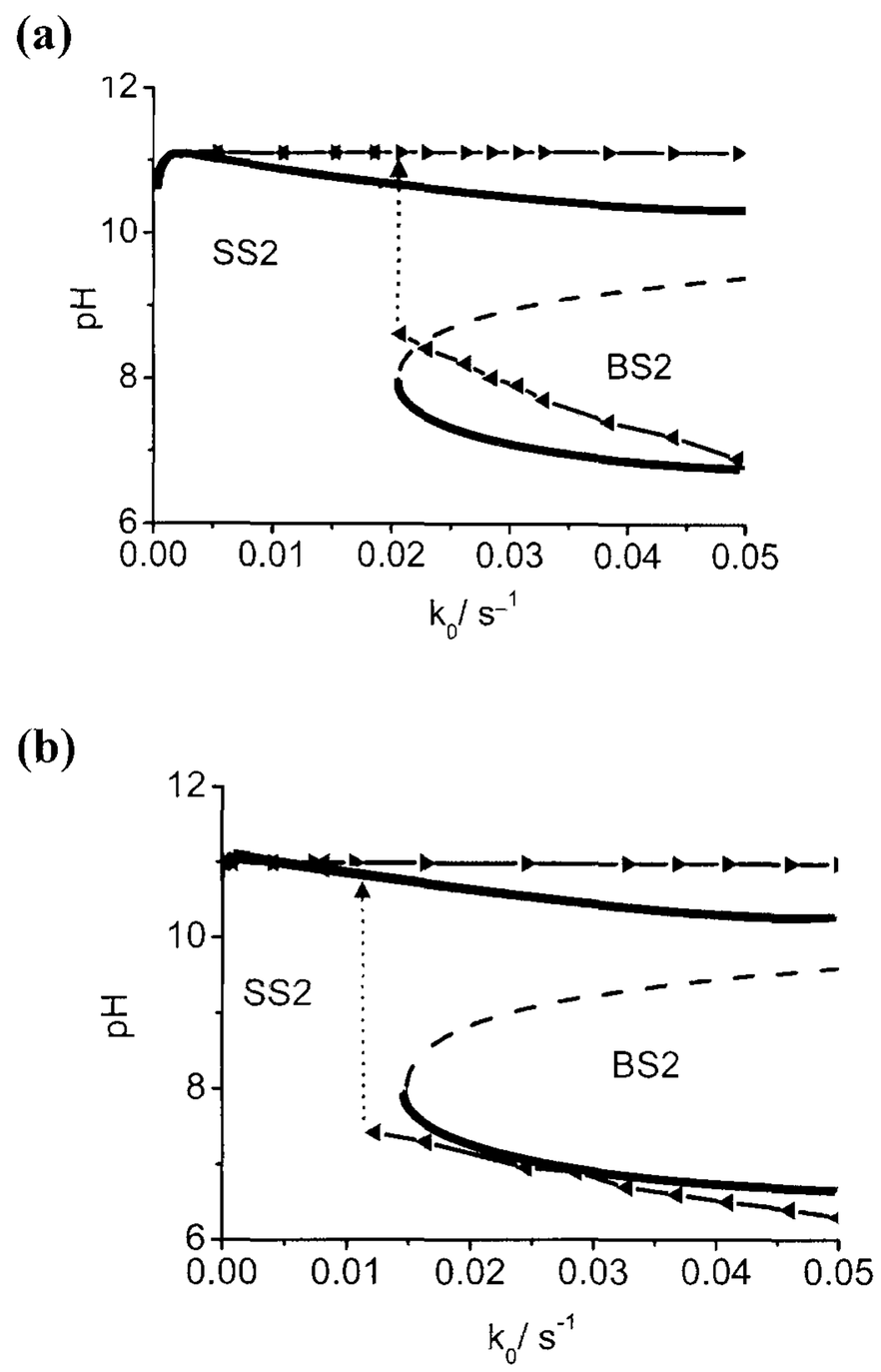

Figure 3.13 Bifurcation diagrams calculated on the basis of model C (thick line is numerical stable steady state, dash line is numerical unstable steady state, thin line is experimental stable steady state) (a) $[CH_2(OH)_2]_0$ = 0.17 M, $[HSO_3^-]_0$ = 0.1 M b/c = 10. (b) as (a) but $[CH_2(OH)_2]_0$ = 0.15 M.

(ii) Bistability and oscillations

A numerically calculated bifurcation diagram is shown in Figure 3.14, with the experimental data for comparison. b/c is equal to 5. While oscillations were observed experimentally for low flow rates, none were found in simulations.

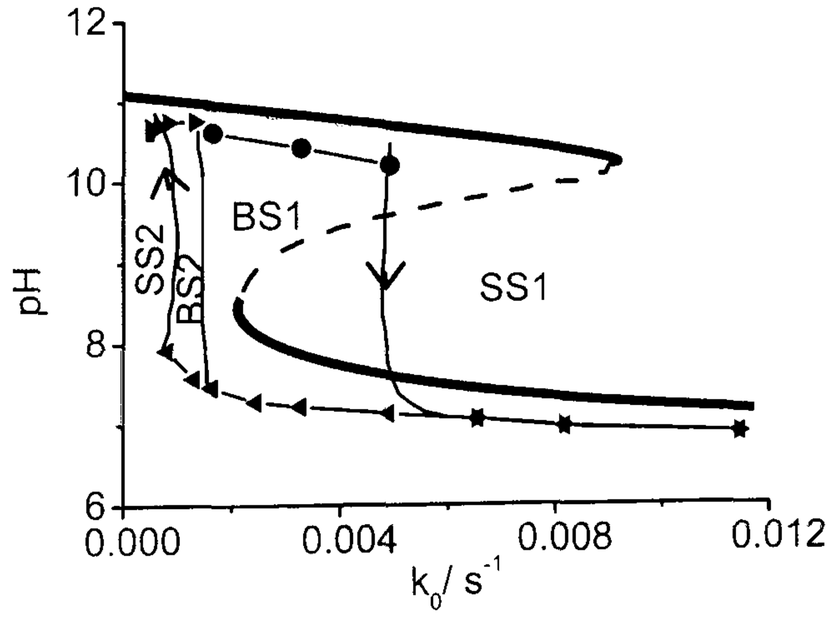

Figure 3.14 $[CH_2(OH)_2]_0$ = 0.069 M, $[HSO_3^-]_0$ = 0.066 M, $[SO_3^{2-}]_0$ = 0.0133 M. b/c = 5. Thick solid line is numerical stable steady state, dashed line is numerical unstable steady state. Thin line is experimental- triangles steady state and circles oscillatory.

Figure 3.15 shows a numerical bifurcation diagram with the corresponding experimental result, for a system with high b/c. Numerical simulations at these conditions again show no oscillations.

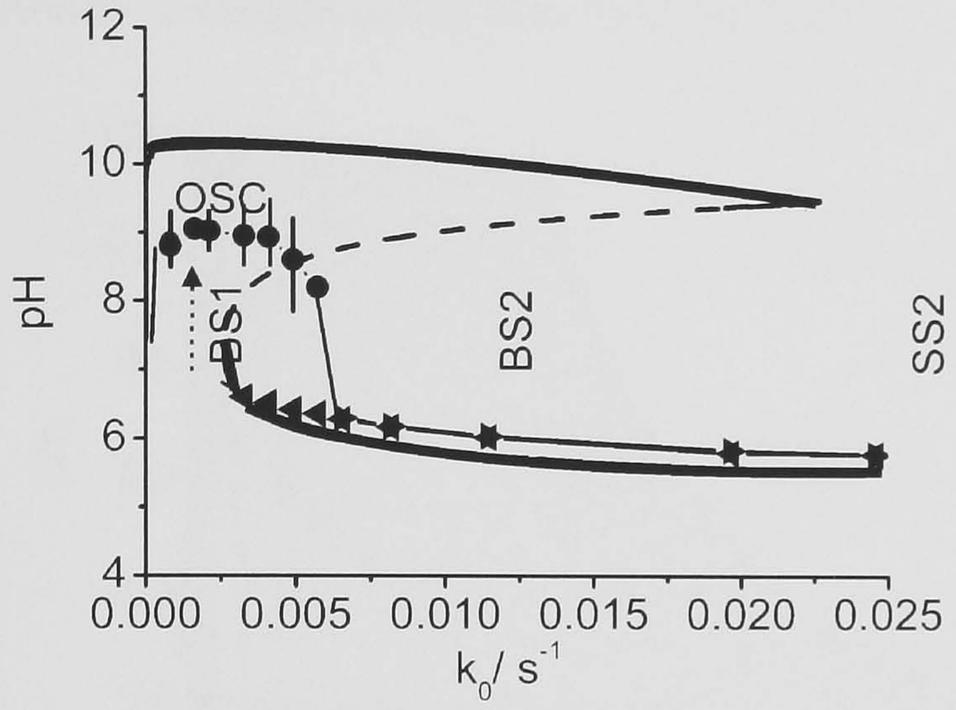

Figure 3.15 Comparison of numerical and experimental $[CH_2(OH)_2]_0$ = 0.089 M, $[HSO_3^-]_0$ = 0.066, $[SO_3^{2-}]$ = 5.7×10^{-4} M. b/c = 115. Thick solid line is numerical stable steady state, dashed line is numerical unstable steady state. Thin line is experimental- triangles steady state and circles oscillatory.

(iii) Phase diagrams

Figure 3.16 shows experimental and numerical methylene glycol- flow rate phase diagrams. Regions of bistability match reasonably well.

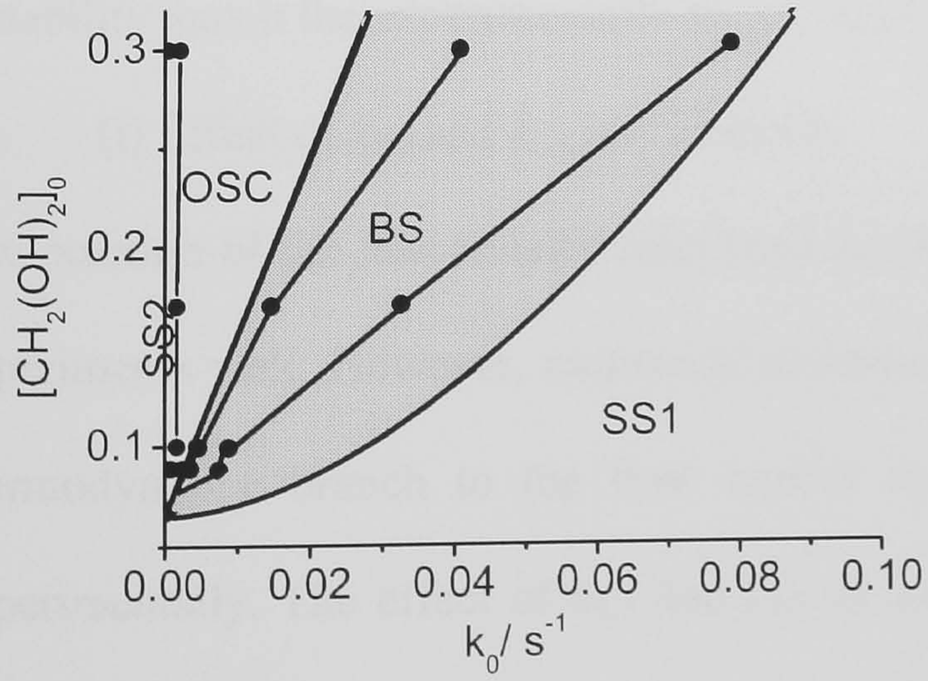

Figure 3.16 Numerical and experimental $[CH_2(OH)_2]_0$ – k_0 phase diagrams. Thick plain line is numerical and thinner line with points is experimental. $[HSO_3^-]_0$ = 0.066 M, $[SO_3^{2-}]_0$ = 5.7×10^{-4} M. b/c = 116. SS1 and SS2 are the flow and thermodynamic steady states respectively.

Figure 3.17 shows the experimental and numerical b/c – flow rate phase diagram. The numerical simulations calculate a much larger area of bistability compared to that found experimentally. The simulations do however show that the region of bistability decreases as the ratio b/c is increased.

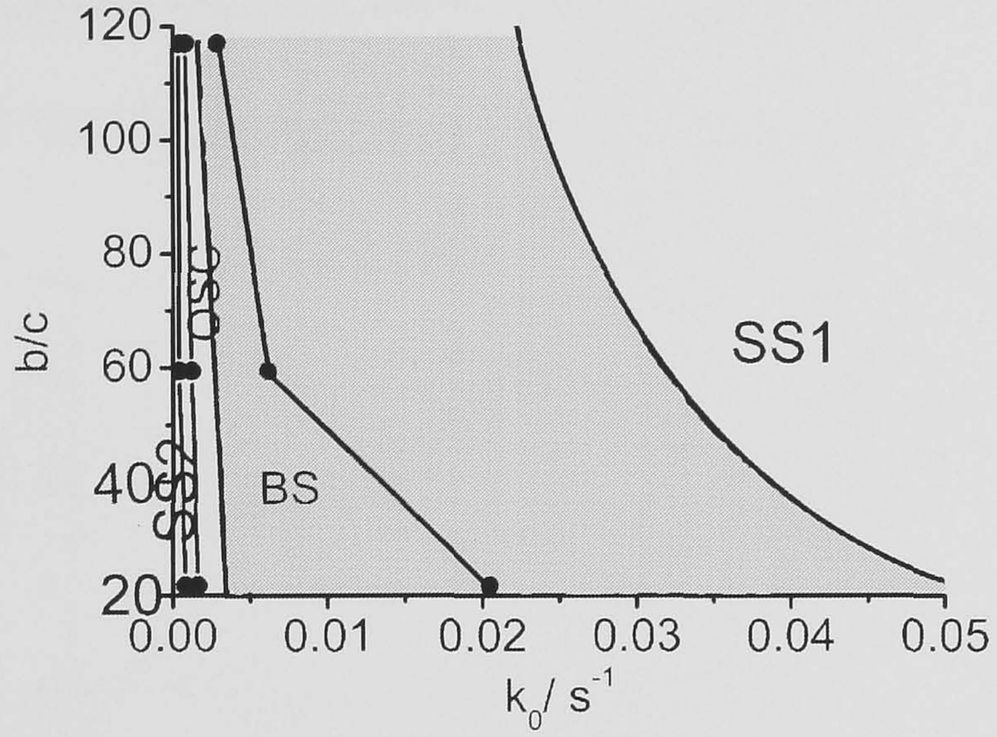

Figure 3.17 $[HSO_3^-]_0$ / $[SO_3^{2-}]_0$ (b/c) – k_0 phase diagram. Thick plain line is numerical and thinner line with points is experimental. $[CH_2(OH)_2]_0$ = 0.089 M, $[HSO_3^-]_0$ = 0.066 M. BS is bistability. OSC is experimental oscillations. SST1 and SST2 are the flow and thermodynamic steady states respectively.

3.4.2 Discussion Model C

Simulations of the MGS reaction with model C provide good agreement with batch results, and display bistability under flow conditions. The calculated regions of bistability match the experimentally found regions reasonably well.

(i) Effect of $k_{3.7}$ and $k_{3.8}$ on bistability

The position of the numerically calculated lower limit point in Figure 3.13 matches experiments well. However, numerical simulations calculate the transition from the thermodynamic branch to the flow branch at lower flow rates than those seen experimentally. The effect of $k_{3.7}$ and $k_{3.8}$ on the calculated regions of bistability is investigated as these rate constants effect the induction time in batch. $k_{3.7}$ and $k_{3.8}$ - k_0 phase diagrams are shown in Figure 3.18 (a) and (b) respectively for the same concentrations as those in Figure 3.13 (a). Varying $k_{3.7}$ does not have any effect on

the form of the bifurcation diagram but an increase in this rate constant moves the low flow rate limit point to higher flow rates ($k_{0,\ low}$ = 0.065 s^{-1} for k_7 = 8 s^{-1}). The position of the higher flow rate limit point does not change for varying k_7. Increasing $k_{3.8}$ again moves the low flow rate limit point to higher flow rates and has no appreciable affect on the position of the higher flow rate limit point. The pH of the flow branch also increases for higher values of k_8.

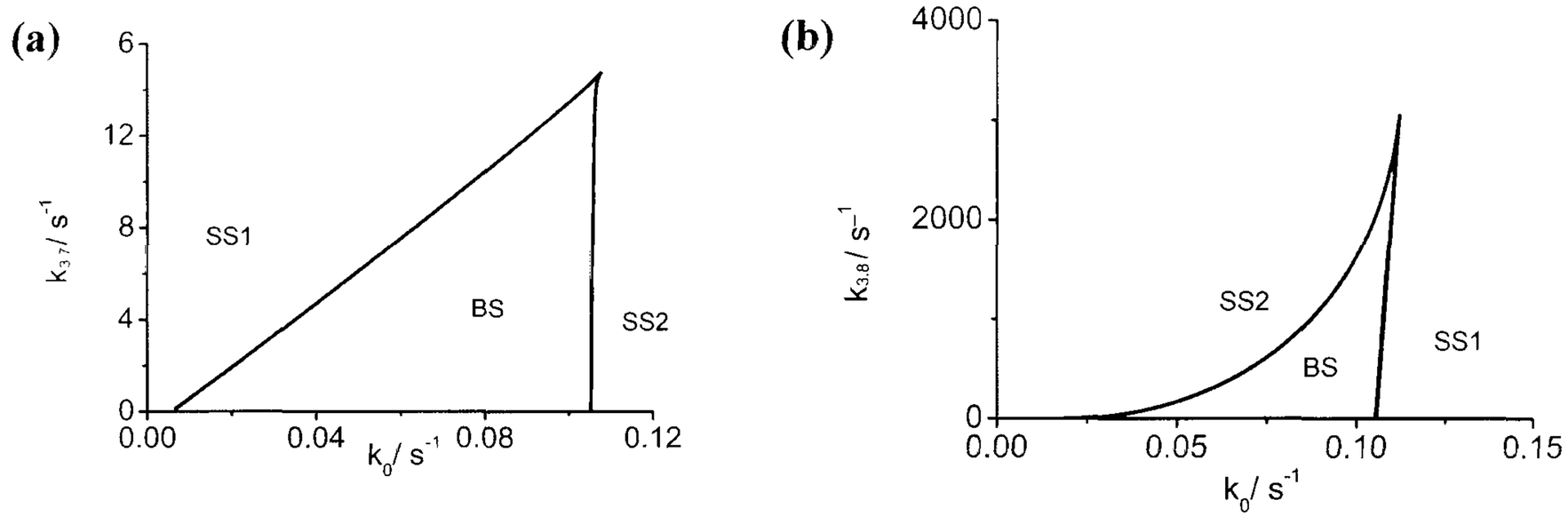

Figure 3.18 (a) k_0 - $k_{3.7}$ phase diagram ($k_{3.8}$ = 0.48 s^{-1}) (b) k_0 - $k_{3.8}$ phase diagram (k_7 = 2 s^{-1}). $[CH_2(OH)_2]_0$ = 0.17 M , $[HSO_3^-]_0$ = 0.1M, b/c = 10. $k_{3.4}$ = 1 × 10^{10} M^{-1} s^{-1} /0.002 s^{-1}.

Realistic alteration of k_7 and k_8 can therefore not provide better correlation between experimental and numerical regions of bistability.

(ii) Effect of $k_{3.4}$/ $k_{3.4r}$ on bistability and phase diagrams

The rate of reaction 3.4 is not well defined (8). The effect of this rate constant on the form of the bifurcation diagram shown in Figure 3.13 (a) is therefore investigated. The results are displayed in Figure 3.19, detailing the form of the thermodynamic branch.

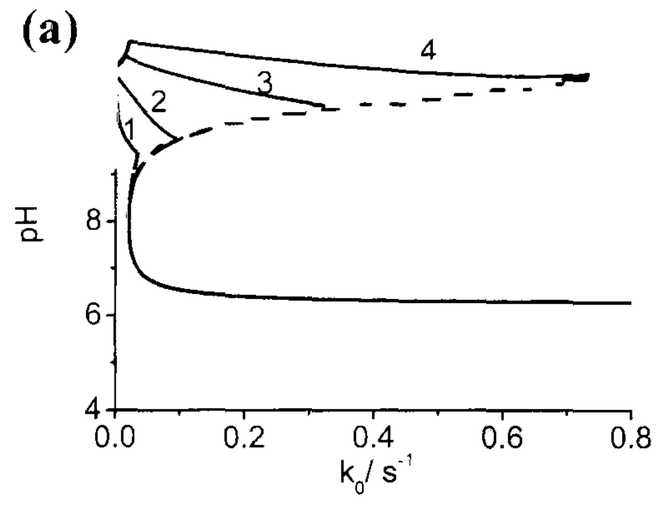

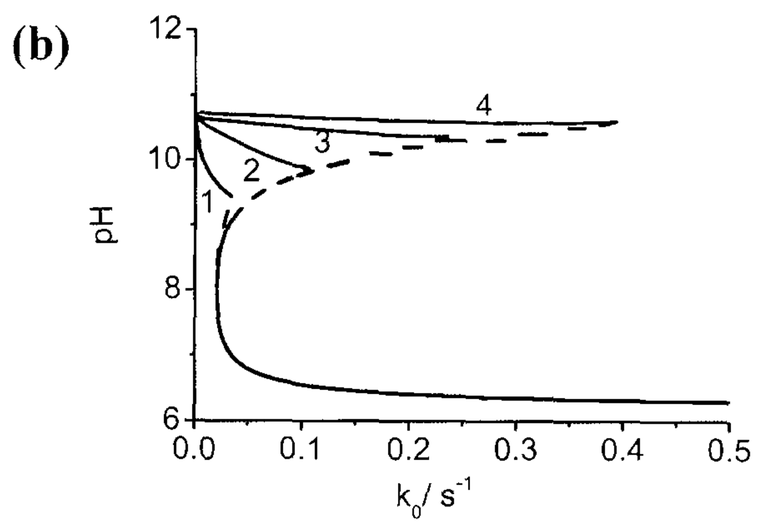

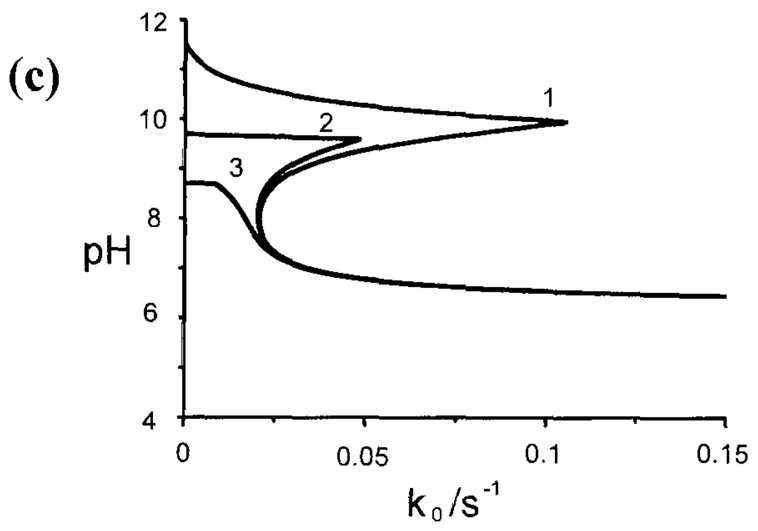

Figure 3.19 Effect of changing (a) $k_{3,4}$ on the form of the bifurcation diagrams computed on the basis of model C in flow. $k_{3,4} = 1 \times 10^9$ M^{-1} s^{-1} (1), 1×10^{10} M^{-1} s^{-1} (2), 1×10^{11} M^{-1} s^{-1} (3) and 1×10^{12} M^{-1} s^{-1} (4). ($k_{3,4r}$ fixed at 0.002 s^{-1}) (b) Effect of keeping $K_{3,4}$ constant at 5×10^{11} M^{-1}. 1×10^9 M^{-1} s^{-1} / 0.002 s^{-1} (1), 1×10^{10} M^{-1} s^{-1} / 0.02 s^{-1} (2), 1×10^{11} M^{-1} s^{-1} / 0.2 s^{-1} (3), 1×10^{12} M^{-1} s^{-1} / 2 s^{-1}, (4) (c) Effect of varying $k_{3,4r} = 0.002$ s^{-1} (1), 0.2 s^{-1} (2) and 2 s^{-1} ($k_{3,4}$ fixed at 1×10^{10} M^{-1} s^{-1}). $[CH_2(OH)_2]_0$ = 0.17 M , $[HSO_3^-]_0 = 0.1$ M, b/c = 10.

The position of the lower limit point in Figures 3.19 (a) and (b) does not noticeably move with variation of $k_{3,4}$ and $K_{3,4}$. Alteration of $k_{3,4}$ and $k_{3,4r}$ can provide a slightly better match between numerical and experimental bifurcation lines. The ratio of $k_{3,4}$/ $k_{3,4r}$ effects the overall change in pH. If the equilibrium constant is increased there is a bigger pH change in batch, and the thermodynamic branch becomes more stable.

The numerical simulations calculate a much larger region of bistability in the b/c – k_0 phase plane than that found experimentally (Figure 3.17). The effect of $k_{3,4}$ and $k_{3,4r}$ on the position of the limit points at b/c = 20, is shown in Figure 3.20. This

is to determine whether realistic alteration of this rate constant could provide better correlation between experimental and numerical results.

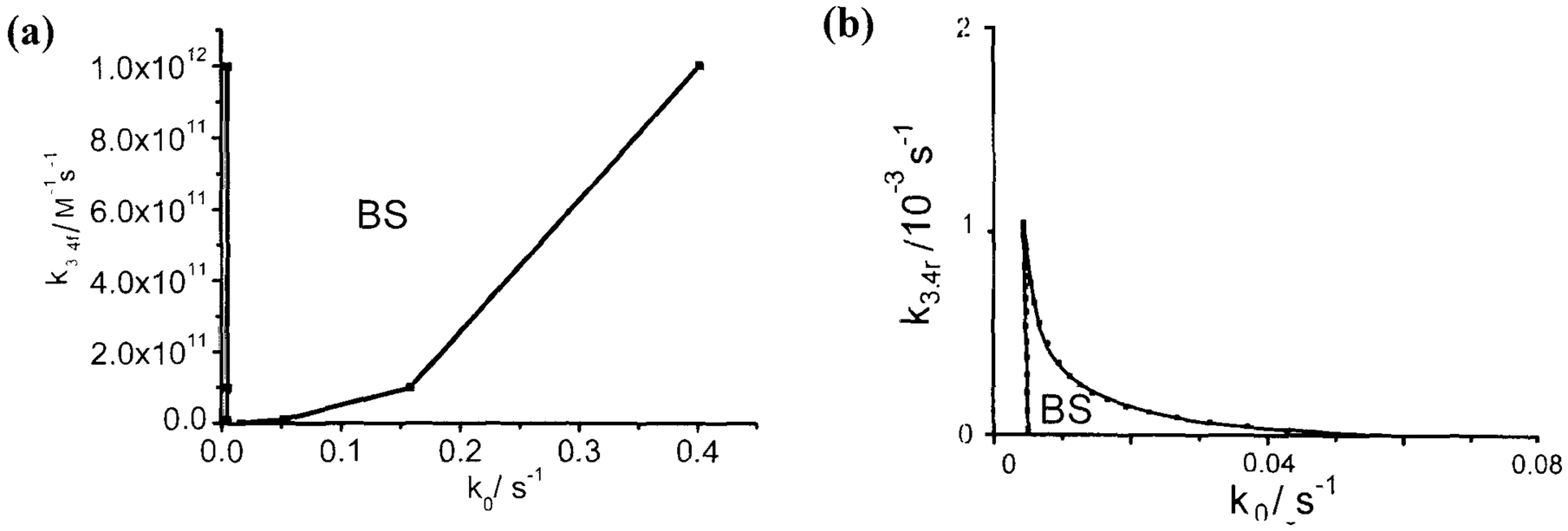

Figure 3.20 Effect of changing (a) $k_{3.4}$ keeping $k_{3.4r}$ constant at 0.002 s^{-1} and (b) $k_{3.4r}$ keeping $k_{3.4}$ at 1 $\times 10^{10}$ M^{-1} s^{-1} constant . $[CH_2(OH)_2]_0$ = 0.089 M, $[HSO_3^-]_0$ = 0.066 M, $[SO_3^{2-}]$ = 0.0033 M (b/c = 20).

Although an increase in $k_{3.4r}$ lowers the position of the high flow rate limit point, this is not a realistic alteration as at values higher than 0.005 s^{-1} there is no real clock behaviour in batch. Values of $k_{3.4}$ = 1 $\times$ 10^{10} $M^{-1}s^{-1}$ and $k_{3.4r}$ = 0.002 s^{-1} were therefore used in further simulations.

(iii) Effect of inflow concentration on bistability and oscillations

Concentration- flow rate phase diagrams are shown in Figure 3.21 for those concentrations in Figure 3.14. This was done to check the surrounding phase space as the region of bistability in Figure 3.14 is relatively small.

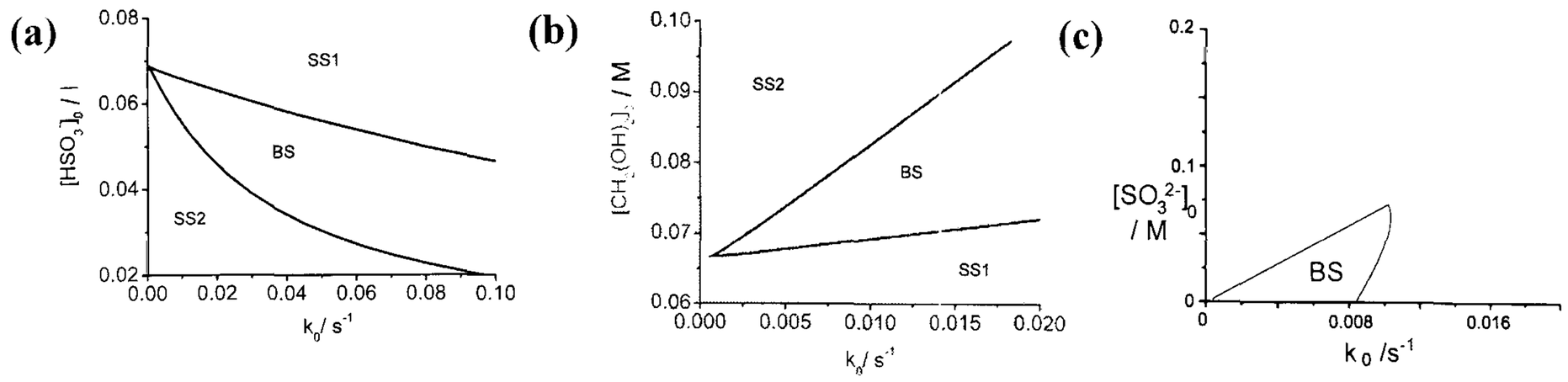

Figure 3.21 [ ] – k_0 phase diagrams for Figure 3.13 (a) $[CH_2OH_2]_0$ = 0.069 M, $[SO_3^{2-}]_0$ = 0.0133 M (b) $[HSO_3^-]_0$ = 0.066 M, $[SO_3^{2-}]_0$ = 0.0133 M . (c) $[CH_2OH_2]_0$ = 0.069 M, $[HSO_3^-]_0$ = 0.066 M.

The numerical simulations show no oscillations for any reasonable values of inflow concentration.

(iv)Conclusion - model C

Model C shows good agreement for the behaviour of the system in batch and shows reasonably good correlation with experimentally observed regions of bistability. The important point of model C is that reaction 3.1 is rate limiting. Although the concentration of OH^- does not directly increase the rate of its own production, that $k_{3.1}$ is rate limiting and catalysed by OH^- means the system displays feedback.

The overall stoichiometry of the reaction is:

$$2CH_2(OH)_2 + HSO_3^- + SO_3^{2-} \rightarrow 2CH_2(OH)SO_3^- + OH^- + H_2O$$

With the rate determining step as:

$$CH_2(OH_2) \underset{OH^-}{\overset{H^+}{\leftrightarrow}} CH_2O + H_2O \qquad v_{3.1} = k_{3.1}[CH_2(OH)_2] + k_{3.14OH}[CH_2(OH)_2][OH^-]$$

We can therefore say that

$$\frac{d[OH^-]}{dt} = k_{3.1}[CH_2(OH)_2] + k_{3.14OH}[CH_2(OH)_2][OH^-] + k_{3.5} - k_{3.5r}[OH^-][H^+] - k_{3.9}[CH_2O][OH^-]$$

Thus, the rate of production of OH^- depends on the concentration of OH^-.

The buffer mechanism is still important in model C as it provides the necessary time delay before the OH^- autocatalysis can take place. An in depth discussion of the effect of varying sensitive rate constants has been presented in this section in an attempt to fully characterize the mechanism.

The simulations tend to overestimate the stability of the thermodynamic branch, and produce larger regions of bistability than those seen experimentally. The chemical steps that result in oscillations are missing from model C so it is possible to conclude that the presence of such mechanistic steps might provide the required destabilization of the thermodynamic branch in numerical simulations. Another possibility is that the experimental thermodynamic branch is destabilized by inefficient stirring in experiments. Macromixing effects were therefore added to model C in an attempt to better fit regions of experimental and numerical bistability.

3.5 Stirring effects

3.5.1 Introduction

The effect of poor mixing on nonlinear chemical systems can result in macroscopic changes in behaviour. Bifurcation points can move or the period and amplitude of oscillations can change. Apparent new bifurcations can arise although these are in reality bifurcations which have shifted due to poor mixing. Nonlinear reactions have an innate tendency to amplify any departure from homogeneity. With stirring rates as high as 600 r.p.m. there is evidence that significant concentration gradients arise and persist within open and closed reactors (11), (19). It has been shown, experimentally (20) and numerically (21), that insufficient stirring can cause a shrinking of a bistable

region (a contraction of the hysteresis loop) in autocatalytic reactions. This section introduces a simple mathematical model which accounts for imperfect mixing in a CSTR (22). This model is then combined with the chemical mechanism for the methylene glycol sulfite system to show that insufficient stirring can cause a shrinking of the bistable region. This shrinking provides better agreement between experimental regions of bistability and those predicted from numerical simulations.

3.5.2 The reactor model

Coupled reactor models are widely used to model the effect of incomplete macro mixing in nonlinear reactions. Figure 3.22 is an idealized representation of a CSTR. The reactants are fed into the reactor at constant flow rate, Q, and enter the reactor with a concentration $c_{i,0}$. The reactor has a total volume V_r and $k_0 = Q/ V_r$ is the reciprocal of the residence time. If the mixing is less than perfect, zones begin to develop in the reactor where concentrations are different from those in the bulk (23) . In the 'dead zone model' of Kumpinski *et. al* (22) these zones are grouped together and called the 'dead zone'. Bigger dead zones imply inefficient mixing. This is represented in Figure 3.23. There are two well mixed tank reactors which are interconnected. The active zone, or bulk, V_a, has a direct active flow from the input reservoirs. The dead zone, V_d has a partially restricted flow via the bulk. The model has two new parameters: the cross flow between the regions which is Q_x and the volume ratio $x = V_d/ V_r = V_d/ (V_a + V_d)$. Q_x is replaced by the ratio of residence times in the active and dead zones $z = k_d/ k_a$ where $k_a = k_0 /(1-x)$.

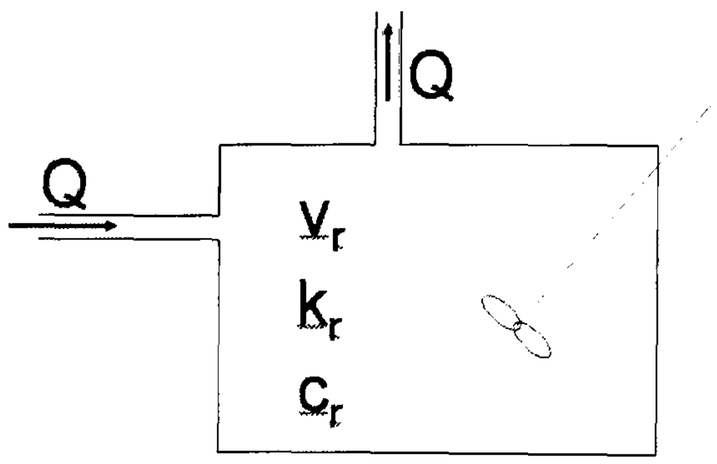

Figure 3.22 Idealized representation of a CSTR with perfect stirring.

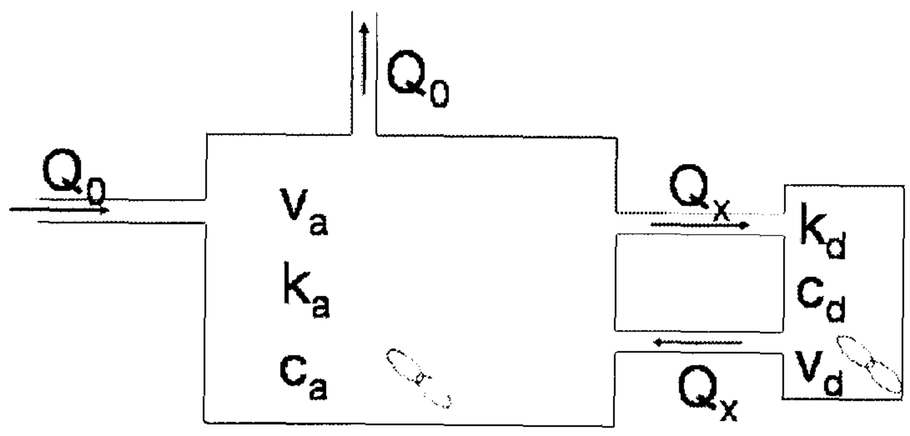

Figure 3.23 Schematic of behaviour in the dead zone model of imperfect mixing in a CSTR.

We can now write that in the active zone:

$$\frac{dc_a}{dt} = \text{chemistry} + \frac{k_0}{1-x}(c_0 - c_a) - z\left(\frac{k_0}{1-x}\right)\left(\frac{x}{1-x}\right)(c_a - c_d)$$

And in the dead zone:

$$\frac{dc_d}{dt} = \text{chemistry} + z\left(\frac{k_0}{1-x}\right)(c_a - c_d)$$

(See appendix II for full mathematics and ODE file)

Numerically we now have two ODEs for each species, one describing the behaviour in active zone, and the other describing behaviour in the dead zone.

A consideration of batch reactor behaviour and chemical mechanism can help predict which branch of a bistable system is stabilized. If the induction period is short

compared to the residence time, poorly mixed regions on the thermodynamic branch (with concentrations of the completed reaction) may be found. Decreasing the stirring rate stabilizes these states and the flow branch is destabilized. Reactants in the dead zone will have enough time to transit from the flow branch, close to the inflow concentrations, to the thermodynamic branch and the latter will thus be stabilized. This behaviour is seen in numerical and experimental studies of the BrO_3^- - Br^- - Mn^{2+} system (24).

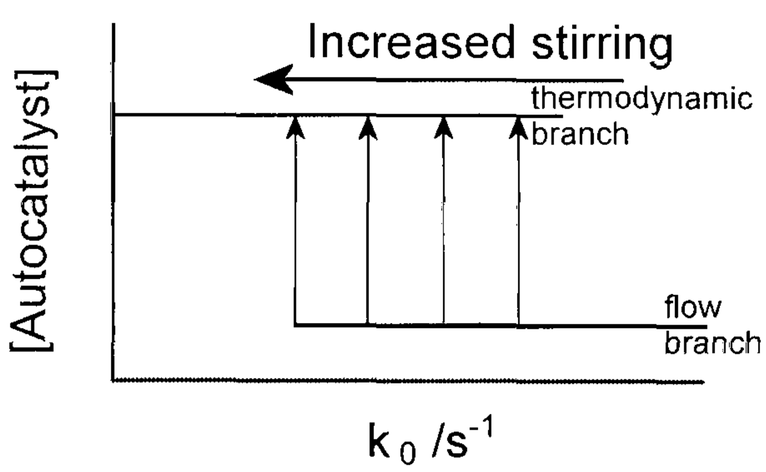

Figure 3.24 Schematic of behaviour in the bromate-bromide-manganous system. The flow rate required for 'nucleation' (transition from low to high autocatalyst concentration) decreases for increasing mixing (decreasing x, the fraction of dead zone)

Conversely, if the induction time is long compared to the residence time, isolated unreacted regions will exist on the flow branch. Reactants will be 'washed out' of the reactor before they have a chance to react and the thermodynamic branch is destabilized. The flow branch is stabilized. This behaviour is seen experimentally and numerically in the chlorite iodide system (20).

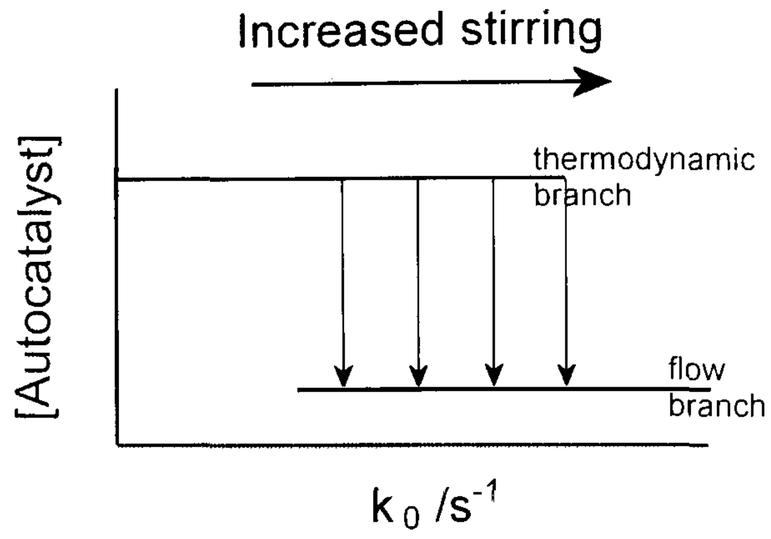

Figure 3.25 Schematic of behaviour in the chlorite iodide system. The flow rate required for 'nucleation' (transition from high to low autocatalyst) increases for increasing mixing (decreasing x, the fraction of dead zone).

This type of behaviour is predicted in the MGS reaction and thus we expect the addition of macro- mixing effects to model C to result in shrinking of the numerically calculated bistable region. Increasing x will increase the fraction of dead zones, thus decreasing the mixing, and result in a contraction of hysteresis loops.

3.5.3. Results - Effect of addition of macro-mixing terms to model C for the methylene glycol-sulfite reaction

The rate equations derived from model C were augmented by macro- mixing terms as detailed above. At these conditions the system is strongly dependent on x and negligibly on z, the cross flow parameter. An increase in x, the dead volume fraction, decreases the region of bistability. Figure 3.26 shows the calculated regions of bistability on the basis of model C with additional macro mixing terms as detailed previously.

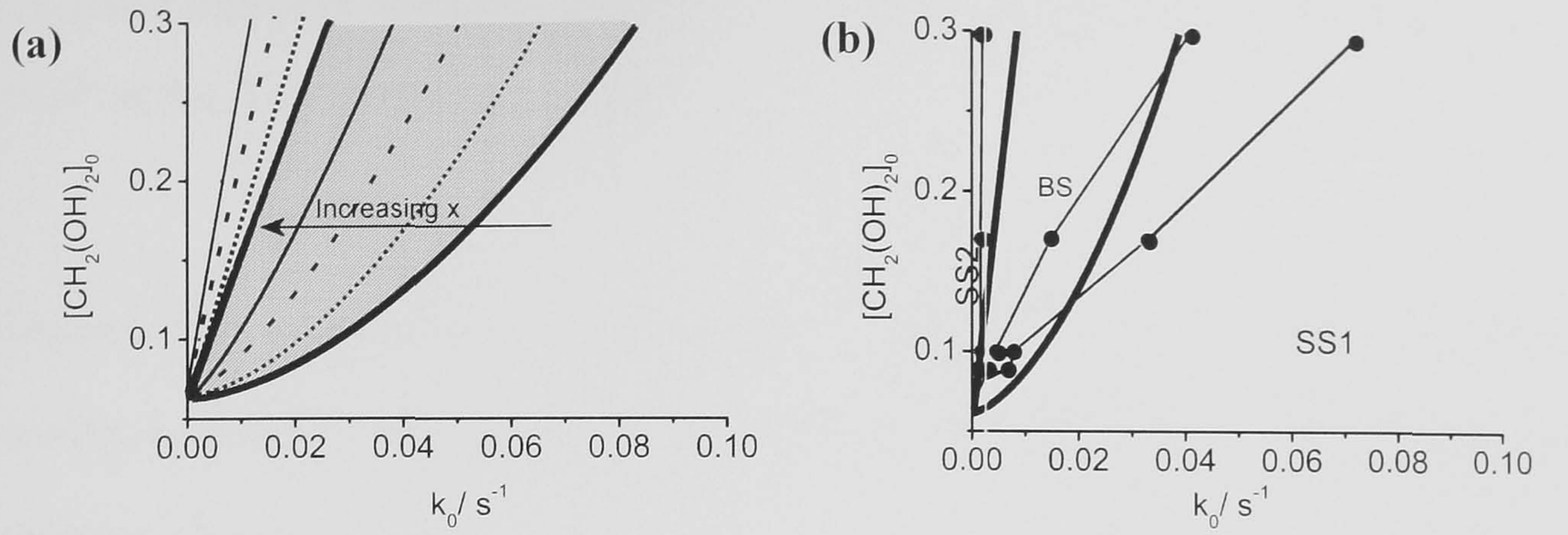

Figure 3.26 (a) k_0 – $[CH_2(OH)_2]_0$ phase diagrams calculated from model C with additional macro- mixing terms. Thick line is x = 0 (original calculation see Figure 3.15), dot line x = 0.2, dash line x = 0.4, thin solid line x = 0.6. (b) Experimental (thin line with points) and numerical where x = 0.6 (thick line) calculated regions of bistability. $[HSO_3^-]_0$ = 0.066 M, $[SO_3^{2-}]_0 = 5.7 \times 10^{-4}$ M (b/c = 116). z is constant at 0.6.

Figure 3.27 shows the k_0 – b/c phase diagrams calculated form model C with the addition of macro mixing effects. Again, the region of bistability is reduced.

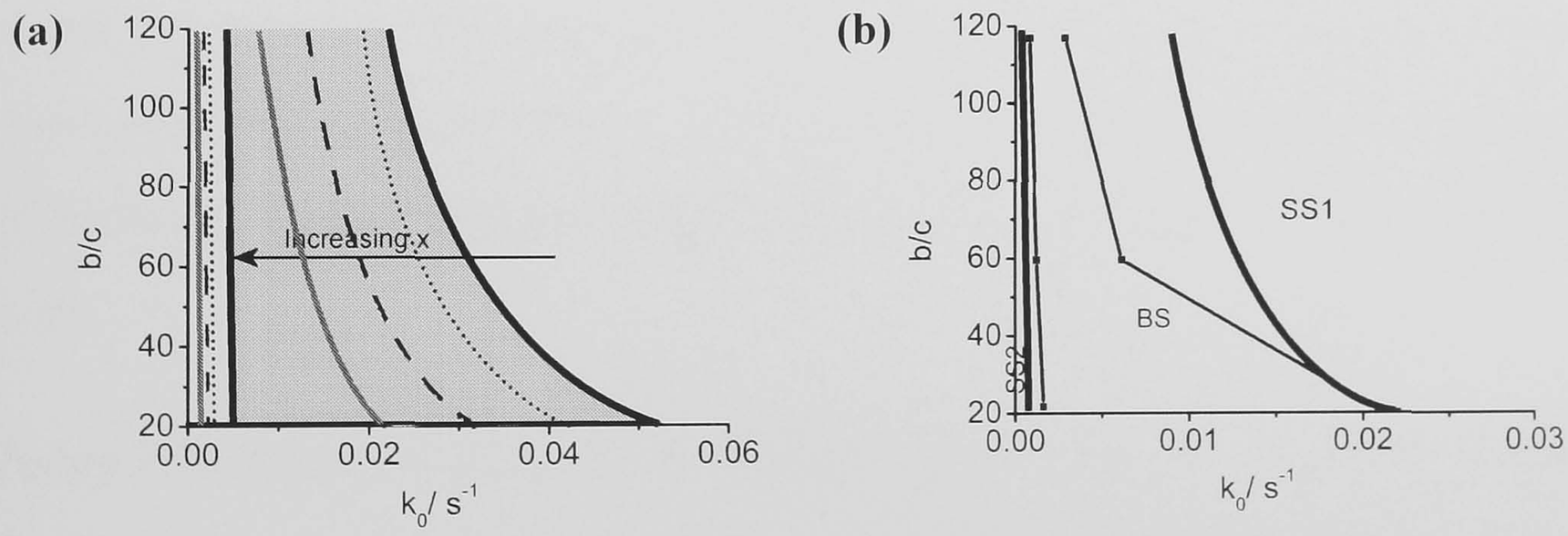

Figure 3.27 $[HSO_3^-]_0$ / $[SO_3^{2-}]_0$ (b/c) – k_0 phase diagrams calculated from model C with additional macro mixing terms.(a) Effect of varying volume ratio. Thick plain line is x = 0 (original calculation, see Figure 3.16), dot line is x = 0.2, dash line x = 0.4, thin solid line x = 0.6 (b) Experimental (thin line with points) and numerical where x = 0.6 (thick line)

calculated regions of bistability. $[HSO_3^-]_0$ = 0.066 M, $[CH_2(OH)_2]_0$ = 0.089 M $[SO_3^{2-}]_0$ = 5.7 × 10^{-4} M (b/c = 116), z is constant at 0.6.

Figure 3.28 shows the bifurcation diagram of Figure 3.14 with the addition of macro mixing to model C. The macro-mixing terms provide the predicted contraction of the hysteresis loop.

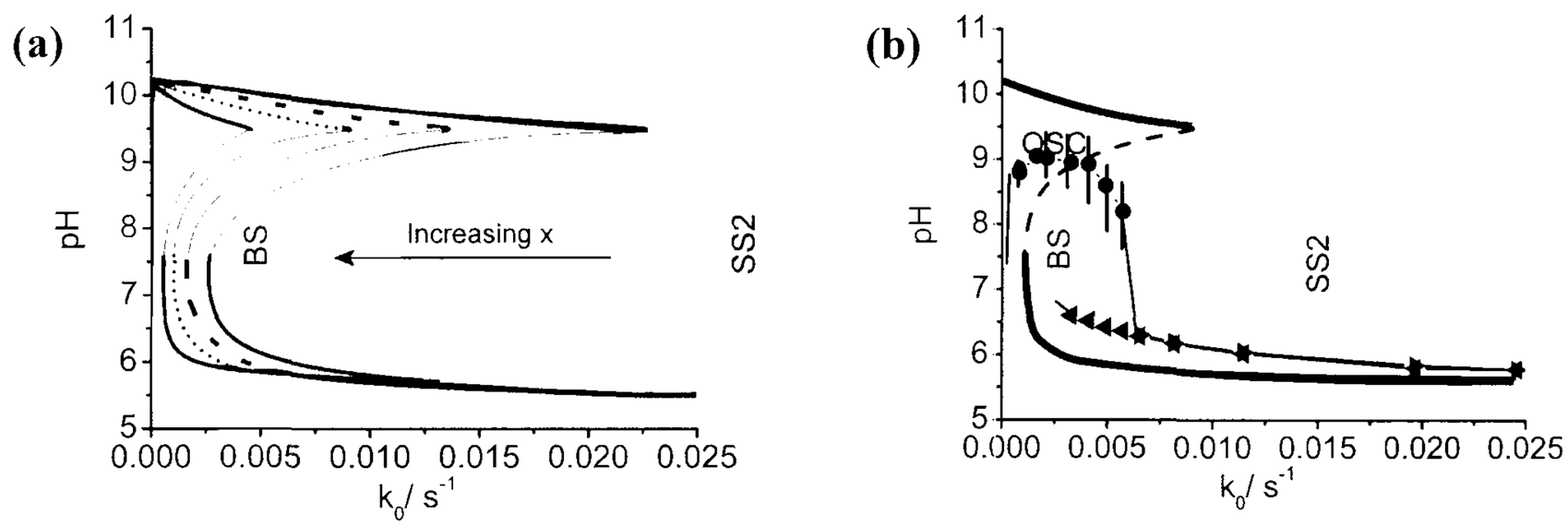

Figure 3.28 Bifurcation diagram calculated from model C with additional macro mixing terms. (a) Effect of varying volume ratio x. Thick line is x = 0, dash x = 0.4, dot x = 0.6 and thinner line is x = 0.8. Thin lines represent unstable branches. (b) Experimental (thin line with points) and numerical where x = 0.6 (thick line) calculated bifurcation diagrams. $[CH_2(OH)_2]_0$ = 0.089 M, $[HSO_3^-]_0$ = 0.066 M, $[SO_3^{2-}]$ = 5.7 × 10^{-4} M. b/c = 115. z is constant at 0.6.

Figure 3.29 shows the critical k_0 for nucleation as functions of x the dead volume fraction for three values of z (= 0.5, 0.6, 0.7) the cross flow parameter. The lines are superimposed showing there is no dependence on cross flow parameter.

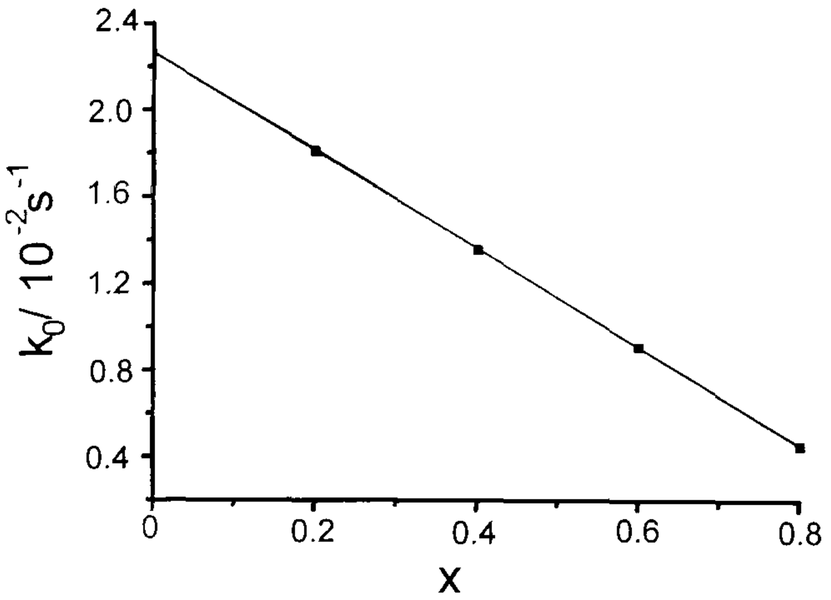

Figure 3.29 Influence of cross flow parameter z and dead volume fraction x on the critical flow rate needed for nucleation (transition from high pH thermodynamic branch to low pH flow branch). Lines are superimposed showing that z has little or no effect on position of the nucleation limit point.

3.5.4. Discussion- Model C with macro mixing

It has been shown that the addition of macro mixing terms to create imperfect mixing to model C has resulted in a contraction of the hysteresis loop and a shrinking of the bistable region in the $CH_2(OH)_2$ and b/c – k_0 parameter planes. The effect of varying the dead volume fraction shows that a decrease in mixing (higher dead volume fraction) gives smaller regions of bistability. As predicted, it is the transition from the thermodynamic to the flow branch which is most sensitive to these stirring effects, with the transition from low (flow) to high (thermodynamic) pH being less so. The effect of changing the cross flow parameter, z, is negligible.

The addition of macro-mixing terms is unlikely to yield periodic oscillations in numerical simulations of any chemical model that does not already display oscillations in any region of phase space. The addition of micro-mixing fluctuations to a model of a chemical system has been shown to produce non periodic time series (25). Micro-mixing models split the reactor up into a large number of small fluid parcels which exchange matter. Each of these reaction domains is subject to its own independent stirring effects. Addition of micro-mixing terms to the MGS reaction model could be the subject of further study.

3.6 Conclusion

The model for the Methylene Glycol-Sulfite reaction system has been developed from model A to model C. The core of model C is the base catalysed dehydration of methylene glycol. The development of model C has allowed greatly improved simulated clock times and facilitated a better understanding of the clock behaviour in batch, in particular the dependence of the clock time on the concentrations of the key reactant species. Model C is also able to reproduce experimentally observed bistability in a flow reactor with regions of simulated behaviour matching experimental results well. Mixing effects have been explored as a potential reason for the difference between experimentally-observed and predicted extents of bistability. The addition of macromixing terms to model C resulted in improved correlation between experimental and numerical limit points, matching areas of bistability well. This macromixing stirring model fails to display any oscillations in numerical simulations.

Several feedback processes have been identified in related systems which may be pertinent to the work reported here. In basic solution the Cannizaro reaction has shown some evidence of a radical chain reaction, although the generally accepted mechanism simply involves hydride transfer (26). Another related reaction is the condensation of formaldehyde in basic solution producing sugars (the Formose reaction), which has been reported to be autocatalytic in hydrated intermediates such as glycol-aldehyde (10). This reaction may display bistability in an open reactor, although this is thought to result from insufficient observation times and no oscillations have been reported. Alternatively, the oxidation of S(IV) by gallic acid has been recently demonstrated to result in nonlinear production of S(VI) (27). Self-

inhibition of the production of an organic radical species was proposed to account for the observed nonlinearity. A more detailed experimental investigation of the system is necessary to determine all intermediate species, and their reactions. The results of such experiments may yield new species present in the system which may contribute to the chemical pathways leading to oscillations.

3.7 References

(1) I Epstein, J Pojman: An Introduction to Nonlinear Chemical Dynamics. New York, 1998.

(2) J Winkleman, M Ottens, A Beenackers: The Kinetics of the Dehydration of Methylene Glycol. Chemical Engineering Science 55 (2000) 2065.

(3) HC Sutton, TM Downes: Rate of hydration of formaldehyde in aqueous solution. Journal of the Chemical Society, Chem. Comm. 1 (1972), 265

(4) P LeHenaff: Sur la vitesse de deshydratation du methylene glycol en formaldehyde. Comptes Rendus de l'Academie des Sciences 250 (1963) 1752- 54.

(5) RP Bell, FRS Evans, PG Evans: Kinetics of the dehydration of methylene glycol in aqueous solution. Proceedings of the Royal Society (1966) 297.

(6) BH Davison, G Stephanopoulos: Effect of Ph Oscillations on a Competing Mixed Culture. Biotechnology and Bioengineering 28 (1986) 1127-37.

(7) EA Betterton, MR Hoffmann: Henry's Law constnats of some environmentally imporatnat aldehydes. Environmental Science & Technology 22 (1988) 1415.

(8) J Lagrange, G Wenger, P Lagrange: Kinetic study of HMSA formation and decomposition: Tropospheric relevance. Journal De Chimie Physique Et De Physico-Chimie Biologique 96 (1999) 610-33.

(9) A Skrabal, R Skrabal: Dynamics of the formaldehyde-bisulfite reaction. A study of the principle of microscopic reversibility. Monatshefte fuer Chemie 69 (1936) 11-41.

(10) WP Huskey, IR Epstein: Autocatalysis and Apparent Bistability in the Formose reaction. Journal of the American Chemical Society 111 (1989) 3185.

(11) Westerhoff, Hauser, Weimer, Satnoianu, Sorensen, Munster, Marek, Scott, Orban, Hantz, Jonnalagadda, Wang, Hanke, Gaspar, Noszticzius, Epstein, Dano, Hunding, Nicolis, Menzinger, Schreiber, Harrison, Maini, Kaern, Merkin, Feigin, Simon: General discussion. Faraday Discussions 120 (2001) 325-51.

(12) SK Scott: Oscillations, Waves, and Chaos in Chemical Kinetics, Oxford, 1995.

(13) J Billingham, DJ Needham: Mathematical-Modeling of Chemical Clock Reactions .1. Induction, Inhibition and the Iodate Arsenious-Acid Reaction. Philosophical Transactions of the Royal Society of London Series a-Mathematical Physical and Engineering Sciences 340 (1992) 569-91.

(14) J Billingham, DJ Needham: Mathematical-Modeling of Chemical Clock Reactions .2. A Class of Autocatalytic Clock Reaction Schemes. Journal of Engineering Mathematics 27 (1993) 113-45.

(15) A Hanna, A Saul, K Showalter: Detailed studies of propagating fronts in the iodate oxidation of arsenous acid. Journal of the American Chemical Society 104 (1982) 3838.

(16) DO Cooke: Inorganic reaction mechanisms, London, 1979.

(17) MG Burnett: The Mechanism of the Formaldehyde Clock Reaction - Methylene Glycol Dehydration. Journal of Chemical Education 59 (1982) 160-62.

(18) P Guthrie: Journal of the American Chemical Society 122 (2000) 357.

(19) E Ochai, M Menzinger: Chemical Instabilities: A Spectroscopic Study of Spatial Inhomogenities in the ClO_2^-/ I^- Reaction in a CSTR. Journal of Physical Chemistry 94 (1990) 8866.

(20) JC Roux, P De Kepper: Phys. Lett. 97 (1983) 168.

(21) J Boissonade: Physica 68 (1982) 1385.

(22) E Kumpinsky, I Epstein: A model for stirring effects on the transition in bistable chemical systems. Journal of Chemical Physics 82 (1985) 53- 57.

(23) PT Woodrow, Chemical Reaction Engineering- Houston, American Chemical Society Symposium Series., ACS, WAshington D.C., 1978, p. 571.

(24) A Dutt, M Menzinger: Stirring and mixing effects on oscillations and inhomogeneities in the minimal bromate oscillator. Journal of Chemical Physics 110 (1999) 7591.

(25) A Ali, P Strizhak, M Menzinger: Stirring effects on bistability in a CSTR. 1. Experiments and Simulations for the AsO_3^-/ IO_3^- Reaction. Journal of Physical Chemistry 103 (1999) 10859-65.

(26) EC Ashby, D Coleman, M Gamasa: Single-electron transfer in the Cannizzaro reaction. Journal of Organic Chemistry 52 (1987) 4079-85.

(27) W Pasiuk-Bronikowska, T Bronikowski, M Ulejczyk: Synergy in the Autoxidation of S(IV) Inhibited by Phenolic Compounds. Journal of Physical Chemistry A 107 (2003) 1742-48.

CHAPTER 4

A novel route to pH oscillators

4.1 Introduction

In this chapter a minimal model is constructed demonstrating that a base-catalysed dehydration of an hydrated carbonyl compound can provide the necessary source of positive feedback for the development of an organic substrate based-pH oscillator (1). This minimal model is based on the methylene glycol-sulfite system discussed in the previous chapter, which displays complex behaviour in a flow reactor. Large amplitude oscillations in pH are observed in the model on the addition of an appropriate OH^- consuming reaction step.

The second part of the chapter presents the first experimental example of such an organic substrate based pH oscillator in a flow reactor (2). The system utilises the base-catalysed dehydration of methylene glycol as a source of positive feedback (OH^- autocatalysis) coupled with the base-catalysed hydrolysis of gluconolactone for negative feedback (H^+ production). The observed large amplitude oscillations in pH (between pH 7 and pH 10) are reproduced in a kinetic model of the system. This system is of interest as the large amplitude pH oscillations are accompanied by small amplitude oscillations in potential, making it less aggressive than conventional redox oscillators. These experiments and numerical simulations provide new possibilities in the design of biocompatible pH oscillators.

4.2 The reduced model

As discussed in chapter 1, the design of pH oscillators is of particular interest. Moreover, the ability to design organic substrate-based non-redox pH oscillators may ultimately provide less aggressive systems for use in conjunction with pH sensitive gels, switches and pumps. The following model originates from the methylene glycol-sulfite system - the only known example of an organic substrate based pH

clock reaction, discussed in the previous chapter (3). This reaction displays an acid to base clock reaction in a batch reactor, bistability and small amplitude pH oscillations in a flow reactor.

The core of the reduced model is an OH^- producing addition reaction. The organic substrate is supplied to the system via a base-catalysed rate-determining dehydration step. Thus, for appropriate conditions the model displays an acid to alkali clock in batch as the rate of production of OH^- is proportional to the concentration of OH^-. The model also displays bistability in flow, and large amplitude pH oscillations when coupled with a first order decay of OH^-.

4.2.1. The model

Inspired by the mechanism of the methylene glycol-sulfite reaction the following minimal model is proposed:

$$O \rightleftharpoons A + H_2O \tag{4.1}$$

$$A + S \rightarrow P^- \tag{4.2}$$

$$P^- + H^+ \rightleftharpoons P \tag{4.3}$$

$$H_2O \rightleftharpoons H^+ + OH^- \tag{4.4}$$

where O is an hydrated aldehdyde (e.g. methlyene glycol), A is the dehydrated form (formaldehyde), S is a general adduct forming compound (e.g. sulfite) and P^- is the basic form of an adduct P. The overall reaction is therefore:

$$O + S \rightarrow P + OH^- \tag{4.5}$$

The corresponding rate equations for steps 4.1 – 4.4 are shown in table 4.1.

Rate	Rate constants
$R_1 = (k_{4.1} + k_{OH}[\mathrm{OH^-}])[\mathrm{O}]$ $R_{-4.1} = k_{-4.1}[\mathrm{A}]$	$k_{4.1}* = 5.5\times10^{-8}\,\mathrm{s^{-1}}$, $k_{OH}* = 310\,\mathrm{M^{-1}s^{-1}}$ $k_{-4.1} = 10\,\mathrm{s^{-1}}$ *
$R_{4.2} = k_{4.2}[\mathrm{A}][\mathrm{S}]$	$k_{4.2} = 5.4\times10^{4}\,\mathrm{M^{-1}s^{-1}}$
$R_{4.3} = k_{4.3}[\mathrm{P^-}][\mathrm{H^+}]$ $R_{-4.3} = k_{-3}[\mathrm{P}]$	$k_{4.3} = 1\times10^{11}\,\mathrm{M^{-1}s^{-1}}$ $k_{-4.3} = 0.2\,\mathrm{s^{-1}}$ $K_{4.3} = 5\times10^{11}$ (constant)
$R_{4.4} = k_{4.4}$ $R_{-4.4} = k_{-4.4}[\mathrm{OH^-}][\mathrm{H^+}]$	$k_{4.4} = 1\times10^{-3}\,\mathrm{Ms^{-1}}$ $k_{-4.4} = 1\times10^{11}\,\mathrm{M^{-1}s^{-1}}$

Table 4.1. Rate equations for R 4.1- R 4.4. * varied in this work.

Reaction (4.1), the dehydration of the organic species, is H^+ or OH^- catalysed depending on the conditions (4). The acid catalysis channel is not significant at the pH in this work, so is omitted for simplicity. Inclusion of the acid catalysis in the rate law makes no difference to the observed behaviour. The most important feature of the model is that 4.1 is slow compared to 4.2, such that 4.1 is rate-limiting. The rate constants chosen are illustrative and the reported behaviour is observed over a wide range of values.

The overall rate of production of OH^- depends on its concentration:

$$d[\mathrm{OH^-}]/dt = (k_{4.1} + k_{OH}[\mathrm{OH^-}])[\mathrm{O}] \qquad (4.6)$$

Numerical integration of the four equations gives rise to an acid to alkali clock under appropriate batch conditions. Bistability is observed in flow, and oscillations are seen when steps 4.1 – 4.4 are coupled with a first order decay of OH^- (4.7), and the rate equations are augmented with the appropriate flow terms.

$OH^- \rightarrow$ (4.7)

Where the rate of 4.7 is given by;

$$R_{4.7} = k_{4.7}[OH^-] \qquad k_{4.7} = 0 - 20\ s^{-1}$$

Numerical integration of the rate equations was performed using package XPPAUT (5) (see appendix I). The method of integration chosen was CVODE, with time step generally taken as $dt = 0.01$ and the tolerance set at $tol = 1 \times 10^{-10}$. A decrease in the time step does not influence the behaviour. Bifurcation diagrams and phase diagrams were computed with the AUTO interface of XPPAUT (5). The maximum time step was 1×10^{-4} with the tolerances set to 1×10^{-6}.

4.3 Results

In the absence of flow ($k_0 = 0\ s^{-1}$) and with $k_{4.7} = 0\ s^{-1}$ we observe a typical acid to base clock reaction, as demonstrated in Figure 4.1(a). When the rate equations derived from the model are augmented by flow terms $k_0[X_0] - k_0[X]$, where k_0 is the flow rate and the input concentration $[X]_0$ is the inflow concentration of species X, the system displays bistability (Figure 4.1(b)). The inflow species are O, S and H^+. The concentrations of A and OH^- in the flow are determined by the equilibrium of (4.1) and (4.4) respectively. Figure 4.1(c) shows the region of bistability in the $k_{4.1}$ - k_0 phase diagram, without any additional removal of OH^- ($k_{4.7} = 0\ s^{-1}$). Bistability is observed over a range of values for $k_{4.2}$ (1×10^{-1} to $1 \times 10^{11}\ M^{-1}s^{-1}$) and $k_{4.3}$ (1×10^{3} – $1 \times 10^{13}\ s^{-1}$). The region of bistability in the $k_{4.1}$ - k_0 parameter plane increases with increasing $k_{4.2}$ and with increasing $k_{4.3}$ (keeping $K_{4.3}$ constant).

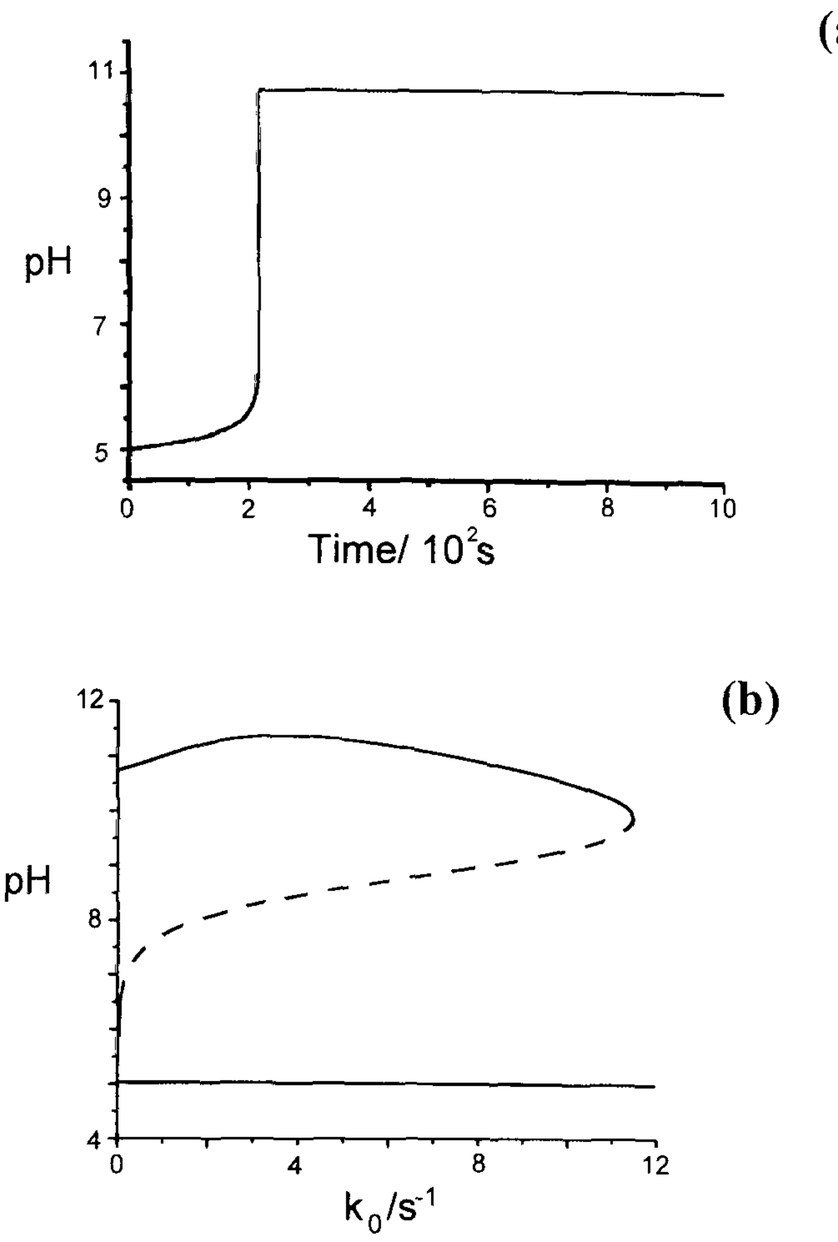

Figure 4.1 (a) Clock reaction for model with rate constants specified in Table 1. $[O]_0$ = 0.089 M, $[S]_0$ = 0.00057 M, $[H]_0 = 1 \times 10^{-5}$ M (b) bifurcation diagram with the same conditions as those in (a). (c) Bistability in the $k_{4.1} - k_0$ plane with the same conditions as in (a).

With the inclusion of $k_{4.7}$ (when $k_0 = 0$ s^{-1}) the reaction displays an increase in pH followed by a decrease (Figure 4.2 (a)). The transition between regular clock behaviour (4.1 (a)) and that observed with a value of $k_{4.7}$, is smooth until $k_{4.7} > 19$ s^{-1} at which point the typical clock is lost and the profile resembles that in (4.2 a(iii)). With $k_0 = 0.001$ s^{-1} and $k_{4.7} = 10$ s^{-1} we are able to observe pH oscillations between the values of 5.5 and 9 (Figure 4.2 (b)). The oscillations have a period of ~1400 s. The period of the oscillations increases with increasing flow rate.

(a)

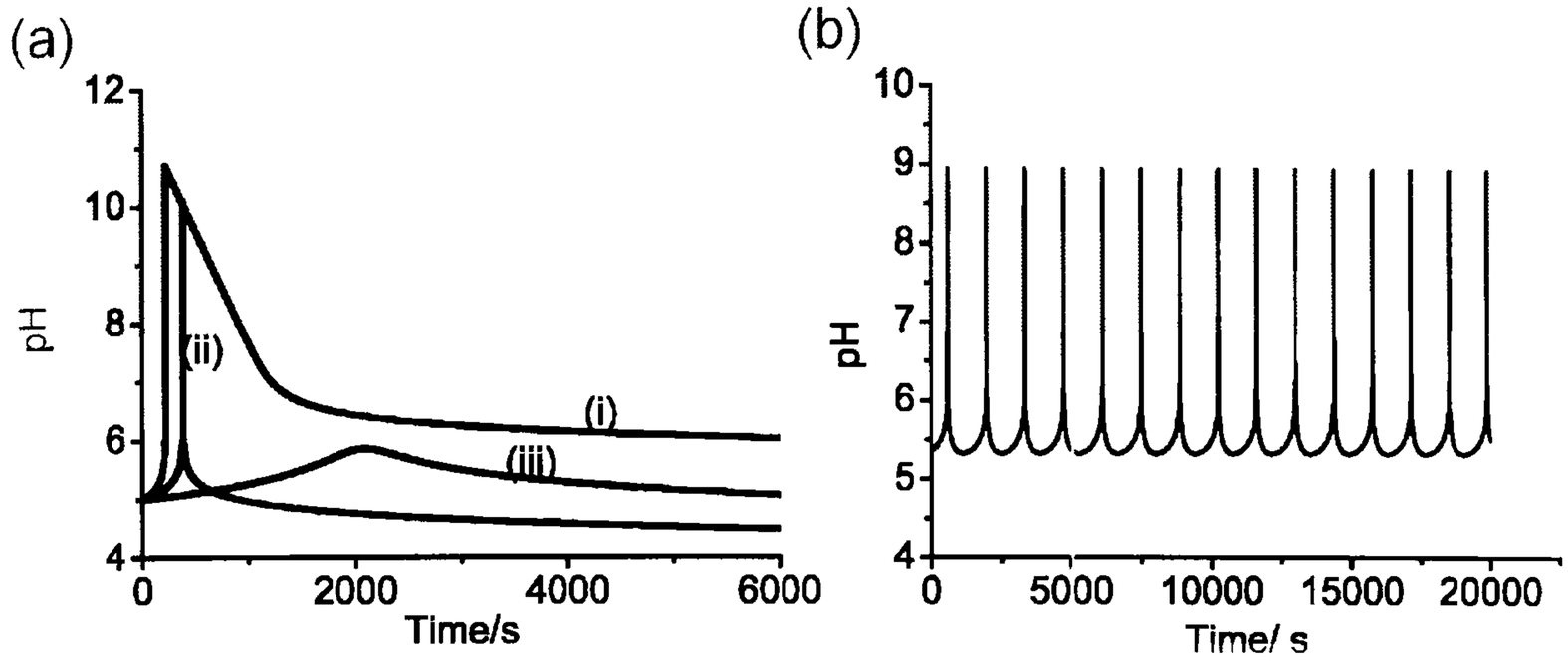

Figure 4.2 (a) Clock reactions for model with $[O]_0 = 0.089$ M, $[S]_0 = 0.00057$ M, $[H]_0 = 1 \times 10^{-5}$ M, $k_0 = 0$ s^{-1}, (i) $k_{4.5} = 1 \times 10^{-2}$ s^{-1} (ii) $k_{4.5} = 10$ s^{-1} (iii) $k_{4.5} = 20$ s^{-1}. (b) pH oscillations with same concentrations as those in (a) and $k_{4.5} = 16$ s^{-1} and $k_0 = 0.001$ s^{-1}.

A phase diagram in the $k_{4.7}$ - k_0 plane is shown in Figure 4.3 (a). It is a typical cross-shaped phase diagram. A bifurcation diagram of pH vs flow rate with $k_{4.7} = 16$ s^{-1} is shown in Figure 3(b). A Hopf bifurcation occurs at $k_0 = 4.749 \times 10^{-4}$ s^{-1} and the limit cycle finishes at a saddle node infinite period bifurcation at $k_0 = 2.529 \times 10^{-3}$ s^{-1}. There is then a region of three steady states, of which only one is stable under these parameter conditions. The oscillations are observed for a range of values of $k_{4.2}$ and $k_{4.3}$. Increasing the value of $k_{4.2}$ shifts the region of oscillations up in the $k_{4.7} - k_0$ plane. Changing the value of $k_{4.3}$ (keeping K_3 constant) does not move the region of oscillations in the $k_{4.7} - k_0$ plane.

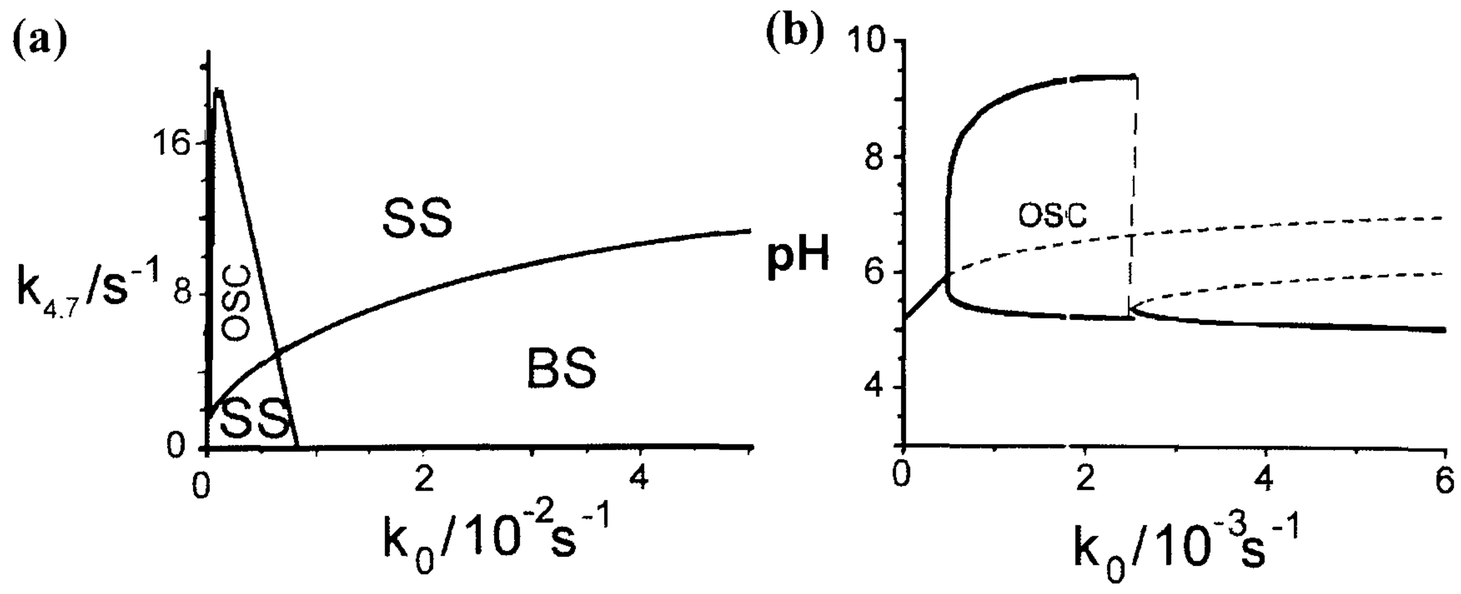

Figure 4.3 (a) Phase diagram in the $k_{4.7} - k_0$ plane with $[O]_0 = 0.089$ M, $[S]_0 = 0.00057$ M, $[H]_0 = 1 \times 10^{-5}$ M. (b) Bifurcation diagram for $k_{4.7} = 16$ s^{-1} with inflow concentrations same as (a). Solid lines show stable states, dashed lines show unstable states. The vertical dashes indicate the end of the stable limit cycle.

With this form of bifurcation (Figure 4.3(b)), where the limit cycle ends at a saddle node,

there is expected to be a lengthening law with the period of oscillations growing as the inverse square root of the difference between a parameter and the critical parameter (6);

$$period\ \alpha\ \frac{1}{(parameter - parameter_{critical})^{\frac{1}{2}}}$$

Where $parameter_{critical}$ is the parameter value of the SNIPER bifurcation ($k_0 = 2.529 \times 10^{-3}$ s^{-1} in this case) and *parameter* is the parameter value at which the value of the period is taken. In this case, a plot of log period against log ($k_{0,\ critical} - k_0$) should yield a straight line of gradient -1/2. This is indeed the case, as shown in Figure 4.4.

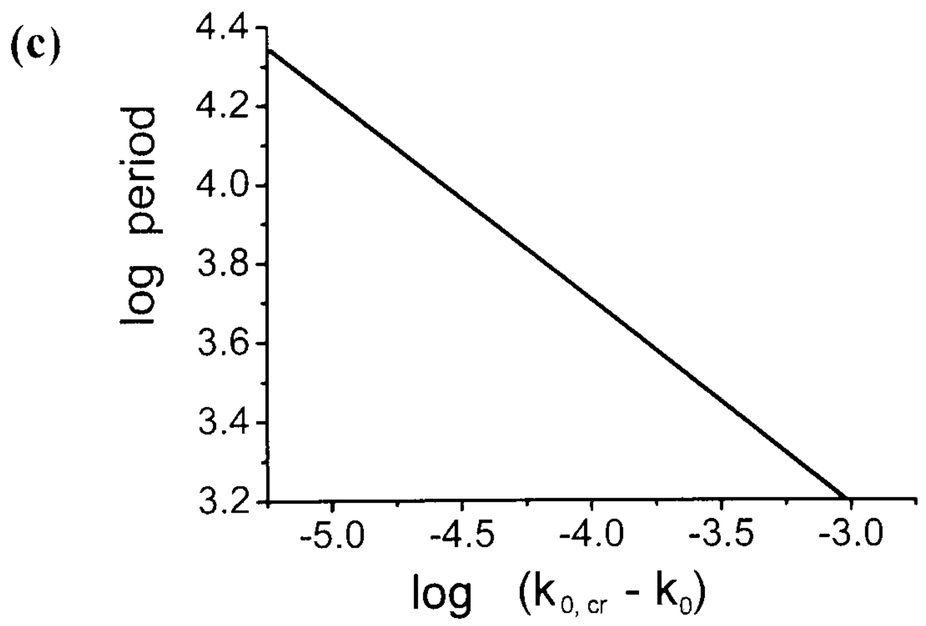

Figure 4.4 Plot of log period against log ($k_{0,\ critical} - k_0$) for the bifurcation diagram in Figure (4.3 b). The straight line has a gradient of -0.515 ± 0.002.

The range of behaviour is also investigated as a function of $k_{4.1}$, $[O]_0$ and $[S]_0$. Figures 4.5 (a,b,c) demonstrate that oscillations exist over a range of reasonable values.

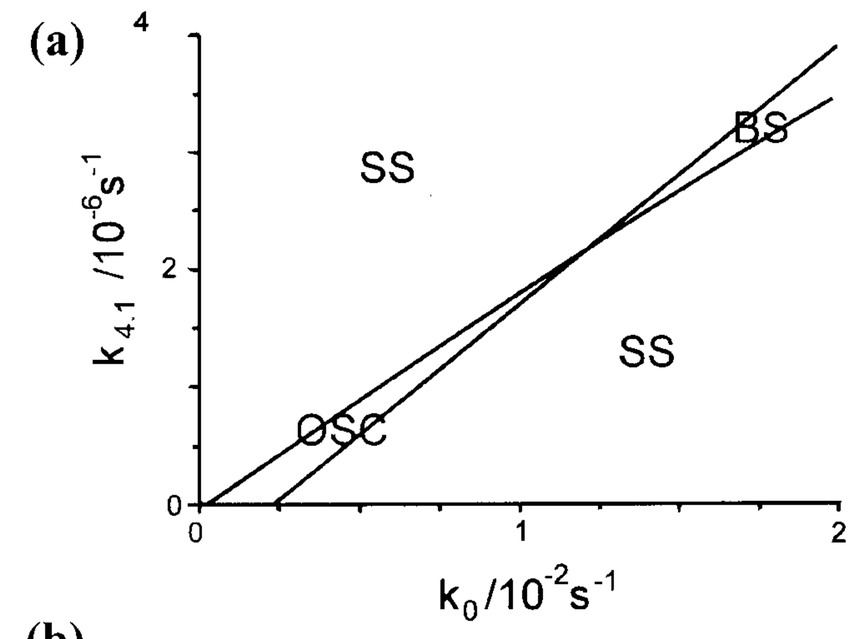

Figure 4.5 (a) Phase diagram in the $k_{4.1}$ - k_0 plane with $[O]_0$ = 0.089 M, $[S]_0$ = 0.00057 M, $[H]_0$ = 1 x 10^{-5} M and $k_{4.7}$ = 16 s^{-1}. (b) Phase diagram in the $[O]_0$ - k_0 plane with $[S]_0$ = 0.00057 M, $[H]_0$ = 1 x 10^{-5} M, $k_{4.1}$ = 5.5 × 10^{-8} s^{-1} and $k_{4.7}$ = 16 s^{-1}. (c) Phase diagram in the $[S]_0$ - k_0 plane with $[O]_0$ = 0.089M, $[H]_0$ = 1 x 10^{-5} M, k_1 = 5.5 × 10^{-8} s^{-1} and $k_{4.7}$ = 16 s^{-1}. OSC II is an additional oscillatory region.

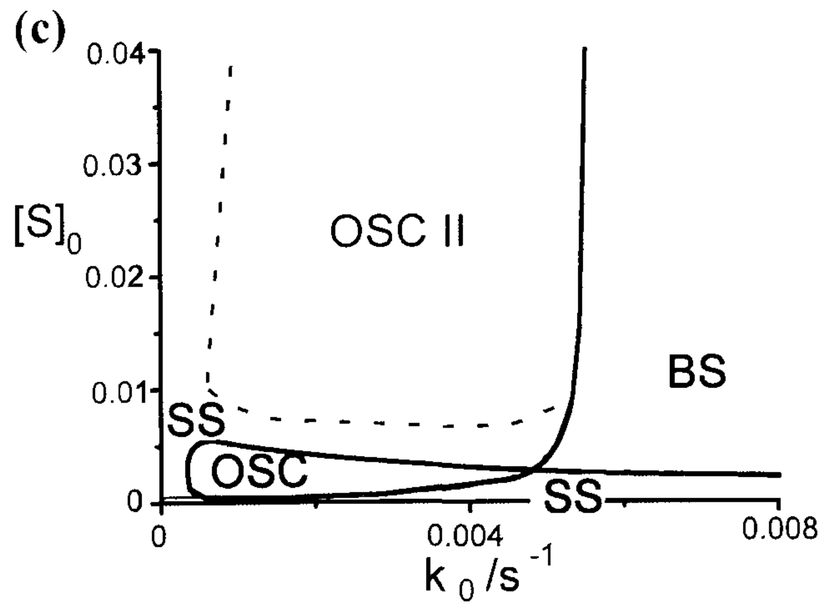

Region OSC II denotes an additional oscillatory region that is bistable with a steady state of pH ~ 7. Figure 4.6 shows the log [S] – log [A] phase plane for $[S]_0 = 0.03$ M and $k_0 = 0.0025$ s^{-1} showing the bistability between the steady state and limit cycle. This stable limit cycle is inaccessible to AUTO calculations, presumably because it exists as an isolated branch of solutions.

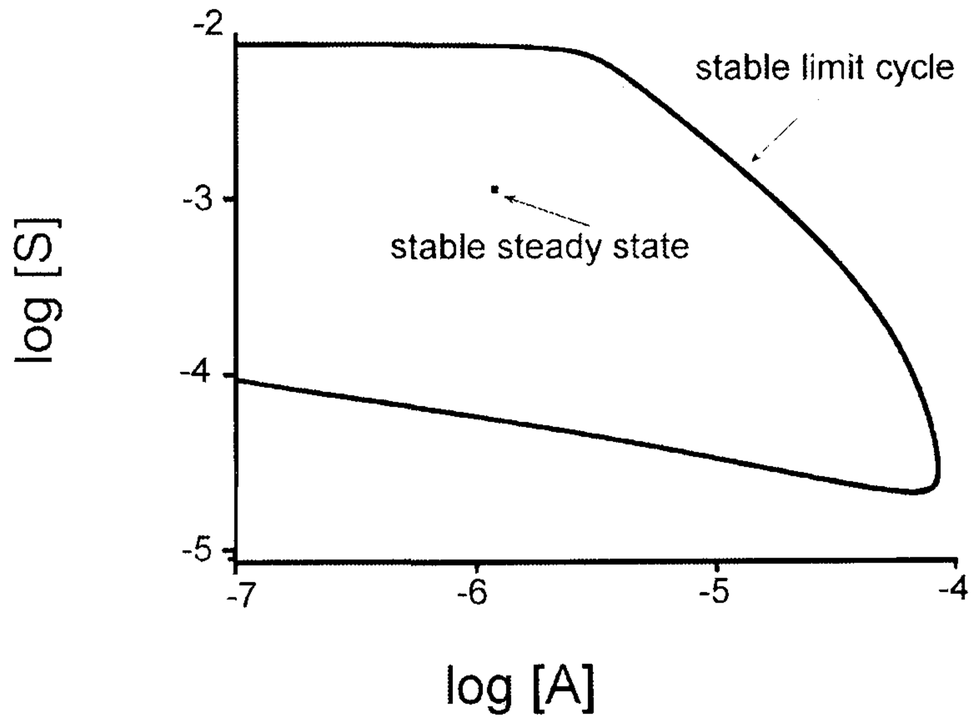

Figure 4.6 Phase plane for $k_0 = 0.0025$ s^{-1}, $[S]_0 = 0.03$ M showing stable limit cycle coexisting with a stable steady state.

4.4. Conclusion

We have shown how a minimal model based on an OH^--catalysed rate-limiting dehydration step can display bistability and oscillations in pH. The behaviour observed is possible over a reasonable range of flow rates and inflow concentrations. This model contains no conventional autocatalysis and may therefore provide a new

approach for the design of open systems which display bistability and oscillations in pH. Base (or acid) catalysed dehydration of carbonyl compounds is a general phenomenon (7). Examples are shown below, where k_{OH} is the base catalysed rate (7), (4).

$CH_2(OH)_2 \leftrightarrow CH_2O + H_2O$ $K = 5.5 \times 10^{-4}$, $k_f = 10\ s^{-1}$, $k_{OH} = 2100\ M^{-1}s^{-1}$

$CHCH_3(OH)_2 \leftrightarrow CH_3CHO + H_2O$ $K = 1.06$, $k_f = 4.6 \times 10^{-3}\ s^{-1}$, $k_{OH} = 47863\ M^{-1}s^{-1}$

$CPhCF_3(OH)_2 \leftrightarrow PhCOCF_3 + H_2O$ $K = 0.33$, $k_f = 3.2\ s^{-1}$, $k_{OH} = 501187\ M^{-1}s^{-1}$

The feedback route may also explain some of the behaviour observed in the methylene glycol-sulfite system, although oscillations in this system were between much smaller values of pH. As discussed in the previous chapter, it seems plausible to suggest that the oscillations in this system arise through an additional feedback system rather than a simple first order drain of the feedback species OH^-. The sulfite-bisulfite buffer also plays an important role in the MGS system as the rate constant for the dehydration of formaldehyde (8) is much faster than the value used for $k_{4.1}$ in this minimal model. The buffer is necessary in the methylene glycol system to maintain the low pH state by providing a slow release of H^+.

4.5 pH oscillations in the Methylene glycol-Sulfite-Gluconolactone (MGSG) reaction - Introduction

The previous section detailed a new approach to the design of organic substrate based pH oscillators by presenting a simplified model on which such systems could be based. In this section, the first experimental evidence of such a pH oscillator is presented. The experimental oscillations are reproduced in a kinetic model of the

system and the general features of this reaction are discussed to illustrate how it may provide the basis for development of further novel pH oscillators.

The experimental system is based on the methylene glycol- sulfite system discussed in the previous chapter, and utilises the base catalysed dehydration of methylene glycol as positive feedback (production of OH^-) and the base catalysed hydrolysis of gluconolactone as negative feedback (production of acid).

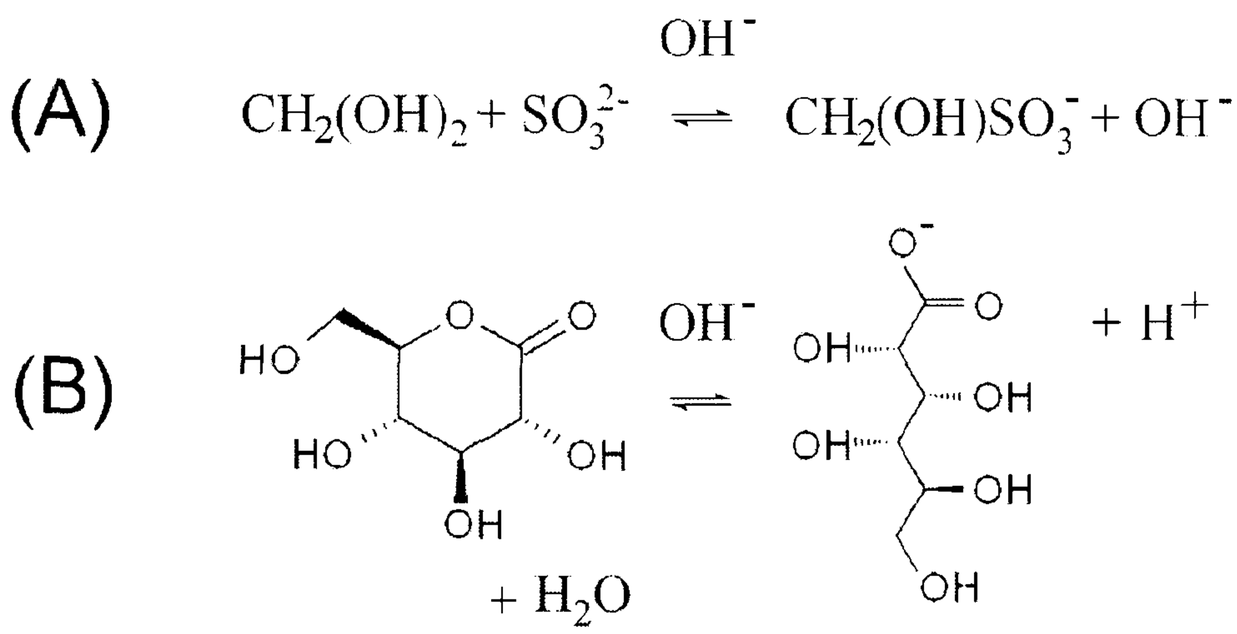

Figure 4.7 The based catalysed base producing methylene glycol reaction (A- positive feedback) and the base catalysed acid producing hydrolysis of gluconolactone (B- negative feedback).

This base catalysed, acid producing reaction provides the necessary delayed negative feedback required for oscillations. The reaction is found to support bistability and oscillations over a wide range of flow rates and displays a typical cross-shaped phase diagram with increasing inhibitor (gluconolactone) concentration. The oscillations in this system are the first example of large-amplitude OH^- autocatalytic oscillations, which run from pH 7 to 10, and are inverted compared to the usual H^+ regulated oscillations.

These results present new possibilities in the design of biocompatible pH oscillators. Interest in this reaction is therefore many fold, not only does it provide the first experimental example of a new design algorithm for pH oscillators, it opens

up possibilities for nonlinear kinetics in organic chemistry as the majority of oscillating chemical reactions presently utilise inorganic reagents. Moreover, gluconolactone itself is produced during the enzymatic oxidation of glucose, a reaction which is widely exploited in biotechnology for the detection for glucose (9). This presents the possibility of having an enzymatic negative feedback step in the MGSG reaction. The reaction displays the unique feature of large amplitude oscillations in hydroxide ion accompanied by small amplitude (10^{-3} V) oscillations in potential, indicating that it is not driven by redox processes and therefore creating a less aggressive pH oscillator. Conventional redox pH oscillators contain strong oxidising agents such as bromate, iodate or chlorate. These species are powerful oxidising agents and attack other components of the system, such as pH sensitive gels or switches.

4.5.1 Experimental

Three stock solutions were prepared in doubly distilled de-ionised water: methylene glycol, sulfite/bisulfite buffer and gluconolactone. The solution of methylene glycol was prepared with diluting 37% formalin solution (Aldrich) one day in advance to allow complete de-polymerization. The buffer solution of sodium sulfite and metabisulfite was freshly prepared daily from reagent grade Na_2SO_3 and $Na_2S_2O_5$ (Aldrich) and bubbled with nitrogen to prevent aerial oxidation. The gluconolactone solution was also prepared freshly from reagent grade D-gluconic acid lactone (Aldrich), and used either immediately or at the recorded time, post dissolution of the solid.

Reactions were performed in a 50 ml water jacketed cylindrical shaped glass reactor. The pH was measured by a calibrated combination pH electrode (METTLER TOLEDO) and a HANNA pH meter connected to a computer. The electrode

potential measurements were carried out with a combination redox electrode and KEITHLEY 2000 multimeter also connected to a PC. The temperature was kept constant at 20 ^{0}C with a HAAKE thermostat. The reactor was stirred by an IKA magnetic stirrer and the stirring rate was kept at 400 rpm in all experiments.

The batch (closed) experiments were started upon addition of the gluconolactone and methylene glycol stock solutions ($[X]_s$) simultaneously to the sodium/ bisulfite buffer solution. The concentrations reported, $[X]_0$, are the calculated initial concentrations in the reactor before the reaction takes place (i.e. $[X]_0 = [X]_s/ 3$).

In open (flow) experiments the three stock solutions were pumped into the reactor by a GILSON peristaltic pump. The flow rate was increased from high to low values with the reactor filled initially with reactant solution or decreased from high to low values with the reactor initially filled with water. The latter situation ensured the low pH state was accessible from high flow rates when the system was bistable.

4.5.2 Numerical modelling

Simulations of the reaction were performed using the following model, steps 4.8-4.17. The rate equations for the various species were constructed from the elementary rate laws shown in appendix III. The rate constants were taken from the literature or adjusted in this work. The methylene glycol reaction, steps 4.8- 4.15, has been previously investigated (3). To these reactions, steps 4.16 and 4.17 are added with previously reported rate constants (10). Reactions 4.8 and 4.16 are base or acid catalysed depending on the conditions. The acid catalysis channel is not significant in this work, and so is omitted for simplicity. Inclusion of the acid catalysis to the rate law makes no difference to the observed behaviour. Numerical simulation of the resulting rate equations was performed using package XPPAUT. The method of

integration was CVODE with, typically, a time step of 0.01. For flow reactions, the rate equations were augmented with terms of the form $k_0([X_0]- [X])$ where X is the species of interest, and k_0 is the flow rate. The inflow concentrations were determined from $[X]_s/ 3$, where $[X]_s$ is the stock concentration of species X. The decay of the gluconolactone stock solution is modelled by reactions 4.16 and 4.17 to give the following rate equations.

$$\frac{d[\mathrm{GL}]_s}{dt} = -(k_{4.16} + k_{4.16\mathrm{OH}}[\mathrm{OH}^-]_s)[\mathrm{GL}]_s + k_{-4.16}[\mathrm{GA}]_s$$

$$\frac{d[\mathrm{GA}]_s}{dt} = (k_{4.16} + k_{4.16\mathrm{OH}}[\mathrm{OH}^-]_s)[\mathrm{GL}]_s - k_{-4.16}[\mathrm{GA}]_s - k_{4.17}[\mathrm{GA}]_s + k_{-4.17}[\mathrm{G}^-]_s[\mathrm{H}^+]_s$$

$$\frac{d[\mathrm{G}^-]_s}{dt} = k_{4.17}[\mathrm{GA}]_s - k_{-4.17}[\mathrm{G}^-]_s[\mathrm{H}^+]_s$$

$$\frac{d[\mathrm{OH}^-]_s}{dt} = k_{4.12} - k_{-4.12}[\mathrm{OH}^-]_s[\mathrm{H}^+]_s$$

$$\frac{d[\mathrm{H}^+]_s}{dt} = k_{4.12} - k_{-4.12}[\mathrm{H}^+]_s[\mathrm{OH}^-]_s + k_{4.17}[\mathrm{GA}]_s - k_{-4.17}[\mathrm{G}^-]_s[\mathrm{H}^+]_s$$

$\mathrm{CH_2(OH_2)} \leftrightarrow \mathrm{CH_2O + H_2O}$	$k_{4.8} = 5.5\times10^{-3}\,\mathrm{s^{-1}}$ $k_{4.8OH} = 500\,\mathrm{M^{-1}s^{-1}}$ * $k_{4.8r} = 10\,\mathrm{s^{-1}}$	(4.8)
$\mathrm{HSO_3^- \leftrightarrow SO_3^{2-} + H^+}$	$k_{4.9} = 3.1\times10^{3}\,\mathrm{s^{-1}}$ $k_{4.9r} = 5\times10^{10}\,\mathrm{M^{-1}s^{-1}}$	(4.9)
$\mathrm{CH_2O + SO_3^{2-} \rightarrow CH_2(O^-)SO_3^-}$	$k_{4.10} = 5.4\times10^{6}\,\mathrm{M^{-1}s^{-1}}$	(4.10)
$\mathrm{CH_2(O^-)SO_3^- + H^+ \leftrightarrow CH_2(OH)SO_3^-}$	$k_{4.11} = 1\times10^{10}\,\mathrm{M^{-1}s^{-1}}$ $k_{4.11r} = 2\times10^{-3}\,\mathrm{s^{-1}}$	(4.11)

$H_2O \leftrightarrow H^+ + OH^-$	$k_{4.12} = 1\times10^{-3}\,Ms^{-1}$ $k_{4.12r} = 1\times10^{11}\,M^{-1}s^{-1}$	(4.12)
$CH_2O + HSO_3^- \rightarrow CH_2(OH)SO_3^-$	$k_{4.13} = 4.5\times10^{2}\,M^{-1}s^{-1}$	(4.13)
$CH_2(OH)_2 + SO_3^{2-} \rightarrow CH_2(O^-)SO_3^- + H_2O$	$k_{4.14} = 1.2M^{-1}s^{-1}$ *	(4.14)
$CH_2(OH)_2 + HSO_3^- \rightarrow CH_2(OH)SO_3^- + H_2O$	$k_{4.15} = 0.1M^{-1}s^{-1}$ *	(4.15)
$GL \leftrightarrow GA$	$k_{4.16} = 8\times10^{-4}\,s^{-1}$ $k_{4.16OH} = 2000M^{-1}s^{-1}$ * $k_{4.16r} = 1.6\times10^{-4}\,s^{-1}$	(4.16) (10)
$GA \leftrightarrow G^- + H^+$	$k_{4.17} = 2.5\times10^{2}\,s^{-1}$ $k_{4.17r} = 1\times10^{6}\,M^{-1}s^{-1}$	(4.17) (10)

Table 4.2 Kinetic mechanism with rate constants for the methylene glycol- sulfite-gluconolactone reaction where GL = gluconolactone, GA = gluconic acid and G^- = gluconate ion. * signifies rate constants adjusted in this work, see page 127 for discussion.

4.5.3 Results- Experiments

Typical batch pH time traces are shown for the MGSG reaction in Figure 4.8. The trace shows a single peak indicative of positive feedback (rapid transition to high pH) coupled with delayed negative feedback (decay to low pH).

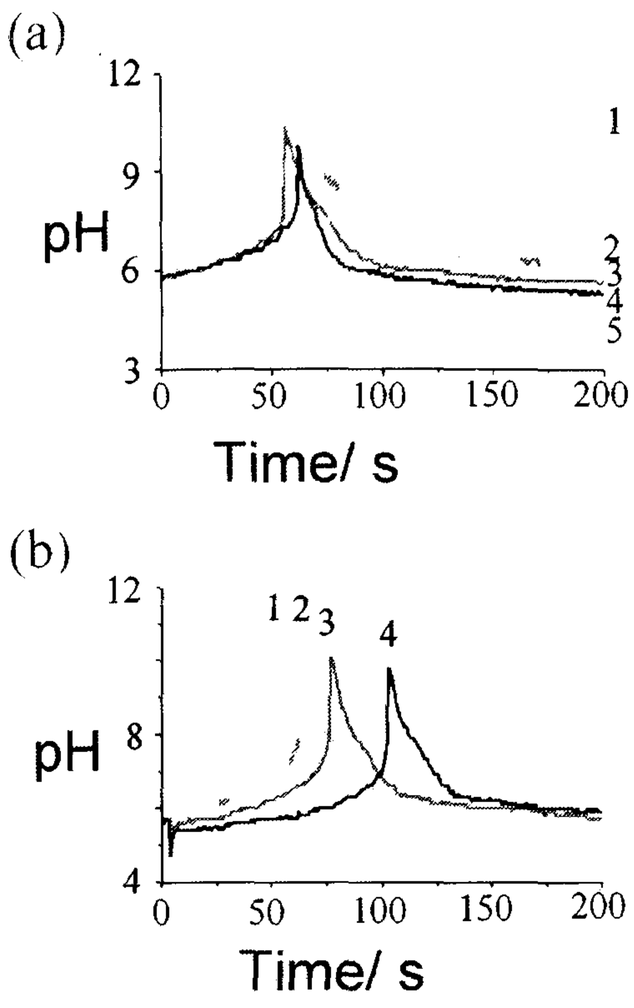

Figure 4.8 Batch (closed) MGSG reactions with initial concentrations of $[CH_2(OH)_2]_0$ = 0.1 M, $[SO_3^{2-}]_0$ = 0.005 M, $[HSO_3^-]_0$ = 0.05M. (a) initial gluconolactone concentrations $[GL]_0$: 1 = 0.003 M, 2 = 0.004 M, 3 = 0.005, M 4 = 0.017 M, 5 = 0.022 M. (b) The pH –time curves with $[GL]_0$ = 0.0067 M and age of the GL stock solution t_{age}: 1 = 0 s (300 s), 2 = 3600 s, 3 = 5400 s, 4 = 7200 s.

Experimental bifurcation diagrams of the pH as a function of flow rate were obtained by increasing the flow rate step wise at regular time intervals. The minimum increment of flow rate was 1×10^{-4} s^{-1}. A typical bifurcation diagram is shown in Figure 4.9 for relatively low concentrations of $[GL]_0$. There is a particularly large region of bistability between a high pH (~11) and lower pH (~7).

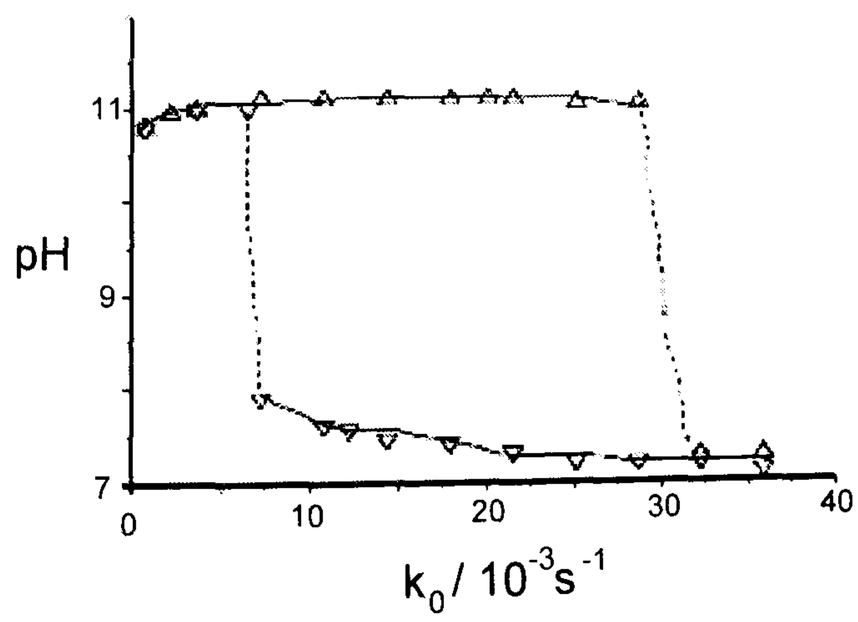

Figure 4.9 Bistability in the MGSG reaction. $[CH_2(OH)_2]_0$ = 0.1 M, $[HSO_3^-]_0$ = 0.05 M, $[SO_3^{2-}]$ = 0.0047 M, $[GL]_0$ = 0.003 M. Δ – steady state with increasing flow rate, ∇ - steady state with decreasing flow rate.

Oscillations are observed for k_0 = 4.5 - 5.4 × 10^{-3} s^{-1} with $[GL]_0$ = 0.008 M (Figure 4.10). The range of flow rates for which oscillatory behaviour is observed is slightly shifted when the flow rate is decreased from a high value rather than increased from a low value. The oscillations grow in amplitude with increasing flow rate and disappear abruptly for a supercritical flow rate. The inset shows the oscillations in potential accompanying the maximum amplitude oscillations in pH are of the order of 5 mV.

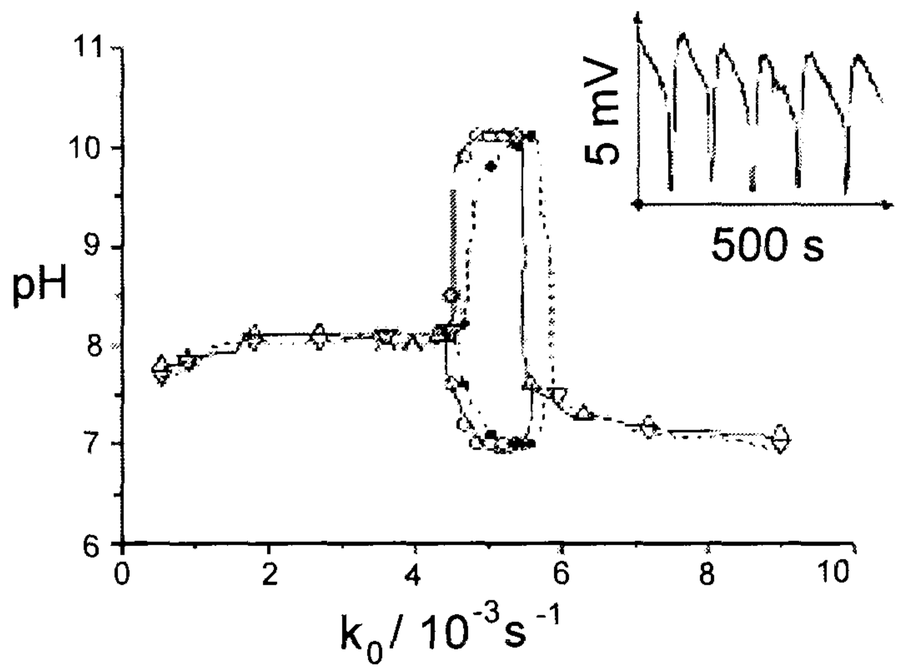

Figure 4.10 Bifurcation diagram in the MGSG reaction in a flow reactor with inflow concentrations $[CH_2(OH)_2]_0$ = 0.1 M, $[HSO_3^-]_0$ = 0.05M, $[SO_3^{2-}]_0$ = 0.0047 M, . $[GL]_0$ = 0.008 M, o = oscillations with increasing flow rate, k_0, • - oscillations with decreasing k_0, Δ - steady state with increasing k_0, ∇ - steady state with decreasing k_0. The inset shows the small amplitude oscillations in potential for k_0 = 5.4 × 10^{-3} s^{-1}.

Figure 4.11 shows examples of the pH oscillations obtained when the MGSG reaction is performed in an open reactor. With the flow rate fixed, there is an induction period before the appearance of oscillations that depends on the concentrations of the reactants. The oscillations increase in amplitude and period with increasing flow rate. Typical examples of pH oscillations are shown in Figure 4.11(a) – (c) where the flow rate is increased from 5.0 × 10^{-3} s^{-1} to 5.4 × 10^{-3} s^{-1} for

$[GL]_0$ = 0.0067 M. The oscillatory amplitude reaches a maximum of three pH units which can be sustained over 10^3 s without dampening, despite the decay of the gluconolactone concentration in the stock solution (Figure 4.11(d)).

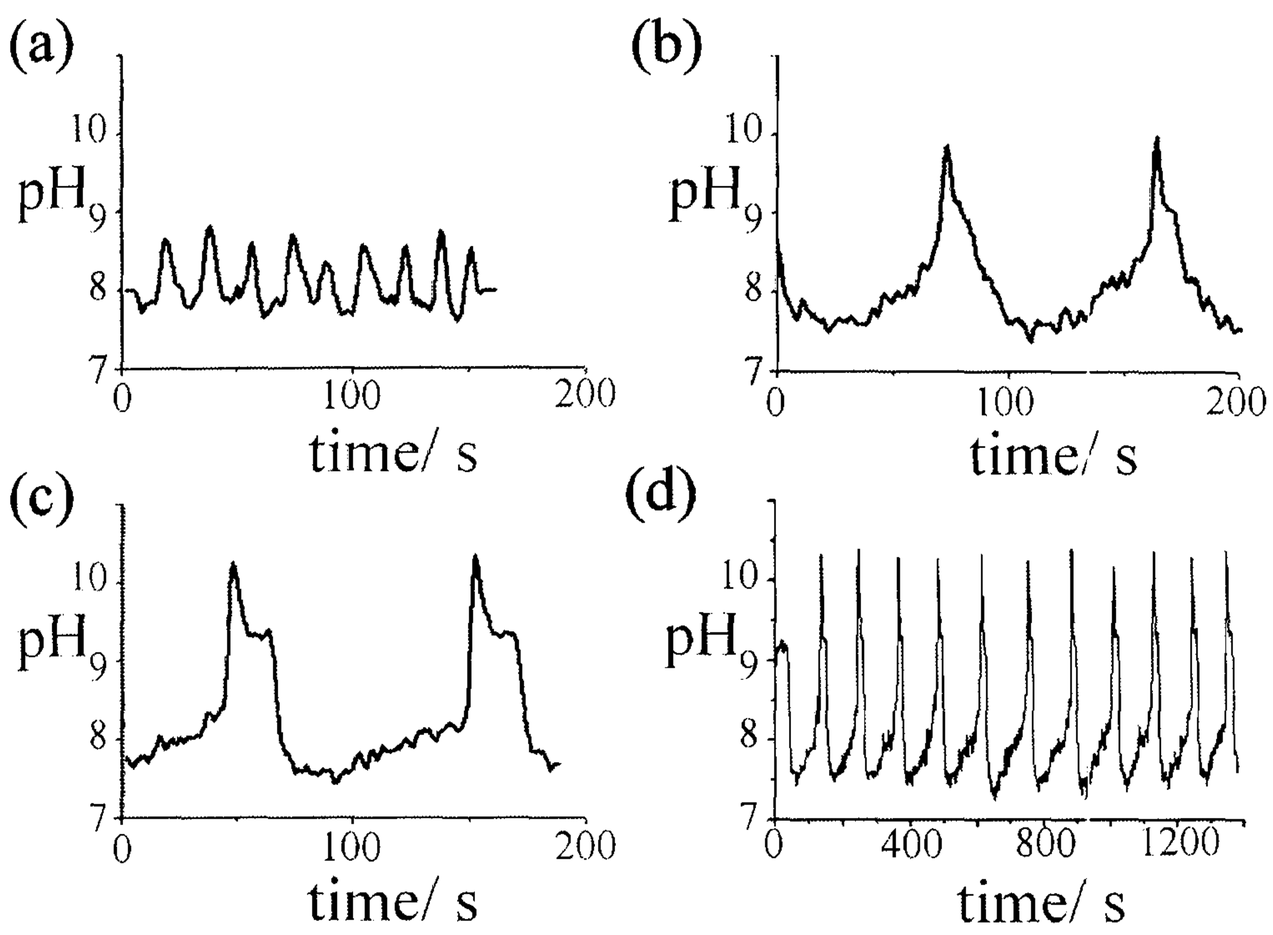

Figure 4.11 Oscillations in a flow reactor with inflow concentrations of $[CH_2(OH)_2]_0$ = 0.1 M, $[HSO_3^-]_0$ = 0.05M, $[SO_3^{2-}]_0$ = 0.005 M, $[GL]_0$ = 0.0067 M and flow rate k_0 = (a) 5.0×10^{-3} s^{-1}; (b) 5.2×10^{-3} s^{-1}; (c) and (d) 5.4×10^{-3} s^{-1}.

The MGSG reaction displays a typical cross shaped phase diagram as a function of the inflow concentration of the inhibitor species, $[GL]_0$, and the flow rate (Figure 4.12 (a)). At low concentrations of inhibitor there is a region of bistability which separates the low and high pH steady states. On increasing the inflow concentration of $[GL]_0$ the region of bistability shrinks and gives rise to a region of oscillations. The oscillations are observed for a range of $[GL]_0$ = 0.005 - 0.023 M and for a reasonable range of flow rates. The system also displays a cross-shaped phase diagram with variation of the ratio of bisulfite to sulfite (b/c) and flow rate (Figure 4.12(b)) Experimentally this is achieved by maintaining a constant value of $[HSO_3^-]_0$

and decreasing the inflow concentration of sulfite in to the reactor. Oscillations are observed for b/c = 7 – 16.

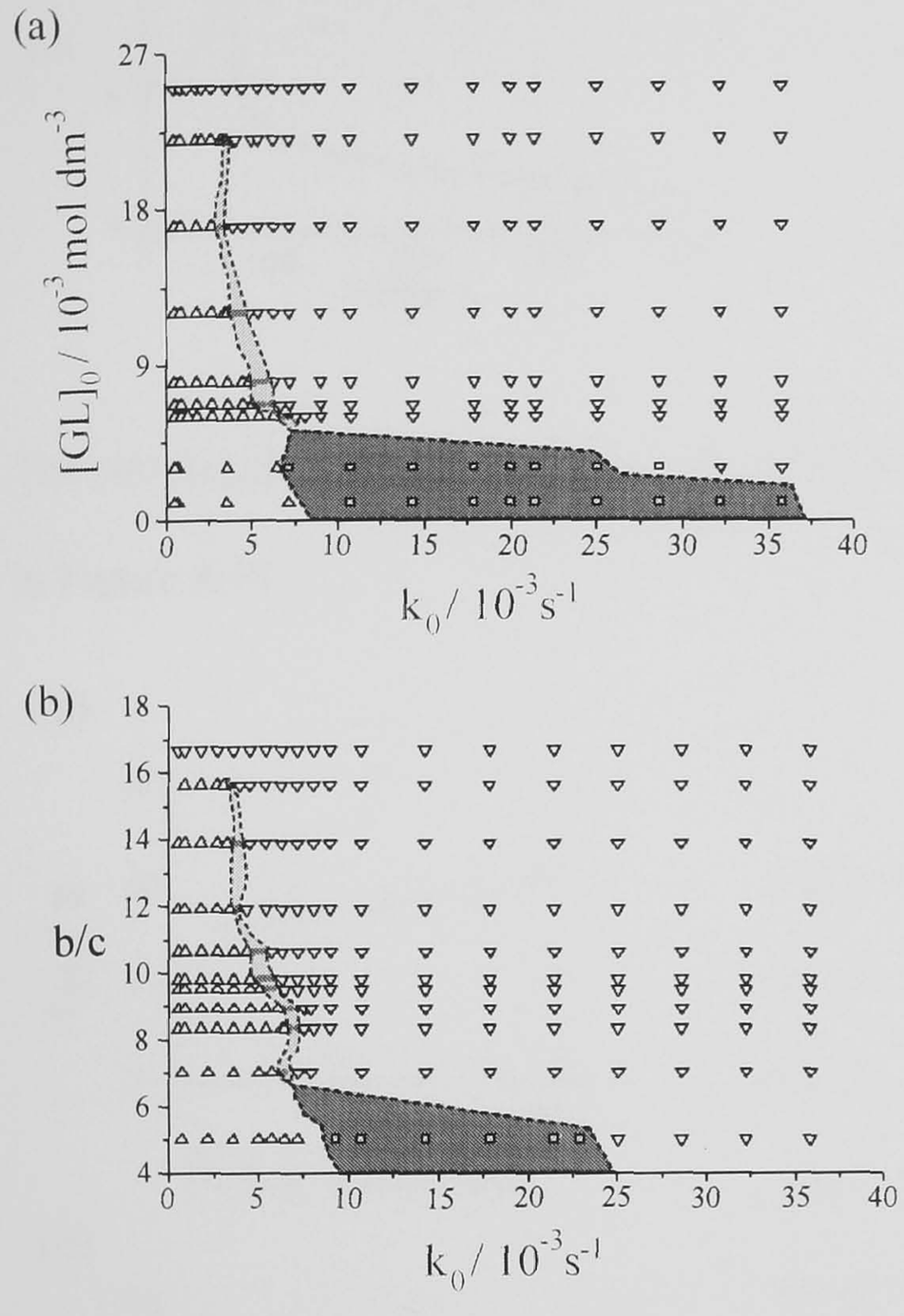

Figure 4.12 Phase diagrams in the MGSG reaction in a flow reactor with inflow concentrations $[CH_2(OH)_2]_0$ = 0.1 M, $[HSO_3^-]_0$ = 0.05M where • (light grey region) - oscillatory state, dark grey region- bistability, Δ - high pH steady state, ∇ - low pH steady state (a) $[GL]_0$ - k_0 parameter plane, $[SO_3^{2-}]_0$ = 0.005 M. (b) Bisulfite/ sulfite (b/c) – k_0 parameter plane, $[GL]_0$ = 0.008 M.

4.5.4 Results- Numerical Modelling

The essential features of the system are reproduced in numerical simulations using the kinetic model consisting of steps 4.8- 4.17. Numerical integration of the resulting ODEs in batch conditions gives rise to a single peak in pH (Figure 4.13).

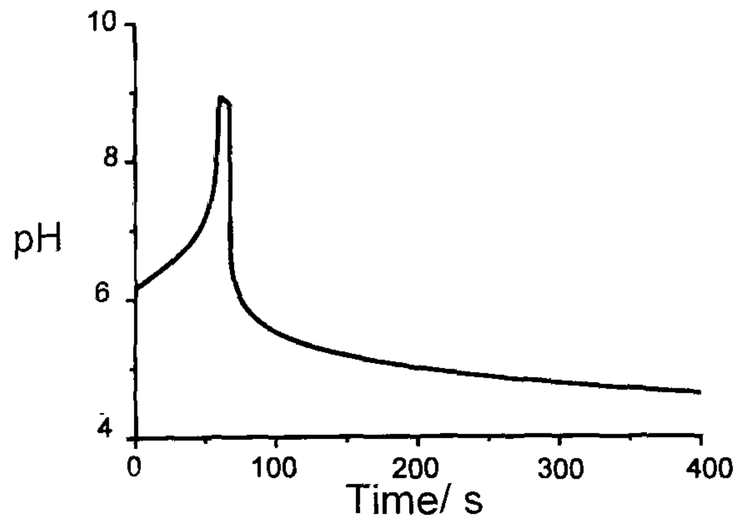

Figure 4.13 Numerical pH time trace for MGSG reaction in a closed system $[CH_2(OH)_2]_0$ = 0.1 M, $[HSO_3^-]_0$ = 0.05 M. $[SO_3^{2-}]$ = 0.005 M, $[GL]_0$ = 0.019 M (t_{age} = 300 s).

The simulated induction times match experimental results reasonably well. as shown in Figure 4.14.

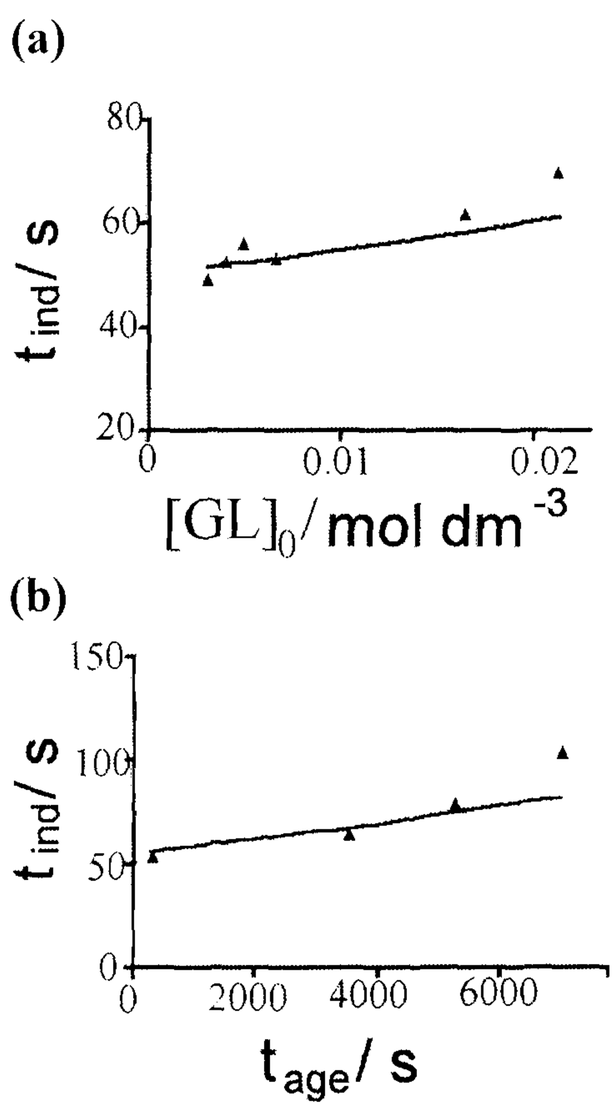

Figure 4.14 Batch (closed) MGSG reactions with initial concentrations of $[CH_2(OH)_2]_0$ = 0.1 M, $[SO_3^{2-}]_0$ = 0.005 M, $[HSO_3^-]_0$ = 0.05 M .Experimental data (▲) compared to numerical simulations (solid lines) (a) Variation of induction time with $[GL]_0$, t_{age} = 300 s (b) Variation of induction time with age of gluconolactone stock solution, $[GL]_0$ = 0.0067 M.

Figure 4.15 (a) and (b) show numerically calculated bifurcation diagrams under flow conditions for two different values of $[GL]_0$. These diagrams were produced by increasing/ decreasing the flow rate stepwise at 300 s intervals.

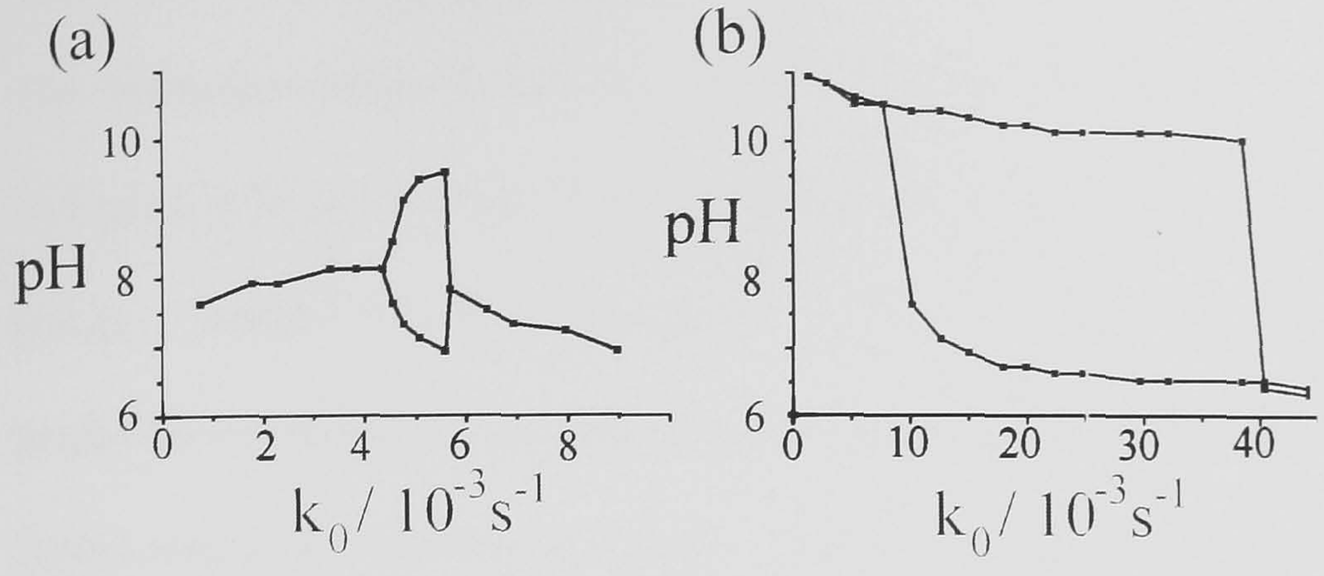

Figure 4.15 Simulations of the MGSG reaction in a flow reactor with inflow concentrations $[CH_2(OH)_2]_0$ = 0.1 M, $[HSO_3^-]_0$ = 0.05 M, $[SO_3^{2-}]$ = 0.005 M (a) oscillations for $[GL]_0$ = 0.008 M (b) bistability for $[GL]_0$ = 0.003 M

Bistability is observed between the high and low pH steady states when $[GL]_0$ = 0.003 M. For $[GL]_0$ = 0.008 M, oscillations emerge via a supercritical Hopf bifurcation at $k_0 = 4.7 \times 10^{-3}$ s^{-1} and grow in amplitude with increasing flow rate, disappearing at $k_0 = 6.0 \times 10^{-3}$ s^{-1}. Figure 4.16 shows examples of the numerically simulated oscillations.

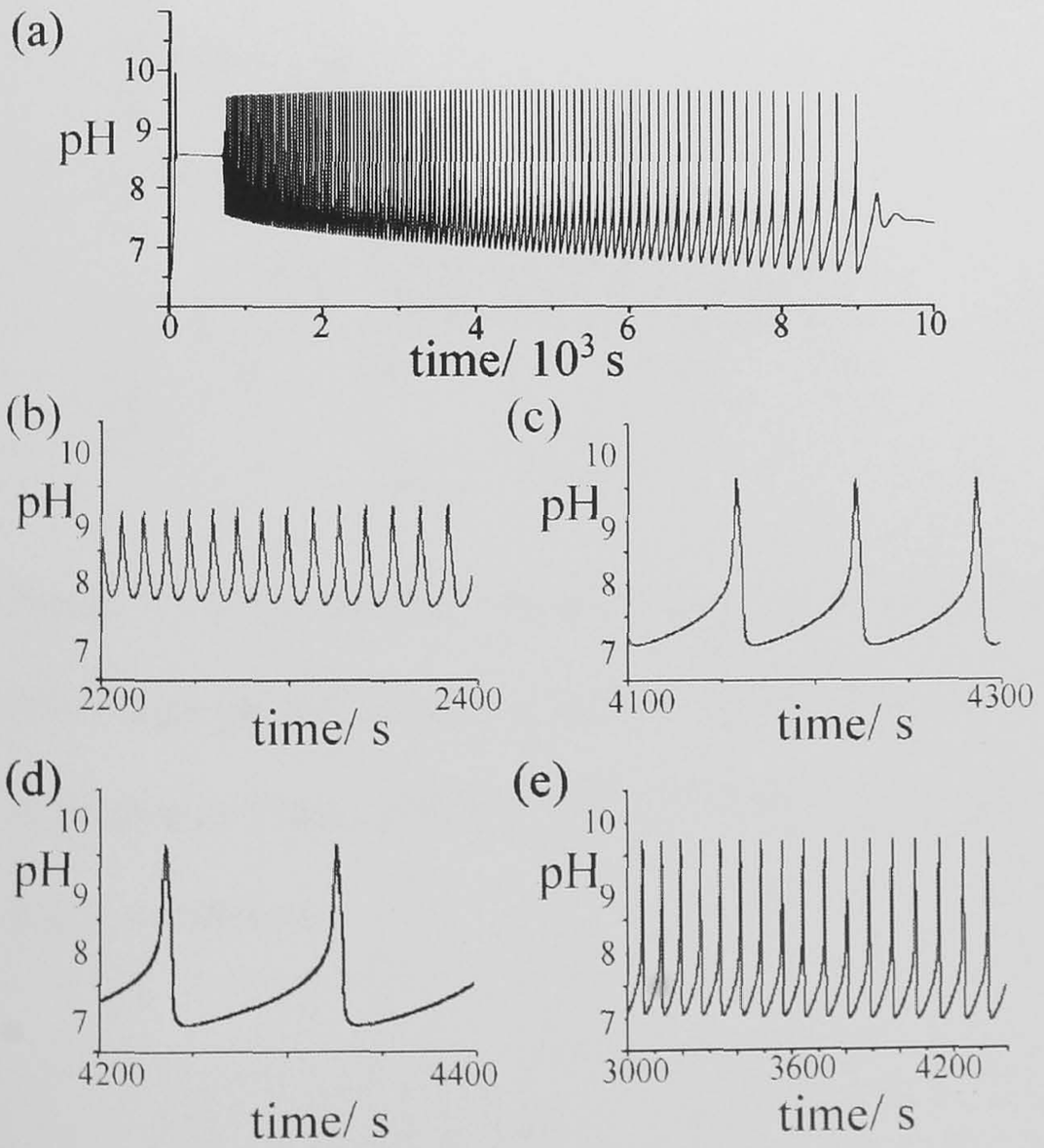

Figure 4.16 Simulated pH oscillations of the MGSG reaction in a flow reactor with $[CH_2(OH)_2]_0$ = 0.1 M, $[SO_3^{2-}]_0$ = 0.005 M, $[HSO_3^-]_0$ = 0.05M, (a) $[GL]_0$ = 0.0067 M and flow rate fixed from t = 0 at 5.3 $\times 10^{-3}$ s^{-1} (b) increased from k_0 = 0 at t = 0 s to $k_0 = 5.0 \times 10^{-3}$ s^{-1}; (c) increased from k_0 = 0 at t = 0 s to 5.2 $\times 10^{-3}$ s^{-1}; (d) and (e)

increased from $k_0 = 0$ at $t = 0$ s to $k_0 = 5.4 \times 10^{-3}$ s^{-1}.

The induction period before the onset of oscillations depends on the concentrations. In Figure 4.16 (a) the flow rate is fixed at $k_0 = 5.3 \times 10^{-3}$ s^{-1} with initial conditions of $[GL]_0 = 0.0067$ M and oscillations emerge at ~1000 s. The oscillations increase gradually in amplitude and period with ageing of the gluconolactone stock solution. Small amplitude oscillations emerge when the flow rate is increased step wise in 300 s intervals from 1.0×10^{-3} to 5.0×10^{-3} s^{-1} (4.16(b)). The amplitude and period of the oscillations increases with increasing flow rate. The large amplitude oscillations do not significantly change form over 10^3 s (Figure 4.16(c)).

Numerical phase diagrams in the $[GL]_0 - k_0$ and b/c – k_0 phase plane are shown in Figures 4.17(a) and (b) respectively. These diagrams are constructed from the relevant bifurcation diagrams. Oscillations are observed for $[GL]_0 = 0.005 - 0.012$ M and b/c = 6- 16.

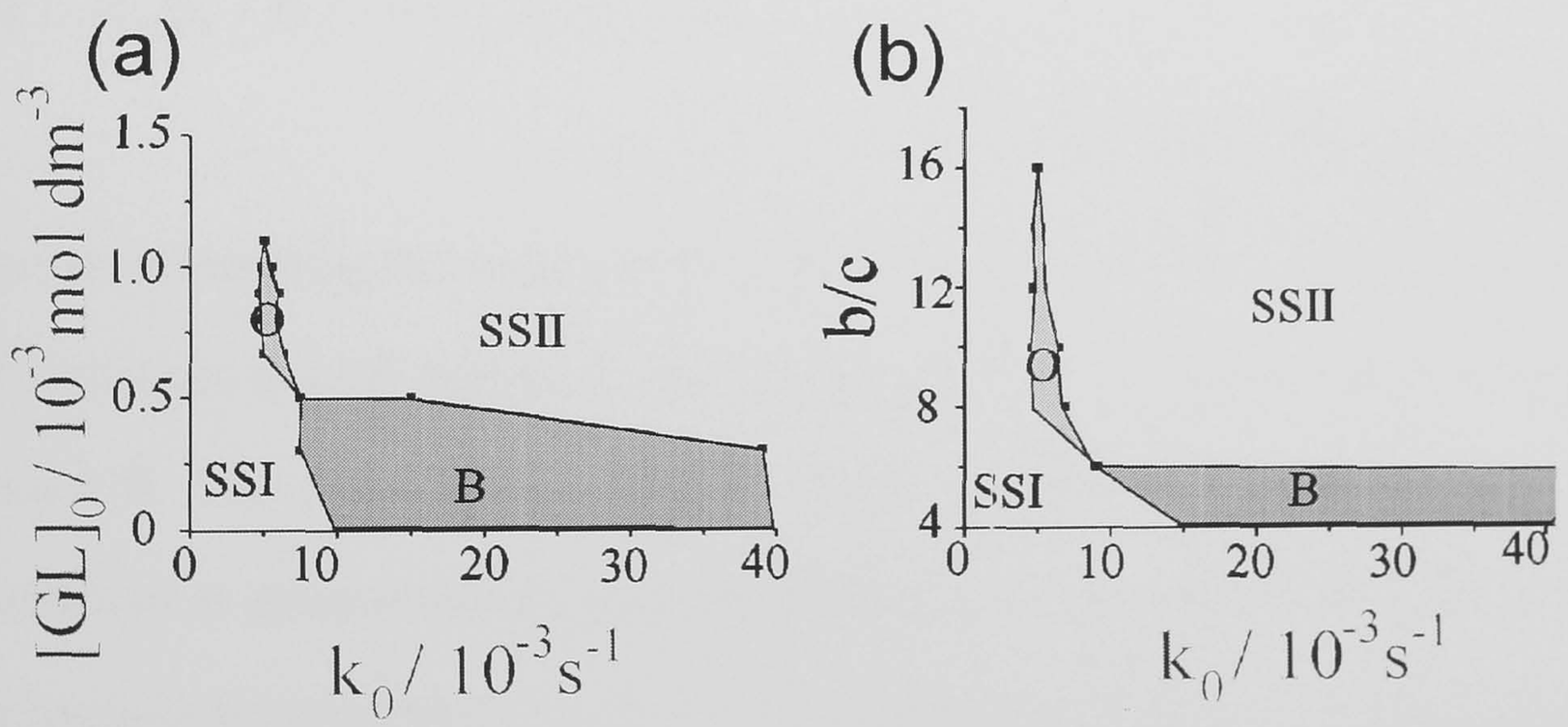

Figure 4.17 Numerically calculated phase diagrams for the MGSG reaction. B = bistability, SSI = high pH steady state, SSII = lower pH steady state, O = Oscillations in the (a) $[GL]_0 - k_0$ parameter plane, $[HSO_3^-] = 0.05$ M, $[SO_3^{2-}]_0 = 0.005$ and the (b) b/c – k_0 parameter plane $[GL]_0 = 0.008$ M.

4.5.5 Discussion- the MGSG reaction

The reaction of methylene glycol with bisulfite/ sulfite buffer in batch initially involves consumption of the buffer. The pH rises slowly during the induction period as the H^+ is consumed through reaction with $CH_2(O^-)SO_3^-$ is replenished by dissociation of HSO_3^-. The pH rises rapidly when HSO_3^- is consumed and $CH_2(O^-)$ abstracts protons from H_2O, producing OH^-. The complex behaviour in flow is explained by the base-catalysed dehydration of the rate determining step, and production of OH^- in the overall reaction.

(A) $2CH_2(OH)_2 + HSO_3^- + SO_3^{2-} \rightleftharpoons 2CH_2(OH)SO_3^- + H_2O + OH^-$

$$v_{4.8} = (k_{4.8} + k_{OH}[OH^-])[CH_2(OH)_2]$$

Coupling the MGS reaction with the hydrolysis of gluconolactone (10) produces a peak in the pH as this reaction produces acid.

(B) $C_6H_{10}O_6 + H_2O \rightleftharpoons C_6H_{11}O_7^- + H^+$

$$v_{4.16} = (k_{4.16} + k_{OH}[OH^-])[C_6H_{10}O_6]$$

The rate-determining step in process B is also base-catalysed. As the concentration of OH^- increases through process A, the rate of production of acid increases through process B. This provides the necessary delayed negative feedback necessary for oscillations in an open system. In closed reactors there is a single peak in pH as all the reactants are consumed.

The gluconolactone hydrolysis (process B) begins upon dissolution of the solid. It is important to consider the effect of the decay of this stock solution on the clock time and oscillations. It is shown that the clock time increases with age of stock solution and increasing $[GL]_0$. This can be explained by the initial decay of the stock solution before its addition to the other reactants. The rate of decay of the stock

concentration increases with $[GL]_0$. The additional acid produced in the gluconolactone stock solution maintains the buffer for longer in the full MGSG system in batch. Numerical simulations are able to reproduce these results by including the decay of the gluconolactone stock solution. The clock time is sensitive to the rates of reactions 4.14 and 4.15, therefore these rates are optimised in modeling of this system to give best match between experimental and numerical results.

An induction time before the appearance of oscillations is observed in both experimental and numerical studies. The decay of gluconolactone is very slow at low values of $[GL]_s$ and oscillations are maintained virtually without any change in form, period or amplitude over a time scale of 10^3 s. The shape of the oscillations depends on the rate constants for OH^- catalysis. Again, these values have been adjusted to provide the best match between experimental and numerical results in this system.

The experimental and numerical bifurcation diagrams match well. The reaction displays bistability for low $[GL]_0$ and b/c, and oscillations for higher values. The expected cross shaped phase diagram is observed experimentally and numerically, as a function of the inhibitor concentration, $[GL]_0$. A cross shaped diagram is also observed in the b/c- k_0 phase plane. Increasing this ratio increases the clock time in batch, as the rate of reaction 4.10 is reduced. At higher b/c, the inhibitive process, i.e. the production of acid from GL, can therefore dominate.

4.6 Conclusion

The large amplitude pH oscillations (pH ~7- 10) seen experimentally and numerically in the MGSG reaction show that the combination of a base producing reaction with a base-catalysed rate determining step (dehydration of methylene glycol) with a base-catalysed reaction that produces acid (hydrolysis of

gluconolactone) can be used to create a pH oscillator. The dehydration and hydrolysis processes in this system are both additionally acid-catalysed. and although not important in this work provide scope for significant advancements in the development of pH oscillators. Many such processes display similar acid base catalysis and it is therefore expected that it will be possible to find an acid producing acid-catalysed reaction to couple with a base producing acid-catalysed to produce a system capable of displaying large amplitude pH oscillations. Although the bisulfite-sulfite buffer, with a pK_a of 7.2, is an important feature of the MGSG reaction it has been demonstrated that oscillations can arise, providing the rate constant of the rate determining step is small enough such that a clock reaction is observed in batch. These experiments therefore provide new possibilities in the design of pH oscillators.

4.7 References

(1) R McIlwaine, K Kovacs. SK Scott. A Taylor: A novel route to pH oscillators. Chem. Phys. Lett. 417 (2006) 39.

(2) K Kovacs, R McIlwaine, SK Scott, A Taylor: An Organic based pH oscillator. J. Phys. Chem., A. Lett 111 (2007) 549.

(3) K Kovacs, R McIlwaine, K Gannon, S Scott, A Taylor: Complex behaviour in the Formaldehyde- Sulfite reaction. Journal of Physical Chemistry A 109 (2005) 283.

(4) LH Funderbunk, L Aldwin, W Jencks: J. Am. Chem. Soc. 100 (1978) 5444.

(5) http://www.math.pitt.edu/~bard/xpp/xpp.html.

(6) SK Scott: Chemical Chaos, Oxford, 1994.

(7) P Guthrie: Journal of the American Chemical Society 122 (2000) 357.

(8) J Winkleman, M Ottens, AA Beenackers: The Kinetics of the Dehydration of Methylene Glycol. Chemical Engineering Science 55 (2000) 2065.

(9) AP Dhanarajan, GP Misra, RA Siegel: Journal of Physical Chemistry A 106 (2002) 8835.

(10) Y Pocker, E Grenn: Journal of the American Chemical Society 95 (1973) 113.

CHAPTER 5

Acid Autocatalysis in Microemulsions

5.1 Introduction

Reverse micelles present a unique environment for carrying out a variety of chemical and biochemical reactions. Reverse micelles, commonly referred to as water-in-oil microemulsions (w/o μE), have been used as a model for studying various reactions in confinement (1). In biochemistry, w/o μE have been widely studied as water trapped in such aggregates is thought to mimic water surrounding biological membranes or proteins (2). The ability to study effects of compartmentalization of reactants and reduced activity of the water pool on reaction kinetics provides a simplified model for reactions in biological cells. Thus enzyme reactions have been performed in this environment (3).

Under certain conditions, an enhanced reaction rate is observed (4) thus making w/o microemulsions attractive in biotechnology applications (5). They have also been exploited due to their ability to solubilise enzymes (6,7). Despite their simplicity, they provide an excellent method to study the fundamental effects of compartmentalization.

The components for a chemical reaction can be incorporated into two separate water-in-oil microemulsions; upon mixing, reaction proceeds at a rate determined by the chemical kinetics in the nano-sized droplet and intermicellar exchange processes. Commercially, reverse micelles represent an excellent medium for the synthesis of nano-particles with uniform morphologies (8). These 'nano-reactors' are used for the synthesis of nano-particles (9), nano-cluster synthesis (10), (9), molecular separations and biochemical catalysis. Reverse micelles have also been used in drug delivery (11,12) catalysis and materials development (13).

Reverse micelles (microemulsions) consist of nanometer-sized polar cores dispersed in an apolar solvent. Water (and polar species) is readily solubilised in the

polar core forming the 'water pool', characterized by w_0 the ratio $[H_2O]$ / [SURFACTANT]. Reverse micelles can exchange their contents in the water cores via both fusion and redispersion processes. The kinetics of reactions are sharply influenced by the microenvironment of reactants. Nonlinear, autocatalytic reactions are particularly sensitive to their environment and oscillatory reactions are capable of displaying complex patterns in nano-structured media. The recent experimental discovery of Turing patterns and other exotic phenomena (see Figure 5.1) (14-16) in the Belousov-Zhabontinsky - sodium bis(2-ethylhexly) sulfosuccinate (BZ-AOT) system encouraged us to look at a nonlinear pH system in a reverse micelle configuration.

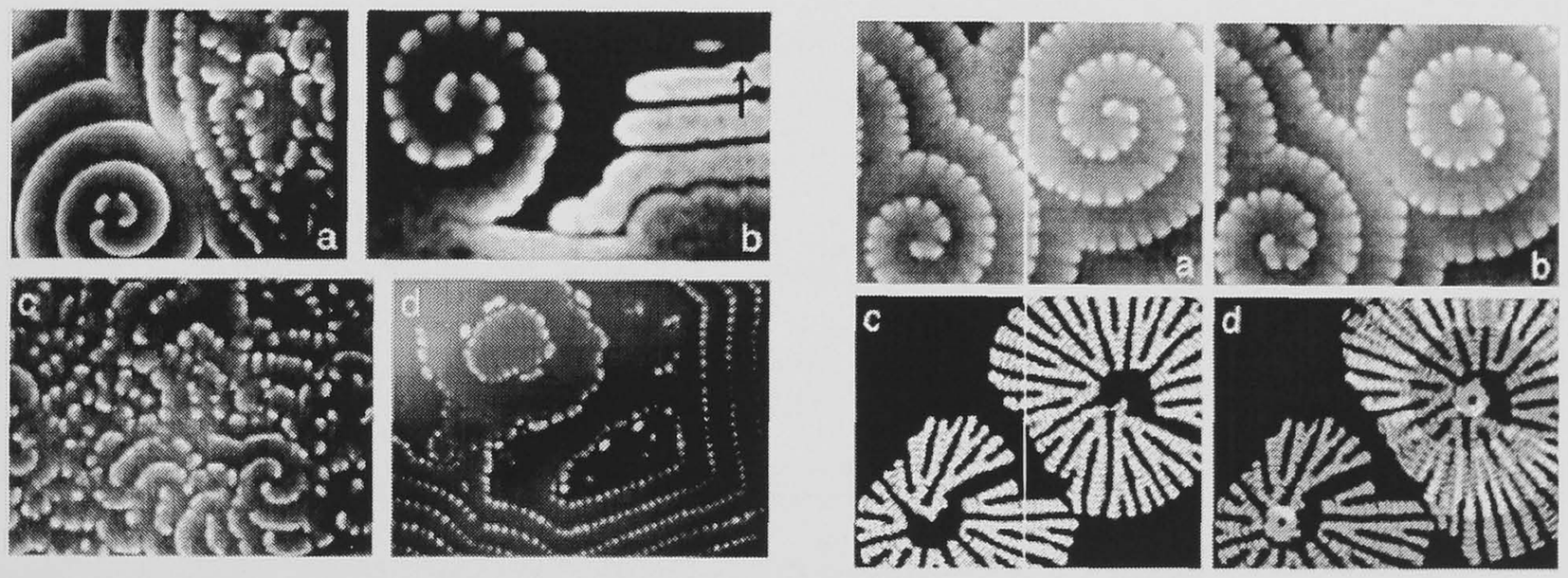

Figure 5.1 Segmented spiral waves in the BZ-AOT system, taken from (17).

The types of patterns generated in the BZ-AOT system are controlled not only by initial concentrations but by the volume droplet fraction (the dispersion of water droplets in the oil phase) of the microemulsion. Figure 5.2 shows the range of behaviour reported as a function of concentration of species and droplet fraction of reverse micelles.

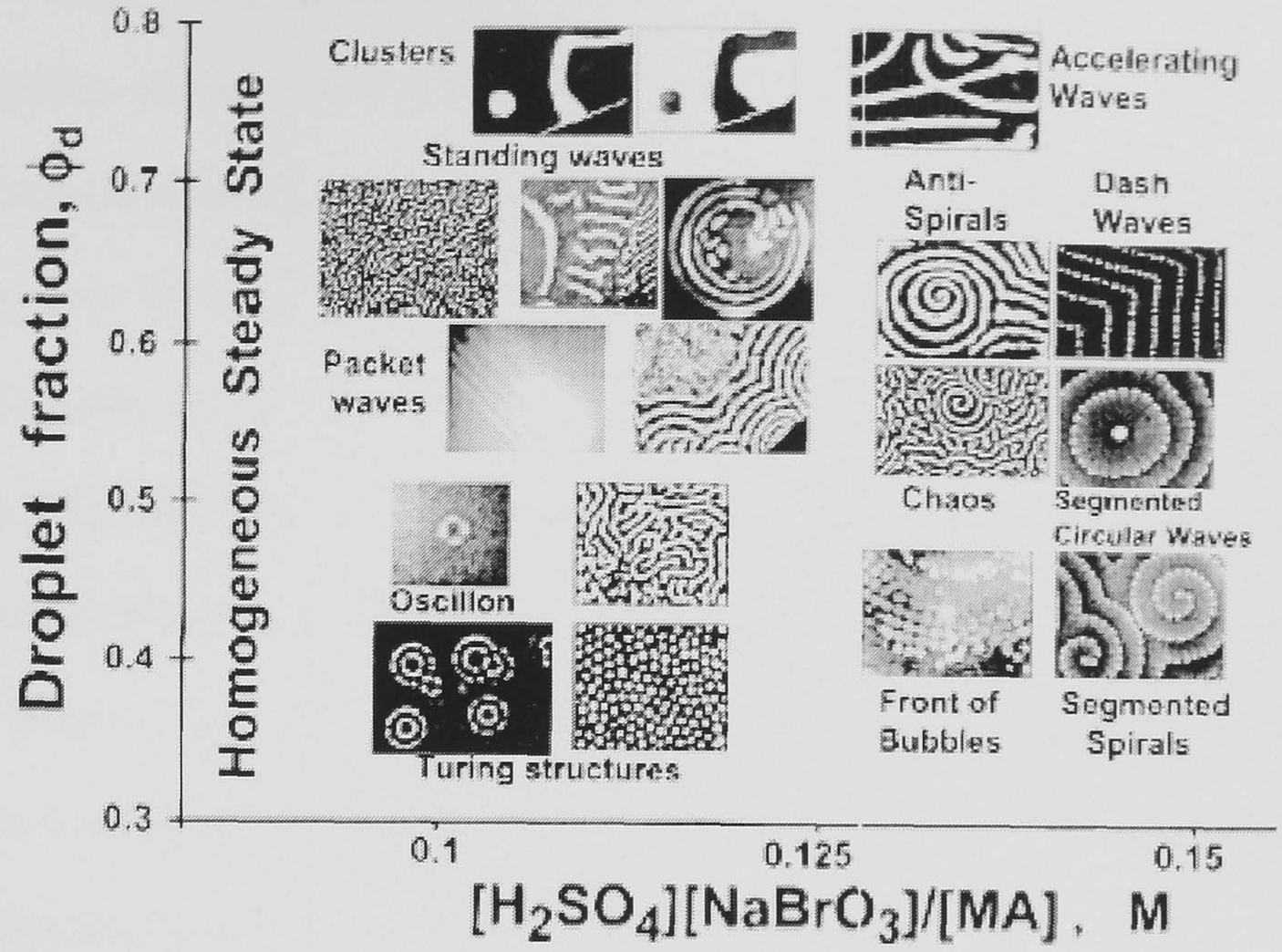

Figure 5.2 Schematic overview of patterns found in the BZ-AOT system (18)

These results display a range of interesting properties that are related to the effect of combining spatial chemical thermodynamic ordering (micellar structure) with ordering of the temporal type (nonlinear chemical reaction) (19). The nature of the water pool and associated pH, ionic concentration and microviscosity in the polar aqueous core of the micelle affects the kinetics of reactions performed in these environments. Studies probing the nature and behaviour of the confined water in these pools are of interest to chemists and life scientists (20).

To date, nonlinear pH reactions have not been performed in water-in-oil microemulsions. Acid autocatalytic reactions display a sudden pH change (clock) in stirred batch reactors and propagating reaction-diffusion fronts in an unstirred reactor, converting the mixture from a high to a low pH. In a water-in-oil μE the major reactants of a typical acid autocatalytic reaction, e.g. the bromate-sulfite reaction, are all ionic and will therefore be partitioned mainly in the aqueous phase. The highly pH-sensitive reaction will depend on the structure and activity of the

aqueous phase, and particularly the effective acid concentration in the μE. Additionally, the reaction is exothermic. Temperature is known to affect the structure of microemulsions (21), thus a feedback between microemulsion structure and reaction may be possible. Almost all studies concerning the dynamics of water in confined nano-spaces have focused on systems containing the anionic surfactant sodium bis(2-ethylhexly) sulfosuccinate (AOT) (20). This is because this system has been well characterized and in known to form mono-disperse reversed micelles with a wide range of sizes. However, the bromate sulfite clock performed in AOT reverse micelles does not display any clock behaviour in batch, as any pH change is buffered by the anionic head groups of the surfactant.

This chapter presents an experimental investigation of the influence of a nonionic/cationic water-in-oil microemulsion (w/o μE) on acid autocatalysis and acid reaction-diffusion fronts in the bromate-sulfite reaction. The bromate-sulfite pH clock reaction is studied in two different ternary μE systems- aqueous phase/ toluene/ non-ionic Triton-X (TX) and aqueous phase/ hexanol/ cationic cetyl trimethylammonium bromide (CTAB). Both these ternary systems are known to form w/o μE in parts of their ternary phase diagram (22,23), (24). Experimental results are presented of the batch, well stirred, acid autocatalytic process performed in the w/o μE. The characteristics of the clock reaction are found to depend on both the water/surfactant ratio (w_0) and the droplet dispersion (ϕ_d) (see section 5.1.1). The maximum rate increases with increasing w_0 in both systems and is greatly suppressed in the TX microemulsion compared to the CTAB w/o μE. The clock times increase with ϕ_d for the Triton-X w/o μE which may be interpreted through the increase in microemulsion viscosity with ϕ_d. A distribution of reaction times is observed in the CTAB w/o μE.

The unstirred w/o μEs support reaction-diffusion pH fronts for certain initial compositions. The speed of the reaction diffusion fronts depends on the composition of the w/o μE and is slower than that of equivalent fronts in the aqueous phase. Both unstirred w/o μEs display features common to systems with convective instabilities. The acid front in the CTAB system is particularly sensitive to the microemulsion environment, and gives rise to interesting front structures which may be associated with changes in micro structure. Thus, the reaction and front propagation are affected by the underlying microheterogeneity of the medium.

5.1.1 Microemulsions

Microemulsions are transparent, isotropic mixtures of oil, water and surfactant. For certain ratios of the three components, the mixture self-organizes to form reverse (inverted) micelles, w/o μE. These thermodynamically stable nanostructures (25) consist of micro-droplets of highly structured polar phase (aqueous components) that are stabilized by a layer of surfactant molecules from the continuous oil phase (26). W/o μE are easily distinguishable from emulsions. The droplet size of the dispersed phase in an emulsion is generally greater than 200 nm, resulting in an opaque solution. W/o μEs normally have a droplet diameter of 100 nm or less and are thus smaller than the wavelength of visible light, therefore transparent. Figure 5.3 illustrates a schematic ternary phase diagram for a water/ oil/ surfactant system.

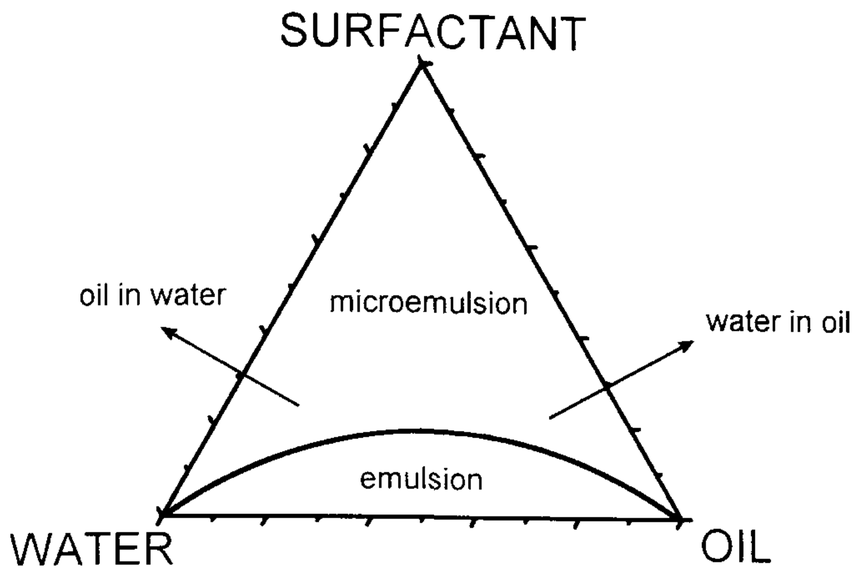

Figure 5.3 Schematic ternary phase diagram for aqueous phase – surfactant – organic oil phase ternary system.

The three components composing the system are each found at an apex of the triangle, where their corresponding volume fraction is 100%. Moving away from that corner reduces the volume fraction of that specific component and increases the volume fraction of one or both of the two other components. Each point within the triangle represents a possible composition of a mixture of the three components which may consist of one, two or three phases. These points combine to form regions with boundaries between them, which represent the 'phase behavior' of the system at constant temperature, pressure and ionic strength. Each phase can be characterized by conductance, viscosity and optical examination.

When a small amount of polar solvent is added to a surfactant/ oil mixture, the reverse micelles swell creating a new confined liquid phase on the inside (27). As more polar solvent is added, the interior pools grow in size and tend to recover the properties of the bulk solvent, normally water. By further addition of the polar solvent, bicontinuous structures and eventually normal micelles are formed (28).

Hydrated reverse micelles are generally referred to as water-in-oil microemulsions (w/o μE). μEs are characterized by two important parameters, the droplet fraction:

$$\varphi_d = (V_{aq} + V_{surf})/ (V_{aq} + V_{surf} + V_{oil})$$

where V_{aq}, V_{surf} and V_{oil} are the volumes of the aqueous, surfactant and oil phase respectively; and the ratio of the water to surfactant concentrations:

$$w_0 = [AQ]/ [SURF]$$

where [AQ] and [SURF] are the concentrations of the aqueous phase and surfactant in the total volume. An increase in the droplet fraction is achieved by decreasing V_{oil}, keeping V_{surf} and V_{aq} constant. An increase in w_0 is achieved by keeping V_{surf} constant, increasing V_{aq} and changing V_{oil} to keep ϕ_d constant. Thus an increase in ϕ_d results in a decrease in the distance between reverse micelles and an increase in the effective concentration of droplets. An increase in w_0 is achieved by keeping V_{aq} constant, decreasing V_{surf} and changing V_{oil} to keep ϕ_d constant. Increasing w_0 is correlated with an increase in the size of the water microdroplets. The activity of water in the water pool increases with increasing w_0.

5.1.2 The Bromate-Sulfite Reaction

The bromate sulfite clock reaction is a prototypical nonlinear pH reaction in which a weak acid (bisulfite) is converted to a strong acid (hydrogen sulfate). This reaction was discussed in detail in chapter 1, section 1.4. The mechanism of the reaction is given as:

$$3HSO_3^- + BrO_3^- \rightarrow 3SO_4^{2-} + Br^- + 3H^+ \qquad (5.1)$$

$$HSO_3^- \rightleftharpoons SO_3^{2-} + H^+ \qquad (5.2)$$

$$HSO_4^- \rightleftharpoons SO_4^{2-} + H^+ \qquad (5.3)$$

$$H_2SO_3 \rightleftharpoons HSO_3^- + H^+ \qquad (5.4)$$

$$3H_2SO_3 + BrO_3^- \rightarrow 3SO_4^{2-} + Br^- + 6H^+ \quad (5.5)$$

$$H_2O \rightleftharpoons H^+ + OH^- \quad (5.6)$$

It is worth noting that in the aqueous phase clock times are reproducible but depend on the stirring rate (decrease with decreasing stirring rate) demonstrating the sensitivity of the reaction to the evolution of a critical acid concentration. The reaction is exothermic but the isothermal density difference between products and reactants is positive. Pojman *et al.* (29) have also demonstrated that the front propagation is sensitive to double-diffusive convective effects when performed in thin tubes.

5.2 Experimental

5.2.1 Materials

Two aqueous stock solutions were freshly prepared daily for use in batch and spatial experiments, using analytical grade chemicals and doubly distilled deionised water. Solution A contained sodium sulfite (Aldrich), sulfuric acid (Aldrich) and bromophenol blue indicator (Ridel de Haen, pKa = 3.4). Solution B contained sodium bromate (Aldrich). A buffer solution (see appendix) of pH = 3 was also prepared using acetic acid (Sigma) and sodium acetate (Sigma) for construction of Figure 5.5. The structure of bromophenol blue is shown in Figure 5.4.

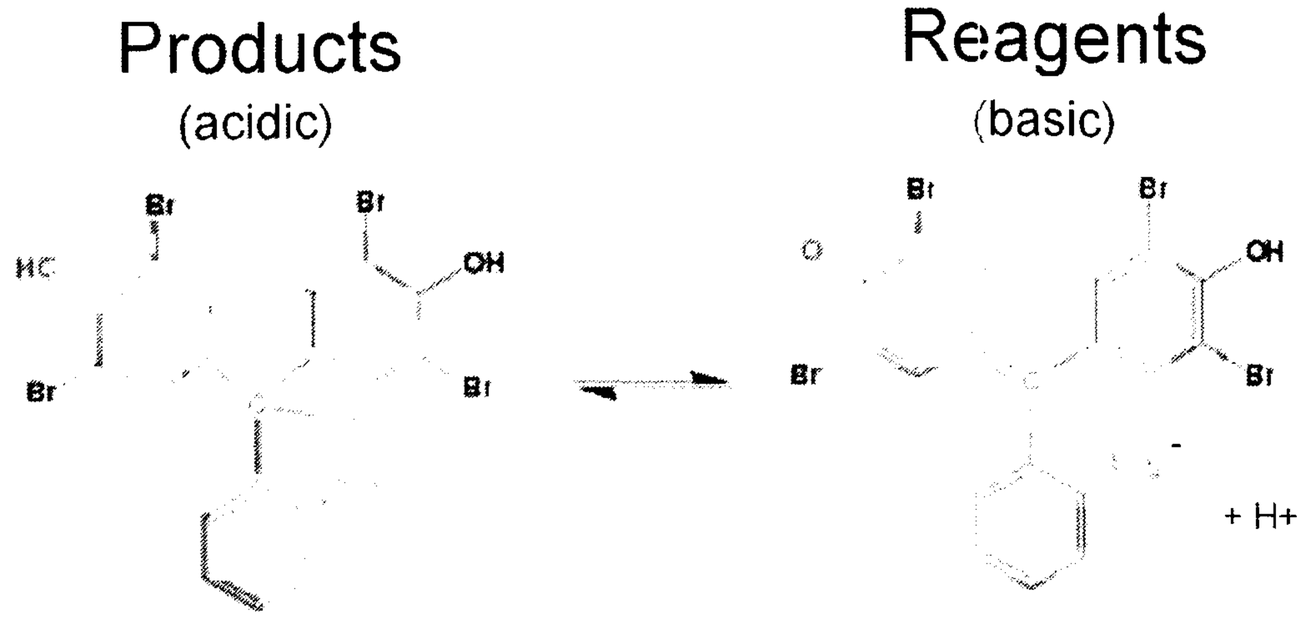

Figure 5.4 Structure of bromophenol blue.

The basic form of the indicator (deprotonated) is ionic. The indicator is therefore expected to reside in the interior polar phase of the microemulsion, and thus reflect the pH of the confined aqueous phase.

5.2.2 Stock solutions

(i) Preparation of 1M H_2SO_4

Sulfuric acid (1 M) was prepared by dilution of concentrated sulphuric acid (18.8 M, 27 ml made up to 500 ml with water).

(ii) Preparation of Solution A

Solution A typically contained 1.26 g sulfite and 0.015 ml of 1M H_2SO_4 in 100 ml. Reactant concentrations reported are those that would be established in the reactor in the absence of reaction, i.e. $[X]_0 = [X]_s/ 2$ where the subscripts 0 and s stand for stock and reactor concentrations respectively. The concentration of bisulfite and sulfite are calculated from consideration of the following equilibria:

$$H_2SO_4 \rightleftharpoons H^+ + HSO_4^- \qquad K = 1\times10^2$$

$$HSO_4^- \rightleftharpoons H^+ + SO_4^{2-} \qquad K = 1\times10^{-2}$$

coupled with the sulfite/ bisulfite equilibrium:

$$SO_3^{2-} + H^+ \rightleftharpoons HSO_3^-$$

When $[H_2SO_4]_{initially} = 0.015$ M, $[SO_3^{2-}]_{initially} = 0.1$ M, the following reaction occurs:

$$2SO_3^{2-} + H_2SO_4 \rightleftharpoons 2HSO_3^- + SO_4^{2-}$$

Intially	0.1	0.015	0	0
At Equil	0.07	0	0.03	0.015

Therefore, $[HSO_3^-]_0 = 0.015$ M, $[SO_3^{2-}]_0 = 0.035$ M.

Solution A was continuously bubbled with nitrogen as sulfur species present are prone to aerial oxidation. Solution A also contained bromophenol blue indicator, necessary to visualise the front (0.05 g / 100 ml)

(iii) Preparation of Solution B

Solution B typically contained 1.51 g of sodium bromate in 100 ml, unless otherwise stated where $[BrO_3^-]_0$ was varied to determine the dependency of front speed on substrate concentration. The initial concentration was $[BrO_3^-]_0 = 0.05$ M.

5.2.3 Preparation of microemulsions

Two ternary μE systems are used:

(1) Aqueous phase, toluene (TOL) and nonionic surfactant Triton-X (TX)

(2) Aqueous phase, hexanol (HEX) and cationic surfactant cetyl trimethylammonium bromide (CTAB)

Both AQ/ TOL/ TX (22,23) and AQ/ HEX/ CTAB (24) mixtures are known to form water-in-oil microemulsions (w/o μE). A ternary phase diagram of each system with bisulfite/ sulfite buffer solution (pH 7.5) was constructed from analysis of optical, conductivity and viscosity measurements. Suitable compositions for experimentation were identified (L_2 (within the dotted lines) in Figure 5.5(a) and L_2 in Figure 5.5(b)). The stability of the microemulsions is dependent on the ionic strength of the aqueous phase (30). Conductivity measurements were performed

using a calibrated electrode with a cell constant of 0.9 cm^{-1} (see appendix III) for potassium chloride calibrating solution conductivities). Conductivities for the microemulsion compositions exploited in the experiments reported here (ionic strength ~ 0.3 M) were of the order of $1 \times 10^{-5} - 1 \times 10^{-4}$ S cm^{-1} (conductivity increases with both ϕ_d and w_0), compared with aqueous solution conductivities of 10^{-2} S cm^{-1}.

(i) Preparation of Triton-X μE

The structure of Triton-X is shown in Figure 5.5 (a). The density of TX is approximately 1 g/ cm^{-3}. The following table was used to prepare the range of TX μE reported in the results. TX w/o μEs were prepared by adding the aqueous phase stock solution to the nonionic surfactant Triton-X-100 (TX, Sigma-Aldrich) dissolved in toluene (Alfa Aesar).

Aq. (ml)	Tol (ml).	TX (ml)	Total V	Moles TX	Conc TX	Moles H_2O	Conc H_2O	Omega (w_0)	Phi $_d$ (ϕ_d)
3	6	5	14	0.008	0.572	0.165	11.786	20	0.57
3.4	6.3	5	14.7	0.008	0.545	0.187	12.721	23	0.57
3.8	6.6	5	15.4	0.008	0.520	0.209	13.571	26	0.57
4.2	6.9	5	16.1	0.008	0.498	0.231	14.348	29	0.57
3	9	5	17	0.008	0.471	0.165	9.706	20	0.47
3	6	5	14	0.008	0.572	0.165	11.786	20	0.57
3	4	5	12	0.008	0.668	0.165	13.750	20	0.67
3	3	5	11	0.008	0.728	0.165	15.000	20	0.73

Table 5.2 Experimental recipe for aqueous phase-toluene-Triton-X microemulsions

A typical calculation for a Triton-X microemulsion with $\phi_d = 0.57$ and $w_0 = 20$ is shown.

$$\text{Moles Triton X} = \frac{5\text{g}}{624\ \text{g mol}^{-1}} = 0.008\text{mol}$$

$$\text{Concentration Triton X} = \frac{\text{moles}}{\text{total V}} = \frac{0.008}{14} \times 1000 = 0.572$$

$$\text{Moles } H_2O = \frac{3}{18\ \text{g mol}^{-1}} = 0.166\text{mol}$$

$$\text{Concetration } H_2O = \frac{\text{moles}}{\text{total V}} = \frac{0.166}{14} \times 1000 = 11.8$$

$$w_0 = \frac{[H_2O]}{[TX[} = \frac{11.8}{0.572} = 20$$

$$\phi_d = \frac{V_{Aq} + V_{TX}}{V_{TOT}} = \frac{3+5}{14} = 0.57$$

(ii) Preparation of CTAB μE

The structure of CTAB is shown in Figure 5.5 (b). The mole volume of CTAB is 1.15 ml per g of dissolved solid. CTAB w/o microemulsions were prepared by dissolving solid CTAB (Sigma) in hexanol (Alfa Aesar) then adding the aqueous phase stock solution. This reaction is highly endothermic. Solutions were therefore allowed ample time to reach room temperature before use. Table 5.3 shows the range of compositions used to prepare the CTAB μE used in experiments.

Aq. (ml)	HEX (ml).	CTAB (g)	Vol (ml) CTAB	Total V	Moles CTAB	Conc CTAB	Moles H_2O	Conc H_2O	Omega (w_0)	Phi $_d$ (ϕ_d)
0.8	6.2	3.05	3.075	10.5	0.008	0.796	0.044	4.187	5	0.41
1.25	7	3.05	3.075	11.7	0.008	0.712	0.069	5.847	8	0.41
1.9	8	3.05	3.075	13.4	0.008	0.624	0.105	7.794	12	0.41
2.5	9	3.05	3.075	15.0	0.008	0.558	0.138	9.162	16	0.41
1.25	5.6	3.05	3.075	10.3	0.008	0.808	0.069	6.637	8	0.47
1.25	7	3.05	3.075	11.7	0.008	0.712	0.069	5.847	8	0.57

1.25	9	3.05	3.075	13.7	0.008	0.608	0.069	4.997	8	0.67
1.25	11	3.05	3.075	15.7	0.008	0.531	0.069	4.363	8	0.73

Table 5.3 Experimental recipe for aqueous phase-hexanol-CTAB microemulsions.

Figure 5.5 shows the measured pH of w/o μE containing three different buffer solutions, recorded as a function of w_0 for (c) the nonionic surfactant, TX and (d) the cationic surfactant, CTAB with the aqueous phase for comparison. The pH was measured with a pH electrode (Sentek, double junction lithium chloride/methanol). The μE solutions were prepared in 10 ml volumes and were well stirred (525 r.p.m.) with a magnetic stirrer bar whilst monitored. Readings of pH were taken when the pH had stabilized. The vertical bars indicate sample standard deviations of pH (± typically 0.2) with measurements performed in triplicate. The pH measured with the electrode (pH_{meas}) reflects the effective pH in the aqueous microenvironment and the color of the bromophenol blue indicator in all experiments agreed with the measured pH. The pH of the w/o μE decreased slightly with increasing w_0 (keeping ϕ_d constant, Figure 5.5(c) and (d)), and is generally higher than that of the aqueous phase stock solution. The pH did not vary with ϕ_d in either system (Figure 5.5 (e) and (f)).

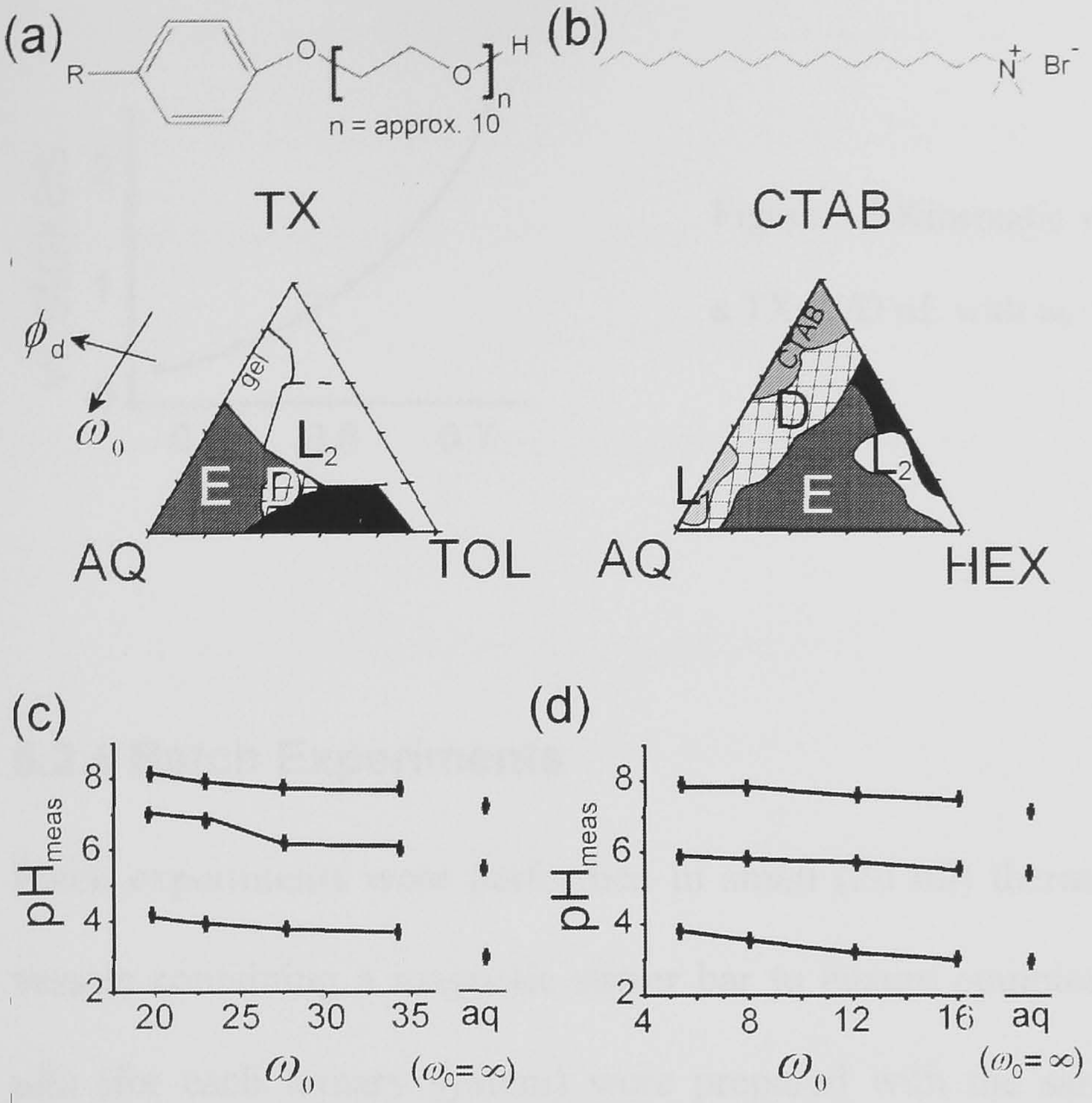

Figure 5.5 Structure of (a) non-ionic surfactant TX (b) Cationic CTAB. Ternary phase diagrams where L_1 = oil-in-water microemulsion (o/w μE), L_2 = water-in-oil microemulsion (w/o μE), D = lamellar and E = emulsion for (a) Triton-X/ toluene/ aqueous phase (buffer) system; (b) CTAB/ hexanol/ aqueous phase (buffer) system. Measured pH and corresponding aqueous phase (buffer) pH (AQ) = 3.1, 5.5 and 7.2 in (c) TX W/O μE with $\phi_d = 0.7$, (d) CTAB W/O μE with $\phi_d = 0.40$, (e) TX W/O μE with $w_0 = 30$, CTAB W/O μE with $w_0 = 12$. Vertical bars indicate sample standard deviations.

Kinematic viscosity measurements were obtained using a Cannon-Fenske routine glass capillary tube Viscometer (size 50). The viscosity of the CTAB w/o μE did not change with the values of ϕ_d or w_0 used here. The viscosity of the TX w/o μE increased with increasing ϕ_d and did not change with w_0 Figure 5.6 shows the range of viscosity with varying ϕ_d in a TX w/o microemulsion.

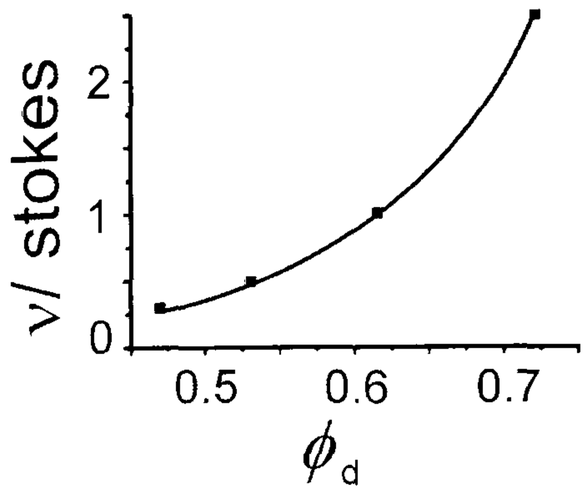

Figure 5.6 Kinematic viscosity measurements for a TX W/O μE with $w_0 = 20$.

5.2.4 Batch Experiments

Batch experiments were performed in small (20 ml) thermostated (22 °C) reaction vessels containing a magnetic stirrer bar to ensure complete mixing. Two separate μEs (for each ternary system) were prepared with the same molar ratio (w_0) and droplet fraction (ϕ_d). One contained stock solution A (sulfite/ bisulfite - μE solution A) and the other stock solution B (bromate - μE solution B). Reactions were started by addition of μE solution B to μE solution A. Upon mixing (constant at 525 r.p.m.) a pH clock reaction takes place (base to acid) that is followed by the pH electrode and the indicator color, suggesting the polar form of the indicator is present in the water core of the μE. Absolute values of pH cannot be measured with a glass pH electrode in microemulsions, as there is no way of calibrating the electrode for the new solvent (the properties of water in the polar core will not be the same as bulk water and therefore calibration with standard solutions is not relevant). Changes and trends in pH can be measured.

5.2.5 Spatial experiments

Spatial experiments were performed in 50 mm length, 2.6 mm i.d. well sealed tubes filled with the reactive μE. The reactive μE was prepared by mixing equal amounts

of μE solution A and μE solution B. In tubes thinner than this diameter fronts did not propagate. The tubes were suspended vertically and fronts initiated at the base of the tube with a thin platinum wire dipped in a w/o μE containing a 1 M H_2SO_4 solution. Images of the propagating front were captured using a CCD camera connected to a frame grabber and image processing package ImagePro.

(i) Spatial calibration and resolution.

Image pro was used to record the progress of the front. Spatial calibration was achieved by placing mm graph paper in the lens view before starting experiments. A line was then drawn in the software corresponding to a known distance on the graph paper. A diagonal line was also drawn to check the aspect ratio of the calibration. Each time the camera was moved a new calibration file was made. The marking of points at certain time spaces then allowed the construction of space time plots to determine the front speed. The plots were linear up to approximately the equivalent reaction time in batch, at which point the reaction had taken place and reaction-diffusion fronts no longer propagated.

5.3 Results

The bromate-sulfite reaction was performed in the water-in-oil microemulsion by preparation of two w/o μE with the same w_0 and ϕ_d, containing the stock solutions A and B. Upon mixing, a pH clock reaction takes place (base to acid) that is followed by the pH electrode and the indicator color. In this work, the initial reactant concentrations in the w/o μE are recorded as the moles of species in the total volume of the aqueous phase ($[X]_{0,aq}$).

Typical clocks ($[BrO_3^-]_{0,aq}$ = 0.05 M, $[SO_3^{2-}]_{0,aq}$ = 0.035 M and $[HSO_3^-]_{0.aq}$ = 0.015 M) in a TX w/o μE with various w_0 are shown in Figure 5.7 (a) compared with the aqueous phase clock (aq). The change in the form of the clock with w_0 is more pronounced for larger initial bisulfite concentration (Figure 5.7(b) - $[SO_3^{2-}]_{0.aq}$ = 0.025 M and $[HSO_3^-]_{0,aq}$ = 0.025 M). The induction time, defined as the time to the maximum rate of change of pH (t_{ind}), decreases with increasing w_0 (Figure 5.7(c)) and the overall pH change (ΔpH) increases (Figure 5.7 (d)). The pH change does not vary with ϕ_d (Figure 5.7(e)) but the induction time increases (Figure 5.7(f)).

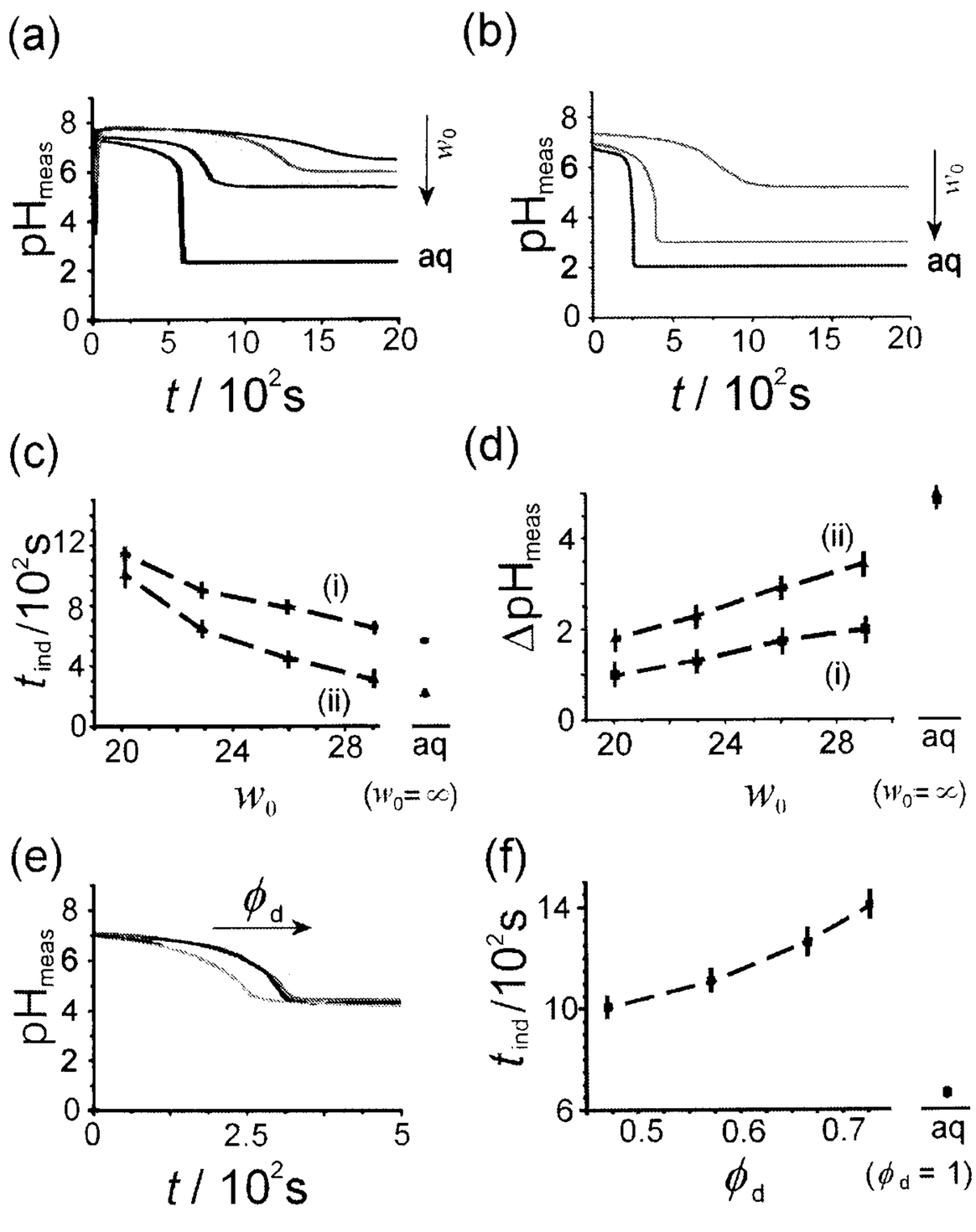

Figure 5.7 Bromate-sulfite clock reactions in a TX W/O μE with $[BrO_3^-]_{0,aq}$ = 0.05 M, $[SO_3^{2-}]_{0,aq}$ = 0.035 M, $[HSO_3^-]_{0,aq}$ = 0.015 M, unless otherwise stated. (a) pH time traces with w_0 = 19, 22, 27 and 34, (ϕ_d = 0.73). (b) pH time traces with $[SO_3^{2-}]_{0,aq}$ = 0.025 M, $[HSO_3^-]_{0,aq}$ = 0.025 M and w_0 = 19, 22, 27 and 34 (ϕ_d = 0.73). (c) Variation of induction time with w_0 (ϕ_d = 0.57) for (i) as above and (ii) $[SO_3^{2-}]_{0,aq}$ = 0.03 M, $[HSO_3^-]_{0.aq}$ = 0.02 M. (d) Variation of overall change in pH with w_0 (ϕ_d = 0.57) for (i) as above and (ii) $[SO_3^{2-}]_{0.aq}$ = 0.03 M, $[HSO_3^-]_{0.aq}$ = 0.02 M. (e) pH time traces with $[BrO_3^-]_{0.aq}$ = 0.1 M,

$[SO_3^{2-}]_{0,aq}$ = 0.025 M, $[HSO_3^-]_{0,aq}$ = 0.025 M and ϕ_d = 0.48, 0.57, 0.62, 0.73 (w_0 = 34). (f) Variation of induction time with ϕ_d (w_0 = 20).

Figure 5.8 shows the variation of induction time (5.7(a)) and overall change in pH (5.7(b)) for different initial conditions of bromate in a TX w/o μE when $[SO_3^{2-}]_{0,aq}$ = 0.035 M and $[HSO_3^-]_{0,aq}$ = 0.015 M. The variation of induction time with ϕ_d for different initial bromate conditions is shown in Figure 5.8(c). Again, $[SO_3^{2-}]_{0,aq}$ = 0.035 M and $[HSO_3^-]_{0,aq}$ = 0.015 M.

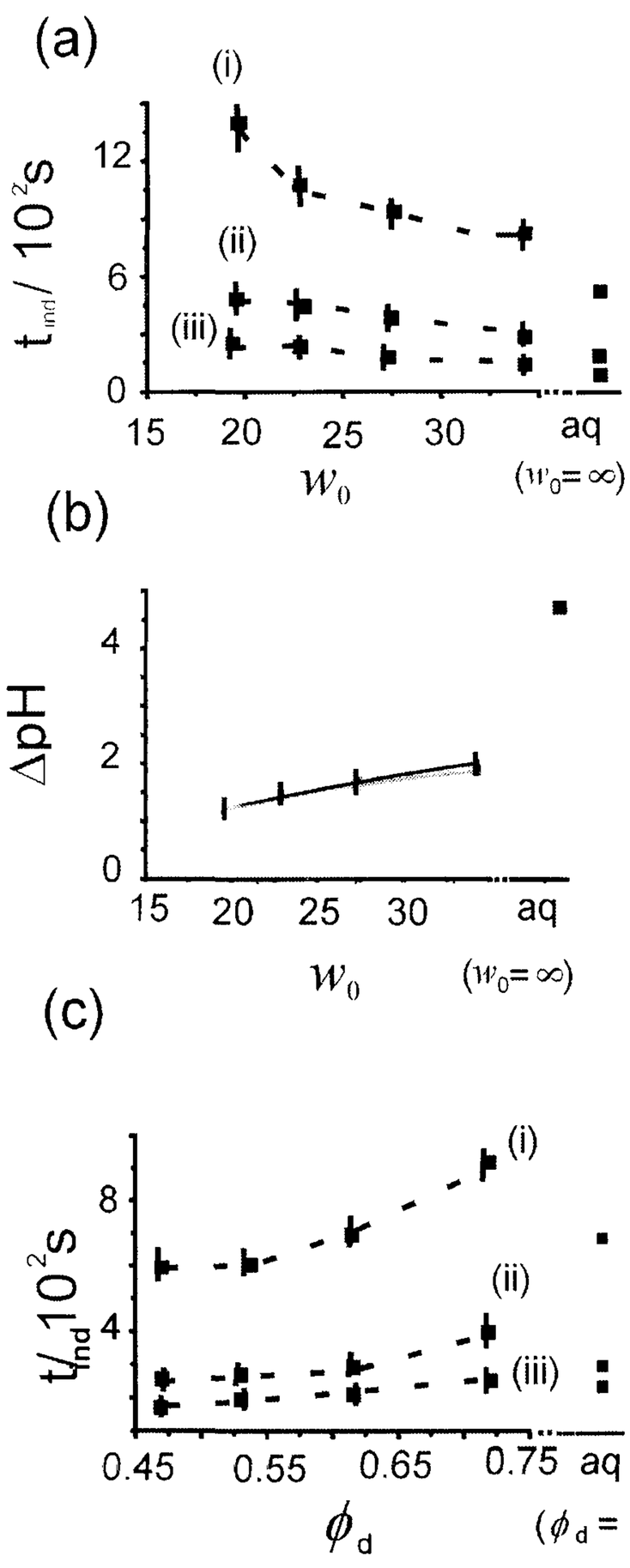

Figure 5.8 Variation of induction time and overall pH change in bromate sulfite clock reaction in a TX W/O μE where $[SO_3^{2-}]_{0,aq}$ = 0.03 M, $[HSO_3^-]_{0,aq}$ = 0.02 M. Variation of (a) induction time with w_0 (ϕ_d = 0.73) for bromate sulfite clock reactions where (i) $[BrO_3^-]_{0,aq}$ = 0.3 M (ii) $[BrO_3^-]_{0,aq}$ = 0.2 M (iii) $[BrO_3^-]_{0,aq}$ = 0.1M (b) overall change in pH with w_0 (ϕ_d = 0.73) for varying bromate. Lines are superimposed showing $[BrO_3^-]_{0,aq}$ has no effect on overall change in pH (c) induction time with ϕ_d (w_0 = 34) (i) $[BrO_3^-]_{0,aq}$ = 0.3 M (ii) $[BrO_3^-]_{0,aq}$ = 0.2 M (iii) $[BrO_3^-]_{0,aq}$ = 0.1M

Clock reactions in the CTAB w/o μE are shown in Figure 5.9(a). There is a distribution of clock times observed for a particular value of w_0 (4 - 5 measurements) with no clear trend upon increasing w_0 (Figure 5.9(b)). The pH change is reproducible however, and increases with increasing w_0, approaching that of the aqueous phase pH change with $w_0 = 16$ (Figure 5.9(c)). There is no clear trend in the induction times with ϕ_d (Figure 5.9(d)).

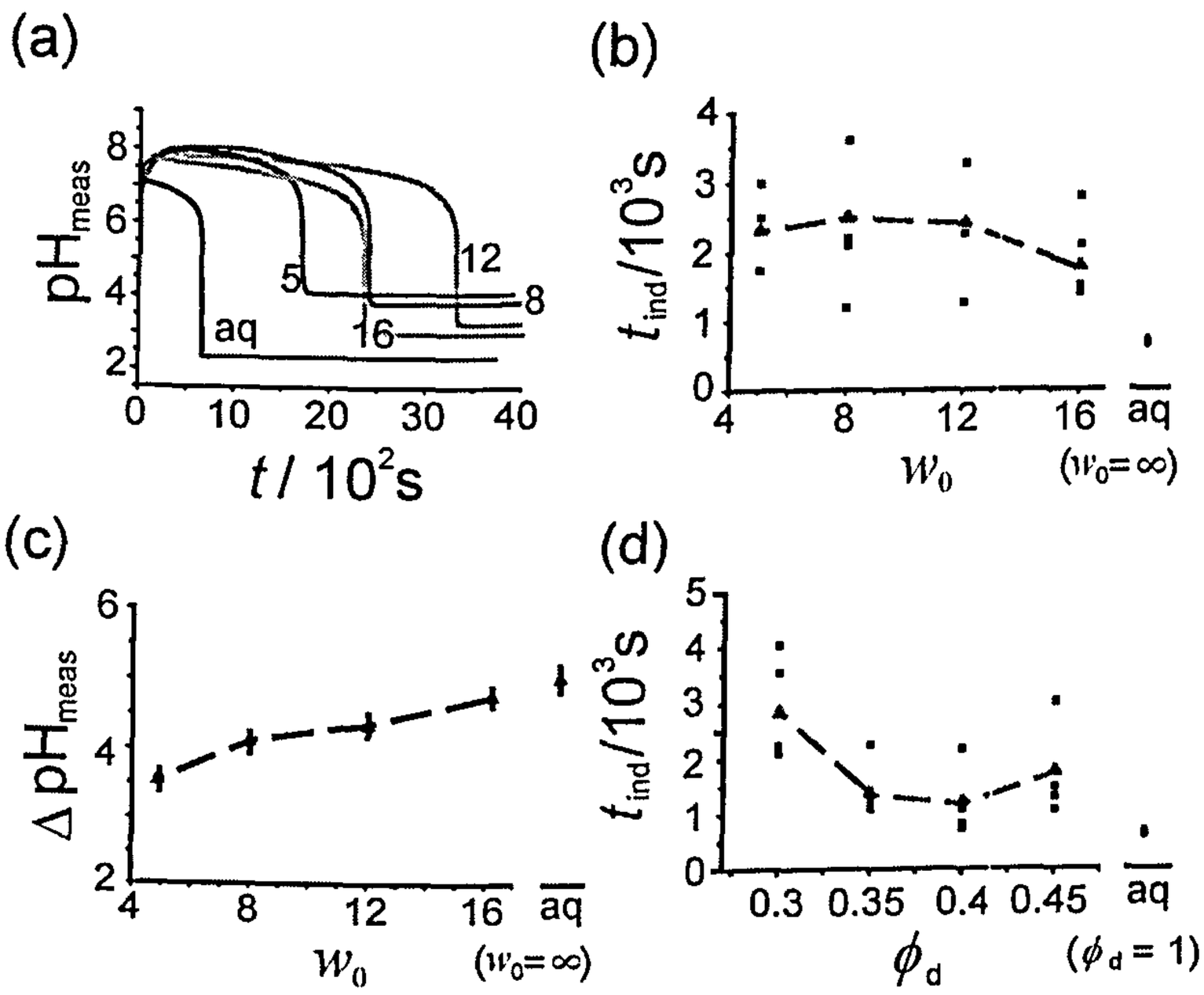

Figure 5.9 Bromate-sulfite clock reactions in a CTAB W/O μE with $[BrO_3^-]_{0,aq}$ = 0.05 M, $[SO_3^{2-}]_{0,aq}$ = 0.035 M, $[HSO_3^-]_{0,aq}$ = 0.015 M. (a) Typical pH time traces with ϕ_d = 0.40 and various w_0. (b) Variation of induction time with w_0 (ϕ_d = 0.40). (c) Variation of overall pH change with w_0 (ϕ_d = 0.40). (d) Variation of induction time with ϕ_d (w_0 = 8).

The rate of change of pH in the two systems (TX and CTAB) is plotted in Figure 5.10 as a function of pH. As the pH decreases, the rate increases to a maximum, then falls to the final pH. The maximum rate of change of pH increases with increasing w_0 in all w/o μE. In the TX system (Figure 5.10(a)), the maximum rate is a magnitude smaller than the equivalent aqueous phase system (Figure 5.10(b), but increases with increasing initial bisulfite concentration (Figure 5.10(c)). The rate of change of pH in

the CTAB system becomes comparable with the aqueous phase system when w_0 = 16 (5.10 (d)) 16).

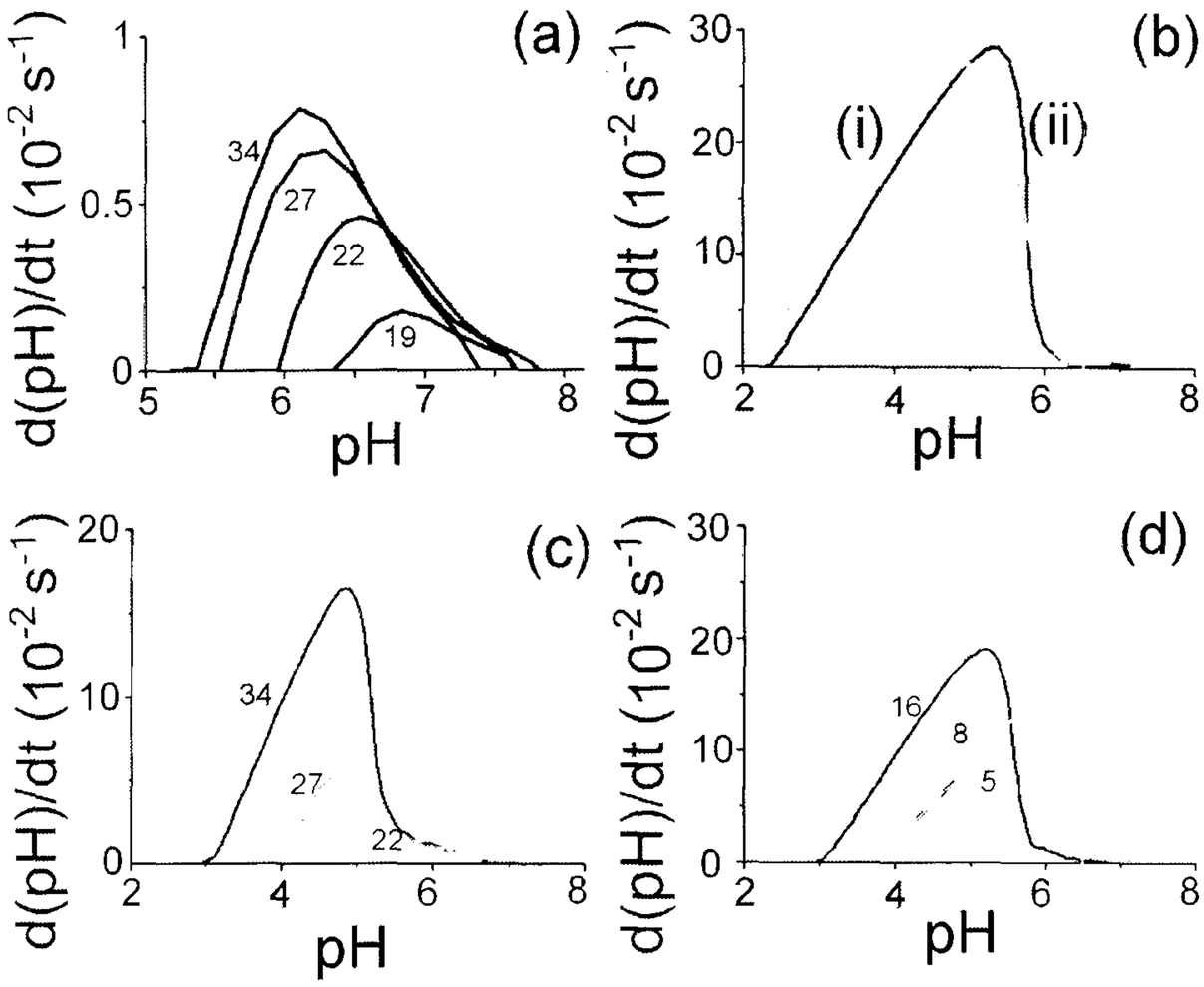

Figure 5.10 Rate of change of pH as a function of pH for the bromate-sulfite clock reactions with $[BrO_3^-]_{0,aq}$ = 0.05 M, $[SO_3^{2-}]_{0,aq}$ = 0.035 M, $[HSO_3^-]_{0,aq}$ = 0.015 M (unless otherwise stated) in (a) TX W/O μE with ϕ_d = 0.61 and various w_0; (b) aqueous phase (i) $[SO_3^{2-}]_{0,aq}$ = 0.03 M, $[HSO_3^-]_{0,aq}$ = 0.02 M and (ii) $[SO_3^{2-}]_{0,aq}$ = 0.035 M, $[HSO_3^-]_{0,aq}$ = 0.015 M; (c) TX W/O μE with $[SO_3^{2-}]_{0,aq}$ = 0.03 M, $[HSO_3^-]_{0,aq}$ = 0.02 M, ϕ_d = 0.61 and various w_0; (d) CTAB W/O μE with ϕ_d = 0.4 and various w_0.

The bromate-sulfite reaction in a TX w/o μE supports reaction-diffusion fronts when performed in a thin tube (i.d. = 2.8 mm). Distance-time plots of the front were linear up to the time at which the aqueous phase clock reaction had completed, thus front speeds were calculated up to this time only. The front speed was observed to markedly decrease with increasing ϕ_d (Figure 5.11(a)) and the structure of the fronts changed from parabolic to planar (Figure 5.11 (b) i – iv). The pH change for this value of w_0 is small and thus the front was green propagating into blue (the colour change is enhanced in the images shown). The front speed increased with increasing initial bromate concentration (inset) for a particular value w_0 of and ϕ_d. The front

speed also decreased when increasing w_0 from 20 to 23, then remained constant, in the TX system (Figure 5.11 (c)).

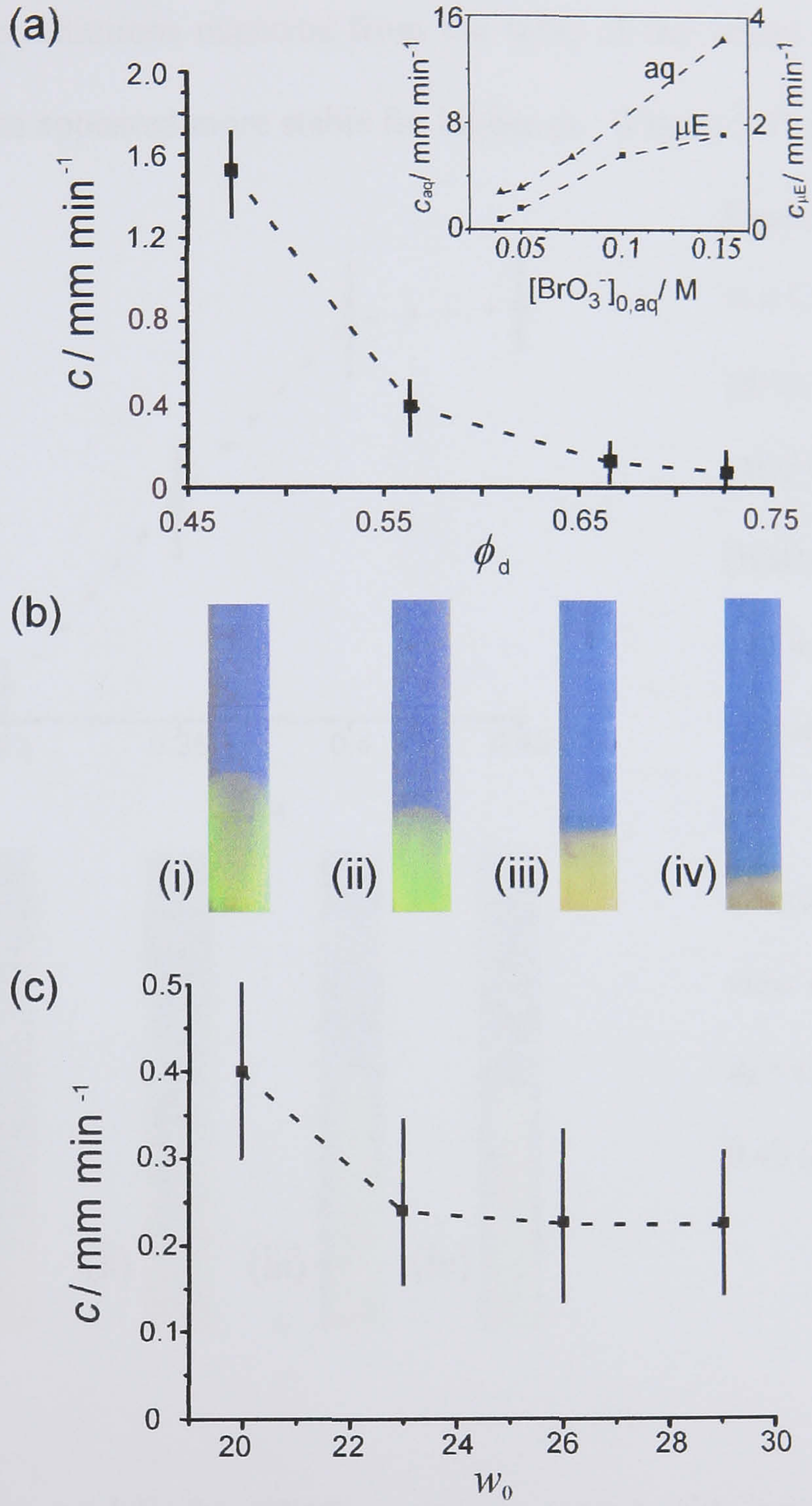

Figure 5.11 Acid fronts in a TX W/O μE with $[BrO_3^-]_{0,aq}$ = 0.05 M, $[SO_3^{2-}]_{0,aq}$ = 0.035 M, $[HSO_3^-]_{0,aq}$ = 0.015 M, ϕ_d= 0.57 and w_0 = 20 (unless otherwise stated). (a) Variation of front speed, c, with ϕ_d. Inset shows variation of front speed with bromate concentration in the aqueous phase and the μE. (b) Colour-enhanced images with a field-of-view of 2 × 9 mm and ϕ_d = (i) 0.45 (ii) 0.57 (iii) 0.65 (iv) 0.73. (c) Variation of front speed, c, with w_0.

The CTAB system also displays fronts, in this case the speed increased with increasing ϕ_d. For low ϕ_d the reaction fronts from the initiation were not well-defined and spontaneous initiations occurred from the sides of the vessel (Figure 5.12 (b)i and ii). The fronts appeared more stable for higher ϕ_d. (Figure 5.12 i and v).

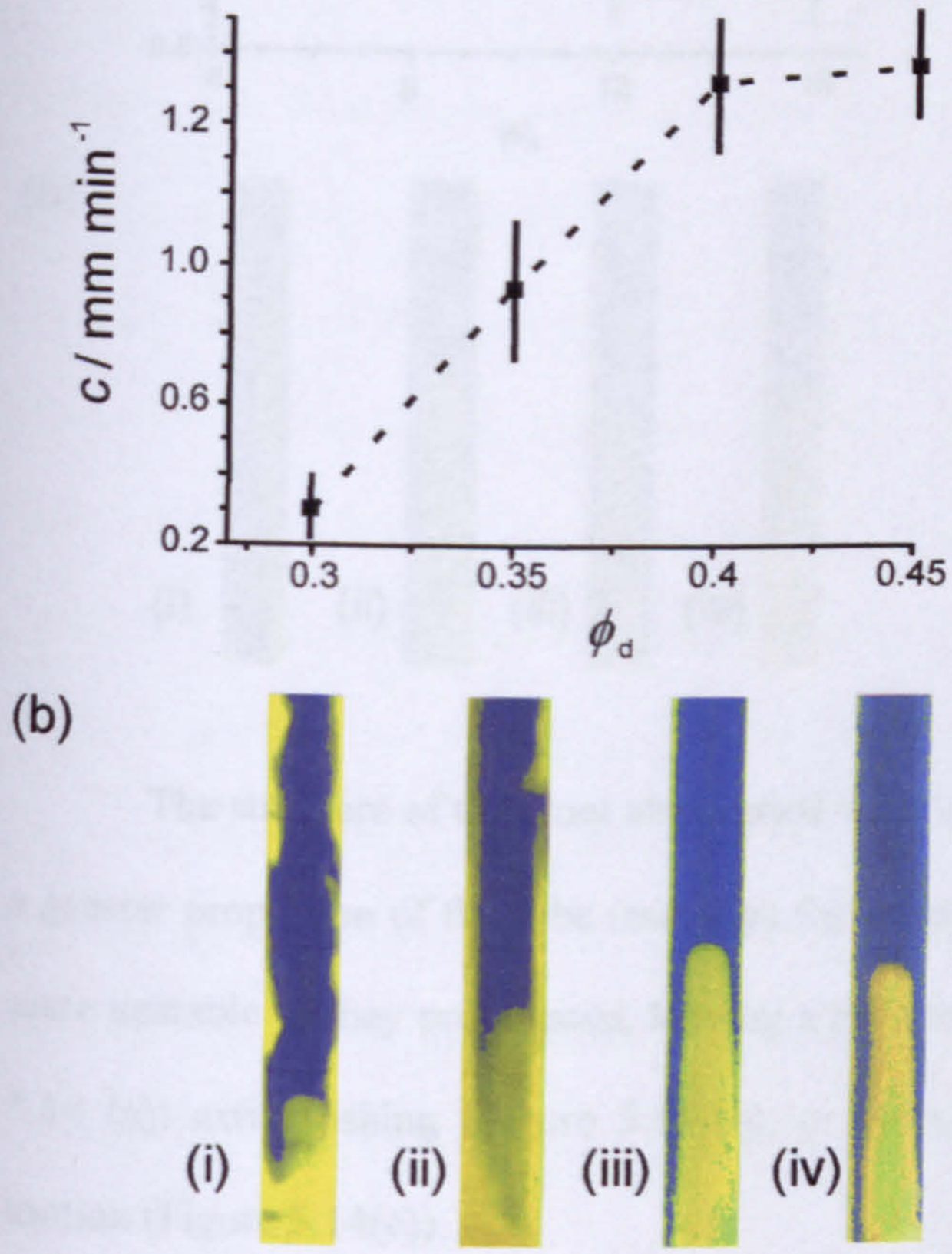

Figure 5.12 Acid fronts in a CTAB W/O μE with $[BrO_3^-]_{0,aq}$ = 0.05 M, $[SO_3^{2-}]_{0,aq}$ = 0.015 M, $[HSO_3^-]_{0,aq}$ = 0.015 M and w_0 = 8. (a) Variation of front speed, c, with ϕ_d. (b) Colour-enhanced images with a field-of-view of 2 × 10 mm and ϕ_d = (i) 0.30 (ii) 0.35 (iii) 0.40 (iv) 0.45

The front speed in the CTAB system decreased with increasing w_0 (Figure 5.13(a)) and increased with increasing bromate for a particular μE composition (inset).

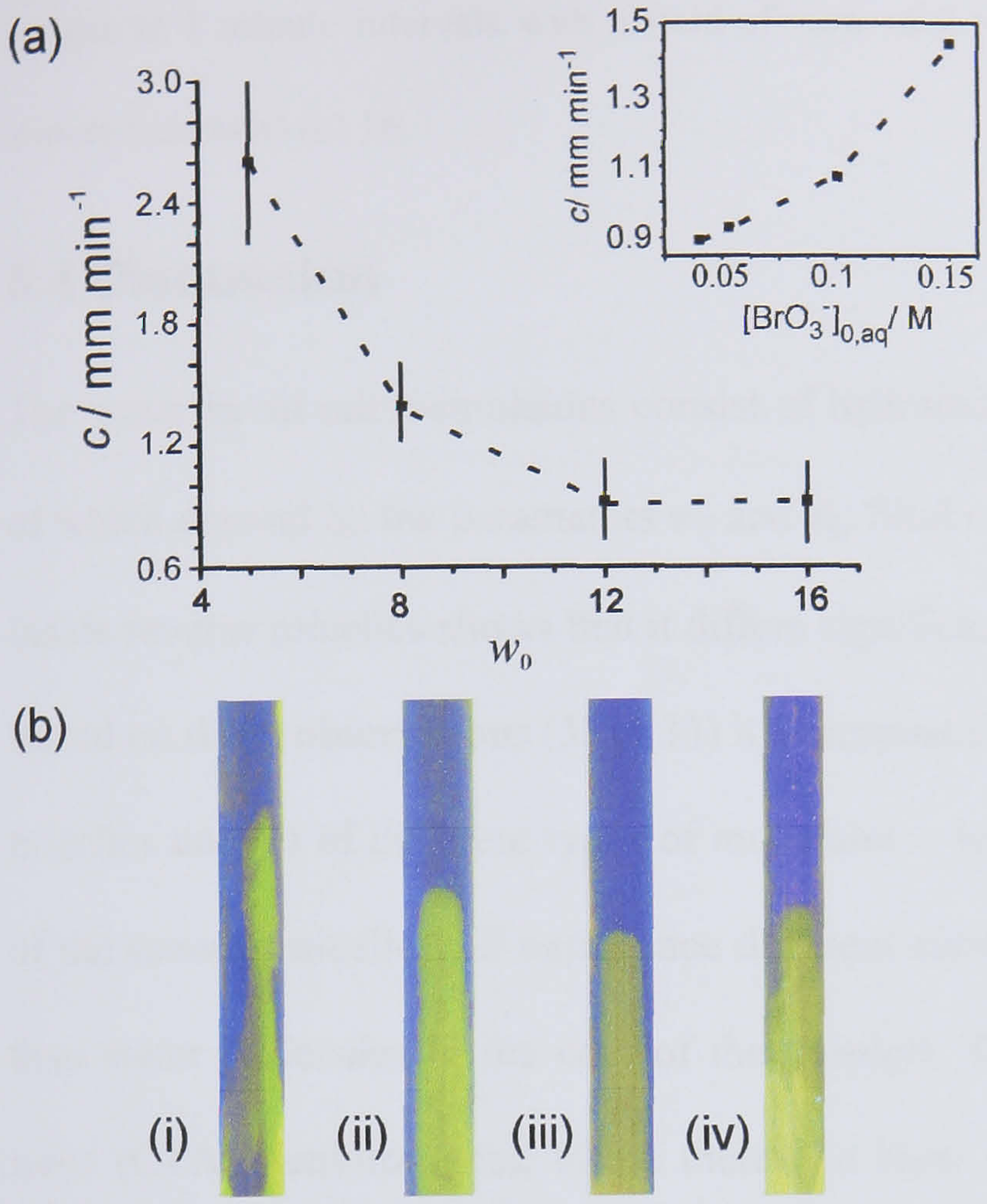

Figure 5.13 Acid fronts in a CTAB W/O μE with $[BrO_3^-]_{0,aq}$ = 0.05 M, $[SO_3^{2-}]_{0,aq}$ = 0.035 M, $[HSO_3^-]_{0,aq}$ = 0.015 M and ϕ_d = 0.40. (a) Variation of front speed, c, with w_0. Inset shows variation of front speed with bromate concentration. (b) Colour-enhanced images with a field-of-view of 2 × 17 mm and w_0 = (i) 4 (ii) 8 (iii) 12 and (iv) 16.

The structure of the front also varied with w_0 – the traveling plumes occupied a greater proportion of the tube (radially) for greater w_0 (Figure 5.14(b)). The fronts were unstable as they propagated, leaving a turbulent structure in their wake (Figure 5.14 (a)) extinguishing (Figure 5.14(b)), or traveling up the tube in a spiral-type motion (Figure 5.14(c)).

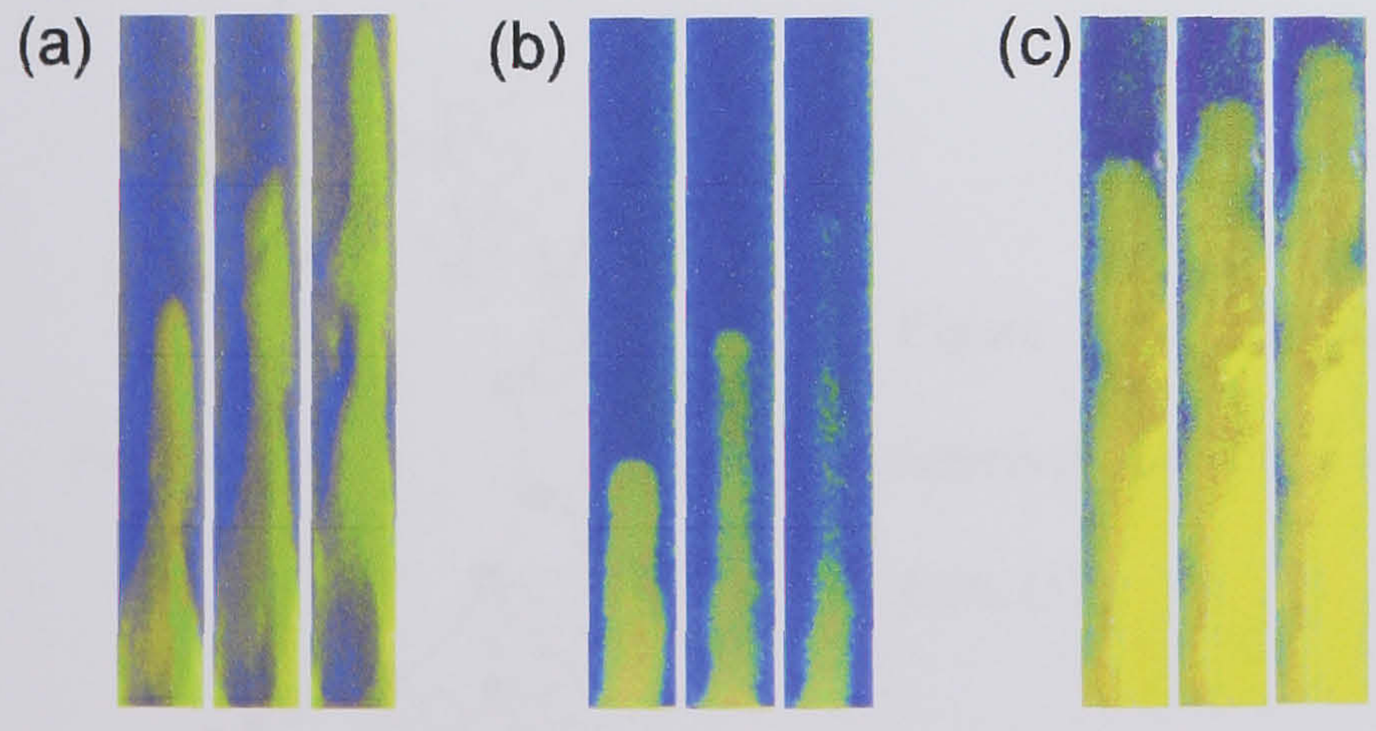

Figure 5.14 Temporal evolution of fronts in a CTAB W/O μE with $[BrO_3^-]_{0,aq}$ = 0.05 M, $[SO_3^{2-}]_{0,aq}$ = 0.035 M, $[HSO_3^-]_{0,aq}$ = 0.015 M and ϕ_d = 0.40. Color-enhanced

images at 1 minute intervals with a field-of-view of 2 × 17 mm and w_0 = (a) 4 (b) 8 (10 minute intervals) (c) 16.

5.4 Discussion

The water in oil microemulsions consist of hydrated reverse micelles, the properties of which depend on the parameters w_0 and ϕ_d. Studies probing the behaviour of water inside reverse micelles shows that it differs significantly from that of bulk water (31). Based on these observations (32), (33) it is proposed that the interior water of reverse micelles consist of different types of molecules – water molecules in the outer shell of the reverse micelle will experience different surroundings and hydrogen bonding than water molecules in the core of the droplets. The stern layer is relevant to the ionic (CTAB) environment, where there is a layer of counterions that attach to the charged surface. These ions are temporarily bound and shield the surface charge. The layer is densely packed with surfactant head groups and counter ions. It is suggested that the water molecules at the interface of a reverse micelles has a much lower mobility (a higher micro-viscosity) than those in the center of the pool (34). Figure 5.15 shows the different regions in the interior of a reverse micelle.

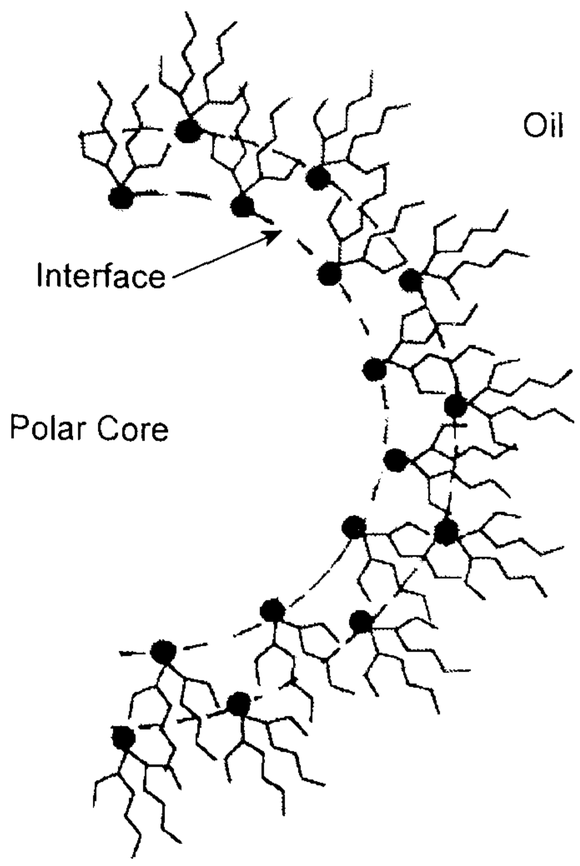

Figure 5.15 Schematic diagram of the assumed interfacial structure of the reverse micelle, adapted from (35).

An increase in w_0 (an increase in $[H_2O]$) is generally correlated with an increase in the diameter of the nano-droplets (35). For small reverse micelles, the characteristics of water are considerably different from those of bulk water; the activity of water in the water pool increases with increasing w_0. An increase in ϕ_d (a decrease in V_{oil}) results in a decrease in the average separation of reverse micelles and therefore an increase in the effective concentration of droplets in the microemulsion.

The measured pH was observed to decrease with increasing w_0, and not markedly change with ϕ_d in both microemulsions. In CTAB at $w_0 = 16$, the measured pH approached that of bulk water. These results correlate with the description of decreased water activity with decreasing w_0. This supports the postulation that the electrode is measuring the pH in the aqueous microenvironment. The deprotonated form of the bromophenol blue indicator cannot penetrate the oil phase, and is thus also expected to reflect the pH in the reverse micelle water pool. This was true in all experiments and a change in colour of the indicator reflected a change in the measured pH. Absolute interpretation of the pH in the reverse micelles is complex, as gradients may be observed with the aqueous pool and pH measurements using indicators depend on the location of the probe (i.e. in the centre of the pool, at the interface or part of the surface).

a) Kinetics in batch

A typical clock simulated from the model (Table 5.1) is shown in Figure 5.16, illustrating the concentrations of the important species H_2SO_3, H^+ and HSO_3^- during the course of the reaction.

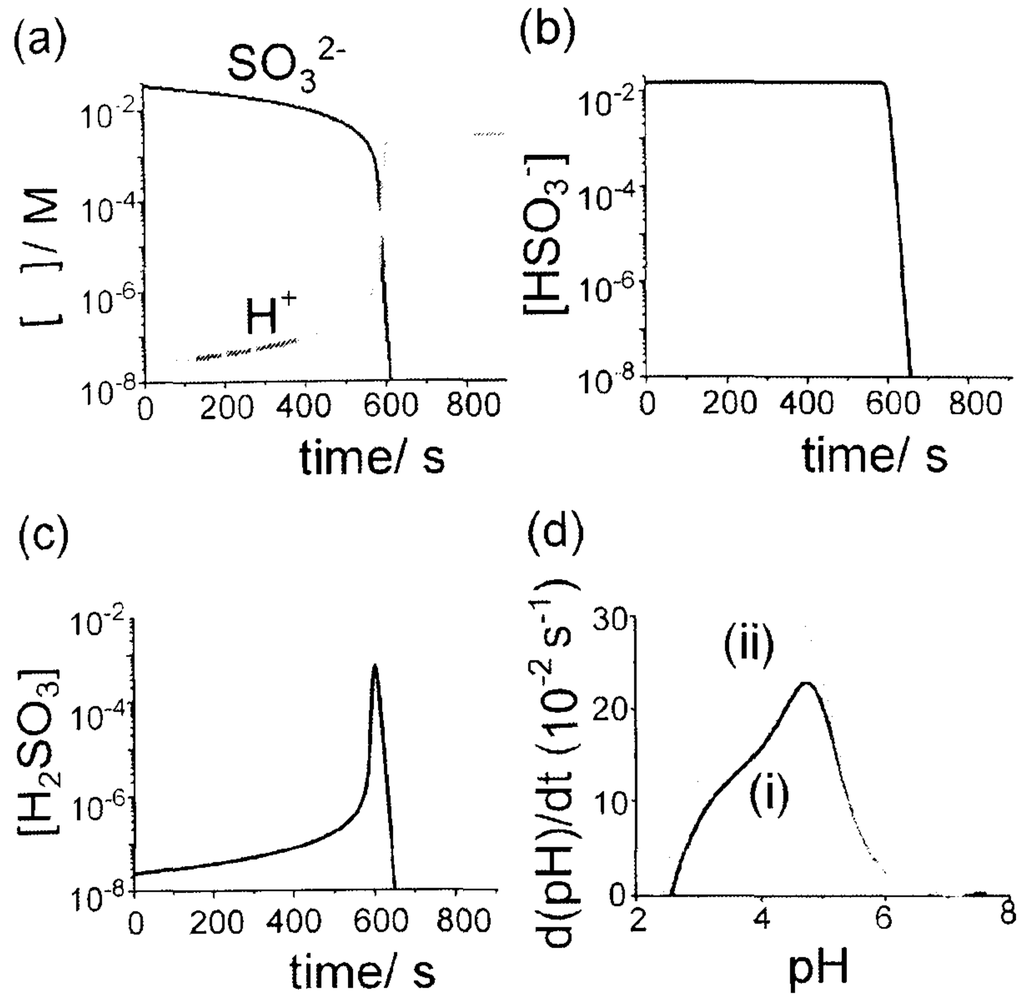

Figure 5.16 Simulated bromate sulfite clock reaction (from model in Table 5.1) with (i) $[BrO_3^-]_0$ = 0.05 M, $[SO_3^{2-}]_0$ = 0.035 M, $[HSO_3^-]_0$ = 0.015 M and (ii) $[BrO_3^-]_0$ = 0.05 M, $[SO_3^{2-}]_{0,aq}$ = 0.03 M, $[HSO_3^-]_{0,aq}$ = 0.02 M.

The induction time in this reaction can be explained by consideration of the sulfite-bisulfite buffer present initially (reaction (5.2)). Acid produced from the overall reaction (5.1) protonates sulfite in reverse reaction (5.2). As sulfite is depleted, the buffering capacity of reaction (5.2) decreases. Buffering typically exists between pH values of the pKa ± 2. The induction time, defined as the time to reach the maximum rate of change of pH, corresponds to the time taken to consume the buffer (pH ~ 5.1 – Figure 5.14(d)). The value of t_{ind} decreases with increasing initial concentrations of bisulfite and bromate. The overall pH change depends on the total initial concentration of sulfite plus bisulfite. Acid autocatalysis is demonstrated from consideration of reactions (5.4) and (5.5). As the concentration of acid increases, the rate of production of H_2SO_3 increases in reverse reaction (5.4), and the rate of formation of acid increases in reaction (5.5). There are therefore two processes responsible for the clock behaviour, (i) the consumption of the buffer to give the induction time and (b) the increase in rate of reaction (5.5) (and therefore increase in $[H^+]$) as the concentration of H^+ increases.

i) Triton-X

The induction time in Triton–X μE is generally shorter than that in CTAB (maximum induction times in TX and CTAB are 1400 s and 300 s respectively), and increases with decreasing w_0 relative to the aqueous phase. The rate of the reaction between HSO_3^- and BrO_3^- (those species that determine the induction time in the clock) is dependent on the water content and will increase with increasing w_0. This may be due to an increase in 'free water' as the nano-pools grow in size, or a consequence of the increased concentration of species per unit volume with increasing water content. A reduction in the rate of enzyme conversion has been noted by Sodre et al (36) in low water content Triton-X μEs. The catalytic activity of enzymes entrapped in reverse micelles is also found to generally increase as the amount of water is increased (w_0 increases), in a Triton-X μE (37).

The acid autocatalysis occurs through a combination of steps reverse 5.4 and 5.5 and is responsible for the clock characteristic of the reaction (the sudden drop in pH). This 'clock' is greatly suppressed in Triton-X μEs. The pH change in a typical aqueous phase clock reaction was not affected however, by addition of Triton-X alone (unlike the anionic surfactant AOT which acts as a buffer (38), thereby masking any pH changes). Thus, this decrease in rate can be correlated with a change in the water characteristics such as an increased micro-viscosity and a decrease in polarity (trend shows decreasing rate with decreasing w_0). Figure 5.17 shows a schematic Triton-X μE with the long surfactant chains residing in the interior of the water pool.

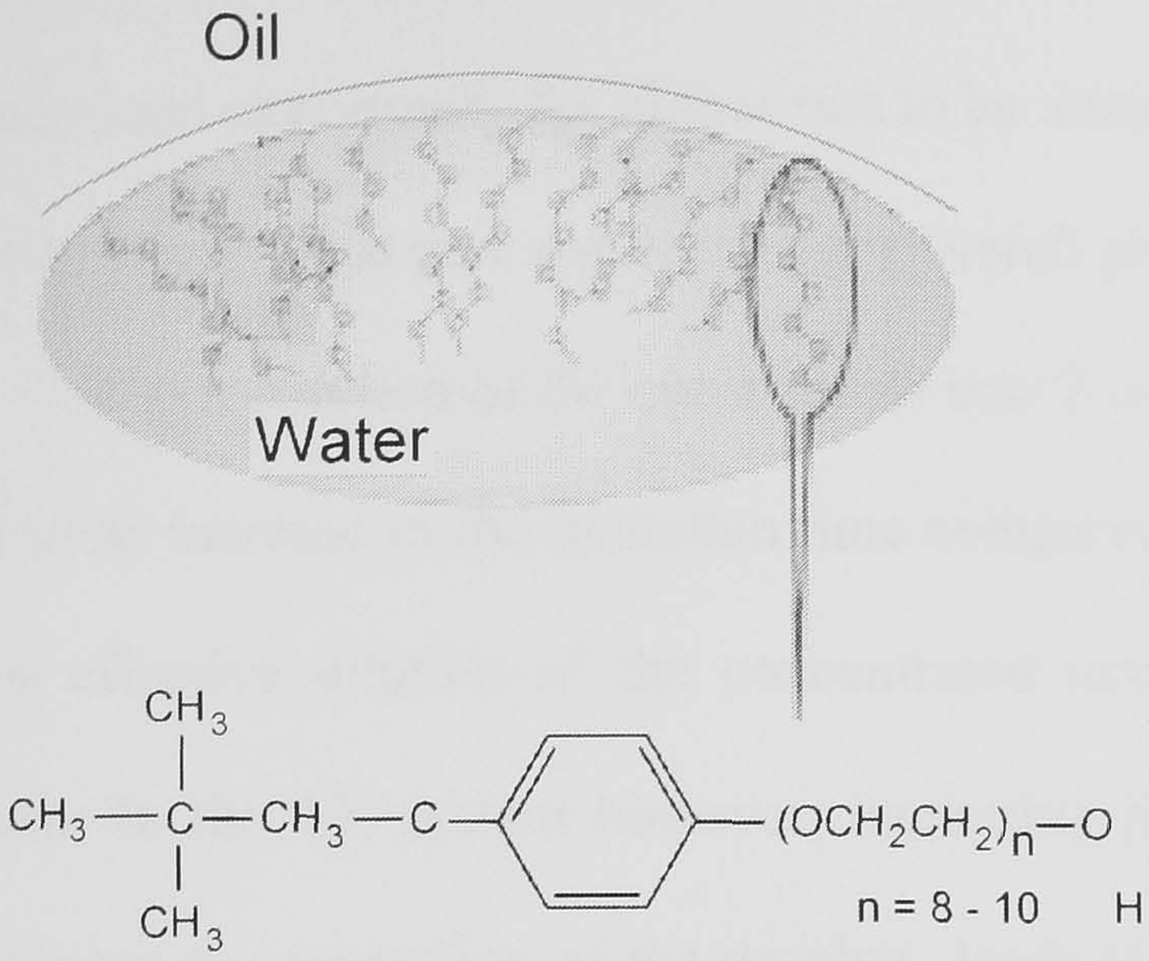

Figure 5.17 Schematic of a Triton-X reverse micelle/ microemulsion.

The deviation from bulk water behaviour may persist in larger values of w_0 in Triton-X μE than expected. This is due to the low amount of free (compared to interfacial) water. In AOT the water pool begins to resemble bulk water at values of $w_0 > 10$ (38) . However, the long ethylene oxide chains present in Triton-X, which are partially hydrated, reduce the size of the water pool in the reverse micelle core and may cause a decrease in the rate of reactions taking place there. In a microemulsion of up to 26 % water, the rate of reaction is still greatly suppressed. Thus, the overall pH change in the Triton-X system is greatly reduced compared to the aqueous phase, and the CTAB system.

The increase in overall pH change with increasing initial bisulfite concentration (at constant water content) may be due to an increased exothermicity of the reaction. As the induction time is greatly reduced with increasing initial bisulfite concentration, the faster rate of production of acid may lead to a greater rate of heat production, which possibly alters the structure of the microenvironment. If reaction is mediated by a fusion-fission process (39) it is plausible to suggest that an

expansion or break down of structured interfaces between reagents may give rise to an increased opportunity for higher rate to be attained due to an increase in the water activity. This would give rise to a bigger overall pH change.

The separation of the constituents into 2 stock microemulsions is expected to lead to an increase in the induction time compared to the aqueous phase as it results in an effective dilution of the concentrated reactants in the total volume of the system. In the TX system however, increasing the droplet fraction, ϕ_d, and hence decreasing the separation of the droplets, leads to an increase in the induction time. This is believed to result from the increased kinematic viscosity of the medium (with decreased oil content) which prolongs the evolution of a critical acid concentration in a similar manner to increasing the stirring rate.

ii) CTAB

In the CTAB cationic surfactant system the induction time of the clock is greatly increased relative to Triton-X and aqueous phase systems. The variation in induction time also follows no defined trend with w_0, however the overall pH change increases with increasing w_0. It is possible that the negatively charged ions responsible for determining the 'clock time' (ie. HSO_3^- and BrO_3^-) may become trapped in the crowded stern layer of the ionic reverse micelle. In AOT reverse micelles, a gradient of acid is observed from the neutral core of the micelle to the interface as a result of the negatively charged surfactant head groups (40). It is reasonable to expect that such a gradient may exist in the CTAB system, but in the reverse direction due to the cationic NH_3^+ groups. The lengthened induction times observed in CTAB could therefore be explained by consideration of the decrease in the rate of reactions involving SO_3^{2-} and BrO_3^- as these species are trapped. If this is the case the

enhanced sensitivity of the clock time to the evolution of a critical acid concentration (41) may be due to external factors, such as stirring rate or slight variation in temperature. This may explain the irreproducibility of the clock times in the CTAB system as slight changes in the microenvironment structure may give rise to reaction of the substrates in an unpredictable manner.

For ionic micelles the local environment in the Stern layer (the layer of counterions that attach to the charged surface) is very complex due to the presence of charged head groups and counterions in a limited space. A variation in the enhancement of rate of reaction of gluthione and 2,4-dinitrochlorobenzene has been found when the reaction is performed in positively or negatively charged reverse micelles (42). Thus, there is evidence that the rate of reactions performed in confined water pools depends on the type of surfactant used in microemulsion preparation.

The maximum rate of reaction in CTAB is much higher than that in TX, approaching bulk water behaviour as the water content is increased to 23 % (w_0 = 16). It has been shown that the water located in the water pool in the cationic CTAB reverse micelles has a higher orientational mobility that water in AOT reverse micelles (43). It seems plausible to suggest that the water pool (the solvent in the core of the structure) in CTAB microemulsions may therefore also be less 'viscous' than that in Triton-X. When reaction 5.5 becomes important it can therefore proceed at a rate which is relatively unhindered by the micro-viscosity of the water core. The overall pH change increases for increasing w_0. This can be explained as an increase in the amount of water in the core available to facilitate reaction.

No trend is seen for variation of the droplet fraction in CTAB microemulsions. This could again be due to the sensitivity of the system to stirring

and any external effects that may result in slight changes of the microenvironment giving rise to release of the reagents.

iii) The pseudo phase model

The previous discussion of the kinetics in batch in both the non-ionic and cationic reverse micelle systems can be discussed in terms of a pseudo phase model. In a pseudo phase model of kinetics in reverse micelles reagents, the solvent (water) is either located in the interior water core, the interfacial layer or is sequestered into the oil phase (44). Only non-polar species will be sequestered into the organic solvent.

The kinetics of water replacement in cationic palladium (II) aquo complexes by thiourea, methylthiourea and ethylthiourea has been successfully fitted to a simplified mechanism considering only the distribution of the complexes and the substrates between the interface and water pseudophase. A bounded water model has also been used to successfully interpret the kinetic data of enzymatic hydrolysis in reverse micelles of AOT (45). A three variable pseudo phase model, involving partition of reactants into the water core, interface and oil phase has also been used to successfully fit kinetic data of nitrosation of amines by alkyl nitrites in AOT/ Isoctane systems (46).

As none of the reagents of the bromate sulfite reaction are non-polar the species can only reside in the water pool, or the interfacial layer. The following type of kinetic scheme may therefore be important as the rates of the important reactions (5.1 and 5.5) will depend on the relative amounts of free and bounded species.

(1)

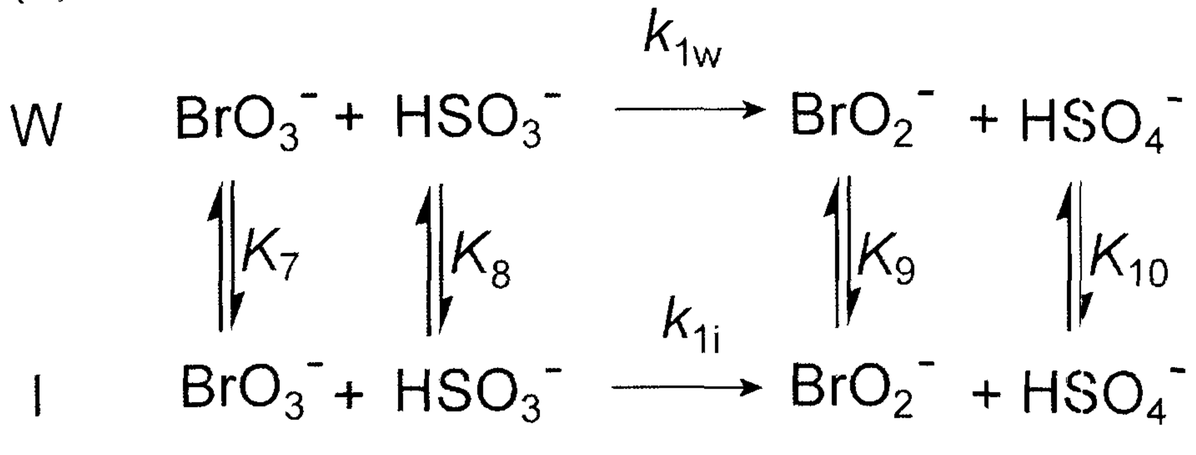

(2)

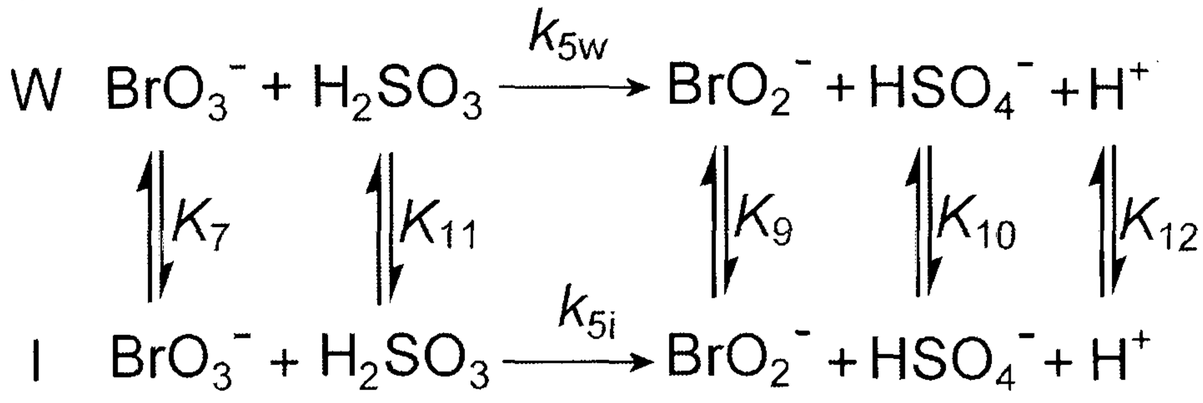

Figure 5.18 Pseudo phase scheme for the bromate sulfite clock reaction in a microemulsion

Reaction (1) is responsible for determining the induction time of the clock and reaction (2) is the kinetic step responsible for the autocatalysis. The K values represent the distribution constants between the water pools (W) and the interface (I) of the surfactant, and will depend on the nature of surfactant, the nature of the polar species, w_0 and ϕ_d. In CTAB, the partition of the anionic reactants into the interface will be large for reaction 1. This means that the reaction will progress at a decreased rate. This will give rise to long induction times. For reaction 2, the partition of reactants at the interface will be lower due to the high mobility of water in CTAB reverse micelles. Therefore the rate of reaction 2 will be relatively high, giving rise to pronounced clock behaviour in CTAB reverse micelles. In Triton-X, the partition of the anionic surfactants on which the rate of reaction 1 depends will be the same as the partition of the reactants necessary for step 2. There is no 'enhanced' partition of reagents due to a cationic stern layer. Clock times in Triton-X will therefore be relatively short, with a relatively slow rate of autocatalysis.

b) Spatial behaviour – acid reaction-diffusion fronts in microemulsions

i) Triton-X

The change in the front speed with ϕ_d reflects the increased viscosity of the medium. The change in the structure of the front is explained by the presence of convective instability driven by the temperature change during the reaction. The less dense, reacted, fluid beneath the un-reacted, more dense fluid gives rise to a curvature of the front. The stability of fronts is characterized by a dimensionless number S (47):

$$S = \frac{dgr^3}{\nu D}$$

where d is the fractional density difference between reacted and unreacted solution, g is the gravitational constant, r is the radius of the tube, D is the diffusion coefficient and ν is the kinematic viscosity. An increase in the kinematic viscosity is predicted to give rise to a transition from symmetric to asymmetric convection to a planar front, in agreement with the results reported here.

The change in front speed with w_0 may be correlated with an effective increase in reagent concentration per unit volume, and a corresponding increase in rate of reaction of autocatalysis. There will be a higher aqueous volume in the tube for higher w_0 values. The increase in velocity with bromate for the same w_0 and ϕ_d is modest compared to the equivalent increase in bromate in the propagation of aqueous phase fronts in the same diameter tube. This might be explained by the dilution of heat in the overall volume of the microemulsion.

ii) CTAB

Reaction-diffusion fronts of the bromate sulfite reaction in a CTAB microemulsion display characteristics of fronts with convective instabilities (48), (49), (50). The corresponding aqueous phase front, when performed in the same i.d. size tube, fills the tube and has a planar front (see chapter 1, section 1.3.4). For low droplet fraction, the reaction-diffusion fronts are turbulent and initiations occur throughout the tube sometimes giving rise to no clear front boundary. As the droplet fraction increases the fronts begin to resemble plumes, taking up an increasing width of the tube. The increase in speed, with increasing ϕ_d could be correlated with an effective increase in concentration of reactants per unit volume. More heat will be evolved as the concentration of acid produced increases and this may give rise to faster fronts, partly driven by stronger convection.

For small w_0 the fronts are turbulent and fingering is observed where single fingers can travel up the tube. Fingering occurs when fluid with lower mobility displaces another of higher mobility. The variation in mobility can be because of differences in viscosity and/ or density between the two fluids. As the reaction diffusion-fronts propagates in the novel microenvironment, changes in microemulsion structure may occur (on the production of acid or due to the exothermicity of reaction). These changes may result in variations in viscosity or density of the microenvironment. These viscosity or density gradients may be the origin of this fingering, which affects the front shape, stability and velocity.

As w_0 is increased the front becomes more stable, up to $w_0 = 16$ where turbulent fronts travel up the tube in a spiral type motion. The fronts can also become 'extinguished' for some values of w_0. The origin of these instabilities is unknown. although similar behaviour has been seen in reaction-diffusion systems displaying

density fingering (51) and viscosity fingering (52). Reaction diffusion fronts in these systems, the CTAB microemulsion in particular, present possibilities for the investigation of these instabilities and the effects on front propagation in heterogeneous media.

5.5 Conclusions

These experiments represent the first investigation of acid autocatalysis in microemulsions. There are two elements of the reported behaviour that need to be considered. First is the kinetics of nonlinear, autocatalytic reactions performed in microemulsions. It has been suggested here that a decrease in the rate of reaction can be correlated with a change in the water properties with decreasing w_0. In support of this postulation, Vanag *et. al* (53) has reported rate constants in reverse micelles of AOT to be an order of 1 -3 smaller than those in aqueous media. It has also been proposed that the micro-viscosity of the water pool can give rise to a decrease in the rate constant of an autocatalytic reaction (54). In addition to this Gandin *et. al* have shown that the micro-viscosity of the pool markedly decreases with increasing w_0 (55). Qualitative descriptions of the interior of the Triton-X and CTAB microemulsions has been given in an attempt to explain the effect on the kinetics in each system. A pseudo phase model is proposed, involving reagents located in the water core and the interface of the microemulsion. A detailed consideration of the mechanism of the clock time and the origin of autocatalysis facilitated an explanation of the batch kinetics in both systems.

Knowledge of the specific water pool properties for each microemulsion system, for example the microviscosity, local polarity, local acidity and their heterogenous structure (distribution along the water pool radius direction) is required

to fully understand the unique reaction kinetics in these hydrophilic nanospaces. To enable a full characterisation of the water pools in CTAB and Triton-X microemulsions further experiments are necessary. Dynamic light scattering can give an insight into the size distribution of reverse micelles (56). Spectroscopic methods, such as infra-red absorption spectroscopy have been used to investigate the dynamics of the water interior (43). Equally, a more in-depth study of the batch kinetics of autocatalytic reactions in a variety of microemulsions may give insight into the structure of water in these structures and how this can affect dynamics.

The results reported here have been explained by consideration of spherical or oval micro-droplets of water dispersed in the oil phase. However, it is important to note that the exact structure of the water-in-oil microemulsions during the bromate sulfite reaction is not known. The structure of the microemulsion may also depend on the chemical composition (57), (58) and change during the course of the reaction, particularly as heat and acid are evolved. This provides the potential of a feedback between changes in thermodynamic structure of microemulsions and the nonlinear chemical reaction.

The second element that should be considered is the formation of spatiotemporal structures, when nonlinear dynamics is coupled with diffusion in a microemulsion environment. These micro-heterogeneous environments present novel systems for the study of acid reaction-diffusion fronts. In particular, reaction diffusion fronts in the CTAB system are subject to convective instabilities that give rise to fingering, and other interesting structures. These effects are not seen in the corresponding aqueous phase, or Triton-X fronts. Unstable fronts leaving turbulent structures in their wake, extinguishing or travelling up the tube in a spiral-type motion were observed. This system therefore provides a novel environment for the

study of convection and viscosity or density related fingering in acid reaction-diffusion fronts. Magnetic resonance imaging (59) of the reaction-diffusion fronts may allow imaging of the fluid flow that gives rise to these fascinating structures. This imaging may also reveal changes in microemulsion structure as the acid front invades the un-reacted micromeulsion.

There is ample scope for continuation of this work, both in terms of the batch kinetics and spatio-temporal behaviour. Studies of the dynamics of water confined in reverse micelles (microemulsions), and of reaction kinetics in these environments are current areas of research in the fields of nano- and materials science. The possibility of studying nonlinear chemical reactions in such an environment offers insight into factors affecting the kinetics and behaviour of these systems in confinement. Interesting spatial behaviour may result from the coupling of changes in microemulsion structure driven by chemical reaction. In this system it is plausible to suggest that the production of acid and heat (due to the exothermicity of reaction) changes the structural properties of the microemulsions. Thus, the chemical reaction drives changes in thermodynamic structure.

5.6 References

(1) M Hossain, Y Hayashi, N Shimizu, T Kawanashi: A kinetic model for Enzymatic Reaction in a Reverse Micellar System, involving water-insoluble substrate. J. Chem. Tech. Biotech. 67 (1996) 190.

(2) G Chang, T Huang, H Hung: Reverse Micelles as Life-Mimicking Systems. Proc. Natl. Sci. Counc. 24 (1999) 89.

(3) M Yoshikazu: Enzymatic reaction in water-in-oil microemulsion. Colloids and Interfaces 109 (1996) 255.

(4) L Brinchi, R Germani, G Savelli, N Spreti: S_N2 displacement by bromide ions in dichloromethane - The role of reverse micelles. European Journal of Organic Chemistry (2006) 4270.

(5) S Abel, M Waks, W Urbach: Journal of the Americal Chemical Society 128 (2006) 382.

(6) B Orlich, R Schomacker: Advances in Biochemical Engineering/ Biotechnology, Springer Berlin/ Heidelberg, Berlin, 2001.

(7) F Menger, K Yamada: Enzyme catalysis in water pools. J. Am. Chem. Soc. 101 (1979) 6731.

(8) V Uskokovic, M Drofenik: Synthesis of materials within reverse micelles. Surface Review and Letters 12 (2005) 239.

(9) V Uskokovic, M Drofenik, I Ban: The characterization of nanosized nickel-zinc ferrites synthesized within reverse micelles of CTAB/ 1- hexanol/ water microemulsion. Journal of Magnetism and Magnetic Materials 284 (2004) 294.

(10) S Xiaomeng, Y Chu, X Shuangxi, C Liu: Synthesis of PANI/ AgCl, PANI BaSO4 and PANI/ TiO_2 nanocomposites in CTAB/ hexanol/ water reverse micelle. Materials letters 58 (2004) 1255.

(11) C Valenta, K Schultz: Influence of carrageenan on the rheology and skin permeation of microemulsion formulations. Journal of Controlled Release 95 (2004) 257.

(12) A Sintov, L Shapiro: New Microemulsion vehicle facilitates percutaneous penetration in vitro and cutaneous drub bioavailability in vivo. Journal of Controlled Release 95 (2004) 173.

(13) A Gupta, M Gupta, S Yarwood, A Curtis: Effect of cellular uptake of gelatin nanoparticles on adhesion morphology and cytoskeleton organisation of human fibroblasts. Journal of Controlled Release 95 (2004) 197.

(14) VK Vanag, IR Epstein: Pattern formation in a tunable medium: The Belousov-Zhabotinsky reaction in an aerosol OT microemulsion. Physical Review Letters 8722 (2001).

(15) VK Vanag, IR Epstein: Dash waves in a reaction-diffusion system. Physical Review Letters 90 (2003).

(16) IR Epstein, VK Vanag: Complex patterns in reactive microemulsions: Self-organized nanostructures? Chaos 15 (2005).

(17) VK Vanag, IR Epstein: Segmented spiral waves in a reaction-diffusion system. Proceedings of the National Academy of Sciences of the United States of America 100 (2003) 14635-38.

(18) IR Epstein, VK Vanag: Complex Patterns in reactive microemulsions: Self-organized nanostructures? . Chaos 15 (2005) 047510/1.

(19) RG Gonda I: Oscillatory behaviour of a BZ reverse micelle system. Journal of Physical Chemistry 94 (1990) 1516-19.

(20) B Baruah, J Roden, M Sedgwick, N Correa, D Crans, N Levinger: When is Water Not Water? Exploring Water Confined in Large Reverse Micelles Using a Highly Charged Inorganic Molecular Probe. Journal of the American Chemical Society 128 (2006) 12758.

(21) L Shrestha, T Sato, K Aramaki: Shape, Size, and Structural Control of Reverse Micelles in Diglycerol Monomyrisate Nonionic Surfactant System. Journal of Physical Chemistry B 111 (2007) 1664.

(22) R Rodriguez, S Vargas, D Fernandez-Valasco: Reverse Micelle Systems Composed of Water, Triton X-100 and phopholipids in organic solvents. Journal of Colloid and Interface Science 197 (1998) 21.

(23) E Dabek-Zlotorzynska, M Piechowski, K Keppel-Jones, R Aranda-Rodriguez: Determination of hydroxymethanesulfonic acid in environmental samples by capillary electrophoresis. Journal of Separation Science 25 (2002) 1123-28.

(24) P Ekwall, L MAndell, K Fontell: The CTAB-Hexanol-Water system. Journal of Colloid and Interface Science 29 (1968) 639.

(25) MW Daoud, C.E.: Soft Matter Physics, Germany, 1995.

(26) AV Barzykin, K Seki, M Tachiya: Kinetics of diffusion-assisted reactions in microheterogeneous systems. Advances in Colloid and Interface Science 89-90 (2001).

(27) J Faeder, BM Ladanyi: Molecular Dynamics Simulations of the Interior of Aqueous Reverse Micelles. Journal of Physical Chemistry B 104 (2000) 1033.

(28) J Tanori, T Gulik- Krzywichi: Langmuir 13 (1997) 632.

(29) A Keresztessy, I Nagy, G Basza, J Pojamn: Travelling Waves in the Iodate Sulfite and Bromate Sulfite Systems. J. Phys. Chem. 99 (1995) 5379.

(30) K Hamada, T Ikeda, T Kawai, K Kon-No: Ionic strength effects of electrolytes on solubilized states of water in AOT reversed micelles. Colloid and Interface Science 233 (2001) 166.

(31) T Jain, A Maitra: Journal of Physical Chemistry 93 (1989) 7409.

(32) H MacDonald, B Bedwell, E Gulari: Langmuir 2 (1986) 704.

(33) D Fioretto, M Freda, G Onori, A Santucci: journal of Physical Chemistry B 103 (1999) 2631.

(34) A Dokter, S Woutersen, H Bakker: Physical Review Letters 94 (2005) 178301.

(35) J Silber, A Biasutti, E Abuin, E Lissi: Interactions of small molecules with reverse micelles. Advances in Colloid and Interface Science 82 (1999) 189.

(36) C Sodre, H Scofano, H Barrabin: Calcium dependence of Pi phosphorylation of sacroplasmin reticulum Ca^{2+}- ATPase at low water content: water dependence of the E_2 - E_1 conversion. Biochimica et Biophysica 1419 (1999) 55.

(37) D Fernandez-Valasco, R Rodriguez, S Vargas, M Tuena de Gomez, A Gomez: Reverse micelles composed of water, TX-100 and phoshpholipids in organic solvents 2. Catalysis and thermostability of hexokinase. Journal of Colloid and Interface Science 197 (1998) 29.

(38) M hasegawa: Buffer- like action in water pool of AOT reverse micelles. Langmuir 17 (2001) 1426.

(39) M Almgren, J Stam, S Swarup, J Lofroth: Structure and transport in the ME phase of the system triton X 100 toleuen water. Langmuir 2 (1986) 432.

(40) D Rosenfeld, C Schmuttenmaer: Dynamics of water confined in reverse micelles. J. Phys. Chem. B 110 (2006) 14304.

(41) VK Vanag, D Melikhov: Asymetrical Concentration Fluctuations in the Autocatalytic Bromate-Bromide-Catalyst Reaction and in the Oscillatory Belousov-Zhabotinsky Reaction in a Closed Reactor: Stirring Effects Journal of Physical Chemistry 99 (1995) 17372.

(42) J Liou, T Huang, G Chang: Reverse micelles as a catalyst for the nucleoplhilic aromatic substitution between glutathione and 2,4-dinitrochlorobenzene. Perkin Transactions 2 (1999) 2171.

(43) A Dokter, S Woutersen, H Bakker: Ultrafast dynamics of water in cationic micelles. Journal of Chemical Physics 126 (2007) 124507.

(44) F Casavino, M Sbriziolo, M Turco Liveri: Journal of Physical Chemistry 102 (1998) 5050.

(45) C Chen, C Yeh: Kinetic model for the enzymatic hydrolysis in reverse micelles. Biotechnology Letters 20 (1998) 49.

(46) L Garcia-Rio, J Leis, J Mejuto: Journal of Physical Chemistry 100 (1996) 10981.

(47) J Masere, V Desiderio, B Edwards, J Wilder, K Showalter: Nonaxisymmetric and Axisymmetric Convestion in Propagating Reaction - Diffusion Fronts Journal of Physical Chemistry 98 (1994) 6505.

(48) T Bansagi, D Horvath, A Toth, J yang, S Kalliadis, A De Wit: Density fingering of an exothermic autocatalytic reaction. Physical Review E 68 (2003) 055301.

(49) J D'Hernoncourt, A Zebib, A De Wit: On the classification of buoyancy driven chemo-hydrodynamic instabilities of chemical fronts. Chaos 17 (2007) 013109.

(50) A De Wit, Y Bertho, M Martin: Viscous fingering of miscible slices. Physics of Fluids 17 (2005) 054114.

(51) A De Wit: Miscible density fingering of chemical fronts in porous media: Nonlinear simulations. Physics of Fluids 16 (2004) 163.

(52) A De Wit, GM Homsy: Viscous fingering in rection-diffusion systems. Journal of Chemical Physics 110 (1999) 8663.

(53) VK Vanag, V Dmitri: Behaviour of the BZ reaction in Reverse micelles of AOT in Octane. J. Phys. Chem. 98 (1994) 1449.

(54) VK Vanag, D Bulanov, M Alfimov: Autocatalytic oxidation of $Fe(Phen)_3^{2+}$ by bromate in water in oil reverse micelles of AOT. Seriya Khimicheskaya - Journal written in Russian 8 (1993).

(55) E Gandin, Y Lion, A Van De Vorst: Journal of Physical Chemistry 88 (1984) 280.

(56) K Poonam, V Sonalika, A Tokeer, A Ganguli: Optimizingthe hyrodynamin radii and polydispersivity of reverse micelles in the triton X / water/ cylcohexane system using dynamic light scattering and other studies. Colloids and Interfaces 293 (2007) 162.

(57) JP Huruguen, MP Pileni: Drastic Change of Reverse Micellar Structure by Protein or Enzyme Addition. European Biophysics Journal 19 (1991) 103-07.

(58) C Petit, P Lixon, MP Pileni: Structural changes in AOT reverse micelles induced by changing the counterions. Progress in Colloid and Polymer Science 89 (1992) 328.

(59) A Taylor, M Britton: Magnetic Resonance Imaging of chemical waves in porous media. Chaos 16 (2006) 037103.

CHAPTER 6

Final conclusions and further work

6.1 Final Conclusions and Further Work

Acid- and base-regulated autocatalytic systems offer an exciting area of study in the field of nonlinear dynamics. The potential of coupling non-equilibrium pH chemical systems with soft matter means that chemical power could be directly converted into mechanical work, as discussed in chapter 1, section 1.1. The complex dynamics of these systems necessitates more work on the kinetics and behaviour of them to facilitate a better understanding of their behaviour.

This thesis has presented a range of studies regarding autocatalysis in pH regulated chemical systems, far from equilibrium. In chapter two an in-depth experimental study of the MGS reaction was reported. The clock times in batch were found to depend on initial concentrations of all species, and relationships were established. New experimental results were presented demonstrating that the system is able to support bistability in an open reactor, and display small amplitude oscillations for some initial conditions. These results encouraged us to look at the mechanism of this reaction as the then currently accepted model possessed no form of feedback in its kinetics. A new kinetic model for this system, based on old and new experimental data, was then developed in chapter 3. This model is able to successfully simulate all batch behaviour, and displays bistability under flow conditions. The core of the model is the base-catalysed dehydration of methylene glycol, a kinetic step vital to the dynamics of this system. Stirring effects were then added to this model to determine the sensitivity of the thermodynamic and flow branches to global mixing effects. It was shown that a decrease in the stirring rate can destabilise the high pH thermodynamic branch, thus giving a contraction of the hysteresis loop and shrinking the bistable region. These results gave improved correlation between experimental and numerical data.

Additional experimental research in to this system may prove beneficial as the origin of the small amplitude high pH oscillations was not sufficiently explored. These small amplitude oscillations are likely to be caused by some chemical species present in the system which has not yet been identified. A thorough experimental investigation may identify these species and allow for interesting kinetic analysis.

In chapter 4 a reduced model is discussed for the design of novel pH regulated chemical systems. The abstract model is based on the kinetic model of the MGS reaction developed in chapter 3, and offers a new route to the design of pH oscillators (different to that discussed in chapter 1, section 1.3). The core of the model is a base (or acid) catalysed dehydration step, coupled with a base (or acid) producing reaction. Kinetically this provides the necessary positive feedback for the observation of a clock reaction in batch conditions. When coupled with a simple consumption of base (or acid) the model is able to display bistability and oscillations in a flow reactor. We expect that this model will be used in the design of organic substrate based pH oscillators that may eventually lead to the development of less aggressive, non-redox oscillators. We point out the range of hydrated aldehydes that are subject to base and acid catalysed dehydrations.

The second part of chapter 4 presented the first example of such a chemical system, designed on the basis of this reduced model. The reaction between methylene glycol, sulfite and gluconolactone displays large amplitude pH oscillations in a flow reactor accompanied by small oscillations in potential. indicating that it is not driven by redox processes, unlike all other pH oscillators. These experiments demonstrated the possibilities for the design of novel pH oscillators. The experimental results were successfully modelled with a kinetic scheme that incorporated the base-catalysed dehydration of methylene glycol as

positive feedback, and the base-catalysed hydrolysis of gluconolactone as negative feedback. The balance between the two based catalysed reaction steps has displayed some interesting dynamic results, such as mixed mode oscillations, that were beyond the scope of discussion in this thesis. We therefore expect that this system will offer an exciting detailed kinetic analysis.

In chapter 5, acid autocatalysis was experimentally explored in a non-ionic (Triton X) and a cationic (CTAB) microemulsion. The bromate sulfite clock reaction was performed in these microemulsion systems and it was shown that the batch kinetics are affected by the change in droplet size (water volume, w_0) and the dispersion of droplets (droplet fraction, ϕ_d). We proposed that it is the change in the water pool characteristics in the polar core of the microemulsion which affects the kinetics. Qualitative descriptions of the interior of the Triton X and CTAB microemulsions was given in an attempt to explain the effect on the kinetics in each system. A pseudo phase model was proposed, involving reagents located in the water core and the interface of the microemulsion. A detailed consideration of the mechanism of the clock time and the origin of autocatalysis facilitated an explanation of the batch kinetics in both systems.

The effect of the micro-heterogeneties of the environment on the reaction-diffusion fronts was also investigated. Both microemulsion systems were able to support acid reaction-diffusion fronts in the bromate sulfite reaction. Fronts in the Triton X system were shown to travel with speeds an order of magnitude lower than the corresponding aqueous phase, and decrease in velocity with an increase in the droplet fraction. The structure of the fronts also changed from parabolic to planar. These results were attributed to changes in viscosity for variation of the droplet

fraction in the Triton X system. The front speed was found to be weakly dependent on the water content.

The cationic surfactant (CTAB) system also supported reaction diffusion fronts. In this system, fronts speeds increased with increasing droplet fraction. The front speed also decreased with increasing water content. Fronts in this particular microenvironment system were subject to convective instabilities giving rise to fingering and other structures not seen in corresponding aqueous phase fronts. Unstable fronts leaving turbulent structures in their wake, extinguishing or travelling up the tube in a spiral-type motion were observed. This system may therefore provide a novel environment for the study of convection and viscosity or density related fingering in acid reaction-diffusion fronts. Examination of the behaviour of the fronts in Hele – Shaw cells of small width would presumably yield some interesting results.

There is ample scope for continuation of this work, both in terms of the batch kinetics and spatio-temporal behaviour. Studies of the dynamics of water confined in reverse micelles (microemulsions), and of reaction kinetics in these environments are current areas of research in the fields of nano- and materials science. The possibility of studying nonlinear chemical reactions in these nano-spaces offers insight into factors affecting the kinetics and behaviour of these systems in confinement. Interesting behaviour may result from the coupling of changes in microemulsion structure driven by chemical reaction. In the bromate sulfite acid autocatalytic system, it is plausible to suggest that the production of acid and heat (due to the exothermicity of reaction) can drive structural changes in the microemulsions. Thus, the chemical reaction drives changes in thermodynamic structure.

APPENDIX

I

Appendix - Numerical Methods. XPP and AUTO

XPP is a tool for solving differential equations. The basic unit for XPP is a single ODE file that has the differential equations, parameters. variables. boundary conditions and functions for the model. Numerical parameters such as time step. method of integration and tolerance are also included, although these can be altered in the programme. Numerical modelling in this thesis exclusively uses CVODE as a solver. The following example is of a four variable reduced model for the oscillatory iodate-sulfite-ferrocyanide reaction (1). The equations describing the chemistry are given in Table A.1

$A + H \leftrightarrow X$	$R_1 = k_1[A][H]$ $R_{-1} = k_{1r}[X]$	$k_1 = 5\times10^{10}\,M^{-1}s^{-1}$ $k_{1r} = 8.1\times10^{3}\,s^{-1}$	(1)
$X \rightarrow H$	$R_2 = k_2[X]$	$k_2 = 6\times10^{-2}\,s^{-1}$	(2)
$2H \rightarrow Z$	$R_3 = k_3[H]^2$	$k_3 = 7.5\times10^{4}\,M^{-1}s^{-1}$	(3)
$Z + X \rightarrow 3H$	$R_4 = k_4[Z][X]$	$k_4 = 2.3\times10^{9}\,M^{-1}s^{-1}$	(4)
$Z \rightarrow$	$R_5 = k_5[Z]$	$k_5 = 30s^{-1}$	(5)

Table A.1 Rate laws for the four variable model describing the iodate-sulfite-ferrocyanide reaction, model A.

Where A = SO_3^{2-}, X = HSO_3^-, H = H^+ and Z = I_2. Reaction 1 corresponds to the sulfite-bisulfite equilibrium, reaction 2 to the direct uncataylsed iodate oxidation of bisulfite. Reaction 3 corresponds to the Dushmann reaction, and reaction 4 to the iodine oxidation of bisulfite. Reaction 5 is the iodine oxidation of ferrocyanide and fulfils the role of the negative feedback.

Appendix I

The ODE is written as:

```
# J. Phys. Chem. 94, (12) 1990
#
A'=-k1*A*Y+k1r*X+k0*(A0-A)
H'=-k1*A*Y+k1r*X+k2*X-2*k3*Y^2+3*k4*Z*X+k0*(Y0-Y)
X'=k1*Y*A-k1r*X-k2*X-k4*X*Z+k0*(X0-X)
Z'=k3*Y^2-k4*Z*X-k5*Z+k0*(Z0-Z)
#
aux pH=-log(H)/log(10)
aux pX=-log(X)/log(10)
#
#parameters
par   H0=0.004,  k0=0.002,  k1=5e10,  k1r=8.1e3,  k2=6e-2,  k3=7.5e4,
k4=2.3e9, k5=3e1, A0=9e-2, X0=0, Z0=0
#
#some initial conditions
init H=4e-3, A=9e-2, X=0, Z=0
@ total=5000,dt=0.01,tol=1e-12,atol=1e-6,meth=cvode
@ xplot=t,yplot=pY,xhi=5000,ylo=3,yhi=12
@ maxstor=5000000
#
done
```

The file is self explanatory. The ODEs are given at the beginning of the file, with a line each. The auxiliary variables pH and pX are defined as these are not variables that define the dynamical system. Parameters and declared with the par statement, and initial conditions with init. The total amount of integration time is set as 5000 s, with dt, the size of the timestep (this is fixed for CVODE) equal to 0.01 s. This means the equations are integrated over 5000 s in time steps of 0.01 s. The tolerance (1×10^{-12} here) is the relative tolerance, and atol (1×10^{-6}) is the absolute tolerance value. If the programme cannot integrate the ODEs tolerances can be changed within the programme (numerics→ method→CVODE→'tolernace set at'). Method is the ODE solver chosen, CVODE here. CVODE is an adaptive integrator written in the computer language 'ANSI-standard C'. It is available through XPPAUT. It uses Adams method for nonstiff systems and backward-differentiation-formula (BDF) methods for stiff problems, such as those investigated here. The command line xplot=t,yplot=pY,xhi=5000,ylo=3,yhi=12 specifies the axes and their ranges. Maxstor=5000000 tells XPP how many points to store. the default is 4000 time

points. The file ends with the statement 'done'. Running the ODE gives the following pH time trace.

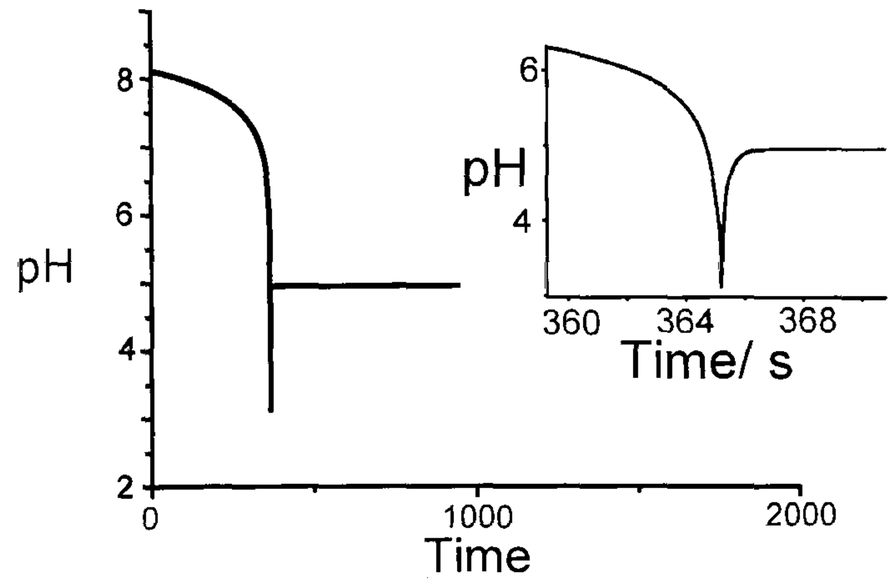

Figure A.1 pH time trace for model .Inset is enlarged axes at the clock time.

When the programme is executed, the main screen appears. To solve the equations and plot results, click the 'initial conditions' tab and press 'go'. The axis can be changed through 'viewaxes' .The data is viewed through the data viewer and can be saved from the 'write data' command. The initial conditions and parameters can be changed with the 'init cond' and 'param' tabs respectively.

AUTO is a continuation package capable of finding fixed points of systems and tracking them as a parameter varies as well as tracking solutions to differential equations, periodic orbits and homoclinic orbits. Bifurcation points can also be tracked in 2 parameter phase space. To start in AUTO, a stable steady state must be found in XPPAUT. This means that the solution should settle onto a fixed point. to do this run 'initial conditions → last' (pH = 4.305 in the present example.) Click 'file → auto' to bring up the auto window. In this window there are additional menu items and several windows. The lower left shows a circle. The number of crosses inside (outside) the circle corresponds to the number of stable (unstable) eigenvaules for a solution. The two windows at the bottom are information about the computed

points and hints or tips window respectively. The main window is where bifurcation diagrams are drawn. Figure A.2 shows the AUTO interface.

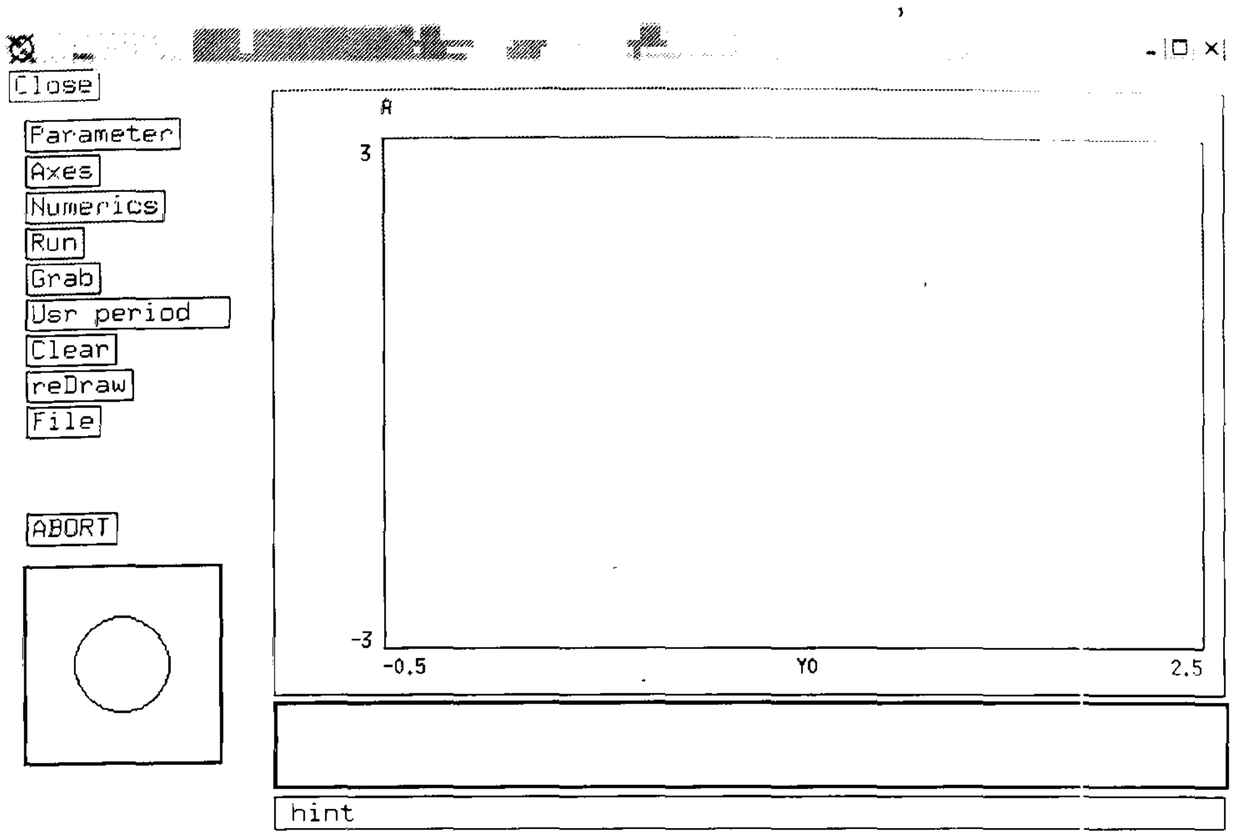

Figure A.2 The AUTO interface

The parameter item tells AUTO the list of parameters that will be varied in this session, the default is the first 5 defined in the ODE file. The axes command is used to define what parameters are to be varied and what is to be plotted as well as the range of the graphs. The numerics command is used to define all the AUTO numerical parameters such as direction, step size and tolerance. The run command runs the bifurcation. Typical values of the numerics used in this work for bifurcation diagrams are Ntst = 60, Nmax = 200000, Npr = 50000, Ds = 2×10^{-6}, Dsmin = 1×10^{-8}, Ncol = 4, EPSL = 0.0001, Dsmax = 1×10^{-5}, Parmin = 0, Parmax = 0.004. Norm min = 0, Normmax = 1000, EPSU = 0.0001, EPSSU = 0.0001. Where Ntst. Nmax and Npr are the tolerances, Ds, Dsmin and Dsmax are the time step, minimum and maximum respectively. Parmin is the lowest parameter value (i.e.the lowest value of H0 required here) and Parmax is the highest parameter value (0.004 here). Normmin, Normmax and EPSU, EPSSU and EPSSS are all associated with tolerance. Click 'run→steady states' to run the bifurcation diagram. The bifurcation diagram in Figure A.3 is drawn from the given data values, calculating the value of –

log (H) to give pH. The first point calculated in AUTO will be for H0 = 0.004, to follow the diagram to the left, 'grab' this point and press 'enter'. Go into numerics and change Ds from 2×10^{-6} to -2×10^{-6}, this means the parameter value (H0) will now be decreased (from 0.004 to 0). Click 'run→steady states' again.

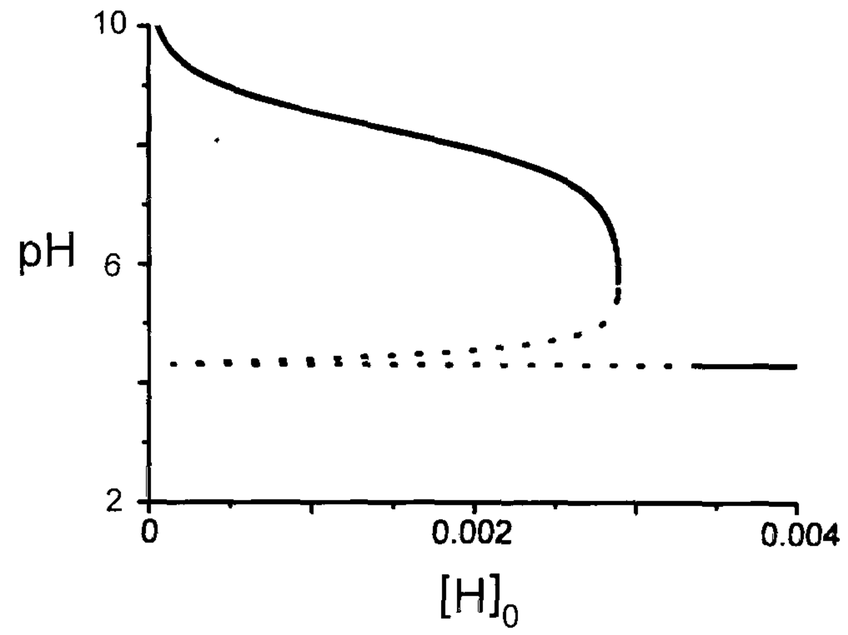

Figure A.3 Bifurcation diagram for model A produced from AUTO

If AUTO fails to follow the fixed points, or misses a bifurcation which is clearly there, the time step and epsilon values should be changed. Time steps should be made smaller (limiting Dsmax to a minimum of 1×10^{-5}). EPS values can be changed to as low as 1×10^{-6}. Sometimes it is useful to change Ntst to 120 or lower to 15. Reset the diagram by grabbing the starting point, then to file→ reset, delete the old diagram and re-compute the result. If XPPAUT is not on a true fixed point it will not be possible to draw the bifurcation diagram.

To move around the bifurcation diagram use the grab command, and the file command to save points. Bifurcation points are labelled in AUTO, and unstable steady states are followed. There is a Hopf point at H_0 = 0.00339, k_0 = 0.002, H = 4.944e-5, Period = 0.8175, and saddle node limit points at H_0 = 0.0001465, k_0 = 0.002, H = 4.849e-5 and H_0 = 0.002893, k_0 = 0.002, H = 1.981e-5. To write the data file 'file → write points'. This example will give data files with 5 columns. The first

is the parameter values (H0), the second and third are the variable values (H) and the fourth and fifth give the stability of the points. 1 is stable steady state, 2 unstable steady state, 3 stable limit cycle and 4 is an unstable limit cycle. To follow a periodic orbit, grab the Hopf bifurcation and press enter, this point is now loaded into AUTO. Press 'run→periodic' .This will give the limits of the oscillations.

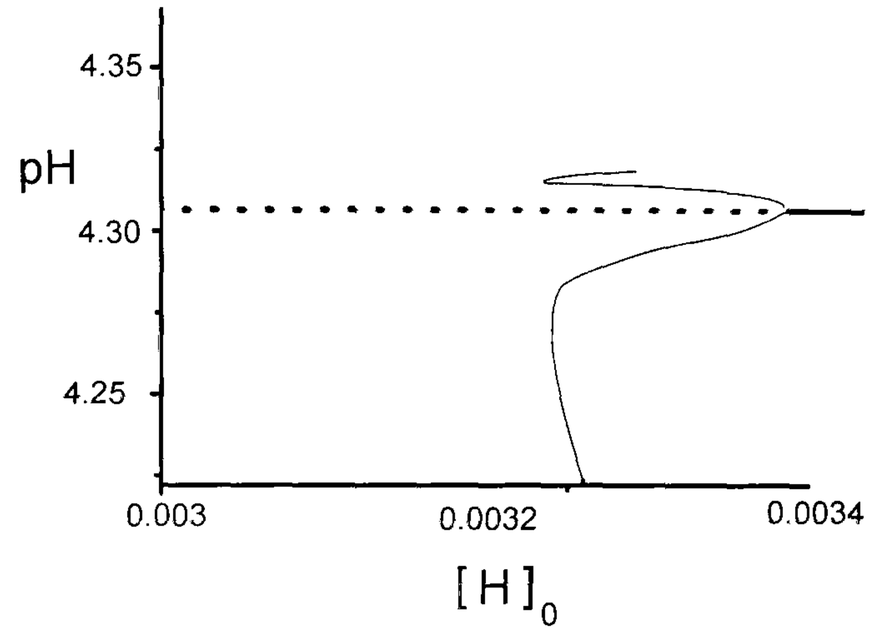

Figure A.3 Enlargement of the hopf bifurcation at k_0 = 0.002, showing 'canard type' behaviour.

Bifurcation points can also be followed in 2 parameter phase space. Grab the BP of interest and go to 'axis → 2 par' to give the new ranges of the axis. We are now plotting the first parameter (H0) here against the second parameter (k_0 here) so the ranges will be different. The numerics will also need to be changed, especially the time steps as we are now looking at a much bigger area of phase space. Typically Ds = 2×10^{-2}, Dsmin = 1×10^{-4}, Dsmax = 1×10^{-2}. The rest of the numerics are usually OK left as they were. Press 'OK' then regrab the BP point of interest, the point now appears in the phase space. Go to 'run→two param' and a line will appear mapping out the line of bifurcation points in phase space. The direction of DS is still important. Again, the data is saved by 'file → write points'

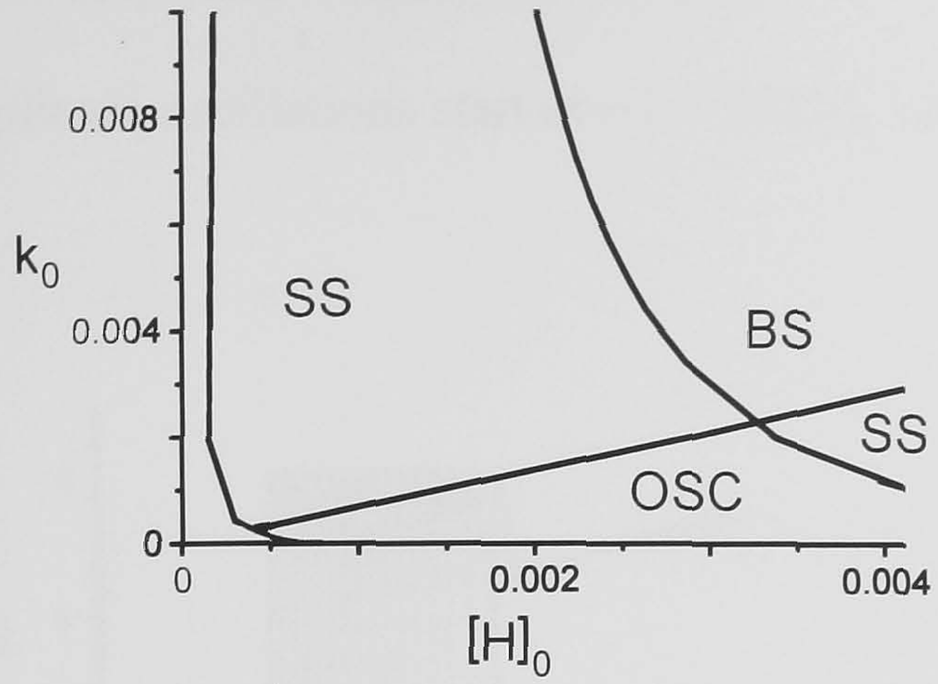

Figure A.4 Phase diagram showing continuation of hopf and limit points in 2 parameter phase space.

The Hopf bifurcation in Figure A.3 (k_0 = 0.002) was originally thought to be a Canard bifurcation (2), (3). However, AUTO facilitates a more detailed numerical investigation than previous numerical techniques (4), and the bifurcation point actually gives rise to a region of coexisting limit cylces. This is not a Canard explosion. The onset of oscillations in H is shown with increasing H0 from H0 = 0.0027, k_H = 1e-8. Final H0 = 0.0035. These traces were computed in XPPAUT. Figure on the right shows an enlargement of the transition (y axis now [H] not pH). The large amplitude oscillations are sustained up to ~ t = 62111s (H0 = 0.0033211), the small amplitude oscillations end at ~ t = 69730, H0 = 0.0033973.

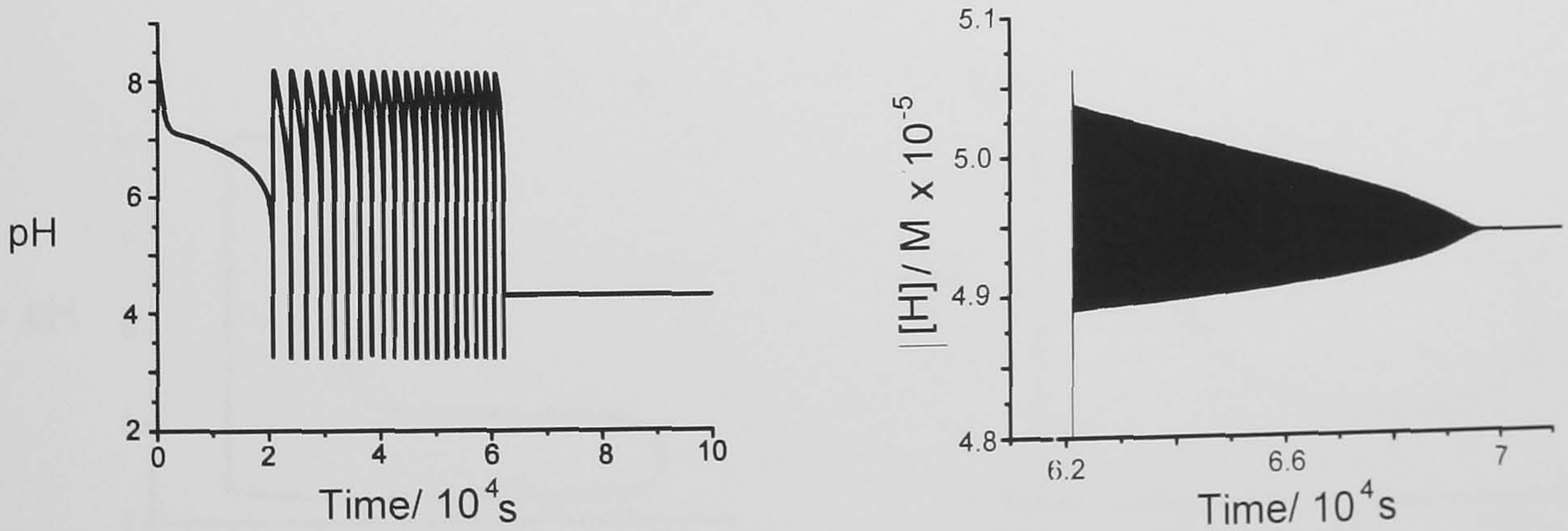

Figure A.5 (a) onset of oscillations in pH with increasing H0 from H0 = 0.0027, k_H = 1e-8

(b) Enlargement of the transition to small amplitude oscillations

If H0 is decreased (Figure A.6) from H0 = 0.0035 with a rate of k_H = -1e-8 we can see the transition from small amplitude oscillations to big amplitude oscillations. The

small amplitude oscillations start at ~ t = 12620s, Y0 = 0.0033738 and the large amplitude oscillations start at ~ t = 26220, Y0 = 0.0032378.

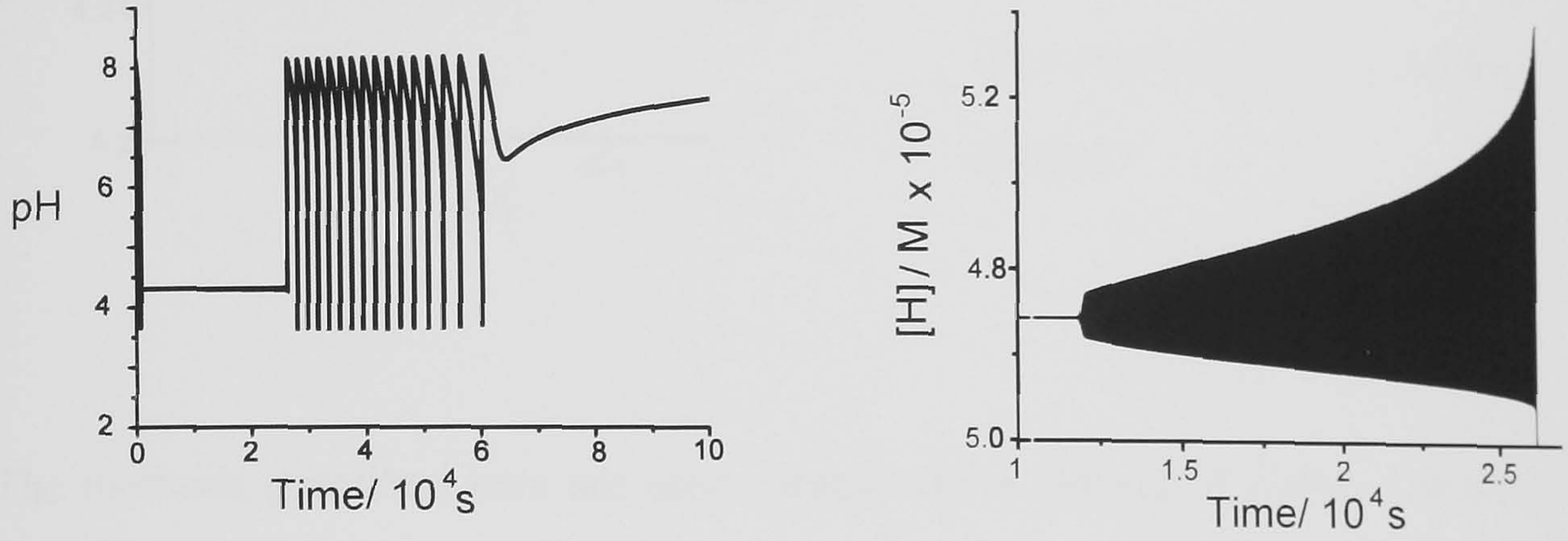

Figure A.6 (a) onset of oscillations in pH with decreasing H0 from H0 = 0.0035, k_H = -1e-8 (b) Enlargement of the transition from small amplitude oscillations to big amplitude.

Therefore, there exists a region of bistability between small and large amplitude oscillations. This is demonstrated by taking H0 = 0.003257 and examining the hysteresis behaviour. Figure A.7 (A) shows the large amplitude, long period and the small amplitude short period limit cycles in the pX pH phase plane respectively for H0 = 0.003257. Figure A.8 shows both limit cycles coexisting (enlargement of axis).

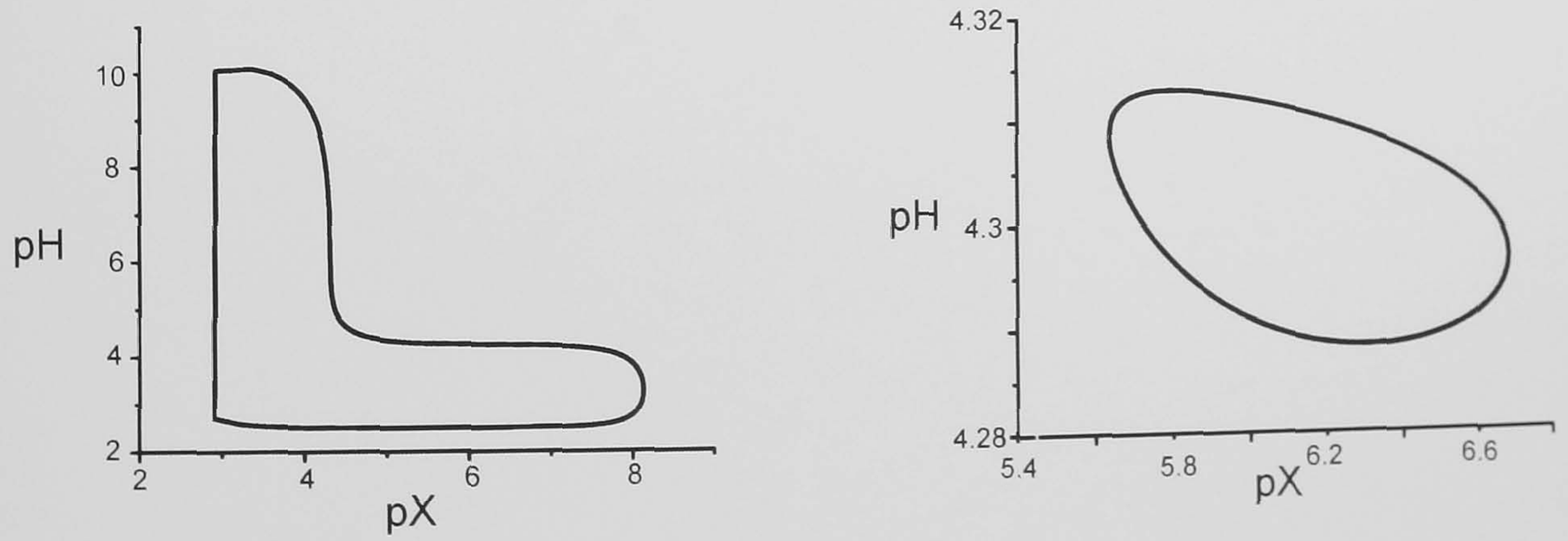

Figure A.7 pX – pH phase planes showing the (a) large amplitude, long period oscillations and (b) Small amplitude, short period limit cycles.

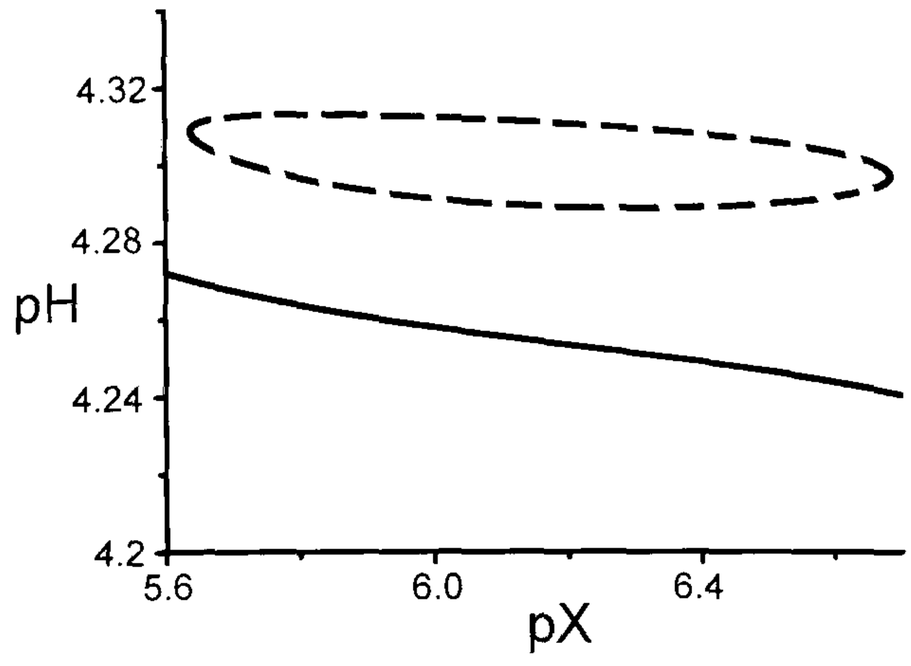

Figure A.8 pX – pH phase planes showing coexistence of small and large amplitude limit cycles for H0 = 0.003257.

The methods described here are used extensively in chapters 3 and 4 of this thesis. Models developed directly from chemical systems (the methylene-glycol - sulfite reaction) and conceptual models (reduced forms) are studied and analysed using XPP and AUTO.

References

(1) V Gaspar, K Showalter: A Simple Model for the Oscillatory Iodate Oxidation of Sulfite and Ferrocyanide. Journal of Physical Chemistry 94 (1990) 4973-79.

(2) B Peng, V Gaspar, K Showalter: False Bifurcations in Chemical-Systems - Canards. Philosophical Transactions of the Royal Society of London Series a-Mathematical Physical and Engineering Sciences 337 (1991) 275-89.

(3) V Gaspar, K Showalter: The Oscillatory Landolt Reaction - Empirical Rate Law Model and Detailed Mechanism. Journal of the American Chemical Society 109 (1987) 4869-76.

(4) V Gaspar, K Showalter: The Oscillatory Iodate Oxidation of Sulfite and Ferrocyanide. Abstracts of Papers of the American Chemical Society 196 (1988) 115-INOR.

I

APPENDIX

II

CHAPTER 3 – Macromixing model

The Macromixing model – Section 3.5.2

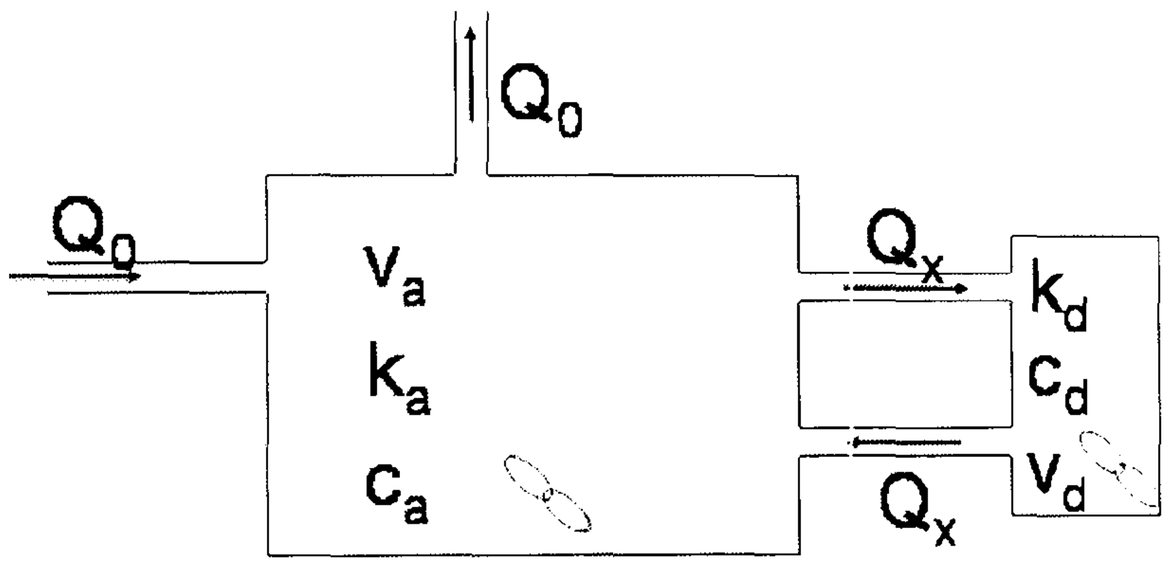

Figure 3.22 Schematic of behaviour in the dead zone model of imperfect mixing in a CSTR.

In the active zone:

$$\frac{dc_a}{dt} = \text{chemistry} + \frac{k_0}{1-x}(c_0 - c_a) - z\left(\frac{k_0}{1-x}\right)\left(\frac{x}{1-x}\right)(c_a - c_d)$$

In the dead zone:

$$\frac{dc_d}{dt} = \text{chemistry} + z\left(\frac{k_0}{1-x}\right)(c_a - c_d)$$

$$\frac{Q_o}{V_a} = k_a, \quad \frac{Q_x}{V_d} = k_d, \quad \frac{Q_0}{V_r} = k_0, \quad V_r = V_a + V_d, \quad x = V_d / V_r, \quad z = k_d / k_a$$

In the active zone :

$$n_a = Q_0 c_0 - Q_x c_a - Q_0 c_a + Q_x c_d$$

$$n_a / V_a = c_a = \frac{Q_0 c_0}{V_a} - \frac{Q_x c_a}{V_a} - \frac{Q_0 c_a}{V_a} + \frac{Q_x c_d}{V_a}$$

$$c_a = k_a c_0 - k_a c_a - \frac{Q_x}{V_a} c_a + \frac{Q_x}{V_a} c_d$$

$$c_a = k_a (c_0 - c_a) - \frac{Q_x}{V_a} (c_a - c_d)$$

$$V_r = V_a + V_d, \quad x = V_d / V_r$$

$$1 = V_a / V_r + V_d / V_r = V_a / V_r + x$$

$$1 - x = V_a / V_r$$

$$k_a = \frac{k_0 V_r}{V_a} = \frac{k_0}{1 - x}$$

$$\frac{Q_x}{V_a} = \frac{Q_x}{V_r - V_d} = \frac{k_d}{1/x - 1} = k_d \frac{x}{1 - x} = k_a z \frac{x}{1 - x} = z\left(\frac{k_0}{1 - x}\right)\left(\frac{x}{1 - x}\right)$$

Thus ODE in the active zone becomes :

$$\frac{dC_a}{dt} = \text{chemistry} + \frac{k_0}{1 - x}(c_0 - c_a) - z\left(\frac{k_0}{1 - x}\right)\left(\frac{x}{1 - x}\right)(c_a - c_d)$$

In the dead zone :

$$n_d = Q_x c_a - Q_x c_d$$

$$n_d / V_d = c_d = \frac{Q_x c_a}{V_d} - \frac{Q_x c_d}{V_d}$$

$$c_d = k_d c_a - k_d c_d = k_d (c_a - c_d)$$

Thus ODE in the dead zone becomes

$$\frac{dC_d}{dt} = \text{chemistry} + z\left(\frac{k_0}{1 - x}\right)(c_a - c_d)$$

:

Appendix II

ODE script for macromixing effects in the model of the MGS reaction

#MGS reaction with macromixing terms
#
CH2OH'=-k1*CH2OH-k1a*CH2OH*OH+k1r*CH2O-k7*CH2OH*S-k8*CH2OH*HS+k0/(1-x)*(CH2OHi-CH2OH)+(x/(1-x))*(z*(k0/(1-x)))*(CH2OH2-CH2OH)

CH2O'=k1*CH2OH+k1a*CH2OH*OH-k1r*CH2O-k3*CH2O*S-k6*CH2O*HS-k9*CH2O*OH+k0/(1-x)*(CH2Oi-CH2O)+(x/(1-x))*(z*(k0/(1-x)))*(CH2O2-CH2O)

HS'=-k2*HS+k2r*S*H-k6*CH2O*HS-k8*CH2OH*HS+k0/(1-x)*(HSi-HS)+(x/(1-x))*(z*(k0/(1-x)))*(HS2-HS)

S'=k2*HS-k2r*S*H-k3*CH2O*S-k7*CH2OH*S+k0/(1-x)*(Si-S)+(x/(1-x))*(z*(k0/(1-x)))*(S2-S)

H'=k2*HS-k2r*S*H-k4*HMSM*H+k4r*HMS+k5-k5r*H*OH-k10*HCOO*H+k10r*HCOOH+k0/(1-x)*(Hi-H)+(x/(1-x))*(z*(k0/(1-x)))*(H2-H)

HMSM'=k3*CH2O*S-k4*HMSM*H+k4r*HMS+k7*CH2OH*S+k0/(1-x)*(HMSMi-HMSM)+(x/(1-x))*(z*(k0/(1-x)))*(HMSM2-HMSM)

HMS'=k4*HMSM*H-k4r*HMS+k6*CH2O*HS+k8*CH2OH*HS+k0/(1-x)*(HMSi-HMS)+(x/(1-x))*(z*(k0/(1-x)))*(HMS2-HMS)

OH'=k5-k5r*H*OH-k9*CH2O*OH+k0/(1-x)*(OHi-OH)+(x/(1-x))*(z*(k0/(1-x)))*(OH2-OH)

CH2OH2'=-k1*CH2OH2-k1a*CH2OH2*OH2+k1r*CH2O2-k7*CH2OH2*S2-k8*CH2OH2*HS2+z*(k0/(1-x))*(CH2OH-CH2OH2)

CH2O2'=k1*CH2OH2+k1a*CH2OH2*OH2-k1r*CH2O2-k3*CH2O2*S2-k6*CH2O2*HS2-k9*CH2O2*OH2+z*(k0/(1-x))*(CH2O-CH2O2)

HS2'=-k2*HS2+k2r*S2*H2-k6*CH2O2*HS2-k8*CH2OH2*HS2+z*(k0/(1-x))*(HS-HS2)

S2'=k2*HS2-k2r*S2*H2-k3*CH2O2*S2-k7*CH2OH2*S2+z*(k0/(1-x))*(S-S2)

H2'=k2*HS2-k2r*S2*H2-k4*HMSM2*H2+k4r*HMS2+k5-k5r*H2*OH2-k10*HCOO2*H2+k10r*HCOOH2+z*(k0/(1-x))*(H-H2)

HMSM2'=k3*CH2O2*S2-k4*HMSM2*H2+k4r*HMS2+k7*CH2OH2*S2+z*(k0/(1-x))*(HMSM-HMSM2)

HMS2'=k4*HMSM2*H2-k4r*HMS2+k6*CH2O2*HS2+k8*CH2OH2*HS2+z*(k0/(1-x))*(HMS-HMS2)

OH2'=k5-k5r*H2*OH2-k9*CH2O2*OH2+z*(k0/(1-x))*(OH-OH2)

CH3OH'=k9*CH2O*OH+k0/(1-x)*(CH3OHi-CH3OH)+(x/(1-x))*(z*(k0/(1-x)))*(CH3OH2-CH3OH)

HCOO'=k9*CH2O*OH-k10*HCOO*H+k10r*HCOOH+k0/(1-x)*(HCOOi-HCOO)+(x/(1-x))*(z*(k0/(1-x)))*(HCOO2-HCOO)

HCOOH'=k10*HCOO*H-k10r*HCOOH+k0/(1-x)*(HCOOHi-HCOOH)+(x/(1-x))*(z*(k0/(1-x)))*(HCOOH2-HCOOH)

CH3OH2'=k9*CH2O2*OH2+z*(k0/(1-x))*(CH3OH-CH3OH2)

HCOO2'=k9*CH2O2*OH2-k10*HCOO2*H2+k10r*HCOOH2+z*(k0/(1-x))*(HCOO-HCOO2)

HCOOH2'=k10*HCOO2*H2-k10r*HCOOH2+z*(k0/(1-x))*(HCOOH-HCOOH2)

```
#
aux pH=-log(H)/log(10)
#
parameters
par k0=0.001, z=0.6, Si=0.00057, x=0, CH2OHi=0.089, k1=5.5e-3, k9=0.5,
k10=1e7, k10r=1780, k1a=2100, k1r=10, k2=3.1e3, k2r=5e10, k3=5.4e6, k4=1e10,
k4r=2e-3, k5=1e-3, k5r=1e11, k6=4.5e2, k7=2, k8=0.48, CH2Oi=CH2OH*5.5e-4,
HSi=0.066, Hi=(6.2e-8*HS)/S, OHi=1e-14/H, HMSMi=0, HMSi=0, CH3OHi=0,
HCOOi=0, HCOOHi=0
#
#some initial conditions2
init H=(6.2e-8*HS)/S, CH2OH=0.089, CH2O=CH2OH*5.5e-4, HS=0.066, S=5.7e-
4, OH=1e-14/H, HMSM=0, HMS=0, H2=(6.2e-8*HS2)/S2, CH2OH2=0.089,
CH2O2=CH2OH2*5.5e-4, HS2=0.066, S2=5.7e-4, OH2=1e-14/H2, HMSM2=0,
HMS2=0, CH3OH2=0, HCOO2=0, HCOOH2=0
@ total=2000,dt=0.1,tol=1e-12, atol=1e-8, meth=cvode
@ xplot=t,yplot=pH,xhi=2000,ylo=5,yhi=14
@ maxstor=10000000
#
done
```

I

APPENDIX

Chapter 4 - A novel route to pH oscillators

The MGSG reaction – Section 4.5.2

Rate laws for MGSG reaction

$R_{4.8} = (k_{4.8} + k_{OH}[\mathrm{OH^-}])[\mathrm{CH_2(OH)_2}]$	$k_{4.8} = 5.5 \times 10^{-3} s^{-1}$
$R_{-4.8} = k_{4.8r}[\mathrm{CH_2O}]$	$k_{4.8OH} = 2100 M^{-1} s^{-1}$
	$k_{4.8r} = 10 s^{-1}$
$R_{4.9} = k_{4.9}[\mathrm{HSO_3^-}]$	$k_{4.9} = 3.1 \times 10^{3} s^{-1}$
$R_{-4.9} = k_{4.9r}[\mathrm{SO_3^{2-}}][\mathrm{H^+}]$	$k_{4.9r} = 5 \times 10^{10} M^{-1} s^{-1}$
$R_{4.10} = k_{4.10}[\mathrm{CH_2O}][\mathrm{SO_3^{2-}}]$	$k_{4.10} = 5.4 \times 10^{6} M^{-1} s^{-1}$
$R_{4.11} = k_{4.11}[\mathrm{CH_2(O^-)SO_3^-}][\mathrm{H^+}]$	$k_{4.11} = 1 \times 10^{10} M^{-1} s^{-1}$
$R_{-4.11} = k_{4.11r}[\mathrm{CH_2(OH)SO_3^-}]$	$k_{4.11r} = 2 \times 10^{-3} s^{-1}$
$R_{4.12} = k_{4.12}$	$k_{4.12} = 1 \times 10^{-3} M s^{-1}$
$R_{-4.12} = k_{4.12r}[\mathrm{H^+}][\mathrm{OH^-}]$	$k_{4.12r} = 1 \times 10^{11} M^{-1} s^{-1}$
$R_{4.13} = k_{4.13}[\mathrm{CH_2O}][\mathrm{HSO_3^-}]$	$k_{4.13} = 4.5 \times 10^{2} M^{-1} s^{-1}$
$R_{4.14} = k_{4.14}[\mathrm{CH_2(OH)_2}][\mathrm{SO_3^{2-}}]$	$k_{4.14} = 1.2 M^{-1} s^{-1}$
$R_{4.15} = k_{4.15}[\mathrm{CH_2(OH)_2}][\mathrm{HSO_3^-}]$	$k_{4.15} = 0.1 M^{-1} s^{-1}$
$R_{4.16} = (k_{4.16} + k_{4.16OH}[\mathrm{OH^-}])[\mathrm{GL}]$	$k_{4.16} = 8 \times 10^{-4} s^{-1}$
	$k_{4.16OH} = 2000 M^{-1} s^{-1}$
$R_{-4.16} = k_{4.16r}[\mathrm{GA}]$	$k_{4.16r} = 1.6 \times 10^{-4} s^{-1}$

$R_{4.17} = k_{4.17}[\mathrm{GA}]$ $\qquad$ $k_{4.17} = 2.5 \times 10^{2} s^{-1}$

$R_{-4.17} = k_{4.17r}[\mathrm{G}^{-}][\mathrm{H}^{+}]$ $\qquad$ $k_{4.17r} = 1 \times 10^{6} M^{-1} s^{-1}$

ODE script for modelling MGSG in flow reactor, with decay of gluconolactone

```
#the formaldehyde clock reaction
#
A'=-k1*A-k1a*A*OH+k1r*X-k7*S*A-k8*HS*A+k0*(Ai-A)
X'=k1*A+k1a*A*OH-k1r*X-k3*X*S+k0*(Xi-X)
HS'=-k2*HS+k2r*S*H-k6*HS*X-k8*HS*A+k0*(HSi-HS)
S'=k2*HS-k2r*S*H-k3*X*S-k7*S*A+k0*(Si-S)
H'=k2*HS-k2r*S*H-k4*XS*H+k4r*HXS+k5-k5r*H*OH+k10*GA-
k10r*G*H+k0*((H0+1e-8)/3-H)
XS'=k3*X*S-k4*XS*H+k4r*HXS+k7*S*A-k0*XS
HXS'=k4*XS*H-k4r*HXS+k6*HS*X+k8*HS*A-k0*HXS
OH'=k5-k5r*H*OH+k0*((OH0+1e-6)/3-OH)
L'=-k9*L-k9a*L*OH+k9r*GA+k0*(L0/3-L)
GA'=k9*L+k9a*L*OH-k9r*GA-k10*GA+k10r*G*H+k0*(GA0/3-GA)
G'=k10*GA-k10r*G*H+k0*(G0/3-G)
#
OH0'=k5-k5r*H0*OH0
H0'=k5-k5r*H0*OH0+k10*GA0-k10r*G0*H0
L0'=-k9*L0-k9a*L0*OH0+k9r*GA0
GA0'=k9*L0+k9a*L0*OH0-k9r*GA0-k10*GA0+k10r*G0*H0
G0'=k10*GA0-k10r*G0*H0
#
aux pH=-log(H)/log(10)
aux pH0=-log(H0)/log(10)
#
parameters
par k0=0.005, k1=5.5e-3, k1a=500, k1r=10, k2=3.1e3, k2r=5e10, k3=5.4e6,
k4=1e10, k4r=2e-3, k5=1e-3, k5r=1e11, k6=450, k7=1.0, k8=0.1, k9=1e-4,
k9a=4000, k9r=2e-5, k10=2.5e2, k10r=1e6
par Ai=0.1, Xi=Ai*5.5e-4, HSi=0.05, Si=0.005
#
#some initial conditions
init H=(6.2e-8*HS)/S, A=0.1, X=A*5.5e-4, HS=0.05, S=0.005, OH=1e-14/H, XS=0,
HXS=0, L=0.0067, G=0, GA=0
init OH0=1e-7, H0=1e-7, L0=0.0134, GA0=0, G0=0

@ total=1500,dt=0.1,tol=1e-12, atol=1e-8, meth=cvode
@ xplot=t,yplot=pH,xhi=1500,ylo=5,yhi=14
@ maxstor=10000000
#
Done
```

APPENDIX

IV

CHAPTER 5 - Acid Autocatalysis in microemulsions

Calibration of the electrode - Section 5.1

Potassium chloride solution conductivities for electrode calibration

0.001 M = 0.147 mS/ cm

0.01 M = 1.41 mS/ cm

0.1 M = 12.8 mS/ cm

1 M = 111 mS/ cm

Conductivity = cell constant × measured conductivity

Preparation of acetic acid buffer

(iv) Preparation of acetic acid buffer

The buffer solution used for Figure 5.3 was prepared with acetic acid (sigma) and sodium acetate (sigma). Acetic acid (1 M) was prepared by dilution of concentrated acetic acid (17.5 M, 29 ml made up to 500 ml with water). 0.4105 g of sodium acetate (M_r = 82.03 $gmol^{-1}$) in 500ml gives 0.01 M. The pH calculated from Henderson-Hasslebach equation is then.

$$pH = pKa + \log\frac{[A^-]}{[HA]}$$

$$pH = 4.76 + \log\frac{0.01}{1} = 2.76$$